MULTIWAVELETS AND OUTLIER DETECTION FOR TROUBLED-CELL INDICATION IN DISCONTINUOUS GALERKIN METHODS

MULTIWAVELETS AND OUTLIER DETECTION FOR TROUBLED-CELL INDICATION IN DISCONTINUOUS GALERKIN METHODS

Proefschrift

ter verkrijging van de graad van doctor
aan de Technische Universiteit Delft,
op gezag van de Rector Magnificus prof. ir. K.C.A.M. Luyben,
voorzitter van het College voor Promoties,
in het openbaar te verdedigen op dinsdag 24 januari 2017 om 15:00 uur

door

Mathea Josina VUIK

Wiskundig ingenieur, Technische Universiteit Delft,
geboren te Capelle aan den IJssel.

Dit proefschrift is goedgekeurd door de

promotor: prof. dr. ir. A.W. Heemink
copromotor: dr. J.K. Ryan

Samenstelling promotiecommissie:

Rector Magnificus,	voorzitter
prof. dr. ir. A.W. Heemink,	Technische Universiteit Delft, promotor
dr. J.K. Ryan,	University of East Anglia, Verenigd Koninkrijk, copromotor
Onafhankelijke leden:	
Prof. dr. ir. C.W. Oosterlee,	Technische Universiteit Delft
Prof. dr. S. Hickel,	Technische Universiteit Delft
Prof. dr. ir. J.J.W. van der Vegt,	Universiteit Twente
Prof. dr. S. Müller,	RWTH Aachen University, Duitsland
Prof. dr. J. Qiu,	Xiamen University, China

The research in this dissertation was supported by the Delft Institute of Applied Mathematics (DIAM), Delft University of Technology. Part of the work was also sponsored by the Air Force Office of Scientific Research (AFOSR), grant FA8655-13-1-3017.

Keywords:	Runge-Kutta discontinuous Galerkin method, high-order methods, limiters, shock detection, multiresolution analysis, wavelets, multiwavelets, troubled cells, outlier detection, boxplots
Printed by:	Proefschriftmaken.nl || Uitgeverij BOXpress
Front & back:	The front cover picture is taken by G.A. Rijsdijk and shows an F-35 reaching the speed of sound. The cover is designed by M.J. Vuik and Proefschriftmaken.nl.

Multiwavelets and outlier detection for troubled-cell indication in discontinuous Galerkin methods
Dissertation at Delft University of Technology

ISBN 978-94-92516-24-4

An electronic version of this dissertation is available at
`http://repository.tudelft.nl/`.

CONTENTS

SUMMARY

Weather forecasts, climate models, storm-surge predictions, turbulence models, aerodynamics, and the petrochemical industry are connected by the fact that they involve complex behavior. Mathematical models of these phenomena use partial differential equations (PDEs) to model this behavior. In this dissertation, the solution to these equations is approximated using the discontinuous Galerkin (DG) method. For smooth applications, the DG method works well, but problems may arise when shock waves or discontinuities appear. In that case, it is challenging to numerically approximate the solution accurately: spurious oscillations are formed close to the discontinuous regions in the approximation. These oscillations can be prevented by applying a limiter or filter near these regions, or by adding artificial viscosity to the PDEs. One of the difficulties in using a limiter is identifying the difference between a true discontinuity (in either the solution or its derivatives) and a local extremum of the approximation. Troubled-cell indicators can help to detect the discontinuous regions where a limiter should be applied. In general, this leads to more accurate results in smooth regions and reduces the computational cost significantly.

In this dissertation, a multiwavelet formulation is used to decompose the DG approximation into a sum of a global average and finer details on different levels. Using this representation, an exact relation between the multiwavelet coefficients of the highest decomposition level and jumps in (derivatives of) the DG approximation is proven. These coefficients act as a troubled-cell indicator since they suddenly increase in the neighborhood of a discontinuity. This leads to the definition of a new multiwavelet troubled-cell indicator: an element is detected as troubled if the corresponding multiwavelet coefficient is large enough in absolute value. This is tested by comparing the coefficient to the maximum coefficient (in absolute value) over the domain. Here, a parameter is required to define the strictness of the indicator. The indicator is tested for several problems based on the Euler equations in one and two dimensions. Results show that the indicator works very well if a suitable value for the parameter is used. In the two-dimensional tensor-product case, the detector can distinguish between nonsmooth regions in the x-, y-, or diagonal directions.

In general, each troubled-cell indicator requires a problem-dependent parameter. The choice of the parameter has an impact on the approximation: it determines the strictness of the troubled-cell indicator. An inappropriate choice of the parameter will result in the detection (and limiting) of too few or too many elements leading to a degrade in the approximation quality. The optimal parameter is chosen such that the minimal number of troubled cells is detected, and the resulting approximation is free of nonphysical spurious oscillations. This motivates the need for indication techniques that do not depend on problem-dependent parameters. In this dissertation, it is shown that the sudden increase or decrease in the indication value with respect to neighboring values is important for detection. Based on this observation, a new outlier-detection

algorithm is defined that uses boxplot theory. Detection occurs when the indication value of a certain element differs significantly from the neighboring value. With this technique, the problem-dependent parameter from the original indicator is no longer necessary as the parameter is chosen automatically. This can be done regardless of the indication technique. Hence, different indication techniques are tested, comparing the original parameter-based method to the outlier-detection approach in one and two dimensions. The outlier-detection approach works well and is generally better than the original parameter-based indicators. Both the weak and the strong shock regions are detected, whereas smooth regions are not selected.

Most troubled-cell indicators work well only for uniform (tensor-product) meshes. Therefore, the applicability to irregular meshes is an important consideration. Although multiwavelets were originally intended for regular meshes, this dissertation contains a construction of a multiwavelet-type basis that can be used to decompose a DG approximation on an irregular mesh. With this basis, it is possible to describe the relation between the coefficients and the jumps in (derivatives of) the DG approximation. In addition to the original outlier-detection strategy, two different techniques are studied. The first option is to weight the indication value by the mesh width; the second approach is to use a sliding-window technique. Tests are performed for different problems based on the Euler equations, using a smoothly-varying or a random mesh. Different troubled-cell indicators are applied, both in the parameter-based form and combined with outlier detection. The parameter-based methods work well as long as an appropriate value for the parameter is used. The outlier-detection results are promising, but for some applications, many elements are detected in smooth regions.

Finally, an extension of the multiwavelet theory to structured triangular meshes is given. Inspection of the multiwavelet coefficients reveals that they are very useful for discontinuity detection. Both a parameter-based and an outlier-detection multiwavelet troubled-cell indicator are constructed for this type of mesh. The indicators are tested on different problems using the two-dimensional advection equation. Applied to the initial conditions, both the parameter-based method and the outlier-detection technique work well. After time integration, the parameter-based method detects the correct elements if a suitable value for the parameter is chosen. As long as the troubled zone is not too wide, the outlier-detection method works well.

To briefly summarize this dissertation, it contains information about the use of multiwavelets and outlier detection for troubled-cell indication for discontinuous Galerkin methods. The theory and results that are presented in this work give more insight and knowledge into the area of multiwavelets, and can be used to improve detection techniques and construct parameter-free indicators.

SAMENVATTING

Weersvoorspellingen, klimaatmodellen, stormvloedvoorspellingen, turbulentiemodellen, aerodynamica, en de petrochemische industrie vertonen vaak complex gedrag. Wiskundige modellen van deze fenomenen gebruiken partiële differentiaalvergelijkingen (PDVs) om dit gedrag te voorspellen. In deze dissertatie wordt de oplossing van deze vergelijkingen benaderd met behulp van de discontinue Galerkinmethode (DG). Voor gladde toepassingen werkt de DG methode goed, maar als er schokgolven of discontinuïteiten voorkomen, kunnen problemen ontstaan. In dat geval is het een uitdaging om de oplossing nauwkeurig met een numerieke methode te benaderen: in de buurt van de discontinue regio's verschijnen ongewenste oscillaties in de benadering. Deze oscillaties kunnen voorkomen worden door een limiter of een filter rond deze regio's toe te passen, of door artificiële viscositeit aan de PDVs toe te voegen. Eén van de moeilijkheden bij het gebruik van een limiter is het verschil te identificeren tussen een echte discontinuïteit (in de oplossing of haar afgeleiden) en een lokaal extremum van de benadering. Troubled-cell indicatoren kunnen helpen om de discontinue regio's te detecteren waar een limiter moet worden toegepast. Over het algemeen leidt dit tot nauwkeuriger resultaten in gladde gebieden, en geeft dit een aanzienlijke afname van de rekentijd.

In deze dissertatie wordt een multiwaveletformulering gebruikt om de DG benadering te ontbinden in een som van een globaal gemiddelde en fijnere details op verschillende niveaus. Met behulp van deze representatie wordt een exacte relatie tussen de multiwaveletcoëfficiënten van het hoogste ontbindingsniveau en sprongen in (afgeleiden van) de DG benadering bewezen. Deze coëfficiënten fungeren als een troubled-cell indicator, aangezien zij plotseling stijgen in de buurt van een discontinuïteit. Dit leidt tot de definitie van een nieuwe multiwavelet troubled-cell indicator: een element wordt als afwijkend gedetecteerd als de bijbehorende multiwaveletcoëfficiënt groot genoeg is in absolute waarde. Dit wordt getest door de coëfficiënt te vergelijken met de maximale coëfficiënt (in absolute waarde) in het domein. Hier is een parameter vereist die de strengheid van de indicator definieert. De indicator wordt getest voor verschillende problemen gebaseerd op de Eulervergelijkingen in één en twee dimensies. Resultaten tonen aan dat de indicator zeer goed werkt mits een geschikte waarde voor de parameter gebruikt wordt. Bij tweedimensionale tensorproductruimten kan de detector onderscheid maken tussen niet-gladde gebieden in de x-, y-, of diagonale richtingen.

Over het algemeen vereist iedere troubled-cell indicator een probleemafhankelijke parameter. De keuze van de parameter heeft invloed op de benadering: het bepaalt de strengheid van de troubled-cell indicator. Een ongeschikte keuze van de parameter zal resulteren in de detectie (en limiting) van te weinig of teveel elementen, wat leidt tot een afname van de benaderingskwaliteit. De optimale parameter wordt op zo'n manier gekozen dat het minimum aantal troubled cells gedetecteerd wordt, en de resulterende benadering vrij van niet-fysische oscillaties is. Dit motiveert de noodzaak voor indicatietechnieken die niet afhangen van probleemafhankelijke parameters. In deze disser-

tatie wordt aangetoond dat de plotselinge stijging of daling van de indicatiewaarde met betrekking tot buurwaarden voor detectie van belang is. Gebaseerd op deze observatie wordt een nieuw outlierdetectiealgoritme gedefinieerd dat boxplottheorie gebruikt. Detectie vindt plaats als de indicatiewaarde van een zeker element significant afwijkt van de buurwaarde. Met deze techniek is de probleemafhankelijke parameter van de originele indicator niet langer nodig, omdat de parameter automatisch gekozen wordt. Dit kan onafhankelijk van de gekozen indicatietechniek gedaan worden. Daarom worden verschillende indicatietechnieken getest, waarbij de originele parameter-based methode vergeleken wordt met de outlierdetectieaanpak in één en twee dimensies. De outlierdetectieaanpak werkt goed, en is over het algemeen beter dan de originele parameterbased indicatoren. Zowel de zwakke als de sterke schokregio's worden gedetecteerd, terwijl gladde gebieden niet geselecteerd worden.

De meeste troubled-cell indicatoren werken alleen goed voor uniforme (tensorproduct)roosters. Daarom is de geschiktheid voor onregelmatige roosters een belangrijke overweging. Hoewel multiwavelets oorspronkelijk bedoeld waren voor regelmatige roosters, bevat deze dissertatie een constructie van een type multiwaveletbasis die gebruikt kan worden om een DG benadering op een onregelmatig rooster te ontbinden. Met deze basis is het mogelijk om de relatie tussen de coëfficiënten en de sprongen in (afgeleiden van) de DG benadering te beschrijven. Naast de originele outlierdetectiestrategie worden twee andere technieken bestudeerd. De eerste optie is om de indicatiewaarde te wegen met de roosterwijdte, de tweede aanpak is om een sliding-window techniek te gebruiken. Tests worden uitgevoerd voor verschillende problemen gebaseerd op de Eulervergelijkingen, gebruikmakend van een gelijkmatig variërend of een willekeurig rooster. Verschillende troubled-cell indicatoren worden toegepast, zowel in de parameter-based vorm, als gecombineerd met outlierdetectie. De methoden die gebaseerd zijn op parameters werken goed, mits een geschikte waarde voor de parameter gekozen wordt. De outlierdetectieresultaten zijn veelbelovend, maar voor sommige toepassingen worden veel elementen in gladde regio's gedetecteerd.

Tot slot wordt een uitbreiding van de multiwavelettheorie naar gestructureerde driehoekige roosters gegeven. Inspectie van de multiwaveletcoëfficiënten wijst uit dat zij zeer geschikt zijn voor discontinuïteitdetectie. Zowel een parameter-based als een outlierdetectie multiwavelet troubled-cell indicator worden voor dit type rooster geconstrueerd. De indicatoren worden getest op verschillende problemen, gebruikmakend van de tweedimensionale advectievergelijking. Bij toepassing op de beginvoorwaarden werken zowel de parameter-based methode als de outlierdetectietechniek goed. Na tijdsintegratie detecteert de parameter-based methode de correcte elementen als een geschikte waarde voor de parameter gekozen wordt. Zolang de troubled zone niet te breed is, werkt de outlierdetectiemethode goed.

Kort samengevat bevat deze dissertatie informatie over het gebruik van multiwavelets en outlierdetectie voor troubled-cell indicatie bij discontinue Galerkinmethoden. De theorie en resultaten die in dit werk gepresenteerd worden geven meer inzicht in en kennis over het multiwaveletdomein, en kunnen gebruikt worden om detectietechnieken te verbeteren en parametervrije indicatoren te construeren.

1

INTRODUCTION

1.1. MOTIVATION

Weather forecasts, climate models, storm-surge predictions, turbulence models, aerodynamics, and the petrochemical industry are connected by the fact that they involve complex behavior. Physical experiments to approximate the behavior of these fluids are usually very expensive and done on a small scale. It is difficult to translate these results to the large scales that occur in nature. Therefore, scientists try to describe these phenomena using mathematical and numerical models. Clearly, it is crucial for the computed results to be accurate. For smooth applications, numerical methods generally work well, but problems may arise when shock waves or discontinuities appear. In that case, the density, velocity, pressure or energy of the fluid is changing very rapidly in a particular region, and can be seen as discontinuous. Three examples appear in Figure 1.1 [117, 118, 128]: a high-velocity flow field around a space shuttle (Figure 1.1(a)); shock waves when an aircraft approaches the speed of sound (Figure 1.1(b)); and a shock tube with different gasses reacting to each other (Figure 1.1(c)). In these cases, it is difficult to predict the fluid behavior accurately using numerical methods.

The mathematical description of a physical phenomenon involving fluids is usually obtained using partial differential equations (PDEs). Several different numerical methods are known for approximating the solutions to these equations. Examples of such methods are the finite-difference method, finite-volume method, and finite-element method. In this dissertation, the discontinuous Galerkin (DG) method is used. This method combines features of the finite-volume method with properties of the finite-element method. This method is useful for higher-order approximations, complex geometries, parallel implementations, and is often used for conservation laws [68]. For all these methods, spurious oscillations are formed close to discontinuous regions in the fluid. These oscillations can be prevented by applying a limiter or filter near these regions, or by adding artificial viscosity to the PDEs.

One of the difficulties is identifying the difference between a true discontinuity (in either the solution or its derivatives) and a local extremum of the fluid quantity. As an

1

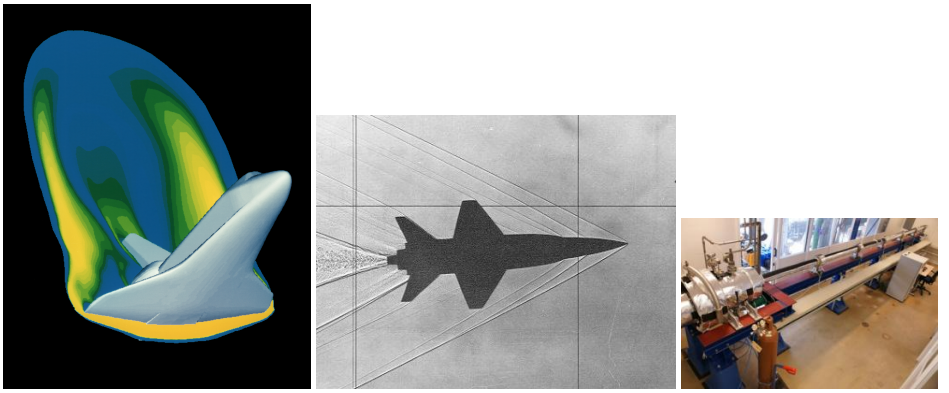

(a) Space Shuttle flow [128] (b) Shock wave around aircraft [118] (c) Shock tube [117]

Figure 1.1: Phenomena in which shock waves appear.

illustration, the DG method is applied to the linear advection equation $u_t + u_x = 0$ using periodic boundary conditions, and an initial profile consisting of a square wave, a triangle, a combination of half-ellipses, and a combination of Gaussians [81, 88] (Figure 1.2). This is an important example because it features functions that are either discontinuous, or discontinuous in the derivative. Without the application of a limiter, spurious oscillations are found. A limiter can remove these oscillations, but it also does not give a good approximation to the smooth extrema in the ellipses and the Gaussians. Therefore, the limited approximation is too diffusive.

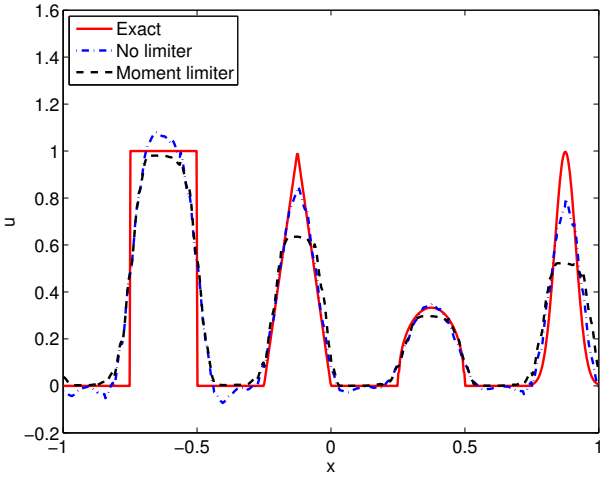

Figure 1.2: Exact solution and two approximations, one with limiting and one without, to the linear advection equation, $u_t + u_x = 0$, at time $T = 1.5$, using a nonsmooth initial condition and periodic boundary conditions. From left to right: square wave, triangle, two half-ellipses, and a combination of Gaussians. Number of elements is 64; polynomial degree is 1.

The performance of limiting techniques can be improved by using a troubled-cell indicator. Such an indicator detects discontinuous regions where a limiter should be applied. In general, this leads to more accurate results in smooth regions and reduces the computational cost significantly. Many troubled-cell indicators use the numerical approximation to detect discontinuities [30, 83]. Others apply multiresolution ideas based on mesh refinement [38, 65, 66, 110]. In this dissertation, we investigate the use of multiwavelet decompositions for discontinuity detection. This idea occurred in earlier work [136], in which we tried to construct a multiwavelet limiter. Wavelets are well-known for edge detection in e.g., images [91, 111] and signal processing [78] and multiresolution-based finite-volume and DG schemes (Section 1.2).

In general, each troubled-cell indicator requires a problem-dependent parameter. The choice of the parameter has an impact on the approximation: it determines the strictness of the troubled-cell indicator. An inappropriate choice of the parameter will result in the detection (and limiting) of too few or too many elements. Detection of too few elements leads to spurious oscillations since not enough elements are limited. If too many elements are detected, then the limiter is applied too often, and therefore, the method is more costly, and the approximation smooths out after a long time. The optimal parameter is chosen such that the minimal number of troubled cells is detected, and the resulting approximation is free of nonphysical spurious oscillations. In general, many tests are required to obtain this optimal parameter for each problem [104, 148].

As an example, the KXRCF shock detector [83] is applied to the linear advection equation on $[-1,1]$ using the smooth initial condition $-1+0.5\sin(10\pi x)$ and periodic boundary conditions. In Figure 1.3, a time-history plot is given that shows the locations of the detected troubled cells in space and time. Here, the threshold value of the indicator is taken equal to 1, which is generally done in the literature [83]. Since the function is smooth, no elements should be detected, but the KXRCF detector selects many cells. This motivates the need for indication techniques that do not depend on problem-dependent parameters and do not detect elements when the function is smooth.

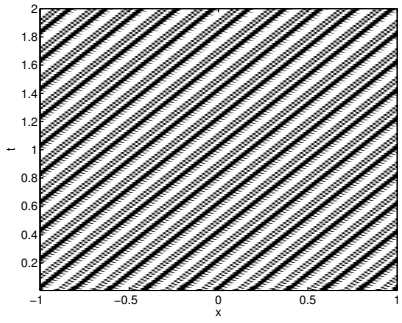

Figure 1.3: Detected troubled cells using the KXRCF shock detector (threshold 1) applied to the linear advection equation using initial condition $-1+0.5\sin(10\pi x)$ and periodic boundary conditions. Number of elements is 128; polynomial degree is 2.

1

1.2. SUMMARY OF EXISTING RESULTS IN THE LITERATURE

In the previous section, a motivation was given for the investigation of troubled-cell indicators. This section contains a summary of the existing literature on the RKDG method and limiting (Section 1.2.1), troubled-cell indicators (Section 1.2.2), multiresolution analysis (Section 1.2.3), multiwavelets (Section 1.2.4), irregular meshes (Section 1.2.5) and triangular meshes (Section 1.2.6).

1.2.1. RKDG METHOD AND LIMITING

Nonlinear hyperbolic partial differential equations (PDEs) are often solved using the Runge-Kutta discontinuous Galerkin (RKDG) method [28–31], which is discussed in Section 2.1. In the case of discontinuous solutions, limiting techniques are used to reduce the spurious oscillations that develop in discontinuous regions. Examples of these limiters are the minmod-based TVB limiter [30], TVD limiters [27], WENO [120, 121], the moment limiter [81], and the vertex-based limiter [85], see Section 2.2. Unfortunately, most of the limiters do not work well for higher-order approximations or multidimensional cases. Limiters tend to detect smooth extrema as being discontinuous and can, therefore, reduce the accuracy in these regions [16, 49]. Troubled-cell indicators help to detect the discontinuous regions.

1.2.2. TROUBLED-CELL INDICATORS

There is a variety of troubled-cell indicators, some that are tied to the limiting procedure and others that are separate from this process. A few of the relevant methods for troubled-cell indication are the minmod-based TVB limiter [30], Harten's subcell resolution [63], moment limiters [81], monotonicity preserving limiters [129], and the shock detector of Krivodonova et al. (KXRCF) [83], which are discussed in more detail in Section 2.3. These methods for indicating troubled cells were explored and compared by Qiu and Shu in [104]. Their motivation was to improve the performance of a WENO-based limiter for DG. They found that there was no universally better performing method for every problem. However, they did conclude that the minmod-based limiter with a suitably-chosen problem-dependent parameter, Harten's method, and the KXRCF shock detector performed better than other methods.

1.2.3. MULTIRESOLUTION ANALYSIS

In addition to the troubled-cell indicators mentioned above, it is possible to use multiresolution analysis for shock detection. This idea was first explored by Harten, who used this approach to design a hybrid scheme where numerical fluxes are computed using either a finite-difference approximation in smooth regions (computationally inexpensive) or an upwind discretization (e.g. ENO, TVB) near discontinuities (computationally expensive). The flux decision was made using multiresolution analysis on discrete data [1, 7, 64, 67, 113]. Here, we give an incomplete list of publications that use his work: [12–15, 26, 34, 41].

Biorthogonal wavelets [22, 33] are a generalization of this framework, and coincide with multiresolution analysis on discrete data for both the discrete [62] and continuous levels. This is related to the convergence of subdivision schemes [24, 32–34, 42, 50].

A second option is to use multiresolution analysis for local grid adaptation for finite-volume schemes [35, 61, 94]. Here, details below a threshold are ignored, and the remaining significant details are used to determine a locally refined mesh. Applications can be found in [18, 19, 35, 37, 45, 61, 77, 94, 96, 109, 110]. The articles [36, 95] present a nice review of this subject.

In addition, it is possible to use Harten's multiresolution method to determine the smoothness of the approximation [38, 65, 66, 110]. In [99], this is done using a threshold depending on the standard deviation of the multiresolution coefficients. Finally, in [123], the B-spline wavelet and the modified multiresolution method of Harten were used to estimate the Lipschitz exponent of the underlying function. Note that this approach is not applicable to the multiwavelet bases that are used in this dissertation.

1.2.4. MULTIWAVELETS

In this dissertation, ideas from Alpert's multiwavelet formulation [4, 5] are used to decompose the DG approximation into a sum of a global average and finer details on different levels. The corresponding multiwavelet coefficients provide useful information about the structure of the approximation.

In the literature, the multiwavelet theory is combined with the DG method in various ways. In [8], a so-called *multiwavelet discontinuous Galerkin method* is presented. In that paper, the DG method is written in terms of its multiresolution decomposition, and grid adaptivity is obtained by manipulating the multiwavelet coefficients [5]. The thresholding technique for adaptive DG methods is formalized using the cancelation property for the decay of multiwavelet coefficients [8, 21, 55, 56, 72, 112] (see Section 2.4.6). Multiwavelets are also important for the construction of sparse-grid discontinuous Galerkin methods [142].

1.2.5. IRREGULAR MESHES IN ONE DIMENSION

Most troubled-cell indicators work well on uniform (tensor-product) meshes but are less accurate for nonuniform irregular meshes. As an example, Figure 1.4 contains time-history plots of the detected troubled cells for the blast-wave problem (Section 2.5.3) using either a uniform or a random mesh. The results for the uniform mesh are much sharper than for the random mesh.

Moreover, it is extremely challenging to design a multiwavelet troubled-cell indicator, since multiwavelets were originally intended for regular meshes. Several different extensions to the irregular case are given in the literature, for example, the review paper [43]. This paper particularly focuses on the use of subdivision schemes, starting from the finest irregular mesh. Subdivision is used to find an approximation on a coarser mesh together with an extrapolation to the finer mesh. This leads to so-called *interpolating wavelets*, which are related to B-spline dual scaling functions and form a biorthogonal basis [43].

A second construction is the design of a multiresolution representation for nonuniform meshes using point-value and cell-average discretizations as scaling-function coefficients [2]. The corresponding prediction error is related to wavelet coefficients. This method does not work for higher-order polynomials and is therefore not applicable to general multiwavelet spaces.

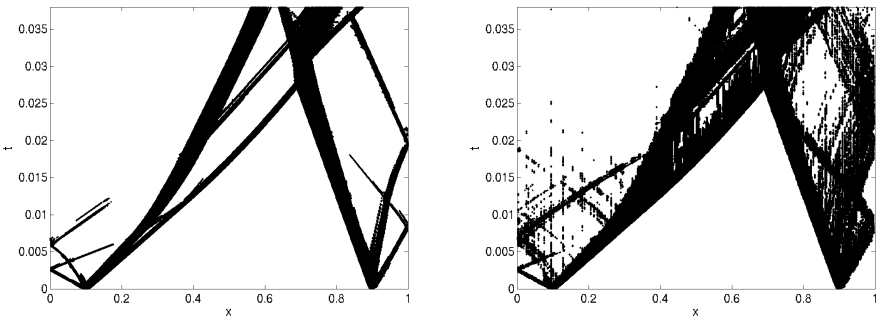

(a) Uniform mesh (b) Random mesh

Figure 1.4: Detected troubled cells using the KXRCF shock detector applied to the blast-wave problem. Number of elements is 512; polynomial degree is 2.

Another option is to project a general nonuniform mesh onto a uniform mesh of 2^n elements, such that the standard multiwavelet techniques can be used. However, this can be costly, introduces artifacts and is not straightforward for multidimensions [43].

Finally, the *lifting scheme* is seen as very promising [131]. In this approach, an existing wavelet is modified by adding linear combinations of the scaling function at the same level, which leads to so-called *second-generation wavelets*. Therefore, the multiresolution analysis, the decomposition and reconstruction steps, and the scaling functions are generalized to apply to irregular meshes. As a result, the filters for decomposition and reconstruction depend on the size of the elements, and finite lifting filters lead to biorthogonal wavelet bases, instead of the orthogonal bases that are used in this dissertation. Lifting has many advantages: the wavelet transform can be computed faster, since no extra memory is needed, and the wavelet transform is easy to invert and to parallelize [9, 44, 57, 76, 78, 90, 91, 101, 107, 130]. Moreover, there is no need to use the Fourier transform which makes it possible to use the lifting approach for irregular meshes. The resulting wavelets are no longer translations and dilations of one function on the coarsest level, but can be adapted to general meshes while maintaining orthogonality [11, 131, 134]. However, lifting wavelets are very different from Alpert's multiwavelets that are used in this dissertation. Note that the lifting scheme is closely related to the more general concept that was proposed and analytically investigated in [22].

It is also possible to combine the lifting scheme with the interpolating wavelet transform [43, 134]. Interpolating wavelets do have shortcomings, of which the aliasing property is the most dangerous one since it can lead to unstable or inaccurate results.

A very different idea is to construct multiwavelets which are adapted to the nonuniform mesh following the construction for nonuniform Haar wavelets [47, 94]. The extension of the work in [47] to higher orders is done for so-called *supercompact* multiwavelets [6]. These functions differ slightly from Alpert's multiwavelets: the basis is not directly constructed, and uniqueness is achieved in a different way [4, 10]. For a nonuniform mesh, the decomposition and reconstruction steps depend on the element size,

which makes them more time consuming than for a uniform mesh. It seems as if the multiwavelet basis in [6] is not able to represent a DG approximation exactly. It is also possible to use Alpert's algorithm directly to design multiwavelets on an irregular mesh [56, 97, 103]. Here, the multiwavelets are location dependent, but it is possible to represent a DG approximation exactly. More information about these approaches can be found in Chapter 5.

1.2.6. STRUCTURED TRIANGULAR MESHES

In two dimensions, wavelet theory is traditionally applied to tensor-product rectangular meshes [91]. However, in practice, triangular meshes are often more useful. Although it is possible to use modal DG based on a PKD-polynomial basis [93], it is more convenient to use the nodal form of the DG method for this mesh type [27, 31, 68], see Section 6.3. These two forms are equivalent: the corresponding degrees of freedom can be transformed with the help of a Vandermonde matrix [68].

Multiwavelets on triangular meshes are investigated in the course of supercompact wavelets [10, 52]. In these papers, the scaling functions are constructed based on the two-dimensional Legendre polynomials. Although the multiwavelets are not constructed explicitly, the multiwavelet coefficients can be computed using the orthogonality relations between scaling functions and multiwavelets. In [52], these coefficients are used to detect troubled cells by taking the Euclidean norm of the coefficients on each element and detecting the elements for which this norm is big enough. Knowledge of the discontinuity line is required to detect the troubled cells [52].

A very different procedure is to construct the wavelet basis on a triangle using the lifting approach [127].

Finally, it is possible to orthogonalize the two-dimensional monomials in barycentric form to obtain scaling functions, and construct barycentric multiwavelets on a triangle using a slight adaptation of Alpert's algorithm [146], see Chapter 6. The corresponding scaling functions and multiwavelets are given in [122], together with a thresholding method for detection of discontinuities on a triangular mesh. Here, a parameter is needed that depends on the exact solution to the problem.

1.3. DISSERTATION OBJECTIVES

This dissertation aims to develop new troubled-cell indication techniques based on multiwavelets and outlier detection. The objectives are defined as follows:

- Construct a troubled-cell indicator based on multiwavelets to detect discontinuous regions in a DG approximation;
- Develop a method to remove problem-dependent parameters in troubled-cell indicators;
- Investigate the applicability of the troubled-cell indicators to irregular meshes.

In the next section, the outline of the dissertation is given.

1

1.4. DISSERTATION OUTLINE

- In Chapter 2, background theory is given on the Runge-Kutta DG method, limiters, troubled-cell indicators, multiresolution analysis, and several test problems.
- In Chapter 3, the relation between the multiwavelet expansion and the DG formulation is given. It is shown that the multiwavelet coefficients are related to the jumps in (derivatives of) the DG approximation. Furthermore, the multiwavelet troubled-cell indicator is introduced and compared with different troubled-cell indicators for several one- and two-dimensional examples.
- In Chapter 4, the outlier-detection algorithm is constructed and applied to various troubled-cell indication variables. The original troubled-cell indicators (with optimal parameter) are compared with the new outlier-detection indicators.
- In Chapter 5, information about the construction of a multiwavelet-type expansion for a one-dimensional irregular mesh is given. Different troubled-cell indication techniques are tested and compared.
- In Chapter 6, the multiwavelet theory is extended to a structured triangular mesh. In particular, a multiwavelet troubled-cell indicator is constructed and tested both in the parameter-based form, and combined with outlier detection.
- Finally, in Chapters 7 and 8, the conclusions of this dissertation and some recommendations for future research are given.

2

BACKGROUND

This chapter contains the theoretical background for the Runge-Kutta DG method (Section 2.1), limiters (Section 2.2), troubled-cell indicators (Section 2.3), multiresolution analysis (Section 2.4), and several test problems (Section 2.5).

2.1. RUNGE-KUTTA DISCONTINUOUS GALERKIN METHOD

In this section, the Runge-Kutta discontinuous Galerkin (DG) method is explained in its modal form. The equivalence with nodal DG is explained in Section 2.1.2.

2

2.1.1. MODAL DISCONTINUOUS GALERKIN METHOD

The Runge-Kutta DG method [28–31] in modal form is illustrated using the following boundary-value problem:

$$\begin{aligned} u_t + f(u)_x &= 0, \qquad x \in [a,b],\ t > 0, \\ u(x,0) &= u^0(x),\ x \in [a,b], \end{aligned} \tag{2.1}$$

where $u = u(x,t)$ is some quantity of interest, $f(u)$ describes the flux function, and periodic boundary conditions are used.

In order to perform a numerical simulation, we must first discretize $[a,b]$. This is obtained by dividing the domain into a uniform mesh of 2^n elements (used in the multiwavelet expansion, Section 2.4) via $\Delta x = (b-a)/2^n$. The element centers are given by $x_j = a + (j+1/2)\Delta x$, and

$$I_j = [x_{j-\frac{1}{2}}, x_{j+\frac{1}{2}}),\ j = 0,\dots,2^n-1,$$

where the choice for half-open intervals follows from the paper of Archibald et al. [8]. Different choices are available in the literature, for example, closed intervals (Hovhannisyan et al. [71]), or open intervals (Gerhard et al. [55]).

The approximation space that we use on each element is $V_h(I_j) = \{v \in \mathbb{P}^k(I_j)\}$, where $\mathbb{P}^k(I_j)$ is the space of polynomials of degree k on element I_j. In order to take advantage of the multiwavelet properties, the basis for $\mathbb{P}^k$ is constructed using the Legendre polynomials, which are defined as

$$P^{(0)}(x) = 1, \quad P^{(1)}(x) = x, \quad (\ell+1)P^{(\ell+1)}(x) = (2\ell+1)xP^{(\ell)}(x) - \ell P^{(\ell-1)}(x), \quad \ell \geq 2.$$

These functions satisfy $\langle P^{(m)}, P^{(n)} \rangle = 2/(2n+1)\delta_{mn}$. The corresponding set of scaled Legendre polynomials is defined as

$$\phi_\ell(x) = \sqrt{\ell + \frac{1}{2}} P^{(\ell)}(x), \tag{2.2}$$

which forms an orthonormal basis for $\mathbb{P}^k$.

The discontinuous Galerkin method is based on the weak formulation of the equation, which is obtained by multiplying the equation by an arbitrary, smooth function $v \in C^1[x_{j-\frac{1}{2}}, x_{j+\frac{1}{2}}]$, and integrating over I_j, $j \in \{0,\dots,2^n-1\}$ [27]. Using integration by parts, this yields

$$0 = \int_{I_j} (u_t + f(u)_x) v dx = \int_{I_j} u_t v dx + f(u) v \,|_{x_{j-\frac{1}{2}}}^{x_{j+\frac{1}{2}}} - \int_{I_j} f(u) v_x dx. \tag{2.3}$$

Next, v is replaced by a test function $v_h \in V_h(I_j)$, and the exact solution u by the approximate solution $u_h \in V_h(I_j)$. Using local coordinates $\xi = 2/\Delta x \cdot (x - x_j)$, these functions

can be expressed as

$$v_h(x) = \phi_m(\xi), \qquad m \in \{0, \dots, k\}, \tag{2.4a}$$

$$u_h(x,t) = \sum_{\ell=0}^{k} u_j^{(\ell)}(t)\phi_\ell(\xi), \text{ on element } I_j, \tag{2.4b}$$

where $u_j^{(\ell)}(t), \ell = 0, \dots, k$, are the unknown DG coefficients. Using equation (2.4) in the weak formulation as given in (2.3) yields

$$\int_{I_j} u_{h,t}(\xi)\phi_m(\xi)dx = \int_{I_j} f(u_h(\xi))\frac{d}{dx}\phi_m(\xi)dx - f(u_h)v_h\,|_{x_{j-\frac{1}{2}}}^{x_{j+\frac{1}{2}}}. \tag{2.5}$$

If we transform to $\xi = 2/\Delta x \cdot (x - x_j)$, with

$$\frac{\Delta x}{2}d\xi = dx \quad \text{and} \quad \frac{d}{d\xi}\frac{d\xi}{dx} = \frac{2}{\Delta x}\frac{d}{d\xi},$$

and use the orthonormality property of the scaled Legendre polynomials, equation (2.5) can be written as

$$\frac{\Delta x}{2}\frac{du_j^{(m)}}{dt} = \int_{-1}^{1} f(u_h(\xi))\phi'_m(\xi)d\xi + \hat{F}_{j-\frac{1}{2}}v^+_{h,j-\frac{1}{2}} - \hat{F}_{j+\frac{1}{2}}v^-_{h,j+\frac{1}{2}}, \tag{2.6}$$

where $\hat{F}_{j\pm\frac{1}{2}}$ denote the flux values through the boundaries $x_{j\pm\frac{1}{2}}$, and the test function v_h at the boundaries $x_{j\pm\frac{1}{2}}$ is taken from inside the cell, given by $v^+_{h,j-\frac{1}{2}}$ and $v^-_{h,j+\frac{1}{2}}$, see Figure 2.1.

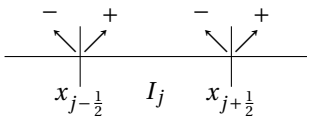

Figure 2.1: Boundaries of interval I_j.

Equation (2.6) presents an ambiguity as the DG approximation is discontinuous at the points $x_{j\pm\frac{1}{2}}$ (Figure 2.2).

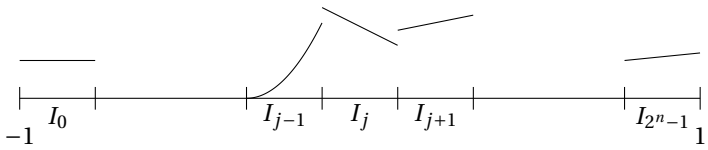

Figure 2.2: Example of a DG approximation, which is typically discontinuous at element boundaries.

In this dissertation, the local Lax-Friedrichs flux is used [88], which is defined as,

$$\hat{F}_{j-\frac{1}{2}} = \frac{1}{2}\left(f(u^-_{h,j-\frac{1}{2}}) + f(u^+_{h,j-\frac{1}{2}}) - a_{j-\frac{1}{2}}(u^+_{h,j-\frac{1}{2}} - u^-_{h,j-\frac{1}{2}})\right), \tag{2.7a}$$

where,

$$a_{j-\frac{1}{2}} = \max(|f'(u_h)|) \text{ over all } u_h \text{ between } u^-_{h,j-\frac{1}{2}} \text{ and } u^+_{h,j-\frac{1}{2}}. \tag{2.7b}$$

If f is convex, this reduces to,

$$a_{j-\frac{1}{2}} = \max(|f'(u^-_{h,j-\frac{1}{2}})|, |f'(u^+_{h,j-\frac{1}{2}})|). \tag{2.7c}$$

Using this flux, equation (2.6) can be written as a system of ordinary differential equations (ODEs) in time. Let $\mathbf{u}_j = (u_j^{(0)}, \ldots, u_j^{(k)})^\top$, then for each $j \in \{0, \ldots, 2^n - 1\}$ we have to find a solution to

$$\frac{d}{dt}\mathbf{u}_j = \frac{2}{\Delta x}\left(\int_{-1}^{1} f(u_h(\xi))\phi_m'(\xi)d\xi + \hat{F}_{j-1/2}v^+_{h,j-1/2} - \hat{F}_{j+1/2}v^-_{h,j+1/2}\right) = L(\mathbf{u}_{j-1}, \mathbf{u}_j, \mathbf{u}_{j+1}).$$

For time evolution, the third-order strong stability-preserving Runge-Kutta scheme is used [58, 120]. Let $\mathbf{w}_j^s,\ j = 0, \ldots, 2^n - 1$ be the DG coefficients at time $t^s = s\Delta t$, where $s = 0, 1, 2, \ldots$, then the DG coefficients $\mathbf{w}_j^{s+1}$ at time t^{s+1} are computed using:

$$\begin{aligned}
\mathbf{w}_j^* &= \mathbf{w}_j^s &&+\ \Delta t L(\mathbf{w}_{j-1}^s, \mathbf{w}_j^s, \mathbf{w}_{j+1}^s),\\
\mathbf{w}_j^{**} &= \frac{3}{4}\mathbf{w}_j^s &&+\frac{1}{4}\mathbf{w}_j^* + \frac{1}{4}\Delta t L(\mathbf{w}_{j-1}^*, \mathbf{w}_j^*, \mathbf{w}_{j+1}^*),\\
\mathbf{w}_j^{s+1} &= \frac{1}{3}\mathbf{w}_j^s &&+\frac{2}{3}\mathbf{w}_j^{**} + \frac{2}{3}\Delta t L(\mathbf{w}_{j-1}^{**}, \mathbf{w}_j^{**}, \mathbf{w}_{j+1}^{**}).
\end{aligned}$$

Note that we could use other strong stability preserving time-stepping methods, [59, 79, 119]: this is only a choice that is made.

The extension to a two-dimensional tensor-product mesh is explained in [28, 31, 137]. In that case, the approximation space equals $\mathbb{Q}^k = \text{span}\{x^m y^n : 0 \le m, n \le k\}$. The DG method for a triangular mesh is discussed in Chapter 6 [27, 31, 68, 140].

2.1.2. NODAL DISCONTINUOUS GALERKIN METHOD

The relation between the modal and the nodal form of the DG method is clearly explained in [68, 98]. The local DG approximation of degree k in element I_j can be written as

$$u_h(x) = \sum_{i=0}^{k} u_j^{(i)}\phi_i(\xi) = \sum_{i=0}^{k} u_h(x_j^{(i)})\ell_i(\xi), \quad \xi = \frac{2}{\Delta x}(x - x_j).$$

The first expression is the modal form in the Legendre-polynomial basis. The degrees of freedom belong to the spectral (Legendre) space. The right-hand side is the corresponding nodal representation, expressed using the function values at local gridpoints $x_j^{(0)}, \ldots, x_j^{(k)}$, based on the Legendre-Gauss-Lobatto nodes $\xi_0, \ldots, \xi_k$, and the corresponding Lagrange polynomials [68]. This form is computationally more efficient since there is no need to transform from the spectral to the physical space. However, in this dissertation we need the modal form for limiting, troubled-cell indication and multiwavelet decomposition.

By construction, the Lagrange polynomials satisfy $\ell_i(\xi_m) = \delta_{im}$. This means that

$$u_h(x_j^{(m)}) = \sum_{i=0}^{k} u_j^{(i)} \phi_i(\xi_m) = \sum_{i=0}^{k} u_h(x_j^{(i)}) \ell_i(\xi_m) = u_h(x_j^{(m)}).$$

This allows for defining a so-called *Vandermonde matrix* to switch between the nodal and the modal form. Let $\mathbf{u}_j = (u_j^{(0)}, \ldots, u_j^{(k)})^\top$ and $\mathbf{u}_j^h = (u_h(x_j^{(0)}), \ldots, u_h(x_j^{(k)}))^\top$, and define the $(k+1) \times (k+1)$ matrix $\mathbf{V}$ by $V_{mi} = \phi_i(\xi_m)$. Then $\mathbf{V}\mathbf{u}_j = \mathbf{u}_j^h$ and $\mathbf{V}^{-1}\mathbf{u}_j^h = \mathbf{u}_j$.

In practical applications, the solution to a hyperbolic PDE often contains shocks and discontinuities. In that case, the DG approximation may contain spurious oscillations. One way to get rid of these oscillations is by the application of a limiter. The next section contains a short discussion of the two different limiters that are used in this dissertation.

2.2. LIMITING

In this dissertation, the moment limiter is used for one-dimensional applications, and for two-dimensional applications based on a tensor-product rectangular mesh [81]. The extension of this limiter to triangular meshes is not known, and therefore, the vertex-based limiter of Kuzmin is used [85]. Note that these are only choices - other limiters are also possible.

2.2.1. MOMENT LIMITER

The moment limiter [81] reduces the DG approximation to a low-order approximation in discontinuous regions and maintains a high order if the approximation is smooth enough.

The DG approximation on element I_j is given by $u_h(x) = \sum_{\ell=0}^{k} u_j^{(\ell)} \phi_\ell(\xi)$, where $u_j^{(\ell)}$ are the DG coefficients (Section 2.1). The moment limiter modifies these coefficients, starting at the highest degree k. For each element I_j, the limited value of coefficient $u_j^{(k)}$ equals

$$\tilde{u}_j^{(k)} = m\left(u_j^{(k)}, \beta_k\left(u_{j+1}^{(k-1)} - u_j^{(k-1)}\right), \beta_k\left(u_j^{(k-1)} - u_{j-1}^{(k-1)}\right)\right), \tag{2.8}$$

with $\beta_k = (\sqrt{k-1/2})/(\sqrt{k+1/2})$ and using the minmod function (equation (2.13)). If $\tilde{u}_j^{(k)} = u_j^{(k)}$, then the limiting procedure is cut off for this element I_j. If not, then $u_j^{(k-1)}$ is limited using the same procedure, continuing until $u_j^{(1)}$ is limited, or stopping the first time $\tilde{u}_j^{(\ell)} = u_j^{(\ell)}$ for some $\ell = k-1, \ldots, 1$.

For systems of equations, the limiter should be applied to the characteristic variables $\mathbf{w}_j^{(\ell)} = R^{-1}\mathbf{u}_j^{(\ell)}$. Due to this approach, it is possible that negative values for density, pressure, or energy are found. In that case, all higher-order coefficients are set equal to zero, and $u_j^{(1)}$ is limited using equation (2.8). If negative values are still found, then the linear coefficient is also set equal to zero.

In two dimensions, the moment limiter uses the neighboring elements both in the x-direction and in the y-direction [81]. This resembles the two-dimensional minmod-based TVB limiter [31]. The difference between these two approaches is that the moment limiter uses forward and backward differences of lower derivatives, whereas the minmod-based TVB limiter uses a finite-difference approach on the element averages.

2.2.2. VERTEX-BASED LIMITER

For a two-dimensional triangular mesh, the vertex-based hierarchical slope limiter of Kuzmin is applied [85]. The DG approximation on a triangle is expressed as a local Taylor expansion about the centroid. The differences between the values at the centroid and the vertices are important for the limiter. Similar to the maximum-principle limiter [147], the vertex-based limiter is constructed such that the approximation at certain nodes in the triangle is bounded by the maximum and minimum values in the neighboring elements.

Although the moment limiter and the vertex-based limiter have their own mechanisms to control which regions should be limited, we will apply troubled-cell indicators as a switch to control where the limiter is applied. This is to prevent limiting smooth extrema. The next section contains information about several indication techniques.

2.3. TROUBLED-CELL INDICATORS

In this section, several troubled-cell indicators are discussed. These troubled-cell indicators are introduced for comparison to a multiwavelet troubled-cell indicator. In Section 2.3.1, the Harten troubled-cell indicator is discussed. Section 2.3.2 contains information about the KXRCF shock detector, and the minmod-based TVB indicator is described in Section 2.3.3.

2.3.1. HARTEN'S TROUBLED-CELL INDICATOR

The first method presented is Harten's troubled-cell indicator. This indicator is based on Harten's subcell resolution idea [63] and developed by Qiu and Shu [104]. It exploits the fact that averages of a discontinuous function which is piecewise smooth inside an element provide information about the exact location of the discontinuity inside the element. In one dimension, define

$$F_j(z) = \frac{1}{\Delta x}\left\{\int_{x_{j-\frac{1}{2}}}^{z} u_h|_{I_{j-1}}\,dx + \int_{z}^{x_{j+\frac{1}{2}}} u_h|_{I_{j+1}}\,dx\right\} - \bar{u}_j,$$

where $u_h|_{I_{j-1}}$ and $u_h|_{I_{j+1}}$ are extensions of the DG approximation in I_{j-1} and I_{j+1} into element I_j. Note that $F_j(x_{j-1/2})$ corresponds to the difference between the average of the continuously-extrapolated function in I_{j+1} to I_j, and the average of I_j, see Figure 2.3. Element I_j is marked as a troubled cell if

$$F_j(x_{j-\frac{1}{2}})F_j(x_{j+\frac{1}{2}}) \le 0 \quad \text{and} \quad |u_j^{(k)}| > \alpha|u_{j-1}^{(k)}|,\ |u_j^{(k)}| > \alpha|u_{j+1}^{(k)}|.$$

The last two conditions exclude the case that the approximation has a smooth extremum inside element I_j. Here, α is a parameter, which is chosen to be equal to 1.5 in [104]. Note that the choice of α also depends on the choice of limiter that is applied in the troubled cells.

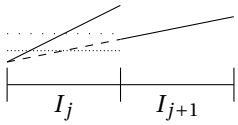

Figure 2.3: Solid lines: DG approximation on elements I_j and I_{j+1}, – – –: $u_h|_{I_{j+1}}$ extended to I_j, · · · · : the average $\bar{u}_j$, ·····: the average of $u_h|_{I_{j+1}}$ on I_j.

2.3.2. KXRCF SHOCK DETECTOR

The shock-detection technique by Krivodonova et al. [83] makes use of the fact that smooth DG approximations are superconvergent at outflow boundaries [3, 82]:

$$\frac{1}{|\partial I_j^+|}\int_{\partial I_j^+}(u_h|_{I_j}-u)ds=\mathcal{O}(h^{2k+1}),$$

where ∂I_j^+ is the outflow boundary of element I_j with length $|\partial I_j^+|$ and u is the solution to the PDE.

The detector considers the jump in u_h across the inflow edges of I_j and examines

$$\mathscr{I}_j=\left|\int_{\partial I_j^-}(u_h|_{I_j}-u_h|_{I_{n_j}})ds\right|. \tag{2.9}$$

Here, ∂I_j^- is the inflow boundary and $u_h|_{I_{n_j}}$ is the DG approximation in the neighbor of I_j on the side of ∂I_j^-. This indicator can be split into

$$\mathscr{I}_j=\left|\int_{\partial I_j^-}(u_h|_{I_j}-u)ds+\int_{\partial I_{n_j}^+}(u-u_h|_{I_{n_j}})ds\right|.$$

For a smooth solution, the first integral is of order $k+2$, whereas the second integral is of order $2k+1$, such that the indication value is $\mathcal{O}(h^{k+2})$. If the solution is discontinuous close to the boundary, then the indication value is $\mathcal{O}(h)$.

The indicator is normalized relative to a convergence rate $\mathcal{O}(h^{(k+1)/2})$:

$$\hat{\mathscr{I}}_j=\frac{\left|\int_{\partial I_j^-}(u_h|_{I_j}-u_h|_{I_{n_j}})ds\right|}{h^{\frac{k+1}{2}}|\partial I_j^-|\,||u_h|_{I_j}||},\quad j=0,\ldots,2^n-1. \tag{2.10}$$

Here, h is the radius of the circumscribed circle in I_j, and the norm is based on the average in one dimension and the maximum norm in quadrature points in two dimensions.

Near a discontinuity, $\hat{\mathscr{I}}_j\to\infty$, whereas $\hat{\mathscr{I}}_j\to 0$ if $h\to 0$ or $k\to\infty$ in smooth-solution regions. In [83], the threshold value is taken equal to 1, such that element I_j is detected as troubled if $\hat{\mathscr{I}}_j>1$, and in that case the limiter is applied in I_j. Note that this threshold parameter is chosen arbitrarily: the value 1 does not necessarily follow from the theory.

2.3.3. MINMOD-BASED TVB INDICATOR

In this section, the minmod-based TVB indicator is explained, which is normally part of the minmod-based TVB limiter [29, 30]. Here, concentration is placed only on the indication and not on the limiting aspect. Element-boundary approximations are split into

$$u^-_{j+\frac{1}{2}} = \bar{u}_j + \tilde{u}_j \quad \text{and} \quad u^+_{j-\frac{1}{2}} = \bar{u}_j - \tilde{\tilde{u}}_j,$$

where

$$\tilde{u}_j = \sum_{\ell=1}^{k} u_j^{(\ell)} \phi_\ell(1), \quad \tilde{\tilde{u}}_j = -\sum_{\ell=1}^{k} u_j^{(\ell)} \phi_\ell(-1), \tag{2.11}$$

see Figure 2.4.

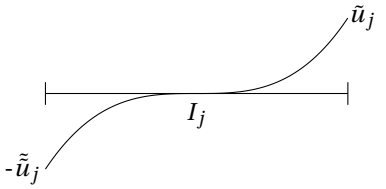

Figure 2.4: Visualization of element-boundary approximations $\tilde{u}_j$ and $\tilde{\tilde{u}}_j$. Note that $\bar{u}_j = 0$ for this particular example.

Element I_j is detected as troubled if either $\tilde{u}_j$ or $\tilde{\tilde{u}}_j$ is modified by the functions

$$\tilde{u}_j^{(\text{mod})} = \tilde{m}(\tilde{u}_j, \bar{u}_{j+1} - \bar{u}_j, \bar{u}_j - \bar{u}_{j-1}), \quad \tilde{\tilde{u}}_j^{(\text{mod})} = \tilde{m}(\tilde{\tilde{u}}_j, \bar{u}_{j+1} - \bar{u}_j, \bar{u}_j - \bar{u}_{j-1}), \tag{2.12}$$

where the TVB-modified minmod function is defined as

$$\tilde{m}(a_1, \ldots, a_q) = \begin{cases} a_1, & \text{if } |a_1| \le M\Delta x^2, \\ m(a_1, \ldots, a_q), & \text{otherwise,} \end{cases}$$

in contrast with the standard minmod function

$$m(a_1, \ldots, a_q) = \begin{cases} s \cdot \min_{1 \le j \le q} |a_j|, & \text{if } \operatorname{sign}(a_1) = \cdots = \operatorname{sign}(a_q) = s, \\ 0, & \text{otherwise.} \end{cases} \tag{2.13}$$

Note that the parameter M is difficult to tune, and hardly any difference is found when M ranges from 1 to 100 [148]. We use the minmod-based TVB indicator for detection and then apply a chosen limiter in the detected troubled cells.

For systems of equations, characteristic field decompositions are required [29]. The corresponding eigenvector matrix is computed using Roe averages [29, 108].

For two-dimensional systems, the procedure for $\mathbb{P}^k$ has been explained in [31], both for rectangular and triangular meshes. The indicator uses solution derivatives (e.g., DG coefficients) for detection. We use $\mathbb{Q}^k$, which means that more 'cross-product' coefficients exist (for example, for $k = 1$, $u_{ij}^{(1,1)}$). However, using the reasoning of Biswas, Devine, and Flaherty [16], we do not use these coefficients for detection, since they have a lesser effect on the numerical approximation than either $u_{ij}^{(1,0)}$ or $u_{ij}^{(0,1)}$.

It is also possible to use information from a multiwavelet expansion for troubled-cell indication. The next section discusses the theory about multiresolution analysis, and a thresholding technique that can be used to detect troubled cells.

2.4. MULTIRESOLUTION ANALYSIS

In this section, a brief description of the theory of multiwavelets [5, 8] and the relation to the DG approximation is given. Although we are using the multiwavelet decomposition in [5, 8], we must modify the definitions to accommodate $[-1,1)$, which helps with the use of the DG coefficients for the multiwavelet expansion. The multiresolution analysis is visualized in Figure 2.5. The global domain $[-1,1)$ is used as one element in level 0, divided into two elements in level 1, into four elements in level 2, etcetera. Mathematically spoken, elements I_{2j}^{m+1} and I_{2j+1}^{m+1} on level $m+1$ are found by splitting element I_j^m on level m into two equal parts ($m = 0,1,\ldots$, $j = 0,\ldots,2^m-1$). In level m, the global domain $[-1,1)$ is divided in 2^m elements, defined as

$$I_j^m = [-1+2^{-m+1}j, -1+2^{-m+1}(j+1)), \quad j = 0,\ldots,2^m-1. \tag{2.14}$$

A visualization of the elements and the notation on different levels is given in Figure 2.6.

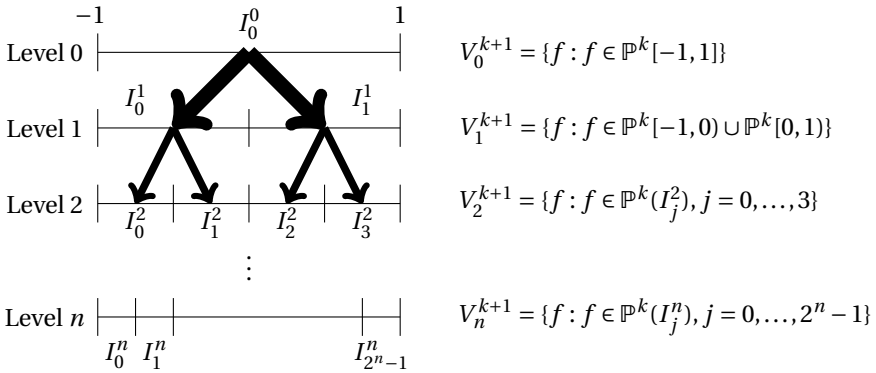

Figure 2.5: Multiresolution analysis: intervals and scaling-function spaces on different levels.

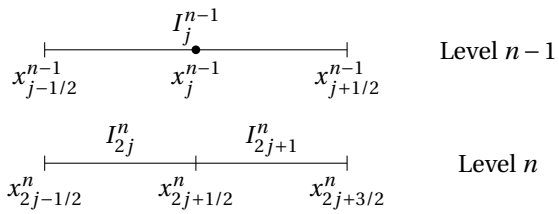

Figure 2.6: Element I_j^{n-1} in level $n-1$ and its subdivision to elements I_{2j}^n and I_{2j+1}^n in level n.

2.4.1. SCALING-FUNCTION SPACE

To begin defining multiwavelets in one dimension, scaling functions are introduced. The scaling-function space on level m is defined as

$$V_m^{k+1} = \{f : f \in \mathbb{P}^k(I_j^m), j = 0, \ldots, 2^m - 1\}, \tag{2.15}$$

where $\mathbb{P}^k(I_j^m)$ is the space of polynomials of degree k on interval I_j^m, see Figure 2.5. Notice that the following nested property holds: $V_0^{k+1} \subset V_1^{k+1} \subset \cdots \subset V_n^{k+1} \subset \cdots$, and that V_n^{k+1} is similar to the DG approximation space $\{V_h(I_j)\}_{j=0}^{2^n-1}$.

The scaled Legendre polynomials, $\phi_0, \ldots, \phi_k$, used in the DG method (Section 2.1), are chosen to be the orthonormal basis for V_0^{k+1}. Next, the space $V_m^{k+1}, m \in \{0, \ldots, n\}$ is spanned by $2^m(k+1)$ functions which are obtained from $\phi_0, \ldots, \phi_k$ by dilation and translation:

$$\phi_{\ell j}^m(x) = \sqrt{\frac{2}{\Delta x^m}}\phi_\ell\left(\frac{2}{\Delta x^m}(x - x_j^m)\right), \quad x \in I_j^m, \tag{2.16}$$

where Δx^m is the mesh width on level m, which is given by 2^{-m+1} for the domain $[-1, 1)$, and x_j^m is the center of element I_j^m. This yields [78, 137]

$$\phi_{\ell j}^m(x) = 2^{m/2}\phi_\ell(2^m(x+1) - 2j - 1), \quad \ell = 0, \ldots, k, \; j = 0, \ldots, 2^m - 1. \tag{2.17}$$

The functions $\phi_\ell, \ell = 0, \ldots, k$, are called *scaling functions*.

As noted in [20], the scaling functions at level $n+1$ are narrower than the scaling functions at level n. This occurs due to dilations and translations, and allows for representing finer details.

The orthogonal projection of an arbitrary function $f \in L^2(-1, 1)$ onto $V_n^{k+1}, n \in \mathbb{N}$ is given by

$$P_n^{k+1} f(x) = \sum_{j=0}^{2^n-1} \sum_{\ell=0}^{k} s_{\ell j}^n \phi_{\ell j}^n(x), \tag{2.18}$$

which is called the single-scale decomposition of f on level n. The scaling-function coefficients are given by

$$s_{\ell j}^n = \langle f, \phi_{\ell j}^n \rangle = \int_{-1+2^{-n+1}j}^{-1+2^{-n+1}(j+1)} f(x)\phi_{\ell j}^n(x)\,dx, \tag{2.19}$$

which is the standard orthogonal projection onto an orthonormal basis. Note that if $f \in V_n^{k+1}$, then $P_n^{k+1} f = f$.

2.4.2. MODAL DG APPROXIMATION AND SCALING-FUNCTION EXPANSION

Because DG approximations and scaling-function expansions are composed of the same basis functions, there is a direct relation between a DG approximation and its scaling-function approximation. The *global* DG approximation of the solution on $[a, b]$ (see

equation (2.4b)) can be written as

$$\begin{aligned} u_h(x) &= \sum_{j=0}^{2^n-1}\sum_{\ell=0}^{k} u_j^{(\ell)}\phi_\ell\left(\frac{2}{\Delta x}(x-x_j^n)\right) = \sum_{j=0}^{2^n-1}\sum_{\ell=0}^{k} u_j^{(\ell)}\phi_\ell\left(\frac{2^{n+1}}{b-a}(x-a)-2j-1\right) \\ &= \sum_{j=0}^{2^n-1}\sum_{\ell=0}^{k} u_j^{(\ell)}\phi_\ell(2^n(y+1)-2j-1) \\ &= 2^{-\frac{n}{2}}\sum_{j=0}^{2^n-1}\sum_{\ell=0}^{k} u_j^{(\ell)}\phi_{\ell j}^n(y), \end{aligned} \tag{2.20}$$

where $y=-1+2(x-a)/(b-a)$, and the dependence on time is omitted for simplicity. On the other hand, exploiting the fact that u_h is a piecewise polynomial of degree k and transforming to a reference domain $[-1,1]$, the DG approximation projected onto the scaling-function basis can be written as

$$u_h(x) = P_n^{k+1}u_h(x) = \sum_{j=0}^{2^n-1}\sum_{\ell=0}^{k} s_{\ell j}^n\phi_{\ell j}^n(y). \tag{2.21}$$

From equations (2.20) and (2.21) it follows that for every $\ell=0,\dots,k$, $j=0,\dots,2^n-1$,

$$2^{-\frac{n}{2}}u_j^{(\ell)} = s_{\ell j}^n, \tag{2.22}$$

thus giving a relation between the DG coefficients and the scaling-function coefficients.

2.4.3. MULTIWAVELETS

The combination of scaling functions and multiwavelets on level m can be used to span the scaling-function space on level $m+1$. The multiwavelet subspace, W_m^{k+1}, is defined as the orthogonal complement of V_m^{k+1} in V_{m+1}^{k+1}:

$$V_m^{k+1}\oplus W_m^{k+1} = V_{m+1}^{k+1}, \tag{2.23}$$

such that $W_m^{k+1}\perp V_m^{k+1}$, $W_m^{k+1}\subset V_{m+1}^{k+1}$, see Figure 2.7. By recursively applying equation (2.23), V_n^{k+1} can be split into $n+1$ orthogonal subspaces:

$$V_n^{k+1} = V_0^{k+1}\oplus W_0^{k+1}\oplus W_1^{k+1}\oplus\cdots\oplus W_{n-1}^{k+1}. \tag{2.24}$$

By definition, W_0^{k+1} should be a subset of V_1^{k+1}. Therefore, the orthonormal basis for W_0^{k+1} is given by $k+1$ piecewise polynomials, $\psi_0,\dots,\psi_k$ (polynomials on $(-1,0]=I_0^1$ and $(0,1]=I_1^1$), which are the so-called *multiwavelets*. The term multiwavelet refers to the fact that the bases for V_0^{k+1} and W_0^{k+1} contain multiple elements. The multiwavelet basis that belongs to the scaled Legendre polynomials was developed by Alpert [4]. Following Alpert [4] and Hovhannisyan [71], the basis should satisfy the following conditions:

1. The restriction of ψ_ℓ to the interval $(0,1)$ is a polynomial of degree k;
2. The function ψ_ℓ is extended to $(-1,0)$ as an even or odd function (depending on whether $\ell+k+1$ is even or odd, respectively);

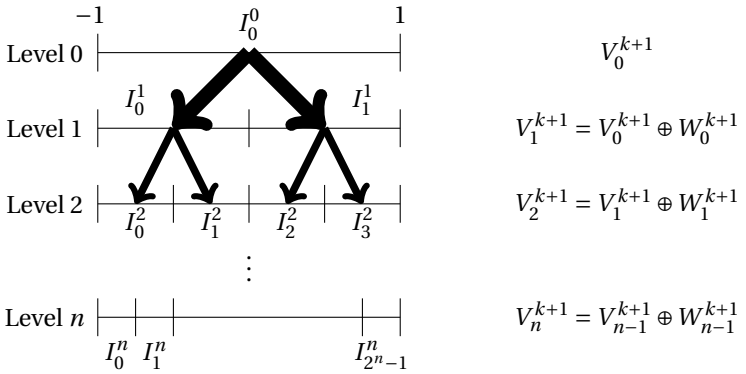

Figure 2.7: The direct sum of V_m^{k+1} and W_m^{k+1} forms V_{m+1}^{k+1}.

3. The basis is orthonormal: $\langle \psi_{\ell_1}, \psi_{\ell_2} \rangle = \delta_{\ell_1,\ell_2}$;

4. The function ψ_ℓ has $k+1$ vanishing moments

$$\int_{-1}^{1} \psi_\ell(x) x^m dx = 0, \quad m = 0, 1, \ldots, k.$$

Using these conditions, we cannot uniquely define a set of multiwavelets. By requiring ℓ additional vanishing moments for multiwavelet ψ_ℓ, this uniqueness (up to sign) is achieved. Alpert's multiwavelet algorithm is given below.

The multiwavelet bases for $k \leq 4$ are presented in Table 2.1. The scaling-function and multiwavelet bases for $k = 2$ on levels 0 and 1 are visualized in Figure 2.8. Note that the scaling functions and multiwavelets on level 0 together can be used to span the scaling-function basis on level 1.

Similar to the basis for V_m^{k+1}, the space W_m^{k+1} is spanned by the functions

$$\psi_{\ell j}^m(x) = 2^{m/2} \psi_\ell(2^m(x+1) - 2j - 1), \quad \ell = 0, \ldots, k, \; j = 0, \ldots, 2^m - 1, \quad x \in I_j^m. \tag{2.25}$$

By construction, multiwavelets ψ_ℓ are piecewise polynomials on I_0^1 and I_1^1. Extending this relation to level $n-1$, $\psi_{\ell j}^{n-1}$ is a piecewise polynomial on I_{2j}^n and I_{2j+1}^n, as visualized in Figure 2.6. Therefore, we expect the multiwavelet expansion on level $n-1$ to be discontinuous at

$$x_{2j+1/2}^n = -1 + 2^{-n+2}(j + 1/2). \tag{2.26}$$

Note that this makes multiwavelet level $n-1$ having the same discontinuity properties as the DG mesh.

The multiwavelet expansion of a function $f \in L^2(-1,1)$ in level m is given by

$$Q_m^{k+1} f(x) = P_{m+1}^{k+1} f(x) - P_m^{k+1} f(x) = \sum_{j=0}^{2^m-1} \sum_{\ell=0}^{k} d_{\ell j}^m \psi_{\ell j}^m(x). \tag{2.27}$$

Algorithm 2.1 Alpert's multiwavelet algorithm for W_0^{k+1} [4].

Define for $\ell = 0,\dots,k$:

$$f_\ell^0(x) = \begin{cases} x^\ell, & \text{if } x \in [0,1), \\ -x^\ell, & \text{if } x \in [-1,0), \\ 0, & \text{else.} \end{cases}$$

Use Gram-Schmidt to orthogonalize f_ℓ^0 with respect to $1, x, \dots, x^k$. This leads to the functions f_ℓ^1, $\ell = 0,\dots,k$.

for $m = 0,\dots,k-1$ **do**

If at least one of the f_ℓ^{m+1} is not orthogonal to x^{k+m+1} ($\ell = m,\dots,k$), then reorder such that $\langle f_m^{m+1}, x^{k+m+1}\rangle \neq 0$.

for $\ell = m+1,\dots,k$ **do**

Construct f_ℓ^{m+2} such that the function is orthogonal to x^{k+m+1}:

$$f_\ell^{m+2} = f_\ell^{m+1} - \frac{\langle f_\ell^{m+1}, x^{k+m+1}\rangle}{\langle f_m^{m+1}, x^{k+m+1}\rangle} \cdot f_m^{m+1}.$$

end for

end for

Gram-Schmidt orthonormalize $f_k^{k+1}, f_{k-1}^k, \dots, f_0^1$ in that order to obtain the multiwavelets $\psi_k, \psi_{k-1}, \dots, \psi_0$.

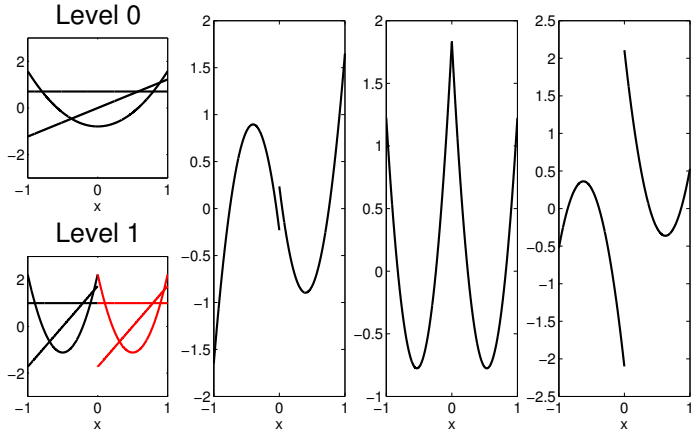

(a) V_0^3 and V_1^3 (b) W_0^3

Figure 2.8: Visualization of the basis functions in V_0^3, W_0^3, and V_1^3. Note that $V_0^3 \oplus W_0^3 = V_1^3$.

Table 2.1: Alpert's multiwavelet basis for W_0^{k+1}, $k = 0,\dots,4$, $x \in (0,1)$. The functions ψ_i, $i = 0,\dots,k$, are extended to the interval $(-1,0)$ as an odd or even function, according to the formula $\psi_i(x) = (-1)^{i+k+1}\psi_i(-x)$.

$k=0$		
$\psi_0(x)$	$=$	$\sqrt{\frac{1}{2}}$
$k=1$		
$\psi_0(x)$	$=$	$\sqrt{\frac{3}{2}}(-1+2x)$
$\psi_1(x)$	$=$	$\sqrt{\frac{1}{2}}(-2+3x)$
$k=2$		
$\psi_0(x)$	$=$	$\frac{1}{3}\sqrt{\frac{1}{2}}(1-24x+30x^2)$
$\psi_1(x)$	$=$	$\frac{1}{2}\sqrt{\frac{3}{2}}(3-16x+15x^2)$
$\psi_2(x)$	$=$	$\frac{1}{3}\sqrt{\frac{5}{2}}(4-15x+12x^2)$
$k=3$		
$\psi_0(x)$	$=$	$\sqrt{\frac{15}{34}}(1+4x-30x^2+28x^3)$
$\psi_1(x)$	$=$	$\sqrt{\frac{1}{42}}(-4+105x-300x^2+210x^3)$
$\psi_2(x)$	$=$	$\frac{1}{2}\sqrt{\frac{35}{34}}(-5+48x-105x^2+64x^3)$
$\psi_3(x)$	$=$	$\frac{1}{2}\sqrt{\frac{5}{42}}(-16+105x-192x^2+105x^3)$
$k=4$		
$\psi_0(x)$	$=$	$\sqrt{\frac{1}{186}}(1+30x+210x^2-840x^3+630x^4)$
$\psi_1(x)$	$=$	$\frac{1}{2}\sqrt{\frac{1}{38}}(-5-144x+1155x^2-2240x^3+1260x^4)$
$\psi_2(x)$	$=$	$\sqrt{\frac{35}{14694}}(22-735x+3504x^2-5460x^3+2700x^4)$
$\psi_3(x)$	$=$	$\frac{1}{8}\sqrt{\frac{21}{38}}(35-512x+1890x^2-2560x^3+1155x^4)$
$\psi_4(x)$	$=$	$\frac{1}{2}\sqrt{\frac{7}{158}}(32-315x+960x^2-1155x^3+480x^4)$

The multiwavelet coefficients are defined by the orthogonal projection of f on the multiwavelet basis:

$$d_{\ell j}^m = \langle f, \psi_{\ell j}^m \rangle = \int_{-1+2^{-m+1}j}^{-1+2^{-m+1}(j+1)} f(x)\psi_{\ell j}^m(x)\,dx. \tag{2.28}$$

From equation (2.24) it follows that for $u_h \in V_n^{k+1}$, we can write

$$u_h(x) = P_n^{k+1}u_h(x) = P_0^{k+1}u_h(x) + \sum_{m=0}^{n-1} Q_m^{k+1}u_h(x) \tag{2.29a}$$

$$= \sum_{\ell=0}^{k} s_{\ell 0}^0 \phi_\ell(x) + \sum_{m=0}^{n-1}\sum_{j=0}^{2^m-1}\sum_{\ell=0}^{k} d_{\ell j}^m \psi_{\ell j}^m(x). \tag{2.29b}$$

The representation in equation (2.29) is called the *multiscale decomposition*. Here, the scaling-function coefficients $\{s_{\ell 0}^0\}_{\ell=0}^k$ represent the approximate solution on the coarsest

level $m = 0$. The multiwavelet coefficients $\{d_{\ell j}^m\}$ carry the multiscale information. These detail coefficients contain the finer details in the approximation [75]. Level $n-1$ is the most important level for the multiwavelet decomposition, since the multiwavelet contribution at this level is used in the multiwavelet troubled-cell indicator, see Chapter 3 and [137]. Therefore, a two-scale representation of the DG approximation would suffice, and the number of elements in the domain can also be even (instead of the restriction to a power of two). However, since this would change the definitions, a discretization of 2^n elements will be used in this dissertation.

2.4.4. MULTIWAVELET DECOMPOSITION AND RECONSTRUCTION

It is important to remark that we do not need to calculate the orthogonal projections to compute the lower-level coefficients. In practice, these coefficients are efficiently computed using multiwavelet decomposition (Figure 2.9) [5, 8]. The decomposition and reconstruction steps are described below.

DECOMPOSITION

In the following, we denote the basis functions of V_{n-1}^{k+1} on I_j^{n-1} by the vector of scaling functions $\boldsymbol{\phi}_j^{n-1} = (\phi_{0j}^{n-1}, \ldots, \phi_{kj}^{n-1})^\top$. Because $V_{n-1}^{k+1} \subset V_n^{k+1}$, we can express $\boldsymbol{\phi}_j^{n-1}$ in terms of $\boldsymbol{\phi}_{2j}^n$ and $\boldsymbol{\phi}_{2j+1}^n$ (using that $I_j^{n-1} = I_{2j}^n \cup I_{2j+1}^n$, Figure 2.6):

$$\boldsymbol{\phi}_j^{n-1} = H_{j,n-1}^{(0)} \boldsymbol{\phi}_{2j}^n + H_{j,n-1}^{(1)} \boldsymbol{\phi}_{2j+1}^n. \tag{2.30a}$$

Here, the $(k+1) \times (k+1)$ *lowpass quadrature-mirror-filter (QMF) coefficient matrices* are given by

$$H_{j,n-1}^{(0)}(\ell, r) = \langle \phi_{\ell j}^{n-1}, \phi_{r,2j}^n \rangle, \quad H_{j,n-1}^{(1)}(\ell, r) = \langle \phi_{\ell j}^{n-1}, \phi_{r,2j+1}^n \rangle.$$

Similarly, $W_{n-1}^{k+1} \subset V_n^{k+1}$, such that the vector of multiwavelets $\boldsymbol{\psi}_j^{n-1} = (\psi_{0j}^{n-1}, \ldots, \psi_{kj}^{n-1})^\top$ can be written as

$$\boldsymbol{\psi}_j^{n-1} = G_{j,n-1}^{(0)} \boldsymbol{\phi}_{2j}^n + G_{j,n-1}^{(1)} \boldsymbol{\phi}_{2j+1}^n, \tag{2.30b}$$

where

$$G_{j,n-1}^{(0)}(\ell, r) = \langle \psi_{\ell j}^{n-1}, \phi_{r,2j}^n \rangle, \quad G_{j,n-1}^{(1)}(\ell, r) = \langle \psi_{\ell j}^{n-1}, \phi_{r,2j+1}^n \rangle.$$

The matrices $G_{j,n-1}^{(0)}$ and $G_{j,n-1}^{(1)}$ are called the *highpass QMF coefficient matrices*.

Due to the dilation and translation properties of the scaling functions and multiwavelets, we find that the QMF coefficients do not depend on j and n [136]:

$$H_{j,n-1}^{(0)}(\ell, r) = \langle \phi_{\ell 0}^0, \phi_{r0}^1 \rangle \equiv H^{(0)}(\ell, r), \quad H_{j,n-1}^{(1)}(\ell, r) = \langle \phi_{\ell 0}^0, \phi_{r1}^1 \rangle \equiv H^{(1)}(\ell, r), \tag{2.31}$$

$$G_{j,n-1}^{(0)}(\ell, r) = \langle \psi_{\ell 0}^0, \phi_{r0}^1 \rangle \equiv G^{(0)}(\ell, r), \quad G_{j,n-1}^{(1)}(\ell, r) = \langle \psi_{\ell 0}^0, \phi_{r1}^1 \rangle \equiv G^{(1)}(\ell, r). \tag{2.32}$$

This means that we can simplify equation (2.30) to

$$\boldsymbol{\phi}_j^{n-1} = H^{(0)} \boldsymbol{\phi}_{2j}^n + H^{(1)} \boldsymbol{\phi}_{2j+1}^n, \tag{2.33a}$$

$$\boldsymbol{\psi}_j^{n-1} = G^{(0)} \boldsymbol{\phi}_{2j}^n + G^{(1)} \boldsymbol{\phi}_{2j+1}^n. \tag{2.33b}$$

For a function $f \in L^2(-1,1)$, the scaling-function and multiwavelet coefficients on level $n-1$ are defined as $\mathbf{s}_j^{n-1} = \langle f, \boldsymbol{\phi}_j^{n-1} \rangle$ and $\mathbf{d}_j^{n-1} = \langle f, \boldsymbol{\psi}_j^{n-1} \rangle$. Using decomposition, they can efficiently be computed using equation (2.33) and the linearity of the inner product:

$$\mathbf{s}_j^{n-1} = H^{(0)}\mathbf{s}_{2j}^n + H^{(1)}\mathbf{s}_{2j+1}^n, \tag{2.34a}$$

$$\mathbf{d}_j^{n-1} = G^{(0)}\mathbf{s}_{2j}^n + G^{(1)}\mathbf{s}_{2j+1}^n. \tag{2.34b}$$

Thus, starting with $2^n(k+1)$ values for $s_{\ell j}^n$, the decomposition procedure can be applied repeatedly to compute the coefficients on coarser levels, $m = n-1, n-2, \ldots, 0$.

RECONSTRUCTION

For reconstruction, we make use of the fact that the matrix

$$U = \begin{pmatrix} H^{(0)} & H^{(1)} \\ G^{(0)} & G^{(1)} \end{pmatrix}$$

is orthogonal: $UU^\top = I$, such that $U^{-1} = U^\top$ [5, 136]. This means that also $U^\top U = I$, from which we deduce that

$$H^{(i_1)\top} H^{(i_2)} + G^{(i_1)\top} G^{(i_2)} = \delta_{i_1,i_2} I, \quad i_1, i_2 = 0, 1.$$

This means that if we left-multiply equation (2.34a) by $H^{(i)\top}$ and equation (2.34b) by $G^{(i)\top}$ and then sum these equations, we find

$$H^{(i)\top}\mathbf{s}_j^{n-1} + G^{(i)\top}\mathbf{d}_j^{n-1} = \mathbf{s}_{2j+i}^n,$$

for $i = 0, 1$.

Multiwavelet coefficients can also be used for the detection of troubled cells. This is because multiwavelet coefficients become small in regions where the underlying solution is smooth, and remain large if the function is discontinuous. In the next section, this property is formalized.

2.4.5. CANCELATION PROPERTY

In this section, the *cancelation property* is stated and proved for the one-dimensional case [40]. Here, we assume that the multiwavelets have $M+1$ vanishing moments. In our case, we have $M = \ell + k$ (Section 2.4.3). If the solution satisfies $u|_{I_j^m} \in C^{M+1}(I_j^m)$, then

$$d_{\ell j}^m \leq \frac{1}{(M+1)!} \cdot ||u^{(M+1)}||_{L^\infty(I_j^m)} \cdot 2^{(-m+1)(M+3/2)}, \tag{2.35}$$

$m = 0, \ldots, n$, $j = 0, \ldots, 2^m - 1$, $\ell = 0, \ldots, k$.

The proof uses a Taylor expansion of u about element center x_j^m: there exists a ξ between x and x_j^m such that

$$u(x) = u(x_j^m) + u'(x_j^m)(x - x_j^m) + \ldots + \frac{u^{(M)}(x_j^m)}{M!}(x - x_j^m)^M + \frac{u^{(M+1)}(\xi)}{(M+1)!}(x - x_j^m)^{M+1}.$$

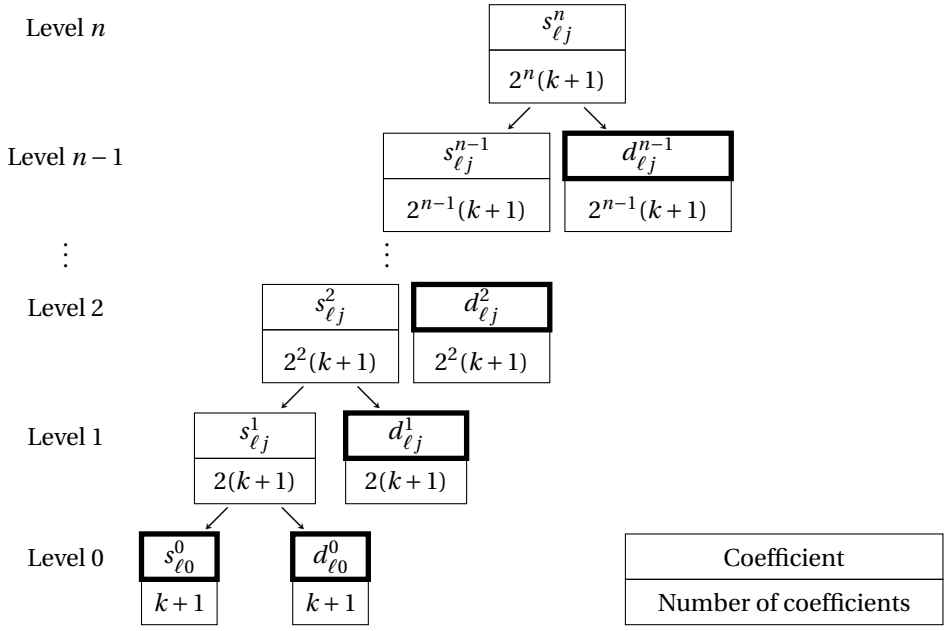

Figure 2.9: Multiwavelet decomposition. Marked coefficients together carry the same information as the coefficients $s^n_{\ell j}$, $\ell = 0,\ldots,k,\ j = 0,\ldots,2^n-1$.

Using that the first $M+1$ moments of the multiwavelets vanish, we find

$$d^m_{\ell j} = \langle u, \psi^m_{\ell j}\rangle_{I^m_j} = \left\langle \frac{u^{(M+1)}(\xi)}{(M+1)!}(x-x^m_j)^{M+1}, \psi^m_{\ell j}\right\rangle_{I^m_j}$$
$$\leq \frac{1}{(M+1)!}||u^{(M+1)}||_{L^\infty(I^m_j)}\langle (x-x^m_j)^{M+1}, \psi^m_{\ell j}\rangle_{I^m_j}. \tag{2.36}$$

Next, we use Cauchy-Schwarz's inequality to find

$$\langle (x-x^m_j)^{M+1}, \psi^m_{\ell j}\rangle_{I^m_j} \leq ||(x-x^m_j)^{M+1}||_{L^2(I^m_j)}\cdot||\psi^m_{\ell j}||_{L^2(I^m_j)} = ||(x-x^m_j)^{M+1}||_{L^2(I^m_j)},$$

because the multiwavelets are orthonormal. Using the notation Δx^m for the element size in level m, we have

$$||(x-x^m_j)^{M+1}||_{L^2(I^m_j)} \leq (\Delta x^m)^{M+1}||1||_{L^2(I^m_j)} = (\Delta x^m)^{M+1}\sqrt{\Delta x^m} = (\Delta x^m)^{M+3/2}.$$

For the domain $[-1,1]$, we have $\Delta x^m = 2^{-m+1}$. This means that

$$||(x-x^m_j)^{M+1}||_{L^2(I^m_j)} \leq 2^{(-m+1)(M+3/2)},$$

which proves the cancelation property. It should be noticed that this result can be generalized to general grid hierarchies and higher-dimensional problems [40, 72].

The next section contains a discussion of the thresholding technique for one-dimensional multiwavelet expansions.

2.4.6. THRESHOLDING OF THE MULTIWAVELET COEFFICIENTS

In this section, the thresholding technique for systems of conservation laws in one dimension is explained, which is based on the cancelation property [55]. This technique is originally used for a multiwavelet-based adaptive strategy in combination with the DG method. However, we are specifically interested in its application for troubled-cell indication. The research described in this dissertation was conducted independently from the work in [55, 75].

Following [55], the element I_j^{n-1} is detected as troubled if

$$\max_{\substack{\ell=0,\dots,k\\ r=1,2,3}} \left(\frac{|d_{\ell j}^{n-1}(r)|}{\max\left\{\max_{j=0,\dots,2^n-1} 2^{(n-1)/2}|s_{0j}^n(r)|, 1\right\}} \right) > \varepsilon_{n-1}\sqrt{2\Delta x}.$$

Here, the value r is related to the conserved quantity in a system of three PDEs. The factor $\sqrt{2\Delta x}$ (with Δx the DG mesh width) occurs because of a scaling difference: the multiwavelets in [55] are scaled with respect to the L^∞-norm, whereas an L^2-norm scaling is used in this dissertation. The level-dependent threshold value ε_{n-1} is chosen as $\varepsilon_{n-1} = \varepsilon/2$. The parameter ε can be chosen using two different strategies [55]. The first option is to use the *a priori* strategy, which is based on the balance between discretization errors and perturbation errors of adaptive meshes [72]. If the solution contains discontinuities, then the a priori strategy leads to $\varepsilon = C\Delta x^2$. The second option is the *heuristic* approach, which is based on numerous computations for practical applications [55]. This method is more efficient since it is less pessimistic than the a priori strategy. For discontinuous solutions, the heuristic approach uses $\varepsilon = C\Delta x$.

This yields detection of element I_j^{n-1} if

$$\max_{\substack{\ell=0,\dots,k\\ r=1,2,3}} \left(\frac{|d_{\ell j}^{n-1}(r)|}{\max\left\{\max_{j=0,\dots,2^n-1} 2^{(n-1)/2}|s_{0j}^n(r)|, 1\right\}} \right) > \frac{1}{\sqrt{2}}\Delta x^{\beta+0.5}C,$$

where $\beta = 2$ for the a priori strategy and $\beta = 1$ for the heuristic strategy. Note that the multiwavelet coefficients are scaled by the cell average if this value is greater than 1 in absolute value (to prevent division by zero).

The optimal choice of the parameter C depends on the problem, in particular on the strength of the shock compared to the normal amplitude of the solution. The smaller C is, the more elements are detected. In general, the value $C = 1/(b-a)$ should work for the domain $[a, b]$ [55]. If C is chosen too small, then too many cells are detected as troubled. For the adaptive strategy this is not really problematic, since the approximation is usually more accurate on a finer grid. However, for troubled-cell indication it is important to detect the correct number of elements.

It should be noticed that this indicator is designed for very fine resolutions (since the strategies use asymptotic arguments). For coarse meshes, smaller values of C should be used, which are difficult to predict a priori.

2.4.7. TWO-DIMENSIONAL TENSOR-PRODUCT MULTIWAVELETS

In this section, the tensor-product multiwavelet decomposition is explained for the domain $[-1,1] \times [-1,1]$, being discretized using $2^{n_x} \times 2^{n_y}$ elements. In that case, the scal-

ing functions and multiwavelets can also be written as tensor products. The scaling-function basis is spanned by $\phi_{\ell_x}(x)\phi_{\ell_y}(y)$, for $\ell_x, \ell_y = 0, \ldots, k$, and the multiwavelet basis is spanned by the functions $\phi_{\ell_x}(x)\psi_{\ell_y}(y)$ (α mode), $\psi_{\ell_x}(x)\phi_{\ell_y}(y)$ (β mode), and $\psi_{\ell_x}(x)\psi_{\ell_y}(y)$ (γ mode). The one-step decomposition is given by

$$u_h(x,y) = \sum_{i=0}^{2^{n_x-1}-1} \sum_{j=0}^{2^{n_y-1}-1} \sum_{\ell_x,\ell_y=0}^{k} \Big\{ s_{\boldsymbol{\ell}\mathbf{j}}^{\mathbf{n}-1} \phi_{\ell_x,i}^{n_x-1}(x)\phi_{\ell_y,j}^{n_y-1}(y) + d_{\boldsymbol{\ell}\mathbf{j}}^{\alpha,\mathbf{n}-1} \phi_{\ell_x,i}^{n_x-1}(x)\psi_{\ell_y,j}^{n_y-1}(y) + d_{\boldsymbol{\ell}\mathbf{j}}^{\beta,\mathbf{n}-1} \psi_{\ell_x,i}^{n_x-1}(x)\phi_{\ell_y,j}^{n_y-1}(y) + d_{\boldsymbol{\ell}\mathbf{j}}^{\gamma,\mathbf{n}-1} \psi_{\ell_x,i}^{n_x-1}(x)\psi_{\ell_y,j}^{n_y-1}(y) \Big\},$$

and the full decomposition can be written as

$$u_h(x,y) = S^0(x,y) + \sum_{m_y=0}^{n_y-1} D^{\alpha,m_y}(x,y) + \sum_{m_x=0}^{n_x-1} D^{\beta,m_x}(x,y) + \sum_{m_x=0}^{n_x-1} \sum_{m_y=0}^{n_y-1} D^{\gamma,\mathbf{m}}(x,y),$$

where,

$$\begin{aligned}
S^0(x,y) &= \sum_{\ell_x,\ell_y=0}^{k} s_{\boldsymbol{\ell}\mathbf{0}} \phi_{\ell_x}(x)\phi_{\ell_y}(y), \\
D^{\alpha,m_y}(x,y) &= \sum_{j=0}^{2^{m_y}-1} \sum_{\ell_x,\ell_y=0}^{k} d_{\boldsymbol{\ell},(0,j)}^{\alpha,(0,m_y)} \phi_{\ell_x}(x)\psi_{\ell_y,j}^{m_y}(y), \\
D^{\beta,m_x}(x,y) &= \sum_{i=0}^{2^{m_x}-1} \sum_{\ell_x,\ell_y=0}^{k} d_{\boldsymbol{\ell},(i,0)}^{\beta,(m_x,0)} \psi_{\ell_x,i}^{m_x}(x)\phi_{\ell_y}(y), \\
D^{\gamma,\mathbf{m}}(x,y) &= \sum_{i=0}^{2^{m_x}-1} \sum_{j=0}^{2^{m_y}-1} \sum_{\ell_x,\ell_y=0}^{k} d_{\boldsymbol{\ell}\mathbf{j}}^{\gamma,\mathbf{m}} \psi_{\ell_x,i}^{m_x}(x)\psi_{\ell_y,j}^{m_y}(y),
\end{aligned}$$

and $\boldsymbol{\ell} = (\ell_x, \ell_y)^\top$, $\mathbf{j} = (i,j)^\top, \mathbf{m} = (m_x, m_y)^\top$. The modes α, β and γ in level $n-1$ detect troubled cells which are oriented in the y-, x-, and xy-directions, respectively [91]. Analogous to the one-dimensional case, the relation between the DG coefficients and the scaling-function coefficients is given by,

$$2^{-\frac{n_x+n_y}{2}} u_{ij}^{(\ell_x,\ell_y)} = s_{\boldsymbol{\ell}\mathbf{j}}^{\mathbf{n}}. \tag{2.37}$$

Furthermore, the coefficients on level $\mathbf{n}-1$ can be efficiently computed using multiwavelet decomposition [137].

2.4.8. MULTIWAVELETS ON A TRIANGULAR MESH

The extension of the multiresolution theory to a triangular mesh is not straightforward. A thorough discussion is given in Chapter 6.

Different techniques can be compared with each other using several test cases. The next section discusses several test problems using the Euler equations for compressible gas dynamics.

2.5. TEST CASES USED IN THIS DISSERTATION

Standard examples in the rest of this dissertation follow from the Euler equations for compressible gas dynamics. A nice introduction to gas dynamics is given in LeVeque, [87]. The most important definitions are repeated in this section [136]. In one dimension, three equations play a role:

1. The continuity equation, which models conservation of mass:

$$\rho_t + (\rho u)_x = 0, \tag{2.38a}$$

where $\rho(x,t)$ is the density, and $u(x,t)$ is the velocity of the gas.

2. Conservation of momentum, ρu, using a macroscopic, convective momentum flux and a microscopic flux due to the pressure of the fluid, $p(x,t)$:

$$(\rho u)_t + (\rho u^2 + p)_x = 0. \tag{2.38b}$$

3. Conservation of energy, $E(x,t)$, using the macroscopic energy flux and a flux in kinetic energy:

$$E_t + \big((E+p)u\big)_x = 0. \tag{2.38c}$$

Here, the equation of state for an ideal polytropic gas is used:

$$E = \frac{p}{\gamma - 1} + \frac{1}{2}\rho u^2, \tag{2.38d}$$

where the term $p/(\gamma-1)$ belongs to the internal energy, and $\rho u^2/2$ is the kinetic energy. Finally, $\gamma = c_p/c_v$ is called the adiabatic exponent, where c_p denotes the specific heat at constant pressure and c_v is the specific heat at constant volume. For air, γ is approximately equal to 1.4.

Introducing $\mathbf{u} = (\rho, \rho u, E)^\top = (u^{(1)}, u^{(2)}, u^{(3)})^\top$, equations (2.38) can be written as,

$$\mathbf{u}_t + \mathbf{f}(\mathbf{u})_x = 0, \tag{2.39a}$$

where,

$$\mathbf{f}(\mathbf{u}) = (\rho u, \rho u^2 + p, u(E+p))^\top. \tag{2.39b}$$

In two dimensions, the Euler equations can be written as [88]

$$\mathbf{u}_t + \mathbf{f}(\mathbf{u})_x + \mathbf{g}(\mathbf{u})_y = 0,$$

using $\mathbf{u} = (\rho, \rho u, \rho v, E)^\top$, with u the velocity in the x-direction, and v the velocity in the y-direction, and

$$\mathbf{f}(\mathbf{u}) = (\rho u, \rho u^2 + p, \rho uv, u(E+p))^\top, \quad \mathbf{g}(\mathbf{u}) = (\rho v, \rho uv, \rho v^2 + p, v(E+p))^\top.$$

The energy is computed as

$$E = \frac{p}{\gamma - 1} + \frac{\rho}{2}(u^2 + v^2).$$

Different sets of initial conditions can be used to construct the test cases. The next sections contain several examples in 1D (Section 2.5.1–2.5.4) and 2D (Section 2.5.5).

2.5.1. SOD'S SHOCK TUBE

One application in which the Euler equations play a role is Sod's shock tube [125]. This example models a tube which is filled with two different gasses, separated by a membrane. The following initial condition is used (see Figure 2.10(a)):

$$(\rho_0, u_0, p_0) = \begin{cases} (1,0,1), & \text{if } x < 0, \\ (0.125,0,0.1), & \text{if } x \geq 0. \end{cases}$$

At time $t > 0$, the membrane is removed, and the gasses start to interact. The physical domain is assumed to be very long (essentially infinite). The computational domain, however, must be finite, and is set equal to $[-5,5]$. The boundary conditions are chosen such that the obtained results using this smaller domain resemble the results computed on a larger domain. These so-called *absorbing* or *nonreflecting* boundary conditions should allow outgoing waves to disappear without generating spurious incoming waves.

In Figure 2.10(b), the exact results for the shock tube are given for some $t > 0$. This figure is given in the report of Sod, [125], and is analyzed with the help of Smoller, [124].

In Region 2, a *rarefaction wave* is situated, where both the density and the pressure decrease. Note that the quantities are not smooth at the end points of the rarefaction wave. The head x_1 and tail x_2 of the rarefaction wave move to the left with time.

Coordinate x_3 belongs to a so-called *contact discontinuity*: the location where the initial discontinuity has traveled in time. Note that density and energy are discontinuous across the contact discontinuity, whereas pressure and velocity are continuous.

The point x_4, which moves to the right, is the location of the shock wave: all quantities are discontinuous across x_4. The nonlinearity of the Euler equations causes this discontinuity.

2.5.2. LAX'S SHOCK TUBE

The second test problem that we consider is the shock-tube problem of Lax [86]:

$$(\rho_0, u_0, p_0) = \begin{cases} (0.445,0.698,3.528), & \text{if } x < 0, \\ (0.5,0,0.571), & \text{if } x \geq 0, \end{cases}$$

and constant initial-state boundary conditions are used.

2.5.3. BLAST-WAVE PROBLEM

The next test problem models the interaction of two blast waves [144]:

$$(\rho_0, u_0, p_0) = \begin{cases} (1,0,1000), & \text{if } 0 \leq x < 0.1, \\ (1,0,0.01), & \text{if } 0.1 \leq x < 0.9, \\ (1,0,100), & \text{if } 0.9 \leq x \leq 1, \end{cases}$$

and the boundary conditions of Shu and Osher [121] are used.

2.5.4. SHU-OSHER PROBLEM

The final set of initial conditions in one dimension that we consider is

$$(\rho_0, u_0, p_0) = \begin{cases} (3.857143,2.629369,10.33333), & \text{if } x < -4, \\ (1+0.2\sin(5x),0,1), & \text{if } x \geq -4, \end{cases}$$

together with constant boundary conditions [121].

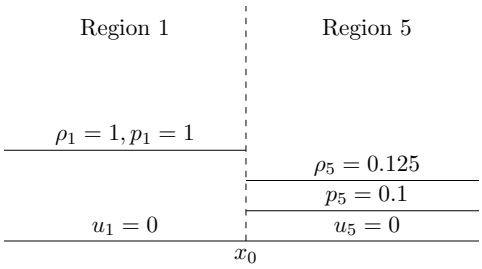

(a) $t = 0$.

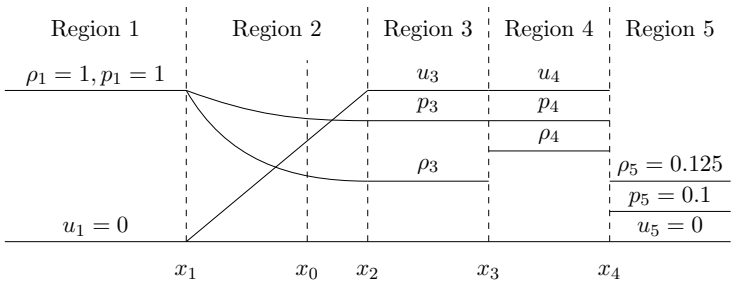

(b) $t > 0$.

Figure 2.10: Sod's shock tube, divided into different regions:
Region 1: Gas in the original state of high pressure;
Region 2: Rarefaction wave, solution is a monotone continuous function of x/t;
Region 3: Rarefied gas (gas at lower pressure than in Region 1);
Region 4: Compressed gas (gas at higher density than in Region 5);
Region 5: Gas in the original state of low pressure.

2.5.5. DOUBLE MACH REFLECTION PROBLEM

The two-dimensional equations of compressible gas dynamics are considered for the double Mach reflection of a strong shock [144]. The computational domain of this problem is $[0,4] \times [0,1]$. At $t = 0$, this domain is divided into two regions that are separated by $y(x) = \sqrt{3}(x - 1/6)$ [132]. The following initial conditions are used:

$$\mathbf{u}_L = (8, 8.25\cos(30°), -8.25\sin(30°), 563.5)^\top, \tag{2.40a}$$

$$\mathbf{u}_R = (1.4, 0, 0, 2.5)^\top. \tag{2.40b}$$

At the left boundary, $\mathbf{u}_L$ is used as a boundary condition, and at the right, $\mathbf{u}_R$. The top boundary is divided into two regions: for $x < 1/6 + (1 + 20t)/\sqrt{3}$, $\mathbf{u}_L$ is used, whereas $\mathbf{u}_R$ is used to the right. At the bottom boundary, $\mathbf{u}_L$ is used for $x < 1/6$, and a reflecting wall is used for $x \geq 1/6$.

3

MULTIWAVELET TROUBLED-CELL INDICATOR

In this chapter, we will first investigate the relation between multiwavelet coefficients and jumps in (derivatives of) the DG approximation (Section 3.1). Next, a multiwavelet troubled-cell indicator will be introduced, which uses the highest-level multiwavelet coefficients for detection (Section 3.2). Several illustrative examples will be given in which the performance with respect to different indication techniques can be compared (Section 3.3). Finally, concluding remarks are given in Section 3.4.

Parts of this chapter have been published in Journal of Computational Physics **270** (2014) and as a contribution to the conference proceedings of ICOSAHOM 2014 (Springer).

3.1. MULTIWAVELETS AND JUMPS IN DG APPROXIMATIONS

In this section, it will be shown that the multiwavelet coefficients on level $n-1$ are related to jumps in (derivatives of) the DG approximation. In Walnut [141], the ideas have been explained for the Haar wavelet system, and general functions.

3.1.1. VANISHING MOMENTS

Alpert's multiwavelets are constructed in such a way that for degree k the first $\ell+k+1$ moments vanish (Section 2.4.3, and [4, 71]):

$$\int_{-1}^{1} x^m \psi_\ell(x)\,dx = 0, \quad m = 0,\ldots,\ell+k, \tag{3.1a}$$

such that

$$\int_{-1}^{0} x^m \psi_\ell(x)\,dx = -\int_{0}^{1} x^m \psi_\ell(x)\,dx. \tag{3.1b}$$

By construction, ψ_ℓ is an even or odd function (Table 2.1), and the same holds for the function x^m. Therefore, the value in equation (3.1b) is only nonzero if $x^m\psi_\ell(x)$ is odd.

In the following lemma, the vanishing-moment property is extended to multiresolution level $n-1$.

Lemma 3.1. *Define I_j^{n-1} and $\psi_{\ell j}^{n-1}$ using equations (2.14) and (2.25), respectively. The vanishing-moment property on multiresolution level $n-1$ yields:*

$$\int_{I_j^{n-1}} (x - x_{2j+1/2}^n)^m \psi_{\ell j}^{n-1}(x)\,dx = 0,\ m = 0,\ldots,k+\ell,\ j = 0,\ldots,2^{n-1}-1. \tag{3.2}$$

Proof. Using equations (2.14) and (2.25), and the fact that

$$x_{2j+1/2}^n = -1 + (2j+1)\Delta x = -1 + (2j+1)\cdot 2^{-n+1} = -1 + 2^{-n+2}(j+1/2),$$

the left-hand side of equation (3.2) equals

$$2^{\frac{n-1}{2}} \int_{-1+2^{-n+2}j}^{-1+2^{-n+2}(j+1)} \left(x + 1 - 2^{-n+2}\left(j+1/2\right)\right)^m \psi_\ell(2^{n-1}(x+1) - 2j - 1)\,dx. \tag{3.3}$$

Next, the transformation $z = 2^{n-1}(x+1) - 2j - 1$ is used, with $x = 2^{-n+1}(z+2j+1) - 1$, and $dx = 2^{-n+1}dz$. Then, equations (3.2) and (3.3) transform into

$$\begin{aligned}\int_{I_j^{n-1}} (x - x_{2j+1/2}^n)^m \psi_{\ell j}^{n-1}(x)\,dx &= 2^{\frac{n-1}{2}} \cdot 2^{-n+1} \int_{-1}^{1} (2^{-n+1}z)^m \psi_\ell(z)\,dz \\ &= 2^{(m+1/2)(-n+1)} \cdot \int_{-1}^{1} z^m \psi_\ell(z)\,dz = 0,\end{aligned} \tag{3.4}$$

using the relation in equation (3.1a). □

A direct consequence of Lemma 3.1 is the following result, in which we use the definition of I_j^{n-1} (equation (2.14) and Figure 2.6):

Corollary 3.1. *For $m = 0,\dots,k+\ell$, $j = 0,\dots,2^{n-1}-1$, it holds that*

$$\int_{x^n_{2j-1/2}}^{x^n_{2j+1/2}} (x - x^n_{2j+1/2})^m \psi^{n-1}_{\ell j}(x)\,dx = -\int_{x^n_{2j+1/2}}^{x^n_{2j+3/2}} (x - x^n_{2j+1/2})^m \psi^{n-1}_{\ell j}(x)\,dx. \tag{3.5}$$

This property will be used to derive the relation between multiwavelets and jumps in (derivatives of) the DG approximation in the next section.

3.1.2. MULTIWAVELET COEFFICIENTS ON LEVEL $n-1$

By construction, multiwavelet coefficients $d^{n-1}_{\ell j}$ corresponding to the DG approximation u_h satisfy

$$d^{n-1}_{\ell j} = \int_{I^{n-1}_j} u_h(x)\psi^{n-1}_{\ell j}(x)\,dx \quad \ell = 0,\dots,k,\ j = 0,\dots,2^{n-1}-1. \tag{3.6}$$

These coefficients are strongly related to the interelement jumps in (derivatives of) the DG approximation, as we will see in the following theorem [138].

Theorem 3.1. *Let u_h be a DG approximation of degree k on $[-1,1]$, using 2^n elements. For each $\ell, m = 0,\dots,k$, define*

$$c^n_{m\ell} = \frac{2^{(-n+1)m}}{m!} \cdot \int_0^1 x^m \psi_\ell(x)\,dx, \tag{3.7a}$$

and let $u_h^{(m)}$ be the mth derivative of u_h. It holds that

$$d^{n-1}_{\ell j} = 2^{-\frac{n-1}{2}} \sum_{m=0}^{k} c^n_{m\ell} \cdot \left(u_h^{(m)}(x^{n,+}_{2j+1/2}) - u_h^{(m)}(x^{n,-}_{2j+1/2}) \right), \quad j = 0,\dots,2^{n-1}-1. \tag{3.7b}$$

Proof. In general, the DG approximation is a piecewise polynomial of degree k on element $I^{n-1}_j = I^n_{2j} \cup I^n_{2j+1}$, with a discontinuity at $x^n_{2j+1/2}$ (see Figure 2.6). This means that we can express u_h as a Taylor polynomial about $x^{n,-}_{2j+1/2}$ for $x \in I^n_{2j}$:

$$u_h(x) = u_h(x^{n,-}_{2j+1/2}) + u_h'(x^{n,-}_{2j+1/2})(x - x^n_{2j+1/2}) + \dots + \frac{1}{k!} u_h^{(k)}(x^{n,-}_{2j+1/2})(x - x^n_{2j+1/2})^k, \tag{3.8a}$$

and about $x^{n,+}_{2j+1/2}$ for $x \in I^n_{2j+1}$:

$$u_h(x) = u_h(x^{n,+}_{2j+1/2}) + u_h'(x^{n,+}_{2j+1/2})(x - x^n_{2j+1/2}) + \dots + \frac{1}{k!} u_h^{(k)}(x^{n,+}_{2j+1/2})(x - x^n_{2j+1/2})^k. \tag{3.8b}$$

The use of this relation in equation (3.6) leads to the following expression for the multiwavelet coefficient $d^{n-1}_{\ell j}$:

$$\begin{aligned} d^{n-1}_{\ell j} = &\sum_{m=0}^{k} \frac{1}{m!} u_h^{(m)}(x^{n,-}_{2j+1/2}) \int_{x^n_{2j-1/2}}^{x^n_{2j+1/2}} (x - x^n_{2j+1/2})^m \psi^{n-1}_{\ell j}(x)\,dx \\ &+ \sum_{m=0}^{k} \frac{1}{m!} u_h^{(m)}(x^{n,+}_{2j+1/2}) \int_{x^n_{2j+1/2}}^{x^n_{2j+3/2}} (x - x^n_{2j+1/2})^m \psi^{n-1}_{\ell j}(x)\,dx. \end{aligned} \tag{3.9}$$

If we apply Corollary 3.1, we arrive at

$$d_{\ell j}^{n-1} = \sum_{m=0}^{k} \frac{1}{m!} \left(u_h^{(m)}(x_{2j+1/2}^{n,+}) - u_h^{(m)}(x_{2j+1/2}^{n,-}) \right) \int_{x_{2j+1/2}^n}^{x_{2j+3/2}^n} (x - x_{2j+1/2}^n)^m \psi_{\ell j}^{n-1}(x)\, dx. \quad (3.10)$$

With the use of $z = 2^{n-1}(x+1) - 2j - 1$, the theorem is proved. □

Theorem 3.1 gives a direct relation between multiwavelet coefficients on level $n-1$ and jumps in (derivatives of) the DG approximation over element boundaries. Since the DG method adopts a discontinuous nature at element boundaries, the multiwavelet coefficients are in general never exactly equal to zero. However, when the solution is sufficiently smooth, then the element-boundary jumps in the approximation and its derivatives will be noticeably smaller than when a discontinuity in (one of the derivatives of) the solution is present due to the cancelation property of multiwavelets (Section 2.4.5). This information can be used to detect troubled cells. In theory, it is possible that large jumps are canceled in the summation of equation (3.7b). In practice, however, this will not occur at more than one successive time step, and therefore, the impact will be negligible.

Equations (3.6) and (3.7b) provide information about the formal definition of the multiwavelet coefficients and the relation to element-boundary jumps in the approximation and its derivatives. It should be noticed that in practice, the multiwavelet coefficients are computed using the efficient decomposition procedure of equation (2.34).

For a two-dimensional tensor-product space, the relations for the multiwavelet coefficients on level $\mathbf{n}-1$ follow naturally from the one-dimensional coefficients: using $\boldsymbol{\ell} = (\ell_x, \ell_y)^\top$, with $\ell_x, \ell_y = 0, \ldots, k$, $\mathbf{n} = (n_x, n_y)^\top$, and $\mathbf{j} = (i, j)^\top$, with $i = 0, \ldots, 2^{n_x-1} - 1$ and $j = 0, \ldots, 2^{n_y-1} - 1$, and $c_{m\ell}^n$ as defined in equation (3.7a), we have

$$d_{\boldsymbol{\ell}\mathbf{j}}^{\alpha,\mathbf{n}-1} = 2^{-\frac{n_y-1}{2}} \sum_{m_y=0}^{k} c_{m_y \ell_y}^{n_y} \int_{x_{2i-\frac{1}{2}}^{n_x}}^{x_{2i+\frac{3}{2}}^{n_x}} \left(\frac{\partial^{m_y} u_h}{\partial y^{m_y}}(x, y_{2j+1/2}^{n_y,+}) - \frac{\partial^{m_y} u_h}{\partial y^{m_y}}(x, y_{2j+1/2}^{n_y,-}) \right) \cdot \phi_{\ell_x, i}^{n_x-1}(x)\, dx,$$

$$d_{\boldsymbol{\ell}\mathbf{j}}^{\beta,\mathbf{n}-1} = 2^{-\frac{n_x-1}{2}} \sum_{m_x=0}^{k} c_{m_x \ell_x}^{n_x} \int_{y_{2j-\frac{1}{2}}^{n_y}}^{y_{2j+\frac{3}{2}}^{n_y}} \left(\frac{\partial^{m_x} u_h}{\partial x^{m_x}}(x_{2i+1/2}^{n_x,+}, y) - \frac{\partial^{m_x} u_h}{\partial x^{m_x}}(x_{2i+1/2}^{n_x,-}, y) \right) \cdot \phi_{\ell_y, j}^{n_y-1}(y)\, dy,$$

$$d_{\boldsymbol{\ell}\mathbf{j}}^{\gamma,\mathbf{n}-1} = 2^{-\frac{n_x-1}{2}} 2^{-\frac{n_y-1}{2}} \sum_{m_x=0}^{k} \sum_{m_y=0}^{k} c_{m_x \ell_x}^{n_x} c_{m_y \ell_y}^{n_y} \left(\frac{\partial^{m_x}}{\partial x^{m_x}} \frac{\partial^{m_y}}{\partial y^{m_y}} \right.$$
$$\left. \left(u_h(x_{2i+\frac{1}{2}}^{n_x,+}, y_{2j+\frac{1}{2}}^{n_y,+}) - u_h(x_{2i+\frac{1}{2}}^{n_x,+}, y_{2j+\frac{1}{2}}^{n_y,-}) - u_h(x_{2i+\frac{1}{2}}^{n_x,-}, y_{2j+\frac{1}{2}}^{n_y,+}) + u_h(x_{2i+\frac{1}{2}}^{n_x,-}, y_{2j+\frac{1}{2}}^{n_y,-}) \right) \right).$$

The proof of these relations follows the same lines as the proof of Theorem 3.1. The definition of the multiwavelet coefficients in the α mode is

$$d_{\boldsymbol{\ell}\mathbf{j}}^{\alpha,\mathbf{n}-1} = \iint_{I_{ij}^{\mathbf{n}-1}} u_h(x, y) \phi_{\ell_x i}^{n_x-1}(x) \psi_{\ell_y j}^{n_y-1}(y)\, dx\, dy.$$

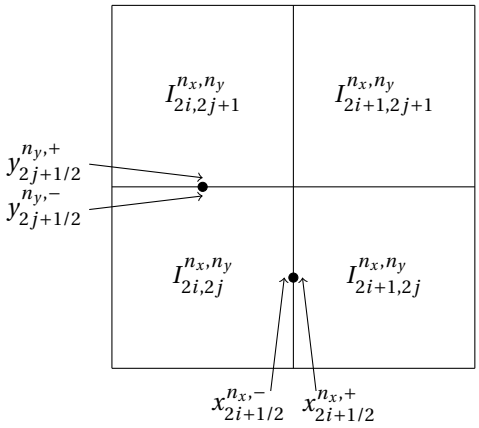

Figure 3.1: Element I^{n_x-1,n_y-1}_{ij}. Inner horizontal line: $\psi^{n_y-1}_{\ell_y j}(y)$ is discontinuous. Inner vertical line: $\psi^{n_x-1}_{\ell_x i}(x)$ is discontinuous.

A visualization of element I^{n_x-1,n_y-1}_{ij} can be seen in Figure 3.1. Using the tensor-product properties of our multiwavelet space, we decompose the integral:

$$d^{\alpha,\mathbf{n}-1}_{\boldsymbol{\ell}\mathbf{j}} = \int_{I^{n_x-1}_i} \left\{ \int_{I^{n_y}_{2j}} u_h(x,y)\psi^{n_y-1}_{\ell_y j}(y)\,dy + \int_{I^{n_y}_{2j+1}} u_h(x,y)\psi^{n_y-1}_{\ell_y j}(y)\,dy \right\} \phi^{n_x-1}_{\ell_x i}(x)\,dx.$$

Similar to equation (3.8), we express the DG approximation as a Taylor polynomial about $y^{n_y,-}_{2j+1/2}$ in the first term, and about $y^{n_y,+}_{2j+1/2}$ in the second term, and apply the vanishing-moment relation of Corollary 3.1:

$$\begin{aligned} d^{\alpha,\mathbf{n}-1}_{\boldsymbol{\ell}\mathbf{j}} &= \sum_{m_y=0}^{k} \frac{1}{m_y!} \int_{I^{n_x-1}_i} \left\{ \frac{\partial^{m_y} u_h}{\partial y^{m_y}}(x, y^{n_y,-}_{2j+1/2}) \int_{I^{n_y}_{2j}} (y - y^{n_y}_{2j+1/2})^{m_y} \psi^{n_y-1}_{\ell_y j}(y)\,dy \right. \\ &\quad \left. + \frac{\partial^{m_y} u_h}{\partial y^{m_y}}(x, y^{n_y,+}_{2j+1/2}) \int_{I^{n_y}_{2j+1}} (y - y^{n_y}_{2j+1/2})^{m_y} \psi^{n_y-1}_{\ell_y j}(y)\,dy \right\} \phi^{n_x-1}_{\ell_x i}(x)\,dx \\ &= \sum_{m_y=0}^{k} \frac{1}{m_y!} \cdot \int_{I^{n_x-1}_i} \left(\frac{\partial^{m_y} u_h}{\partial y^{m_y}}(x, y^{n_y,+}_{2j+1/2}) - \frac{\partial^{m_y} u_h}{\partial y^{m_y}}(x, y^{n_y,-}_{2j+1/2}) \right) \\ &\quad \cdot \left\{ \int_{I^{n_y}_{2j+1}} (y - y^{n_y}_{2j+1/2})^{m_y} \psi^{n_y-1}_{\ell_y j}(y)\,dy \right\} \phi^{n_x-1}_{\ell_x i}(x)\,dx. \end{aligned}$$

Using $z = 2^{n_y-1}(y+1) - 2j - 1$ (cf. equation (3.4)), we find

$$\int_{I^{n_y}_{2j+1}} (y - y^{n_y}_{2j+1/2})^{m_y} \psi^{n_y-1}_{\ell_y j}(y)\,dy = 2^{(m_y+1/2)(-n_y+1)} \int_0^1 z^{m_y} \psi_{\ell_y}(z)\,dz.$$

Defining $c^{n_y}_{m_y\ell_y}$ as in equation (3.7a), we end up with

$$d^{\alpha,\mathbf{n}-1}_{\boldsymbol{\ell}\mathbf{j}} = 2^{-\frac{n_y-1}{2}} \sum_{m_y=0}^{k} c^{n_y}_{m_y\ell_y} \int_{I_i^{n_x-1}} \left(\frac{\partial^{m_y} u_h}{\partial y^{m_y}}(x, y^{n_y,+}_{2j+1/2}) - \frac{\partial^{m_y} u_h}{\partial y^{m_y}}(x, y^{n_y,-}_{2j+1/2}) \right) \cdot \phi^{n_x-1}_{\ell_x i}(x)\, dx.$$

Note that coefficient $d^{\alpha,\mathbf{n}-1}_{\boldsymbol{\ell}\mathbf{j}}$ corresponds to jumps in (derivatives in) the y-direction.

It is straightforward to show that

$$d^{\beta,\mathbf{n}-1}_{\boldsymbol{\ell}\mathbf{j}} = 2^{-\frac{n_x-1}{2}} \sum_{m_x=0}^{k} c^{n_x}_{m_x\ell_x} \int_{I_j^{n_y-1}} \left(\frac{\partial^{m_x} u_h}{\partial x^{m_x}}(x^{n_x,+}_{2i+1/2}, y) - \frac{\partial^{m_x} u_h}{\partial x^{m_x}}(x^{n_x,-}_{2i+1/2}, y) \right) \cdot \phi^{n_y-1}_{\ell_y, j}(y)\, dy :$$

these coefficients are related to jumps in (derivatives in) the x-direction.

For the γ mode, we have

$$\begin{aligned} d^{\gamma,\mathbf{n}-1}_{\boldsymbol{\ell}\mathbf{j}} &= \int_{I_i^{n_x-1}} \left\{ \int_{I^{n_y}_{2j}} u_h(x,y) \psi^{n_y-1}_{\ell_y j}(y)\, dy + \int_{I^{n_y}_{2j+1}} u_h(x,y) \psi^{n_y-1}_{\ell_y j}(y)\, dy \right\} \psi^{n_x-1}_{\ell_x i}(x)\, dx \\ &= 2^{-\frac{n_y-1}{2}} \sum_{m_y=0}^{k} c^{n_y}_{m_y\ell_y} \int_{I_i^{n_x-1}} \left(\frac{\partial^{m_y} u_h}{\partial y^{m_y}}(x, y^{n_y,+}_{2j+1/2}) - \frac{\partial^{m_y} u_h}{\partial y^{m_y}}(x, y^{n_y,-}_{2j+1/2}) \right) \cdot \psi^{n_x-1}_{\ell_x i}(x)\, dx. \end{aligned}$$

Writing

$$f(x) = \frac{\partial^{m_y} u_h}{\partial y^{m_y}}(x, y^{n_y,+}_{2j+1/2}) - \frac{\partial^{m_y} u_h}{\partial y^{m_y}}(x, y^{n_y,-}_{2j+1/2}),$$

this means that

$$\begin{aligned} d^{\gamma,\mathbf{n}-1}_{\boldsymbol{\ell}\mathbf{j}} &= 2^{-\frac{n_y-1}{2}} \sum_{m_y=0}^{k} c^{n_y}_{m_y\ell_y} \cdot \left\{ \int_{I^{n_x}_{2i}} f(x) \cdot \psi^{n_x-1}_{\ell_x i}(x)\, dx + \int_{I^{n_x}_{2i+1}} f(x) \cdot \psi^{n_x-1}_{\ell_x i}(x)\, dx \right\} \\ &= 2^{-\frac{n_x-1}{2}} 2^{-\frac{n_y-1}{2}} \sum_{m_x=0}^{k} \sum_{m_y=0}^{k} c^{n_x}_{m_x\ell_x} c^{n_y}_{m_y\ell_y} \left(\frac{\partial^{m_x}}{\partial x^{m_x}} f(x^{n_x,+}_{2i+1/2}) - \frac{\partial^{m_x}}{\partial x^{m_x}} f(x^{n_x,-}_{2i+1/2}) \right) \\ &= 2^{-\frac{n_x-1}{2}} 2^{-\frac{n_y-1}{2}} \sum_{m_x=0}^{k} \sum_{m_y=0}^{k} c^{n_x}_{m_x\ell_x} c^{n_y}_{m_y\ell_y} \cdot \left(\frac{\partial^{m_x}}{\partial x^{m_x}} \frac{\partial^{m_y}}{\partial y^{m_y}} \left(u_h(x^{n_x,+}_{2i+1/2}, y^{n_y,+}_{2j+1/2}) \right.\right. \\ &\quad \left.\left. - u_h(x^{n_x,+}_{2i+1/2}, y^{n_y,-}_{2j+1/2}) - u_h(x^{n_x,-}_{2i+1/2}, y^{n_y,+}_{2j+1/2}) + u_h(x^{n_x,-}_{2i+1/2}, y^{n_y,-}_{2j+1/2}) \right) \right). \end{aligned}$$

Note that in the γ mode, the DG approximation is investigated in the center of element I^{n_x-1,n_y-1}_{ij}, see Figure 3.2. Indeed, the γ mode considers the jump in both the x- and the y-direction.

Note that these relations indeed confirm the observations that the α mode detects discontinuities in the y-direction, the β mode in the x-direction, and the γ mode in the xy-direction, as was stated in [91] and seen in [137].

3.2. TROUBLED-CELL INDICATION

In this section, we first discuss the multiwavelet troubled-cell indicator introduced in [137]. Then, a slight modification to the multiwavelet troubled-cell indicator is made.

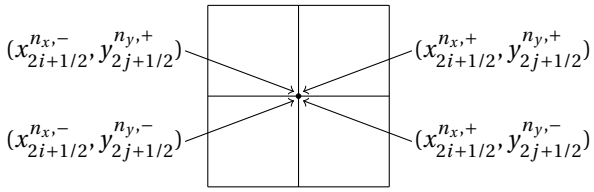

Figure 3.2: Element $I_{ij}^{n_x-1,n_y-1}$: locations where DG approximation is investigated in the γ mode.

First, the number of multiwavelet coefficients is increased by renumbering the internal elements. Next, a careful choice is made for the multiwavelet coefficients that will be used for detection. Finally, the modified multiwavelet troubled-cell indicator is defined.

3.2.1. ORIGINAL MULTIWAVELET TROUBLED-CELL INDICATOR

In this section, the original multiwavelet troubled-cell indicator is presented [137]. In the neighborhood of a discontinuity in the DG approximation, the multiwavelet contribution of the higher levels will suddenly become large with respect to this contribution in continuous regions. In the original indicator, the contribution

$$D^{n-1}(x) = \sum_{j=0}^{2^{n-1}-1} D_j^{n-1}(x) = \sum_{j=0}^{2^{n-1}-1} \sum_{\ell=0}^{k} d_{\ell j}^{n-1} \psi_{\ell j}^{n-1}(x)$$

is used for troubled-cell indication [91, 137]. Troubled cells were indicated using the absolute averages on each element of the DG discretization:

$$\bar{D}_i^{n-1} = \frac{1}{\Delta x} \int_{I_i} \left| D^{n-1}(x) \right| dx, \quad i = 0, \ldots, 2^n - 1, \tag{3.11}$$

which is the weighted L^1-norm on the element I_i, generally used for discontinuity detection [66]. The element where the average (3.11) is maximal, is assumed to be the element where the strongest shock occurs.

Due to the computational cost of integral evaluation, the three-point trapezoidal rule is implemented. This is done in place of exact integral evaluation, because finding the roots of the absolute multiwavelet decomposition is not easy. This discrete average of D^{n-1} is easy and fast to compute and gives a good approximation of the continuous average.

In [137], element I_i is detected as troubled if $\bar{D}_i^{n-1}$ is large enough. This is the case if the value is close enough to the maximum absolute average, where the strongest shock occurs:

$$\bar{D}_i^{n-1} > C \cdot \max\{\bar{D}_i^{n-1}, i = 0, \ldots, 2^n - 1\}, \quad C \in [0, 1].$$

Here, C is a problem-depending parameter that defines the strictness of the indicator (see Section 3.2.4 for more discussion about the value of C).

The complexity of extending these ideas to two dimensions does not increase considerably. The main difference is the use of three different contributions: $D^{\alpha,\mathbf{n}-1}$, $D^{\beta,\mathbf{n}-1}$, and $D^{\gamma,\mathbf{n}-1}$.

To compute the averages of $D^{\alpha,\mathbf{n}-1}$, one bases the computation on its construction through the functions $\phi_{\ell_x i}^{n_x-1}$ (polynomial on $I_i^{n_x-1}$) and $\psi_{\ell_y j}^{n_y-1}$ (piecewise polynomial on $I_{2j}^{n_y}$ and $I_{2j+1}^{n_y}$) for $i \in \{0,\ldots,2^{n_x-1}-1\}$, $j \in \{0,\ldots,2^{n_y-1}-1\}$, and $\ell_x, \ell_y \in \{0,\ldots,k\}$. Similar to the one-dimensional approach, we compute

$$\bar{D}_{ij}^{\alpha,\mathbf{n}-1} \equiv \bar{D}^{\alpha,\mathbf{n}-1}(I_i^{n_x-1} \times I_j^{n_y}), i = 0,\ldots,2^{n_x-1}-1, j = 0,\ldots,2^{n_y}-1,$$

resulting in $2^{n_x-1} \cdot 2^{n_y}$ averages.

For the β mode, we need

$$\bar{D}_{ij}^{\beta,\mathbf{n}-1} \equiv \bar{D}^{\beta,\mathbf{n}-1}(I_i^{n_x} \times I_j^{n_y-1}), i = 0,\ldots,2^{n_x}-1, j = 0,\ldots,2^{n_y-1}-1,$$

because multiwavelet $\psi_{\ell_x i}^{n_x-1}$ is used in the x-direction and scaling function $\phi_{\ell_y j}^{n_y-1}$ in the y-direction ($2^{n_x} \cdot 2^{n_y-1}$ averages).

In mode γ, multiwavelets are used both in the x-direction and in the y-direction, such that

$$\bar{D}_{ij}^{\gamma,\mathbf{n}-1} \equiv \bar{D}^{\gamma,\mathbf{n}-1}(I_i^{n_x} \times I_j^{n_y}), i = 0,\ldots,2^{n_x}-1, j = 0,\ldots,2^{n_y}-1$$

is found ($2^{n_x} \cdot 2^{n_y}$ averages).

Analogous to the one-dimensional case, the element $I_i^{n_x-1} \times I_j^{n_y}$ is indicated to be a troubled cell in the α mode if

$$\bar{D}_{ij}^{\alpha,\mathbf{n}-1} > C^{\alpha} \cdot \max\{\bar{D}_{ij}^{\alpha,\mathbf{n}-1}, i = 0,\ldots,2^{n_x-1}-1, j = 0,\ldots,2^{n_y}-1\},\ C^{\alpha} \in [0,1].$$

Shock detection in the β and γ mode is done in the same manner, using the parameters C^{β} and C^{γ} to determine the strictness of the troubled-cell indicator. Note that this gives us three parameters to choose.

In [137], the results for several test problems in one and two dimensions have been given. The technique performs well and has a robust performance compared with other methods. A simplification was performed after the relation between the multiwavelet coefficients on level $n-1$ and the jumps over element boundaries was determined [138] (Section 3.1). The indicator was adapted to use the multiwavelet coefficients directly. In addition, the new indicator always selects two elements which share a common boundary. In the rest of this dissertation, this modified multiwavelet troubled-cell indicator is used.

3.2.2. INCREASING THE NUMBER OF MULTIWAVELET COEFFICIENTS

The multiwavelet coefficient $d_{\ell j}^{n-1}$ contains information about the jump in the DG approximation at boundaries $x_{2j+1/2}^n$, $j = 0,\ldots,2^{n-1}-1$. This means that only half of the element-boundary jumps can be investigated using these coefficients. To also include the boundaries $x_{2j-1/2}^n$, the internal elements, $I_1,\ldots,I_{2^n-2}$, are virtually renumbered to $I_0,\ldots,I_{2^n-3}$, and the multiwavelet decomposition procedure is again applied on these elements (Section 2.4.4, [123]). This leads to $2^{n-1}-1$ extra coefficients for level $n-1$.

The combination of the coefficients corresponding to element boundaries $x^n_{2j-1/2}$ and $x^n_{2j+1/2}$ is expressed as a vector $\tilde{d}^{n-1}_{\ell j}$, $\ell = 0,\ldots,k$, $j = 0,\ldots,2^n-2$. In order to use the outlier-detection technique in later chapters, it is important to work with vectors of length 2^n. This is achieved by defining the value $\tilde{d}^{n-1}_{\ell,2^n-1} = \tilde{d}^{n-1}_{\ell,2^n-2}$, such that $\tilde{d}^{n-1}_{\ell j}$ is related to the jump at element boundary $x^n_{j+1/2}$, $j = 0,\ldots,2^n-1$.

Similarly, the two-dimensional multiwavelet coefficients $\tilde{d}^{\alpha,\mathbf{n}-1}_{\boldsymbol{\ell}\mathbf{j}}$ ($i = 0,\ldots,2^{n_x-1}-1$, $j = 0,\ldots,2^{n_y}-1$), $\tilde{d}^{\beta,\mathbf{n}-1}_{\boldsymbol{\ell}\mathbf{j}}$ ($i = 0,\ldots,2^{n_x}-1$, $j = 0,\ldots,2^{n_y-1}-1$), and $\tilde{d}^{\gamma,\mathbf{n}-1}_{\boldsymbol{\ell}\mathbf{j}}$ ($i = 0,\ldots,2^{n_x}-1$, $j = 0,\ldots,2^{n_y}-1$) are used.

3.2.3. COEFFICIENTS USED FOR DETECTION

From equation (3.1b) it follows that $c^n_{m\ell}$ is only nonzero when $x^m\psi_\ell(x)$ is an odd function. Because ψ_k is an odd function [4] and all even powers of x are even, coefficients $c^n_{0k}, c^n_{2k},\ldots$ are always nonzero. According to Theorem 3.1, this means that coefficient d^{n-1}_{kj} contains information about the jump $u_h(x^{n,+}_{j+1/2}) - u_h(x^{n,-}_{j+1/2})$ itself (and all even derivatives). In a similar manner we notice that ψ_{k-1} is even, and therefore it holds that $c^n_{0,k-1}$ is zero, whereas $c^n_{1,k-1}$ is nonzero, such that coefficient $d^{n-1}_{k-1,j}$ considers the jump in the odd derivatives, but not in the approximation itself. Since we mostly focus on the jumps in the approximation, the coefficients d^{n-1}_{kj} are useful for detection. In this dissertation, the extended coefficients $\tilde{d}^{n-1}_{kj}$ (Section 3.2.2) are used in the troubled-cell indicator.

In two dimensions, we use the coefficients with index $\boldsymbol{\ell} = (0,k)^\top$ for indication in the α mode. In the β mode, the index $\boldsymbol{\ell} = (k,0)^\top$ is used, and for γ we take $\boldsymbol{\ell} = (k,k)^\top$.

3.2.4. MODIFIED MULTIWAVELET TROUBLED-CELL INDICATOR

Coefficient $\tilde{d}^{n-1}_{kj}$ is related to the jump in the approximation at $x^n_{j+1/2}$. Therefore, elements I_j and I_{j+1} are detected as troubled if $\tilde{d}^{n-1}_{kj}$ is too large:

$$|\tilde{d}^{n-1}_{kj}| > C\cdot\max\{|\tilde{d}^{n-1}_{kj}| : j = 0,\ldots,2^n-1\},\ \text{with } C\in[0,1]. \tag{3.12}$$

The moment limiter is then applied only to the detected troubled cells.

If $C = 1$, then no element will be detected, and the smaller C is, the more elements will be labeled as troubled. In this way, the value of C is a useful tool to prescribe the strictness of the detector. In general, it is difficult to choose a sufficient value for C. For each problem, several tests should be done to obtain an optimal parameter [137].

Analogous to the one-dimensional case, element $I_i^{n_x-1}\times I_j^{n_y}$ is indicated as a troubled cell in the α mode if

$$|\tilde{d}^{\alpha,\mathbf{n}-1}_{(0,k),(i,j)}| > C^\alpha\cdot\max\{|\tilde{d}^{\alpha,\mathbf{n}-1}_{(0,k),(i,j)}| : i = 0,\ldots,2^{n_x-1}-1,\ j = 0,\ldots,2^{n_y}-1\},\ \text{with } C^\alpha\in[0,1].$$

Shock detection in the β and γ mode is done in the same manner, using the parameters C^β and C^γ to determine the strictness of the troubled-cell indicator. Note that this gives us three parameters to choose. Similar to the one-dimensional case, the number of elements that is detected increases if the values of C^α, C^β, and C^γ decrease. With this

approach, the α mode detects discontinuities in the y-direction (because multiwavelets are used in the y-direction), and the β mode detects discontinuities in the x-direction (multiwavelets in x). The γ mode is used for diagonal shock detection [91].

3.3. NUMERICAL RESULTS

In this section, we investigate several examples to inspect the effectiveness of the multiwavelet troubled-cell indicator applied to the discontinuous Galerkin approximation. We compare the results with the subcell-resolution method of Harten ($\alpha = 1.5$) and the shock-detection method of Krivodonova et al. (Section 2.3). It was previously found that these two indicators perform better than other indication methods [104]. Once the troubled cells are determined, the moment limiter (Section 2.2.1) is applied only to the detected troubled cells. All figures in this section correspond to polynomial degree $k = 1$. The computations, however, were also done for $k = 2$ and $k = 3$. To compare the accuracy of the different troubled-cell indicators, it is useful to look at time-history plots of detected troubled cells as is commonly done [149]. The results demonstrate that the multiwavelet troubled-cell indicator performs well. For the two-dimensional example, the computational cost of the KXRCF indicator and the multiwavelet approach is similar.

3.3.1. ONE-DIMENSIONAL EXAMPLES

We begin by investigating the performance of the multiwavelet troubled-cell indicator for the one-dimensional Euler equations and comparing this to existing troubled-cell indicators. Below the results and comparisons are given using four different sets of initial conditions: the shock tubes of Sod and Lax, the interaction of two blast waves, and the Shu-Osher problem (Section 2.5). We compare the cells that are detected by our multiwavelet indicator with the KXRCF and Harten's troubled-cell indicator. For the KXRCF and Harten's indicator, a combination of density and energy is used in the literature [83, 104]. In the multiwavelet approach, however, only density is used in the indicator. The multiwavelet approach using density detects exactly the same elements as the combination of density and energy does. Table 3.1 contains the average and maximum number of detected troubled cells over time.

SOD'S SHOCK TUBE

As we have seen in Section 2.5.1, the solution to Sod's test problem develops a shock, contact discontinuity and rarefaction wave in time. This gives rise to a time-history profile of troubled cells as is shown in Figure 3.3 [124].

The detected troubled cells using the multiwavelet indicator (on density) for different values of C are shown in Figure 3.4, together with the corresponding approximations at $T = 2$. For $k = 1$, it is clearly visible that $C = 0.9$ and $C = 0.5$ only select the shock wave, and the contact discontinuity is not found. To make the indicator more strict, we need to decrease the value of C. For $C = 0.1$, the shock, contact discontinuity and the left end point of the rarefaction wave (where the derivative of the approximation is discontinuous) are detected. This means that our indicator is very accurate if the value of C is chosen appropriately. If not only density but also energy is used in our multiwavelet troubled-cell indicator, exactly the same elements are detected as troubled. This behavior can be seen in Figure 3.5 for Sod's shock tube, and is true for each test problem that

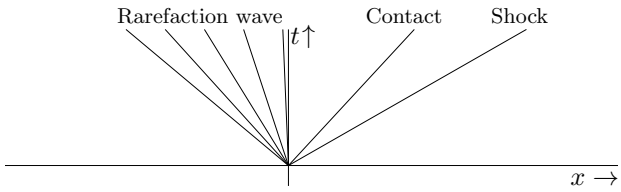

Figure 3.3: Time history of troubled cells, Sod's shock tube.

we investigated. For $k = 2$ and $k = 3$ (not visualized here), the multiwavelet indicator detects fewer elements than in the linear case if the same value of C is chosen. This means that C should be chosen smaller than in the piecewise linear case in order to select the same regions. However, the approximation is less oscillatory if fewer elements are limited (see Table 3.1), which has to do with the relation between the polynomial degree and the number of elements in the mesh [68].

The KXRCF and Harten results are visualized in Figure 3.6. It is surprising to see that the KXRCF indicator can detect the shock, but the contact discontinuity is not found, which was also observed in [83]. Taking $k = 2$ or $k = 3$ improves the approximation, but still the contact discontinuity is not detected. Using Harten's troubled-cell indicator, the detected elements are more scattered over the domain and the approximation at the final time is still oscillatory. Taking a higher polynomial degree does not improve this detector.

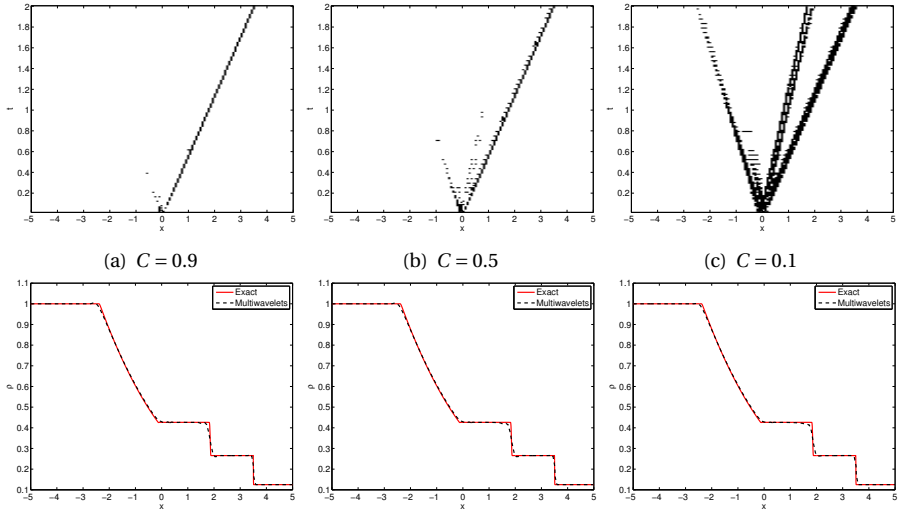

(a) $C = 0.9$ (b) $C = 0.5$ (c) $C = 0.1$

(d) $C = 0.9$ (e) $C = 0.5$ (f) $C = 0.1$

Figure 3.4: Sod's shock tube: time-history plot of detected troubled cells (first row), and approximation at final time $T = 2$ (second row), using the multiwavelet troubled-cell indicator (density), 128 elements, $k = 1$.

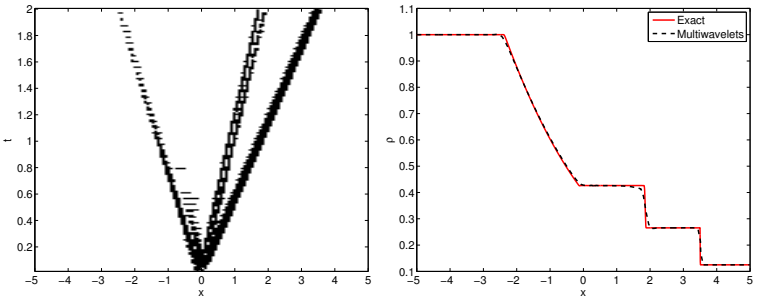

(a) Detected troubled cells (b) Approximation

Figure 3.5: Sod's shock tube: time-history plot of detected troubled cells and approximation at final time $T = 2$ using the multiwavelet troubled-cell indicator with $C = 0.1$ (density and energy), 128 elements, $k = 1$. Compare to Figure 3.4(c) and 3.4(f).

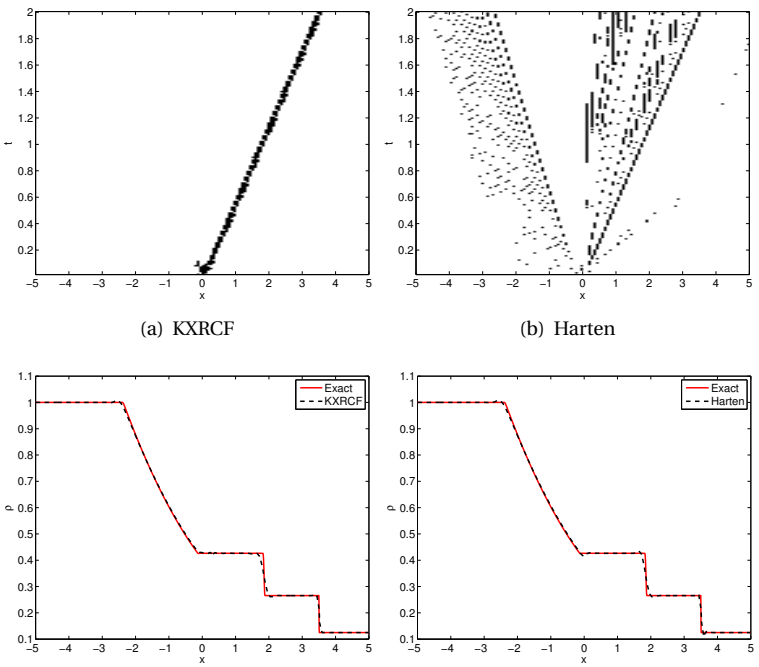

(a) KXRCF (b) Harten

(c) KXRCF (d) Harten

Figure 3.6: Sod's shock tube: time-history plot of detected troubled cells (first row), and approximation at final time $T = 2$ (second row), using the KXRCF indicator or Harten's indicator (density and energy), 128 elements, $k = 1$.

LAX'S SHOCK TUBE

The second test problem that we consider is the shock-tube problem of Lax [86] (Section 2.5.2). The results using the multiwavelet indicator can be seen in Figure 3.7, and the KXRCF and Harten results are visualized in Figure 3.8. Note that the multiwavelet indicator does not detect the rarefaction wave for the given values of C as this wave is more smooth than in Sod's shock tube. The values $C = 0.9$ and $C = 0.5$ are not restrictive enough, since the contact discontinuity is not detected, and oscillations are present in the approximation at the final time. The value $C = 0.1$ gives much better results. For $k = 2$ and $k = 3$, we again find that the value of C should be chosen smaller than in the linear case in order to detect the correct features using the multiwavelet technique.

Also for this example, the KXRCF indicator is not able to detect the contact discontinuity. Therefore, the final-time approximation is oscillatory. For $k = 2$ or $k = 3$, the KXRCF indicator does detect both the shock and the contact discontinuity.

The detected elements using Harten's subcell resolution are scattered. Although this method detects all regions with interesting features, it seems not to select enough neighboring elements to remove the oscillations. This can, however, be influenced by the choice of α as well as the choice of the limiter. For $k = 2$, Harten's indicator selects fewer cells than for $k = 1$, and they are very scattered over the domain. The approximation for $k = 3$ looks even worse.

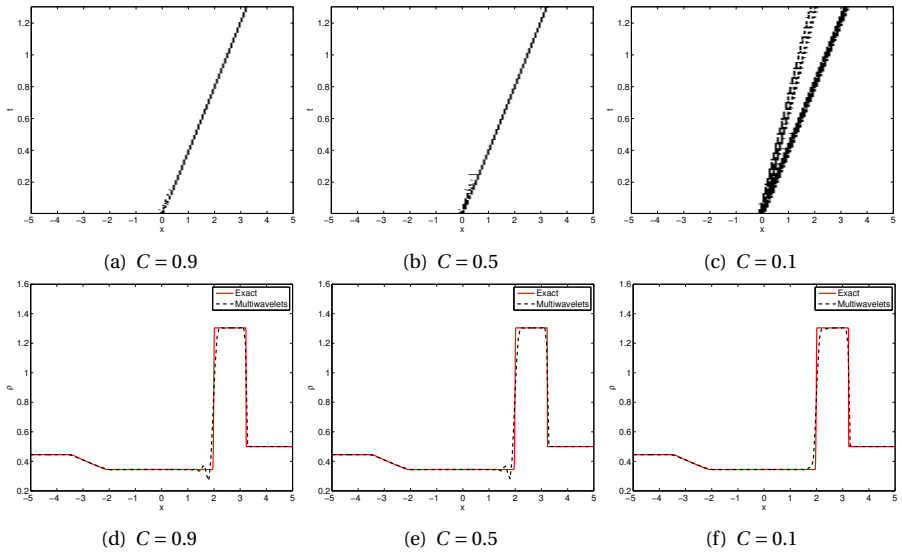

(a) $C = 0.9$ (b) $C = 0.5$ (c) $C = 0.1$

(d) $C = 0.9$ (e) $C = 0.5$ (f) $C = 0.1$

Figure 3.7: Lax's shock tube: time-history plot of detected troubled cells (first row), and approximation at final time $T = 1.3$ (second row), using the multiwavelet troubled-cell indicator, 128 elements, $k = 1$.

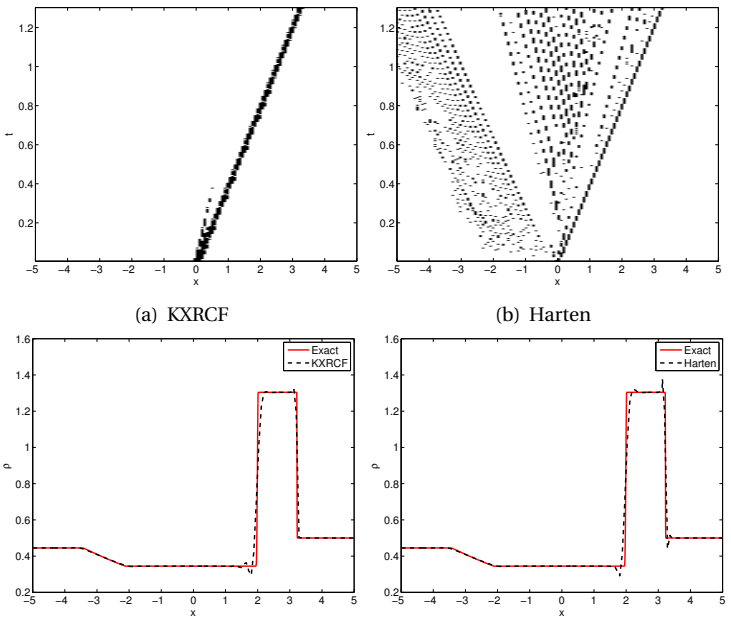

(a) KXRCF (b) Harten

(c) KXRCF (d) Harten

Figure 3.8: Lax's shock tube: time-history plot of detected troubled cells (first row), and approximation at final time $T = 1.3$ (second row), using the KXRCF indicator or Harten's indicator, 128 elements, $k = 1$.

BLAST-WAVE PROBLEM

Next, we investigate the interaction of two blast waves [144] (Section 2.5.3). The detected troubled cells in time are compared using different troubled-cell indicators. Time-history plots of the detected troubled cells using the multiwavelet troubled-cell indicator with 512 elements and $k = 1$ can be seen in Figure 3.9, together with the corresponding approximation at $T = 0.038$. Note that although this is an extremely nonlinear problem, only a few elements should be limited to obtain nonoscillatory results. Our parameter C is a useful tool to prevent limiting too many elements. For $k = 2$ and $k = 3$, the value of C should be chosen smaller in order to detect the same regions as for $k = 1$. However, also here a larger value of C can be used to find a nonoscillatory approximation, see Table 3.1 [68].

The KXRCF indicator selects more elements, as can be seen in Figure 3.10. Both the multiwavelet and the KXRCF indicator detect regions that are visible in the exact shock solution, which was given by Woodward and Colella [144]. We speculate that the multiwavelet indicator will detect the same regions as KXRCF if a smaller C is chosen. For $k = 2$ and $k = 3$, the number of detected elements increases considerably (see also Table 3.1).

Harten's indicator detects too few elements and the pattern is again more scattered. The approximation is still oscillatory, see Figure 3.10. The approximation does not improve if the polynomial degree is increased.

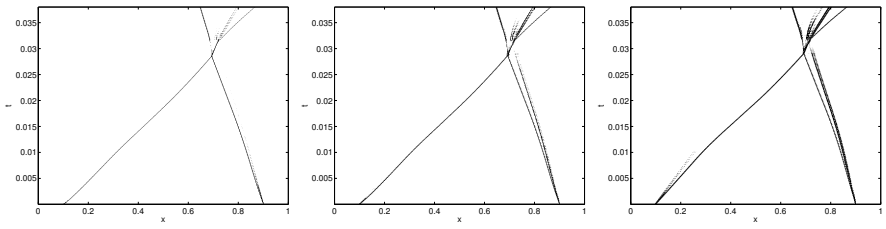

(a) $C = 0.25$ (b) $C = 0.1$ (c) $C = 0.05$

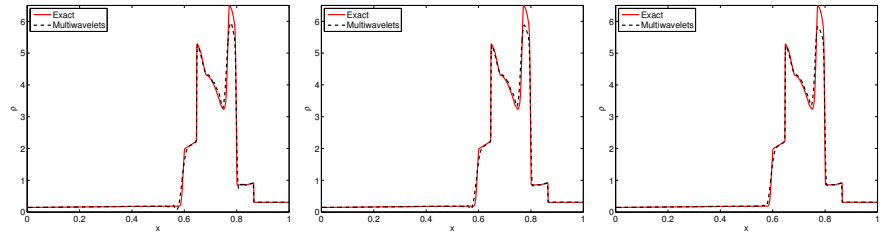

(d) $C = 0.25$ (e) $C = 0.1$ (f) $C = 0.05$

Figure 3.9: Blast-wave problem: time-history plot of detected troubled cells (first row), and approximation at final time $T = 0.038$ (second row), using the multiwavelet troubled-cell indicator, 512 elements, $k = 1$.

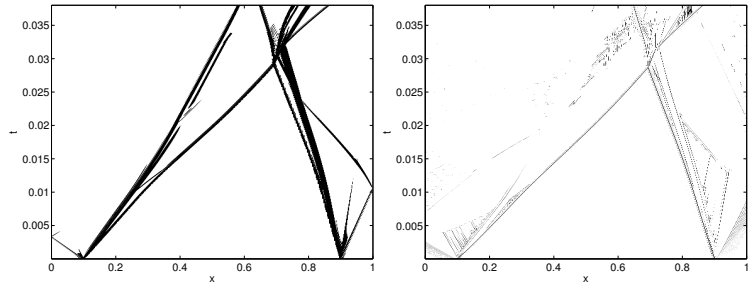

(a) KXRCF (b) Harten

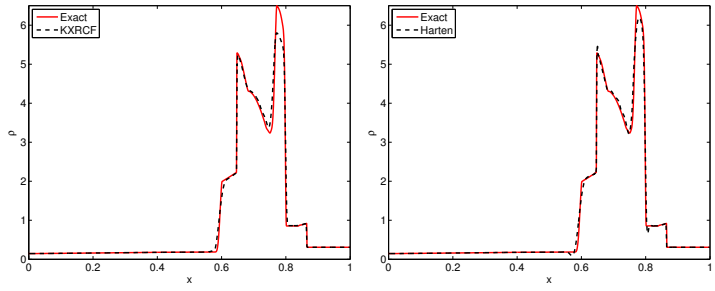

(c) KXRCF (d) Harten

Figure 3.10: Blast-wave problem: time-history plot of detected troubled cells (first row), and approximation at final time $T = 0.038$ (second row), using the KXRCF indicator or Harten's indicator, 512 elements, $k = 1$.

SHOCK DENSITY WAVE INTERACTION PROBLEM (SHU-OSHER PROBLEM)
In this section, the results are studied for the Shu-Osher problem [121] (Section 2.5.4). The exact solution at $T = 1.8$ is approximated using a fine mesh, see Figure 3.11. Here, we see that the initial contact discontinuity has traveled to the right. To the left of this discontinuity, a highly-oscillatory region has formed. Newly-formed sine waves at the most-left part of the domain are tilted in time to form a sawtooth structure. These new shocks are caused by the nonlinearity of the Euler equations.

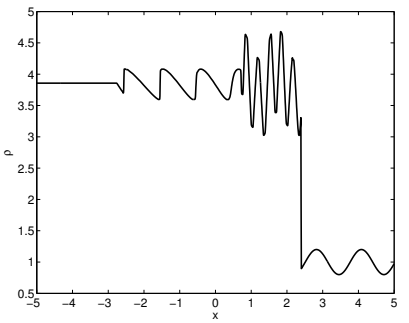

Figure 3.11: Fine-mesh approximation of the solution to the Shu-Osher problem at $T = 1.8$.

For this example, results that correspond to the application of the moment limiter in every element are given in Figure 3.12. It is clearly visible that almost every element is limited, and the peaks in the oscillating region at the left side of the initial discontinuity ($0.5 \leq x \leq 2$) have been lowered. The application of a troubled-cell indicator makes a clear difference.

The multiwavelet troubled-cell indicator was applied using the values of C equal to 0.5, 0.1, and 0.05 (Figure 3.13). If $C = 0.5$ is used, then the left shocks are not captured: only the contact discontinuity is detected. The value $C = 0.1$ is more useful since some elements belonging to the newly-formed shocks are detected. The approximation looks much better in this region. The value $C = 0.05$ is too small: the continuous oscillating region is detected as well. For this example, the choice of C is very delicate. For $k = 2$, the multiwavelet indicator shows a similar behavior, and also here, the value of C should be chosen smaller in order to detect the same regions, whereas a larger C can be used to find a nonoscillatory approximation. The indicator works nicely for $k = 3$ if the parameter is chosen sufficiently.

The results using the KXRCF or Harten's indicator can be inspected in Figure 3.14. The KXRCF indicator performs very poorly: in the linear case, the contact discontinuity is detected only. Therefore, the approximation is very oscillatory. For the quadratic case, parts of the two left shocks are detected, which leads to better results. For $k = 3$, the KXRCF detector perfectly detects the newly-formed shocks but also starts to detect several elements in the smooth oscillatory region. For Harten's indicator, the troubled cells are very scattered over the domain, and the final approximation contains small oscillations.

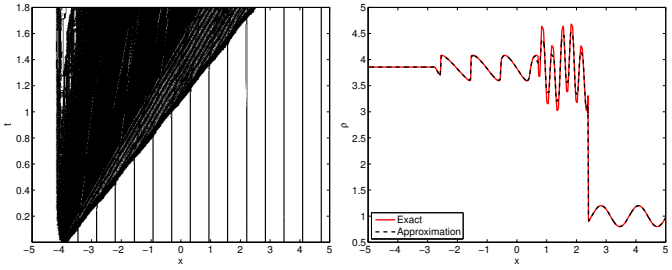

(a) Limited elements (b) Approximation

Figure 3.12: Shu-Osher problem: time-history plot of limited elements, and approximation at time $T = 1.8$, using the full moment limiter, 512 elements, $k = 1$.

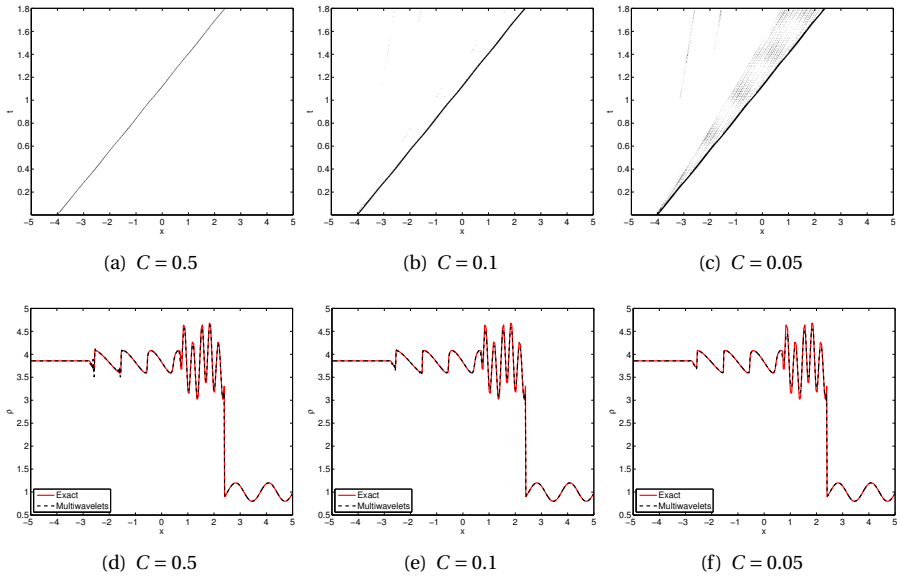

(a) $C = 0.5$ (b) $C = 0.1$ (c) $C = 0.05$

(d) $C = 0.5$ (e) $C = 0.1$ (f) $C = 0.05$

Figure 3.13: Shu-Osher problem: time-history plot of detected troubled cells (first row), and approximation at final time $T = 1.8$ (second row), using the multiwavelet troubled-cell indicator, 512 elements, $k = 1$.

DISCUSSION

For the one-dimensional test cases, we have seen that the multiwavelet troubled-cell indicator works well if a suitable value for the parameter C is chosen. For higher polynomial degrees, C should be chosen smaller in order to detect the correct troubled regions. However, we see in Table 3.1 that although fewer elements are detected, the higher-order approximations are often still nonoscillatory. This is related to the number of degrees of freedom that should be used per wavelength. The higher the polynomial degree of the approximation is, the fewer points are needed in the mesh to obtain the same accuracy of the approximation [68]. Therefore, often a larger value of C than for the linear case

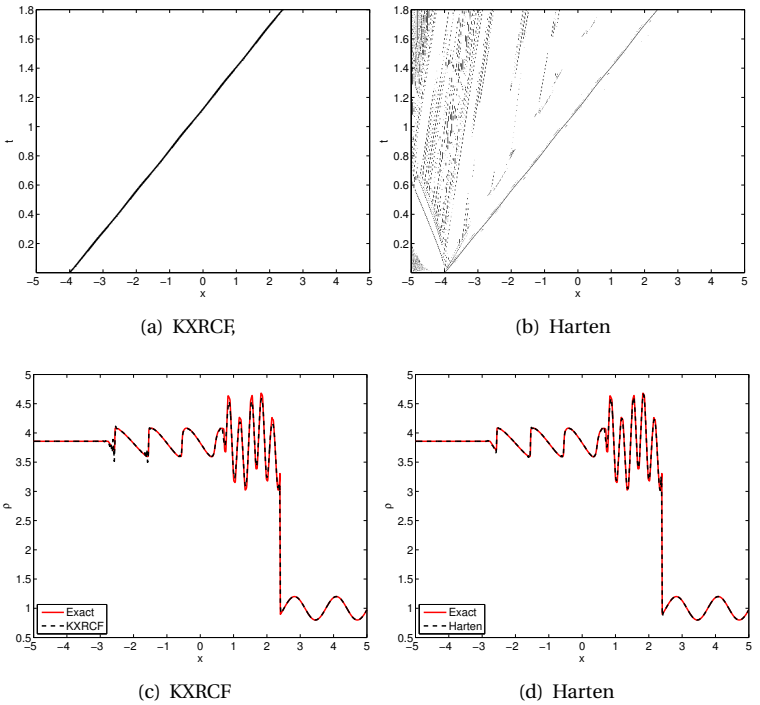

(a) KXRCF, (b) Harten

(c) KXRCF (d) Harten

Figure 3.14: Shu-Osher problem: time-history plot of detected troubled cells (first row), and approximation at final time $T = 1.8$ (second row), using the KXRCF indicator or Harten's indicator, 512 elements, $k = 1$.

is used in practice. The KXRCF indicator works well in some cases and for the higher degrees, but in the linear case often selects too few elements to remove all oscillations. Harten's indicator gives rise to a very scattered pattern of troubled cells, and most approximations are still oscillatory.

In Table 3.1, the average and maximum percentages of troubled elements in time are compared for each test problem, as in [104]. A troubled-cell indicator is said to be more accurate if smaller percentages of troubled cells are found. However, the approximation allows for more oscillations when fewer elements or incorrect regions are detected. This can, for example, be seen in the linear cases of Sod's problem ($C = 0.9$), Lax's problem ($C = 0.9$), the blast-wave problem ($C = 0.25$), and the Shu-Osher problem ($C = 0.5$), where, although the smallest percentage is found, the resulting approximation oscillates. Marked in bold are the smallest average percentages that give rise to a visually nonoscillatory approximation. It seems that the multiwavelet indicator leads to the best results, thereby detecting the smallest possible percentages.

Note that for the blast-wave problem and the Shu-Osher problem, different values of C are used for different polynomial degrees. This is because the interacting waves form an extremely nonlinear problem, thereby requiring a very accurate choice of C. We use the fact that a smaller C is needed to detect all nonsmooth regions.

Table 3.1: Average and maximum percentages of cells that are indicated as troubled by our multiwavelet troubled-cell indicator, for different C, the KXRCF indicator or Harten's indicator. Marked in bold are the smallest average percentages that belong to a visually nonoscillatory approximation.

Sod, 128 elements, $k = 1$ (first row), $k = 2$ (second row), and $k = 3$ (third row)

$C = 0.9$		$C = 0.5$		$C = 0.1$		KXRCF		Harten, $\alpha = 1.5$	
Ave	Max	Ave	Max	Ave	Max	Ave	Max	Ave	Max
0.8191	2.3438	1.2458	6.2500	**6.0431**	13.2812	1.6892	3.9062	4.6791	11.7188
0.8049	2.3438	1.1020	5.4688	**3.5906**	10.1562	2.6486	6.2500	1.2982	6.2500
0.8069	1.5625	**1.2000**	4.6875	3.3953	8.5938	3.5275	7.0312	6.0957	13.2812

Lax, 128 elements, $k = 1$ (first row), $k = 2$ (second row), and $k = 3$ (third row)

$C = 0.9$		$C = 0.5$		$C = 0.1$		KXRCF		Harten, $\alpha = 1.5$	
Ave	Max	Ave	Max	Ave	Max	Ave	Max	Ave	Max
0.8130	1.5625	0.9451	4.6875	**3.8251**	6.2500	1.8229	3.9062	5.7213	12.5000
0.8051	2.3438	1.0258	3.1250	**2.5576**	6.2500	3.2777	4.6875	1.7059	7.0312
0.8219	2.3438	1.1022	3.9062	**2.1980**	5.4688	5.9074	8.5938	5.8894	14.0625

Blast, 512 elements, $k = 1$ (first row), $k = 2$ (second row), and $k = 3$ (third row)

$C = 0.25$		$C = 0.1$		$C = 0.05$		KXRCF		Harten, $\alpha = 1.5$	
Ave	Max	Ave	Max	Ave	Max	Ave	Max	Ave	Max
0.5037	2.7344	1.1176	4.1016	**1.8533**	5.4688	6.5907	8.9844	1.3265	3.3203
$C = 0.1$		$C = 0.05$		$C = 0.01$		KXRCF		Harten, $\alpha = 1.5$	
Ave	Max	Ave	Max	Ave	Max	Ave	Max	Ave	Max
0.7158	2.3438	1.0805	4.1016	2.3799	7.6172	12.4968	20.3125	0.7616	3.1250
0.6810	2.7344	0.9928	3.3203	1.8240	6.2500	20.1565	29.6875	6.6963	16.2109

Shu-Osher, 512 elements, $k = 1$ (first row), $k = 2$ (second row), and $k = 3$ (third row)

$C = 0.5$		$C = 0.1$		$C = 0.05$		KXRCF		Harten, $\alpha = 1.5$	
Ave	Max	Ave	Max	Ave	Max	Ave	Max	Ave	Max
0.2338	0.7812	0.6346	1.9531	**1.2813**	11.9141	0.6646	0.7812	2.1844	5.2734
0.2673	0.7812	**0.5308**	1.9531	0.6780	4.1016	1.2213	2.3438	0.7085	3.1250
$C = 0.1$		$C = 0.05$		$C = 0.01$		KXRCF		Harten, $\alpha = 1.5$	
Ave	Max	Ave	Max	Ave	Max	Ave	Max	Ave	Max
0.5682	1.7578	0.7358	2.1484	1.2231	5.2734	2.4808	5.0781	2.2626	7.4219

A useful property of troubled-cell indicators is the decrease of percentages if the resolution is increased [104]. In all examples, $C = 0.1$ is a good choice for detecting troubled cells. Therefore, we keep it fixed for each example, and double the number of elements in the discretization. The percentages of detected troubled cells are approximately halved, which can be seen in Table 3.2. The KXRCF and Harten's troubled-cell indicator have the same property, although the rate of decrease is smaller, [104].

Table 3.2: Average and maximum percentages of cells that are indicated as troubled by the multiwavelet troubled-cell indicator ($C = 0.1$), using twice as many elements as in Table 3.1.

	Sod 256 elements		Lax 256 elements		Blast 1024 elements		Shu-Osher 1024 elements	
k	Ave	Max	Ave	Max	Ave	Max	Ave	Max
1	2.6031	6.6406	1.7777	3.1250	0.4930	2.1484	0.3076	0.7812
2	1.6877	5.0781	1.2632	3.1250	0.3431	1.4648	0.2607	0.6836
3	1.4882	4.2969	1.0692	2.7344	0.3301	1.7578	0.2800	0.6836

THRESHOLDING OF THE MULTIWAVELET COEFFICIENTS

It is also possible to use the thresholding technique for multiwavelet coefficients to detect troubled cells ([55], Section 2.4.6). It turns out that this indicator works very well as long as an appropriate value for C is chosen, and the mesh is taken fine enough. The results for the different test cases are visualized in Figure 3.15 using the heuristic strategy. Here, we take the value $C = 1/(b-a)$ where $[a,b]$ is the domain on which the test problem is defined. Note that this thresholding technique is very accurate. However, many elements should be used to meet the asymptotic properties of the indicator.

If the number of elements is taken smaller, then C should decrease to detect the correct features. In that case, it is difficult to guess the correct value of C. Another option is to use the a priori strategy for coarser meshes, see Figure 3.16. If $C = 1/(b-a)$ is used, then this approach works well for Sod's and Lax's shock tube, but too many elements are detected for the blast-wave and the Shu-Osher problem. Also here, the value of C should be adapted to find the correct results.

Note that the multiwavelet troubled-cell indicator described in this chapter was developed independently from the thresholding technique.

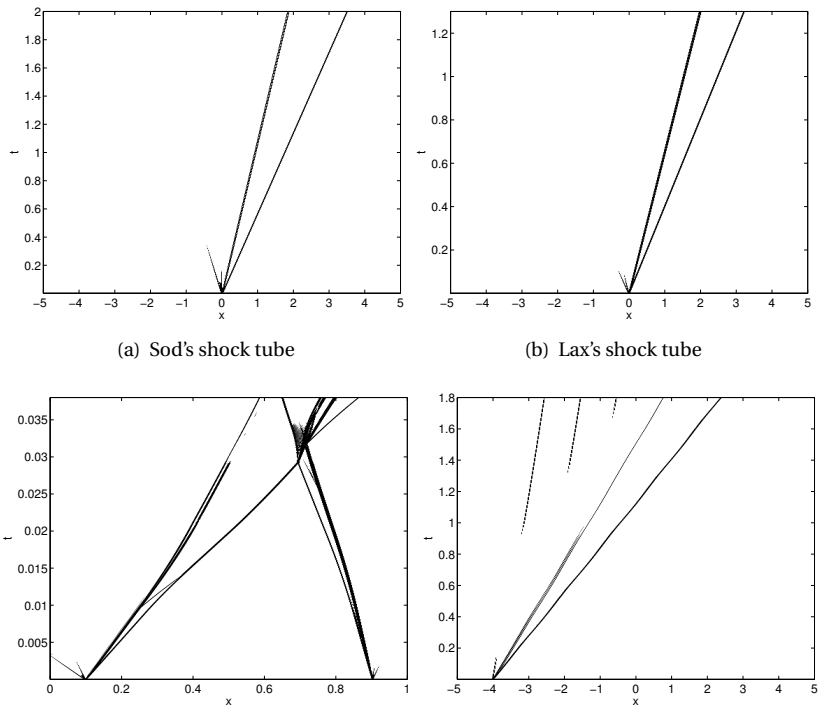

(a) Sod's shock tube

(b) Lax's shock tube

(c) Blast-wave problem

(d) Shu-Osher problem

Figure 3.15: Thresholding technique with heuristic approach: time-history plot of detected troubled cells, 1024 elements, $k = 1$, $C = 1/(b-a)$, with $[a,b]$ the computational domain.

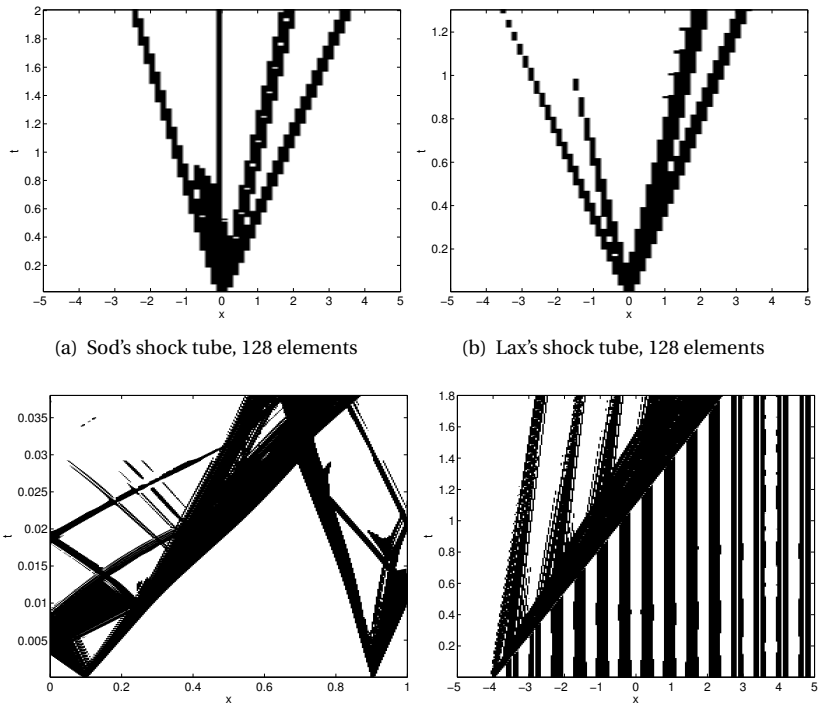

(a) Sod's shock tube, 128 elements

(b) Lax's shock tube, 128 elements

(c) Blast-wave problem, , 512 elements

(d) Shu-Osher problem, 512 elements

Figure 3.16: Thresholding technique with a priori approach on coarser meshes: time-history plot of detected troubled cells, $k = 1$, $C = 1/(b-a)$, with $[a,b]$ the computational domain.

3.3.2. TWO-DIMENSIONAL EXAMPLE

For the last example, the two-dimensional equations of compressible gas dynamics are considered [88] for the double Mach reflection of a strong shock [144] (Section 2.5.5). The combination of Harten's troubled-cell indicator and the moment limiter is unstable for this example. This possibility was also noticed in [149]. Therefore, the multiwavelet approach will be tested against the fully moment-limited approach and the KXRCF indicator.

The results at $T = 0.2$ using $\Delta x = \Delta y = 1/128$ are given in Figures 3.17 and 3.18. For the multiwavelet troubled-cell indicator, the parameters $C^{\alpha}, C^{\beta}, C^{\gamma}$ are chosen equal to $C = 0.05$. The approximations of the multiwavelet and the KXRCF approach look similar. In the turbulent region, more details of the DG simulation can be seen because we allow the approximation to oscillate in continuous regions.

As in [91], we can see that the α, β and γ modes detect different troubled cells based on direction. Although Qiu and Shu use both density and energy to compute troubled cells [104], for our multiwavelet indicator using only density is enough. The use of energy does not produce significant changes. The KXRCF indicator using density and energy as indicator variables works very well, detecting exactly the discontinuous regions in the

solution. For $k = 2$ the KXRCF indicator detects more elements in the turbulent region than if the multiwavelet indicator ($C = 0.05$) is used. For $k = 3$, this effect is even more emphasized, since the number of detected elements for $C = 0.05$ stays approximately the same, whereas it increases much more for the KXRCF indicator.

The percentages of detected troubled cells are given in Table 3.3. Note that the full limiter limits on average approximately 27% of the elements, with a maximum of more than 50%. In that case, the only elements that are not limited are in regions where the original state is still found (above the bow, or in the right part where $x \in [3,4]$). The application of the moment limiter in combination with a troubled-cell indicator results in limiting only a small portion of the elements. Therefore, we would expect the total computation time to decrease by using a troubled-cell indicator. In Table 3.4, the total computation times using one of the different indicators can be compared. Note that for $k = 1$, it seems as if the overhead of computing the troubled-cell indication values makes these methods more costly than expected. However, we remark that in the current approach, we save the matrices with troubled or limited elements at each time step. This means that at each time step, one matrix is saved if the full limiter is used, three matrices are saved if the multiwavelet troubled-cell indicator is applied (α, β, and γ mode), and two matrices if the KXRCF shock detector is used (density and energy). Therefore, the computation times are larger than necessary. We expect that the use of an appropriate profiler will improve these results. For $k = 2$ and especially $k = 3$, the multiwavelet and KXRCF troubled-cell indicators are much faster than the full moment limiter.

3.4. CONCLUDING REMARKS

In this chapter, the relation between multiwavelet coefficients and jumps in (derivatives of) the DG approximation has been explained and the use of these coefficients for the detection of troubled cells has been investigated. The multiwavelet troubled-cell indicator that has been constructed in this chapter compares the multiwavelet coefficients in absolute value with the maximum coefficient (in absolute value) over the domain. A parameter C is used to define the strictness of the indicator.

The indicator has been tested on different problems using the Euler equations of gas dynamics in one and two dimensions. The technique performs well if a suitable value for the problem-dependent parameter C is chosen. Compared to the KXRCF shock detector and Harten's indicator, the multiwavelet indicator leads to the best results, since the smallest possible percentages of troubled cells are detected resulting in nonoscillatory approximations. For higher polynomial degrees in two dimensions, the computation of a fully moment-limited approximation takes much more time than if the moment limiter is only applied to the detected troubled cells.

Since the choice of the parameter C is related to the accuracy of the troubled-cell indicator, the next chapter focuses on automating this process. The new technique proposed in that chapter can also be used for the detection of local structures.

Table 3.3: Average and maximum percentages of cells that are limited for the double Mach reflection problem, $\Delta x = \Delta y = 1/128$.

	Full limiter		$C = 0.05$		KXRCF	
k	Ave	Max	Ave	Max	Ave	Max
1	26.8356	50.6927	1.7939	2.9312	1.3889	1.9714
2	28.3570	53.9673	1.7590	2.7695	3.4451	5.3375
3	27.2912	52.1011	2.7832	2.7832	8.0253	12.4573

Table 3.4: Total computation time for double Mach, $\Delta x = \Delta y = 1/128$.

k	Full limiter	$C = 0.05$	KXRCF
1	39	91	89
2	367	326	324
3	3286	2280	2274

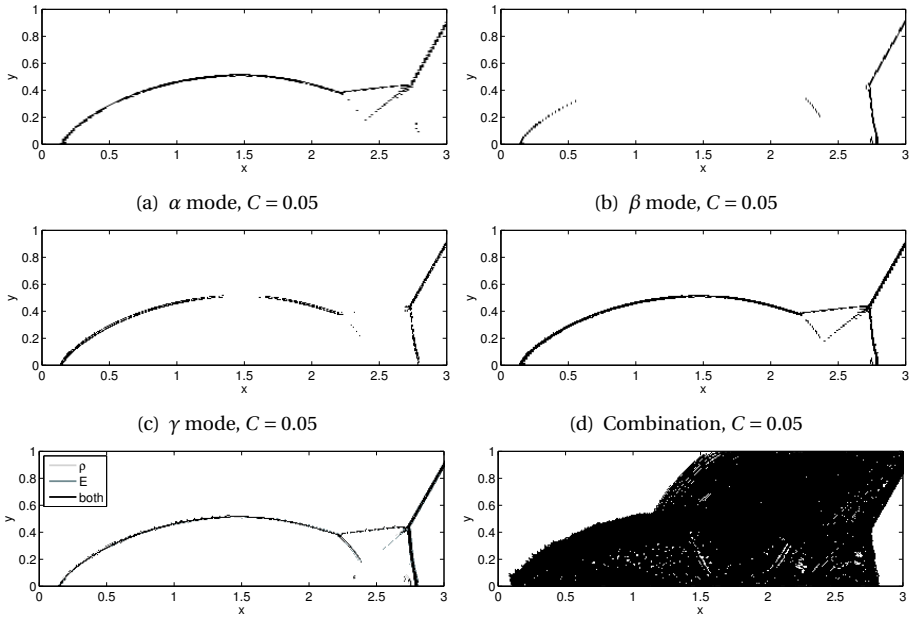

(a) α mode, $C = 0.05$ (b) β mode, $C = 0.05$

(c) γ mode, $C = 0.05$ (d) Combination, $C = 0.05$

(e) KXRCF (f) Full limiter

Figure 3.17: Detected troubled cells at $T = 0.2$, double Mach reflection problem, $k = 1$, $\Delta x = \Delta y = 1/128$.

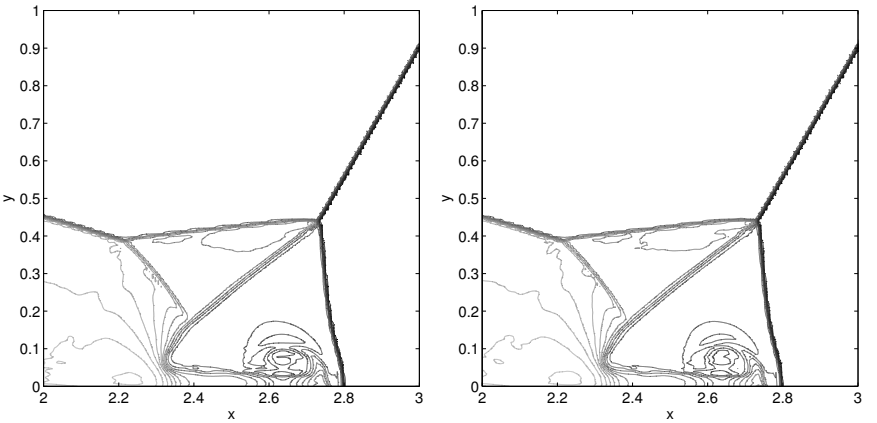

(a) $C = 0.05$ (b) KXRCF

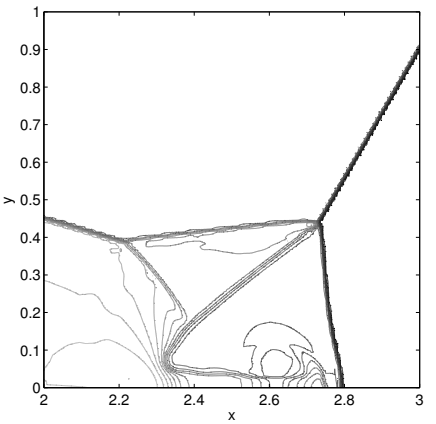

(c) Full limiter

Figure 3.18: Contour lines of approximation, double Mach reflection problem at $T = 0.2$, $\Delta x = \Delta y = 1/128$, $k = 1$.

4

AUTOMATED PARAMETERS USING OUTLIER DETECTION

As we have seen in Chapter 3, the multiwavelet troubled-cell indicator only works well if a suitable problem-dependent parameter is chosen. In this chapter, we develop an outlier-detection algorithm for troubled-cell indication and compare various techniques using outlier detection in place of a problem-dependent parameter. Section 4.1 discusses the parameters that are used in the different indication techniques. Section 4.2 contains a motivation for the switch to outlier detection. In Section 4.3, the outlier-detection algorithm is explained, with specific details for the application of troubled-cell indication in Section 4.4. Section 4.5 considers the choice of the outlier-detection vectors for the different indication methods. Numerical results are shown in Section 4.6, and a discussion about the computational costs is given in Section 4.7. Concluding remarks are given in Section 4.8.

Parts of this chapter have been published in SIAM Journal on Scientific Computing **38**(1) (2016).

4.1. PARAMETERS FOR TROUBLED-CELL INDICATION

In this section, the parameters that are used for troubled-cell indication are discussed. In particular, we consider the multiwavelet troubled-cell indicator (Chapter 3), the KXRCF shock detector (Section 2.3.2) and the minmod-based TVB indicator (Section 2.3.3).

4.1.1. MULTIWAVELET TROUBLED-CELL INDICATOR

The multiwavelet troubled-cell indicator [137, 138] detects elements I_j and I_{j+1} on the DG mesh if

$$|\tilde{d}_{kj}^{n-1}| > C \cdot \max\{|\tilde{d}_{kj}^{n-1}| : j = 0, \ldots, 2^n - 1\}, \text{ with } C \in [0,1].$$

The accuracy of this indicator depends on the choice of the problem-dependent parameter C. If C decreases, then the number of detected troubled cells increases. Several tests should be performed to find an appropriate value for each problem.

4.1.2. KXRCF SHOCK DETECTOR

The KXRCF shock detector detects element I_j depending on the value of

$$\hat{\mathscr{I}}_j = \frac{\left| \int_{\partial I_j^-} (u_h|_{I_j} - u_h|_{I_{n_j}}) ds \right|}{h^{\frac{k+1}{2}} |\partial I_j^-| \, ||u_h|_{I_j}||}.$$

Motivated by the discussion in [83], the threshold value is taken equal to 1, such that element I_j is detected as troubled if $\hat{\mathscr{I}}_j > 1$ (Section 2.3.2). However, this threshold parameter is chosen arbitrarily: the value 1 does not necessarily follow from the theory.

4.1.3. MINMOD-BASED TVB INDICATOR

For the minmod-based TVB indicator, element I_j is detected as troubled if either $\tilde{u}_j$ or $\tilde{\tilde{u}}_j$ (equation (2.11)) is modified by the functions

$$\tilde{u}_j^{(\text{mod})} = \tilde{m}(\tilde{u}_j, \bar{u}_{j+1} - \bar{u}_j, \bar{u}_j - \bar{u}_{j-1}), \quad \tilde{\tilde{u}}_j^{(\text{mod})} = \tilde{m}(\tilde{\tilde{u}}_j, \bar{u}_{j+1} - \bar{u}_j, \bar{u}_j - \bar{u}_{j-1}),$$

where the TVB-modified minmod function is defined as

$$\tilde{m}(a_1, \ldots, a_q) = \begin{cases} a_1, & \text{if } |a_1| \leq M\Delta x^2, \\ m(a_1, \ldots, a_q), & \text{otherwise,} \end{cases}$$

and $m(a_1, \ldots, a_q)$ is the original minmod function as given in equation (2.13) [29, 30]. The parameter M is difficult to tune, and hardly any difference is found when M ranges from 1 to 100 [148].

In [145], a parameter-free minmod marker was constructed. Although the results in that paper are promising, the method cannot be used for different troubled-cell indication values. One option that may work for several indication values, is the use of a statistical tool: outlier detection. In the next section, the motivation for this switch is explained.

4.2. MOTIVATION FOR SWITCH TO OUTLIER DETECTION

In this section, the switch to outlier detection is motivated using a particular test problem for the multiwavelet troubled-cell indicator. Similar observations hold for the other troubled-cell indicators that are discussed in this dissertation.

Problems can arise when the troubled-cell indicator is applied to an approximation that is varying substantially over the domain. As an example, the multiwavelet troubled-cell indicator is used for the following functions:

$$f_1(x) = \begin{cases} 1, & \text{if } x \in [-0.5,-0.25], \\ 0.75, & \text{if } x \in [0,0.25], \\ 0, & \text{else,} \end{cases} \qquad f_2(x) = \begin{cases} 1, & \text{if } x \in [-0.5,-0.25], \\ 0.25, & \text{if } x \in [0,0.25], \\ 0, & \text{else,} \end{cases}$$

see Figures 4.1(a) and 4.1(c). The corresponding values of the multiwavelet coefficients are depicted in Figures 4.1(b) and 4.1(d). Horizontal lines mark the bounds for troubled-cell indication for different values of C. Note that $C = 0.5$ suffices for f_1, whereas for f_2 the value $C = 0.2$ should be taken to detect all discontinuities. In short, C ideally depends on the approximation.

Similar observations can be made for the KXRCF shock detector and the minmod-based TVB indicator. The three indicators attach a value to each element of the domain (multiwavelet coefficient, jump across inflow boundary, or boundary approximations, respectively). Discontinuous regions usually correspond to the locations where the indicator value suddenly increases or decreases with respect to the neighboring values. This means that indication can be reduced to detecting the outliers of a vector with troubled-cell indication values.

4.3. OUTLIER DETECTION

In this section, an outlier-detection algorithm is proposed to detect outliers in a vector. Therefore, we use a boxplot mechanism that is often applied in statistics [54, 135] and described by Tukey [133]. Ogden mentions the boxplot technique for the detection of outliers in wavelet coefficients in [100], and boxplots are also used in combination with wavelet coefficients in [84]. Important properties of this method are that only a few 'false positives' are found if the data are well behaved (i.e., Gaussian [70]) and that it is not necessary to specify the number of possible outliers in advance. This is in contrast to many standard outlier-detection techniques which require stating the exact or the maximum number of outliers that may be present [69]. The technique will be applied to the troubled-cell indicators discussed in Section 4.1.

We use a vector $\mathbf{d} = (d_0, \ldots, d_N)^\top$, of which outliers (suddenly changing coefficients with respect to neighbors) should be detected. A general outline of the outlier-detection algorithm that we use is provided in Algorithm 4.1 [139]. In the following, we discuss the details.

4.3.1. QUARTILES

Quartiles separate the data into four equal groups [105]. The values of Q_1, Q_2 (the median), and Q_3 provide useful information about the structure of $\mathbf{d}$. As a preparation, it is

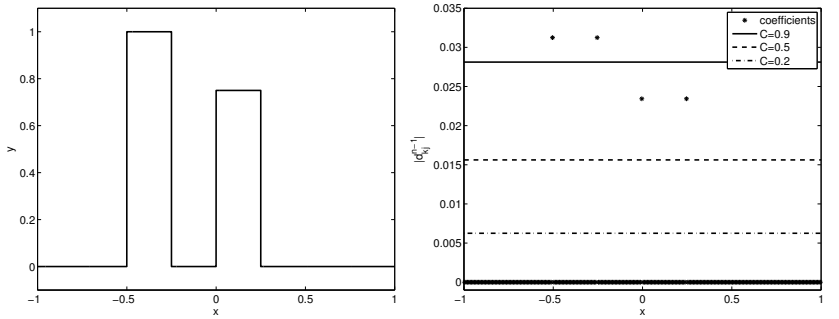

(a) f_1 (b) $|\tilde{d}_{kj}^{n-1}|$ corresponding to f_1

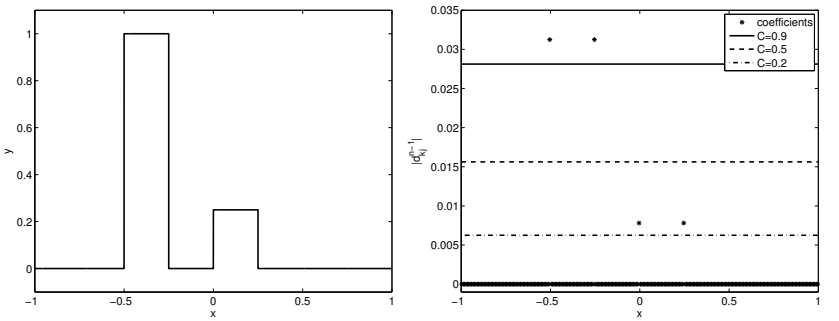

(c) f_2 (d) $|\tilde{d}_{kj}^{n-1}|$ corresponding to f_2

Figure 4.1: Functions, corresponding multiwavelet coefficients, and bounds for detection, $k = 1$, $n = 8$.

convenient to sort $\mathbf{d}$, such that we obtain the vector $\mathbf{d}^s$:

$$\mathbf{d}^s = (d_0^s, d_1^s, \ldots, d_N^s)^\top, \quad \text{where,} \quad d_0^s \leq d_1^s \leq \cdots \leq d_N^s.$$

The median of $\mathbf{d}$ is defined as the 'middle value' of the vector [92]. It equals

$$\text{med}(\mathbf{d}) = \begin{cases} d_{N/2}^s, & \text{if } N \text{ is even,} \\ \frac{1}{2}\left(d_{(N-1)/2}^s + d_{(N+1)/2}^s\right), & \text{if } N \text{ is odd.} \end{cases}$$

The median is also called the second quartile of the vector $\mathbf{d}$.

The first quartile is defined as the value below which 25% of the data fall and is denoted by Q_1. Similarly, the third quartile, Q_3, equals the value that separates the lowest

Algorithm 4.1 Outlier-detection algorithm.

Send in a suitable troubled-cell indication vector $\mathbf{d}$.
Sort $\mathbf{d}$ to obtain $\mathbf{d}^s$.
Compute the quartiles of $\mathbf{d}^s$.
Construct the outer fences.
Determine the outliers.

75% of the data and the highest 25% [105]. Many different definitions of the first and third quartiles are used. In this work we apply Tukey's definition (definition 6 in [54]):

$$Q_1 = (1-g)d^s_{j-1} + g d^s_j, \tag{4.1}$$

where $[(N+4)/2]/2 = j+g$, and $[x]$ denotes the largest integer that does not exceed x. By construction, $g = 0$ or $g = 1/2$. The third quartile, Q_3, is then computed symmetrically using the upper end of the vector $\mathbf{d}^s$.

In the numerical examples, we will always use a troubled-cell indication vector with $N+1 = 4r$ coefficients, where $r \in \mathbb{N}$. In that case, the quartiles equal $Q_1 = (d^s_{r-1} + d^s_r)/2$ and $Q_3 = (d^s_{3r-1} + d^s_{3r})/2$.

4.3.2. FENCES AND OUTLIER DETECTION

The values of the quartiles provide useful information about the structure of the vector. However, this is not enough to define outliers in the vector. Outliers are the coefficients in the vector that occur apart from the others. To pick out certain coefficients as outliers, inner and outer fences are constructed, which were originally defined by Tukey [133]. The inner fences are chosen equal to $[Q_1 - 1.5(Q_3 - Q_1),\ Q_3 + 1.5(Q_3 - Q_1)]$ (coefficients outside this interval are called *soft outliers*). When the data are normally distributed, only 0.7% of the data set is seen as a soft outlier (asymptotically) [69]. The value 1.5 is referred to as the *whisker length* of the boxplot.

The outer fences of a vector are $[Q_1 - 3(Q_3 - Q_1),\ Q_3 + 3(Q_3 - Q_1)]$ (coefficients outside are called *extreme outliers*). The coverage for this whisker length is 99.9998%, such that only 0.0002% of the data in a normally distributed vector is detected as an extreme outlier (asymptotically) [69]. The choices of the whisker lengths (1.5 and 3) were proposed by Tukey [133] and are commonly used in the literature [54, 69, 73, 74, 114, 115]. We will use the extreme outliers to detect troubled cells, since then very outstanding coefficients in the vector are selected. Because the data were sorted, the outer fences and outliers can easily be determined.

4.3.3. APPLICATION OF OUTLIER-DETECTION ALGORITHM

In this section, we apply the outlier-detection algorithm to the following fictive troubled-cell indication vector:

$$\mathbf{d} = (-1,\ -1,\ -1,\ 0,\ 1,\ 0,\ 20,\ 2,\ 3,\ 1,\ 0,\ -3,\ -2,\ 0)^\top,$$

see Figure 4.2(a). Visual inspection of the vector leads to detection of the value 20. It turns out that the application of Algorithm 4.1 yields the same result.

The sorted vector $\mathbf{d}^s$ equals

$$\mathbf{d}^s = (-3,\ -2,\ -1,\ -1,\ -1,\ 0,\ 0,\ 0,\ 0,\ 1,\ 1,\ 2,\ 3,\ 20)^\top.$$

In this case, $N = 13$, such that $[(N+4)/2]/2 = 8/2 = 4 = j+g$, with $j = 4$ and $g = 0$. From equation (4.1), it follows that $Q_1 = d^s_3 = -1$, and similarly, $Q_3 = d^s_{10} = 1$. This means that the bounds for outlier detection are given by

$$Q_1 - 3(Q_3 - Q_1) = -7, \quad Q_3 + 3(Q_3 - Q_1) = 7,$$

such that every value in **d** that is smaller than −7 or greater than 7 is detected as troubled. Indeed, this leads to detection of the value 20. A boxplot visualization of this vector is depicted in Figure 4.2(b).

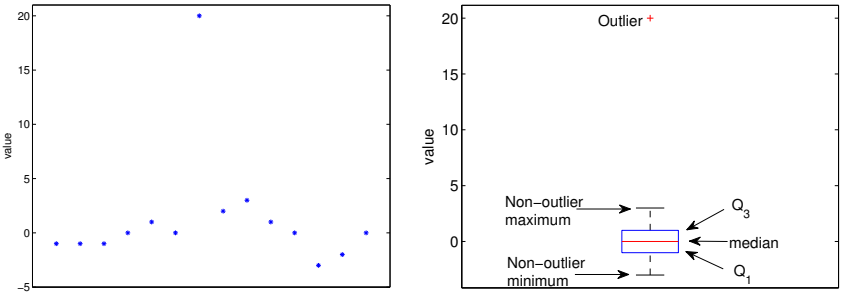

(a) Troubled-cell indication vector (b) Boxplot

Figure 4.2: Troubled-cell indication vector and corresponding boxplot using Algorithm 4.1.

4.4. OUTLIER DETECTION FOR TROUBLED-CELL INDICATION

In this section, the particular application of outlier detection for troubled-cell indication is discussed. As we have seen in Section 4.2, a troubled-cell indicator should detect the elements where indication values suddenly increase or decrease with respect to the neighboring values. This means that indication basically reduces to detecting the outliers of a vector with troubled-cell indication values. By applying the new outlier-detection technique, the threshold to be an extreme outlier is fixed, and the indicator no longer depends on problem-dependent parameters.

When an approximation contains several discontinuous regions, outlier detection applied to the global vector **D** will only select the strongest discontinuities. To also take into account the weaker discontinuities and the local structure of the approximation, the vector **D** will be split into local vectors of fixed length. For each subvector, the outlier-detection mechanism is applied [133]. In the local approach, we ignore the detected coefficients in the left half of the local region if they are not detected with respect to the left-neighboring vector, and similarly, the detected coefficients in the right half of the local region are tested. In this way, the spatial information can still be used.

The outlier-detection algorithm executes the steps as provided in Algorithm 4.2, and explained below [139].

Since the global vector **D** consists of 2^n coefficients, it is useful to split **D** into 2^{n-p} local vectors of length 2^p, where $p \in \{2,\dots,n\}$. Each local vector is then sorted. For convenience, we denote the sorted local vector of coefficients by $\mathbf{d}^s = (d_0^s, d_1^s, \dots, d_N^s)$, where $N = 2^p - 1$. By definition this vector has the following 25th and 75th percentiles (see equation (4.1)):

$$Q_1 = \frac{d^s_{2^{p-2}-1} + d^s_{2^{p-2}}}{2}, \quad Q_3 = \frac{d^s_{3\cdot 2^{p-2}-1} + d^s_{3\cdot 2^{p-2}}}{2}. \tag{4.2}$$

Algorithm 4.2 Outlier-detection algorithm using local vectors.

Send in a suitable troubled-cell indication vector **D**.
Split this vector into local vectors, **d**.
for all local vectors **do**
  Sort **d** to obtain $\mathbf{d}^s$.
  Compute Q_1 and Q_3 using equation (4.1).
  Detect d_j^s in the smallest 25% of $\mathbf{d}^s$ if $d_j^s < Q_1 - 3(Q_3 - Q_1)$, and d_j^s in the largest 25% of $\mathbf{d}^s$ if $d_j^s > Q_3 + 3(Q_3 - Q_1)$.
end for
Ignore the detected outliers in the left half of the local region when they are not detected with respect to the left-neighboring vector, and similarly, test the detected coefficients in the right half of the local region.

Next, we compute outer fences. Outliers are determined by comparing the smallest vector values with $Q_1 - 3(Q_3 - Q_1)$ and the largest components with $Q_3 + 3(Q_3 - Q_1)$. For the smallest values we start with testing whether $d_0^s < Q_1 - 3(Q_3 - Q_1)$. If d_0^s is not an outlier, then there are no other outliers, since $d_j^s \geq d_0^s \geq Q_1 - 3(Q_3 - Q_1)$, $j = 0, \ldots, N$. If d_0^s is an outlier, then we test d_1^s, etcetera. By construction, $Q_1 - 3(Q_3 - Q_1) \leq Q_1$, such that the only possibilities for low outliers are $d_0^s, \ldots, d_{2^{p-2}-2}^s$ ($2^{p-2} - 1$ coefficients). This means that at most $d_0^s, d_1^s, \ldots, d_{2^{p-2}-2}^s$ should be tested.

Similarly, we test d_N^s and (possibly) $d_{N-1}^s, \ldots, d_{3 \cdot 2^{p-2}+1}^s$ against $Q_3 + 3(Q_3 - Q_1)$ (depending on the outcome). Also here, at most $2^{p-2} - 1$ coefficients should be tested.

Finally, the detected outliers in the left half of the local vector are compared with the fences of the left-neighboring vector, and the outliers in the right half are compared with the right-neighboring fences.

It is important to choose the number of elements in each local vector appropriately, such that this parameter is not problem dependent. It should be noticed that $p = 3$ results in 8 coefficients per vector, which is too few to find a boxplot that is meaningful. Using $p = 4$ (16 coefficients per vector) means that at maximum six outliers can be detected per local vector. Therefore, the maximum number of possible outliers in **D** equals $2^{n-4} \cdot 6 = 3 \cdot 2^{n-3}$. If we take more coefficients per local vector, for example, $p = 5$ (32 coefficients per vector), then the 'stencil' is too wide to extract all local information of the approximation. Therefore, the use of 16 coefficients per local vector is proposed ($p = 4$), which worked well in all test cases that were performed. It should be noticed that this number of coefficients is also used by Tukey [133].

In two dimensions, outlier detection is applied to the x- and y-direction separately.

4.5. CHOICE OF INDICATION VECTORS

The outlier-detection algorithm requires passing in a vector of troubled-cell indication variables. In this section, the indication vectors are given on which outlier detection will be applied. In particular, the multiwavelet troubled-cell indicator (Chapter 3), the KXRCF shock detector (Section 2.3.2) and the minmod-based TVB indicator (Section

2.3.3) are considered [139]. In Chapter 3, Harten's subcell resolution idea [63] was used for indication [104, 137]. However, this method was not accurate for every test problem [145, 149], and will therefore not be investigated here.

4.5.1. MULTIWAVELET TROUBLED-CELL INDICATOR

The multiwavelet troubled-cell indicator uses coefficients $\tilde{d}_{kj}^{n-1}$ for detection. The indication vector is therefore chosen as $\mathbf{D} = (\tilde{d}_{k,0}^{n-1}, \ldots, \tilde{d}_{k,2^n-1}^{n-1})^\top$.

In two dimensions, we use the fact that the α mode detects troubled cells in the y-direction and the β mode in the x-direction. Therefore, the one-dimensional outlier-detection algorithm is applied to the following α-mode vectors for each x:

$$\mathbf{D}_i = \left(\tilde{d}_{(0,k),(i,0)}^{\alpha,\mathbf{n}-1}, \ldots, \tilde{d}_{(0,k),(i,2^{n_y}-1)}^{\alpha,\mathbf{n}-1}\right)^\top, \quad i = 0, \ldots, 2^{n_x-1} - 1.$$

Similarly, the β-mode vectors are chosen as

$$\mathbf{D}_j = \left(\tilde{d}_{(k,0),(0,j)}^{\beta,\mathbf{n}-1}, \ldots, \tilde{d}_{(k,0),(2^{n_x}-1,j)}^{\beta,\mathbf{n}-1}\right)^\top, \quad j = 0, \ldots, 2^{n_y-1} - 1.$$

Detection on the γ mode selects too many elements, and therefore, this mode is not used in the outlier-detection scheme.

4.5.2. KXRCF SHOCK DETECTOR

The KXRCF shock detector uses a normalization of the jump across inflow edges for detection. When outlier detection is used for this variable, too few elements are detected. The original discontinuity detector without normalization is more suitable, such that the jump across the interfaces is used in the indicator (equation (2.9)): we choose $\mathbf{D} = (\mathscr{I}_0, \ldots, \mathscr{I}_{2^n-1})^\top$.

In two dimensions, a matrix $\mathbf{D} = \{\mathscr{I}_{ij}\}$ is found. Here, the one-dimensional outlier-detection approach is applied in the x- and y-direction separately (row and column wise) [133].

4.5.3. MINMOD-BASED TVB INDICATOR

For the minmod-based TVB indicator we define two vectors: $\mathbf{D}_1 = (\tilde{u}_0, \ldots, \tilde{u}_{2^n-1})^\top$ and $\mathbf{D}_2 = (\tilde{\tilde{u}}_0, \ldots, \tilde{\tilde{u}}_{2^n-1})^\top$. The element I_j is detected as troubled if either $\tilde{u}_j$ or $\tilde{\tilde{u}}_j$ is detected as an outlier.

For the two-dimensional case, DG coefficients $u_{ij}^{(1,0)}$ and $u_{ij}^{(0,1)}$ are used for detection. Outlier detection will be applied to the vectors

$$\mathbf{D}_j = \left(u_{0,j}^{(1,0)}, \ldots, u_{2^{n_x}-1,j}^{(1,0)}\right)^\top, \; j = 0, \ldots, 2^{n_y} - 1,$$

in the x-direction and

$$\mathbf{D}_i = \left(u_{i,0}^{(0,1)}, \ldots, u_{i,2^{n_y}-1}^{(0,1)}\right)^\top, \; i = 0, \ldots, 2^{n_x} - 1,$$

in the y-direction [133]. In this way, it is possible to detect discontinuities in different directions.

4.6. NUMERICAL RESULTS

In this section, the original troubled-cell indicators are compared with the new outlier-detection approaches [139]. This is done for the multiwavelet troubled-cell indicator of Vuik and Ryan [137, 138], the KXRCF indicator [83], and the minmod-based TVB indicator [30]. The results were computed using $k = 1, 2, 3$. In this dissertation only the case $k = 2$ is presented.

The results for the one-dimensional test cases are presented using time-history plots of detected troubled cells.

4.6.1. ONE-DIMENSIONAL EXAMPLES

The test cases in one dimension include one continuous example using the Euler equations on $[-1, 1]$ with initial conditions $\rho_0(x) = 1 + 0.5\sin(10\pi x)$, $u_0(x) = 1$, $p_0(x) = 1$, and periodic boundary conditions. The density at $T = 2$ is given by $\rho(x, 2) = \rho_0(x)$. Using this example, we can validate our algorithm: since no discontinuities are present, no element should be detected. Indeed, the original troubled-cell indicators do detect certain elements, except the case KXRCF, $k = 3$ (chosen parameters are reasonable and commonly used [30, 83, 137]). This is depicted in Figure 4.3, in which the detected troubled cells using the original indicators are visualized. These so-called *time-history plots* show which elements are detected in space for each time step.

The application of the outlier-detection algorithm together with the troubled-cell indication vectors does not select any element (except for KXRCF, $k = 1$, where 0.02% of the elements is detected on average), which is the desirable result.

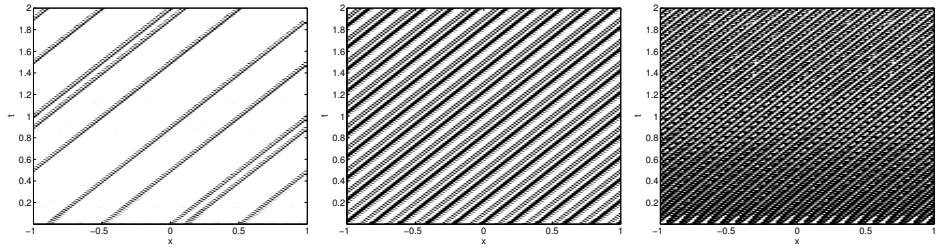

(a) Multiwavelets, $C = 0.5$ (b) KXRCF, threshold 1 (c) Minmod, $M = 10$

Figure 4.3: Detected troubled cells for continuous example, 128 elements, $k = 2$, using original troubled-cell indicators. Corresponding outlier-detection approaches do not detect any element.

In the second example, we investigate what happens if many shocks are located very close to each other. We use the Euler equations on $[-1, 1]$ with initial conditions

$$\rho_0(x) = \begin{cases} 0.1, & \text{if } x \in [-1, -0.75) \cup [-0.5, 0) \cup [0.1, 0.2) \cup [0.5, 0.75), \\ 0.125, & \text{if } x \in [-0.75, -0.5) \cup [0, 0.1) \cup [0.2, 0.5) \cup [0.75, 1], \end{cases}$$

$u_0(x) = 1$, $p_0(x) = 1$, and periodic boundary conditions. The results using the different troubled-cell indicators in their original or outlier-detection form can be seen in Figure 4.4. It is interesting to see that the KXRCF indication value is not able to detect the shocks, neither in the original form nor in the outlier-detection approach. The original multiwavelet troubled-cell indicator perfectly selects the eight discontinuities at all

times. The original minmod-based TVB indicator selects the correct elements in the first time steps but is not able to detect the shocks at later times. The outlier-detection multiwavelet troubled-cell indicator has difficulties selecting the three shocks that are closest to each other. The other discontinuities are selected at the majority of time steps but ignored when the limiter smoothed enough cells in that region. The results for the minmod-based TVB indicator are much improved when the outlier-detection approach is applied. However, also in this case the three closest discontinuities are not detected. Since these three shocks are very close to each other, the fences in this local region are large enough to include the shocks in the non-outlier region.

It should be noticed that the indication problems are related to the fact that the mesh was slightly underresolved. Using more elements in the mesh will improve the results.

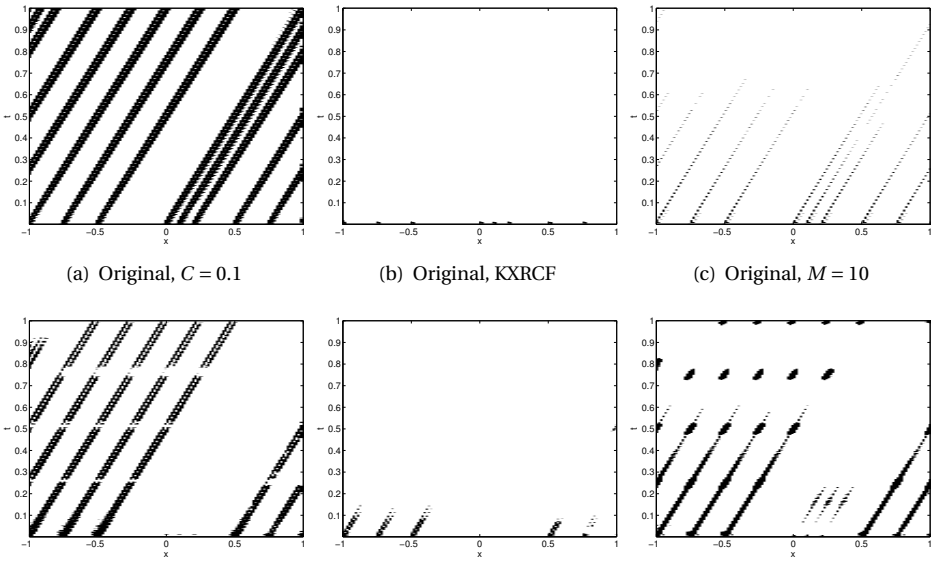

(a) Original, $C = 0.1$ (b) Original, KXRCF (c) Original, $M = 10$

(d) Outlier, multiwavelets (e) Outlier, KXRCF value (f) Outlier, minmod-based TVB

Figure 4.4: Detected troubled cells for example with many weak shocks, 128 elements, $k = 1$.

The standard numerical examples for the Euler equations are also investigated. The results and comparisons are shown using four different sets of initial conditions: the shock tubes of Sod [125] and Lax [86], the blast-wave problem [144], and the Shu-Osher problem [121] (Section 2.5, Figures 4.5-4.9). The outlier-detection technique is applied to density for the multiwavelet indicator, density and energy for KXRCF, and the characteristic variables for the minmod-based TVB indicator, as have been done by Qiu and Shu [104]. The first row of each figure consists of time-history plots of detected troubled cells using the original indicators. The second row belongs to the outlier-detected troubled cells. The corresponding approximations at the final times are given in the third and fourth rows. Note that these results are computed using the moment limiter in the detected troubled cells. A different choice for the limiter will result in different approximations.

Note that the original troubled-cell indicators are applied with the optimal problem-dependent parameters as found in [104, 137]. We stress that the outlier-detected results are computed without problem-dependent parameters, but with a fixed whisker length equal to 3, and with local indication vectors of size 16.

The new outlier-detection approach detects the troubled regions very accurately and generally better than the original parameter-based methods for the blast-wave and Shu-Osher problem. For the shock tube problems of Sod and Lax, most discontinuous regions are selected. Note that the outlier-detection indicators sometimes detect jumps in derivatives, as can be seen at the end points of the rarefaction waves. The original indicators, however, do mostly not detect these structures. This difference can be explained by recalling that the original indicators focus on the actual value of the indication variable, whereas the outlier-detection techniques investigate the relative value with respect to the neighboring region. A discontinuity in the derivative usually causes sudden differences, and therefore these regions are labeled as troubled. By applying a limiter at these locations, the discontinuity in the derivative is smeared a bit, such that at some time steps these elements are not detected. Note that all approximations are very accurate and close to the exact solution. This can also be seen in plots of the errors of the Sod shock tube problem (Figure 4.6) and the corresponding L^1-norms (Table 4.1). Note that the error of the non-limited approximation is very oscillatory (Figure 4.6(a)), although its L^1-norm is minimal. On the other hand, the fully moment-limited approximation has a very smooth error profile (Figure 4.6(b)), but the L^1-norm of the error is maximal. Here, we recognize that the full moment limiter limits many elements and therefore smooths out the approximation. The troubled-cell indication approaches are typically positioned in between these extremes. They show oscillations in the error profiles since fewer elements are detected than when the moment limiter is applied in all cells. This leads to more details in the accompanying approximations. The corresponding norms are smaller than that of the fully-moment limited approximation. Note that the troubled-cell indication error plots are very similar to each other. However, the outlier-detection approaches lead to a minor increase in the norms compared to the original norms. This could be because the end points of the rarefaction waves are detected by the outlier-detection scheme but not found by the original troubled-cell indicators (Figure 4.5). The application of the limiter in these cells makes the approximation more diffusive than needed. Notice that the choice of the troubled-cell indication variable does not have much impact on the quality of the approximation.

The most important improvements are found for the blast-wave and the Shu-Osher problem. For the interaction of two blast waves, the original KXRCF detector and minmod-based TVB indicator detect many elements. However, the new outlier-detection approach combined with these detection variables only selects a few of them, thereby still producing very accurate results.

For the Shu-Osher problem, we especially zoom into the results which are found for $k = 2$, in Figure 4.9. In the Shu-Osher problem, an initial discontinuity is moving to the right, thereby evolving (highly oscillatory) continuous regions and developing new shocks in the left side of the domain.

The first row of the figure consists of time-history plots of detected troubled cells using the original indicators. Note that both the multiwavelet indicator with $C = 0.01$ and

the minmod-based TVB indicator with $M = 100$ detect the highly-oscillatory region as being discontinuous. In this case, the KXRCF indicator gives more accurate results. For $k = 1$ however, the KXRCF indicator only detects the largest discontinuity and neglects the other three shocks in the left side of the plot, which leads to some spurious oscillations in the approximation.

In the second row of the figure, the time-history plots are shown when the indication vectors are used in the outlier-detection algorithm. All three indication techniques detect the correct regions, and the approximations are as expected (rows 3–4 of Figure 4.9). Note that the results are very close to the exact solution: the outlier-detection algorithm is indeed able to replace the problem-dependent parameters in the original indicators.

For $k = 1$ and $k = 3$, the same behavior is found: the new outlier-detection approach perfectly selects the discontinuous regions in the domain.

4.6.2. TWO-DIMENSIONAL EXAMPLE

In two dimensions, we investigate the double Mach reflection of a strong shock [144], which satisfies the two-dimensional Euler equations. Again, the original troubled-cell indicators (with optimal parameter) are compared to the outlier-detection approaches. The results for $k = 2$ can be compared in Figures 4.10-4.11 for the multiwavelet troubled-cell indicator, in Figure 4.12 for the KXRCF shock detector, and in Figure 4.13 for the minmod-based TVB indicator ($k = 1$ only). The spatial domain is split into $2^9 \times 2^7$ rectangular elements: $\Delta x = \Delta y = 1/128$. In each figure, the left plots are computed using the original troubled-cell indicators, and the right plots correspond to the outlier-detection approaches. Contour plots of the approximation at the final time are given as well.

As mentioned earlier, the multiwavelet technique can distinguish between x- and y-directed discontinuous regions. This is also the case if outlier detection is used. We point out that a sharp detection of the discontinuous region is found. Only a few elements outside the discontinuous region are added. This happens because a finite domain is used in the numerical model. In that case, numerical artifacts related to the boundary conditions give rise to a kind of numerical Riemann problem, and therefore more shocks and contact discontinuities are found [51]. The approximations at the final time are comparable to the results using the original multiwavelet troubled-cell indicator.

The original KXRCF shock detector is compared to the outlier-detection application in Figure 4.12. The detected troubled cells at the final time are similar for $k = 1$. For $k = 2$ and especially for $k = 3$ the outlier-detection scheme detects fewer elements. However, more elements are detected in the top region of the domain, where numerical artifacts cause extra shocks [51].

For the minmod-based TVB indicator, the results improve considerably when using outlier detection. In Figure 4.13(a), the detected troubled cells at the final time are shown for the original minmod-based TVB indicator. Note that too many elements are detected: continuous regions are also selected. However, the outlier-detection technique applied to the DG coefficients only selects the correct discontinuity profile (Figure 4.13(b)). It should be noted that this approach detects discontinuities in the x- and y-directions, since DG coefficients $u_{ij}^{(1,0)}$ are related to the first derivative in the x-direction, and $u_{ij}^{(0,1)}$ to the first derivative in the y-direction. Fewer elements are detected in this case, and the approximation at time $T = 0.2$ is still accurate.

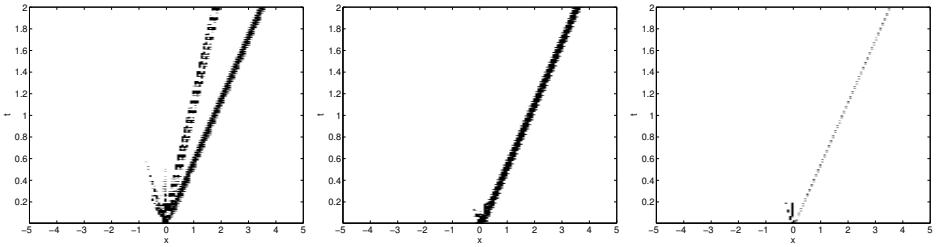

(a) Original, $C = 0.1$ (b) Original, KXRCF (c) Original, $M = 10$

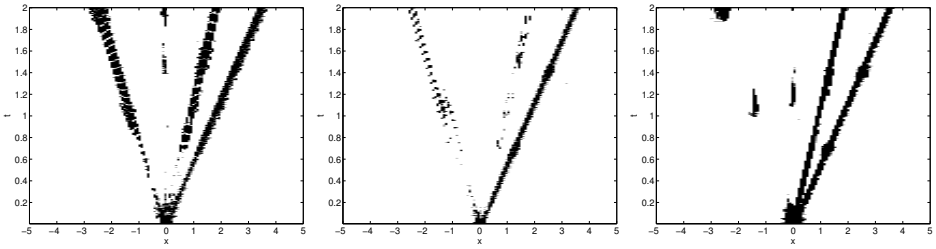

(d) Outlier, multiwavelets (e) Outlier, KXRCF value (f) Outlier, minmod-based TVB

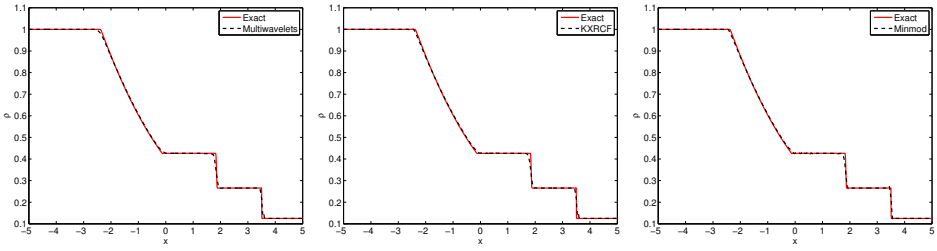

(g) Original, $C = 0.1$ (h) Original, KXRCF (i) Original, $M = 10$

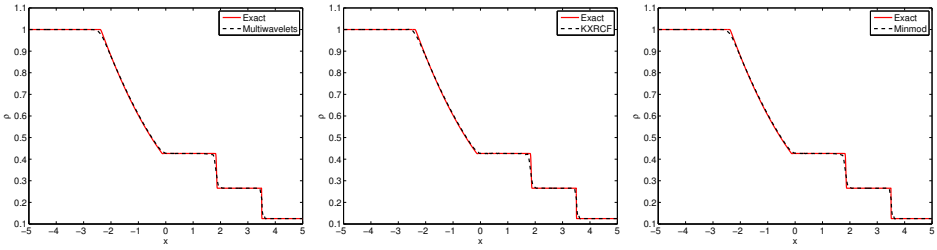

(j) Outlier, multiwavelets (k) Outlier, KXRCF value (l) Outlier, minmod-based TVB

Figure 4.5: Sod's shock tube: time-history plot of detected troubled cells (rows 1 and 2), and approximation at final time $T = 2$ (rows 3 and 4), 128 elements, $k = 2$.

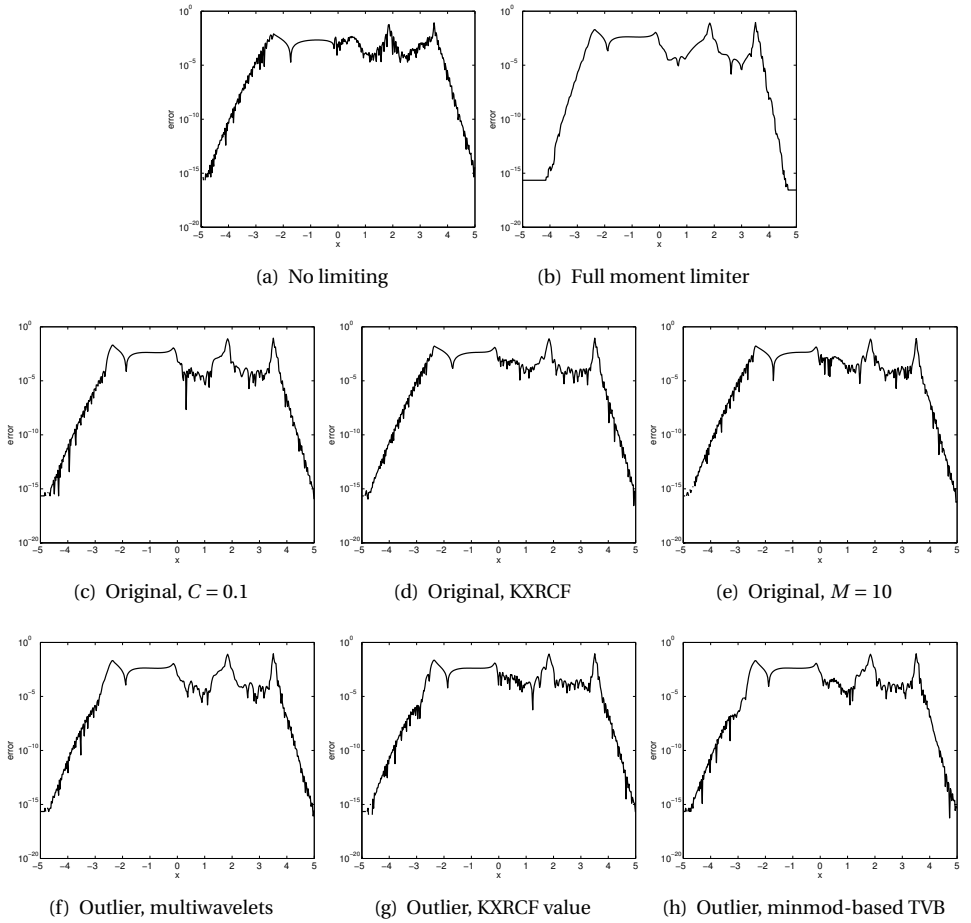

(a) No limiting (b) Full moment limiter

(c) Original, $C = 0.1$ (d) Original, KXRCF (e) Original, $M = 10$

(f) Outlier, multiwavelets (g) Outlier, KXRCF value (h) Outlier, minmod-based TVB

Figure 4.6: Sod's shock tube: plots of the errors in the approximation without limiter, with the full moment limiter, and when the moment limiter is applied in the detected troubled cells using the multiwavelet, KXRCF or minmod-based TVB indicator, 128 elements, $k = 2$.

Table 4.1: L^1-norm of errors in the approximation without limiter, with the full moment limiter, and when the moment limiter is applied in the detected troubled cells using the multiwavelet, KXRCF or minmod-based TVB indicator, Sod's shock tube, 128 elements, $k = 2$.

No limiting	0.0157		
Full moment limiter	0.0214		
	Multiwavelets	KXRCF	Minmod
Original	0.0208	0.0199	0.0188
Outlier	0.0213	0.0211	0.0214

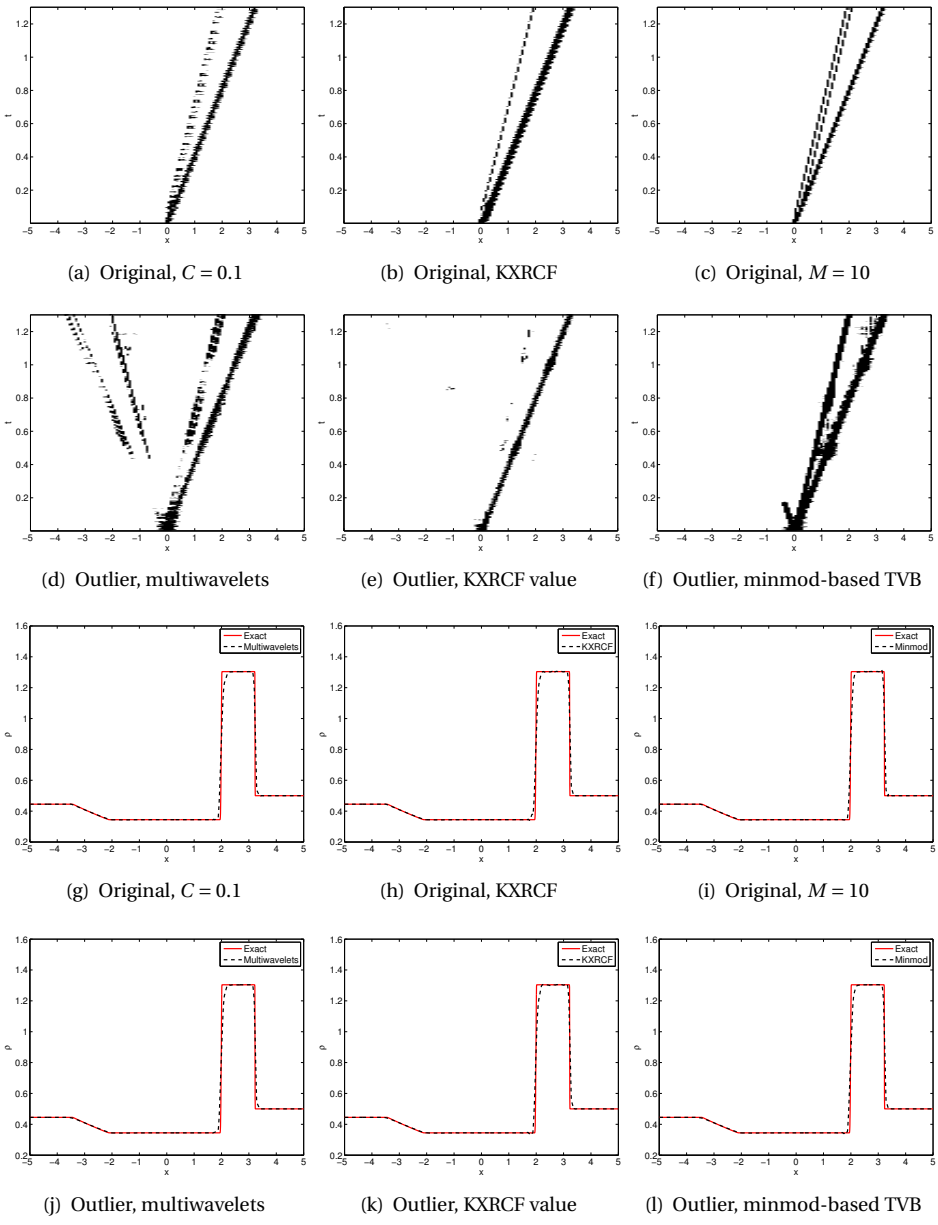

(a) Original, $C = 0.1$ (b) Original, KXRCF (c) Original, $M = 10$

(d) Outlier, multiwavelets (e) Outlier, KXRCF value (f) Outlier, minmod-based TVB

(g) Original, $C = 0.1$ (h) Original, KXRCF (i) Original, $M = 10$

(j) Outlier, multiwavelets (k) Outlier, KXRCF value (l) Outlier, minmod-based TVB

Figure 4.7: Lax's shock tube: time-history plot of detected troubled cells (rows 1 and 2), and approximation at final time $T = 1.3$ (rows 3 and 4), 128 elements, $k = 2$.

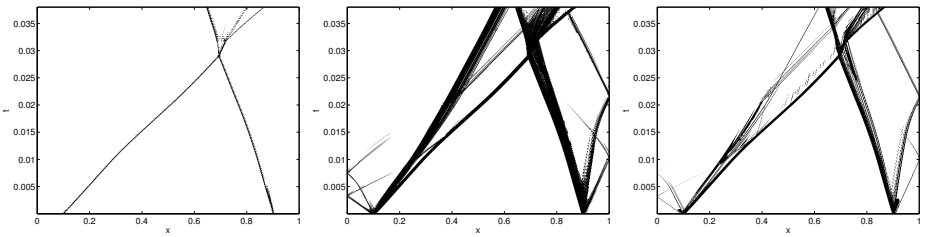

(a) Original, $C = 0.05$ (b) Original, KXRCF (c) Original, $M = 100$

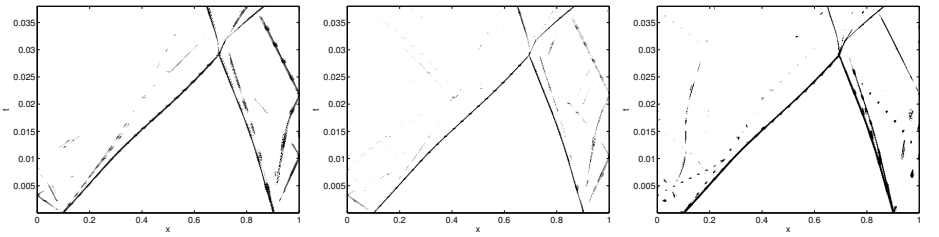

(d) Outlier, multiwavelets (e) Outlier, KXRCF value (f) Outlier, minmod-based TVB

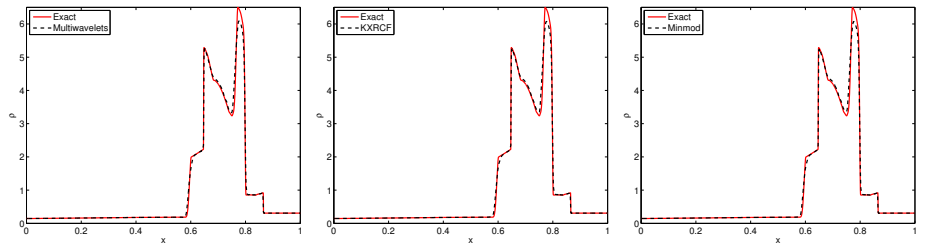

(g) Original, $C = 0.05$ (h) Original, KXRCF (i) Original, $M = 100$

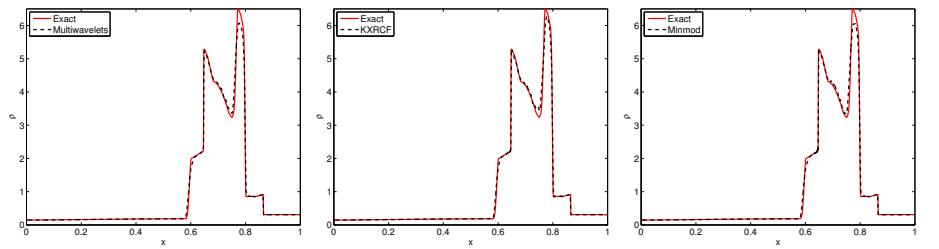

(j) Outlier, multiwavelets (k) Outlier, KXRCF value (l) Outlier, minmod-based TVB

Figure 4.8: Blast-wave problem: time-history plot of detected troubled cells (rows 1 and 2), and approximation at final time $T = 0.038$ (rows 3 and 4), 512 elements, $k = 2$.

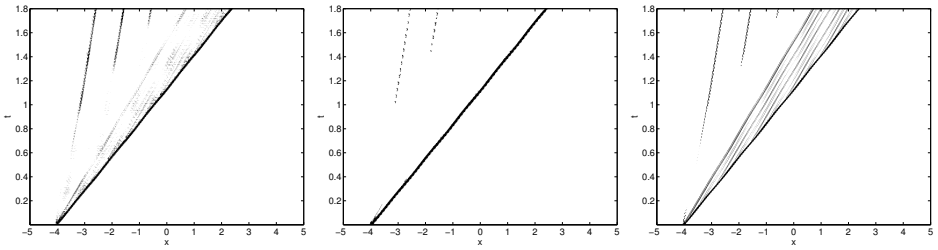

(a) Original, $C = 0.01$ (b) Original, KXRCF (c) Original, $M = 100$

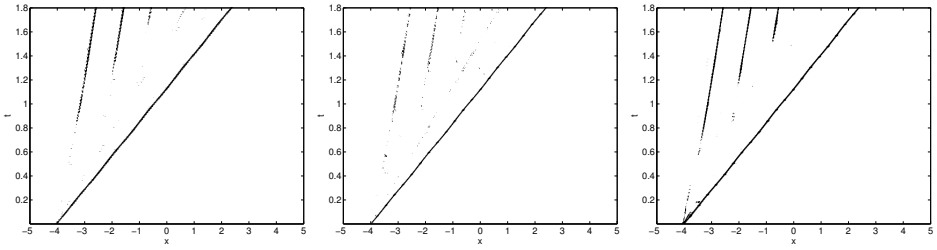

(d) Outlier, multiwavelets (e) Outlier, KXRCF value (f) Outlier, minmod-TVB

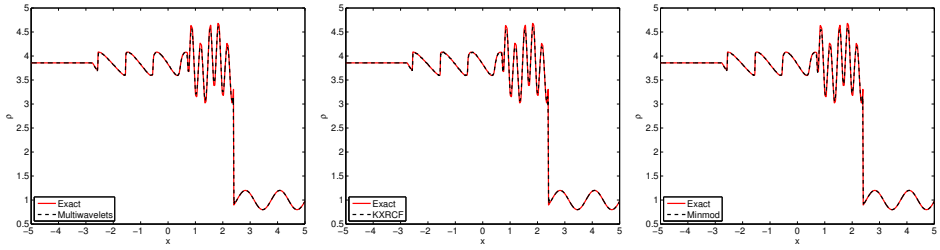

(g) Original, $C = 0.01$ (h) Original, KXRCF (i) Original, $M = 100$

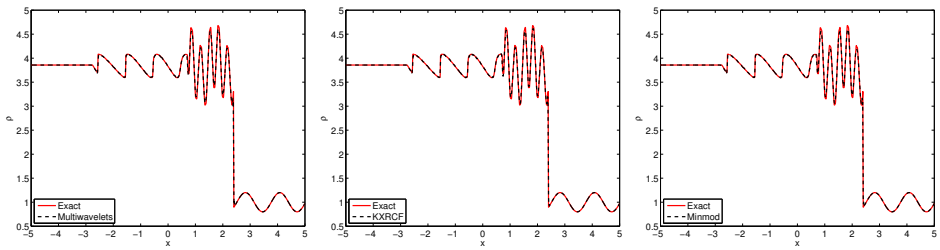

(j) Outlier, multiwavelets (k) Outlier, KXRCF value (l) Outlier, minmod-based TVB

Figure 4.9: Shu-Osher problem: time-history plot of detected troubled cells (rows 1 and 2), and approximation at final time $T = 1.8$ (rows 3 and 4), 512 elements, $k = 2$.

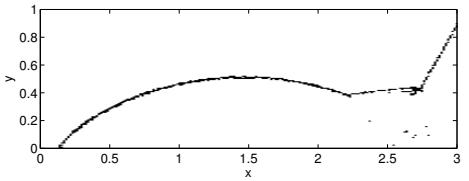

(a) Original, $C = 0.05$, α

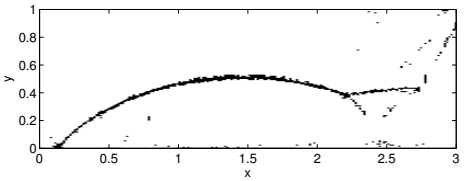

(b) Outlier, α

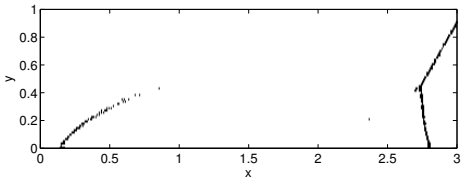

(c) Original, $C = 0.05$, β

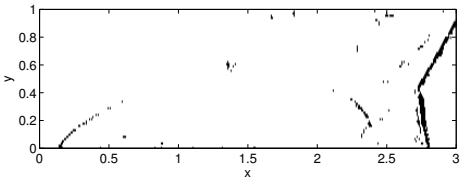

(d) Outlier, β

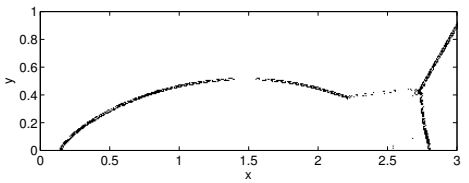

(e) Original, $C = 0.05$, γ

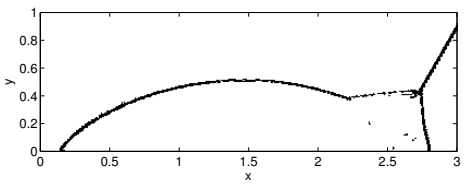

(f) Original, $C = 0.05$, total detected

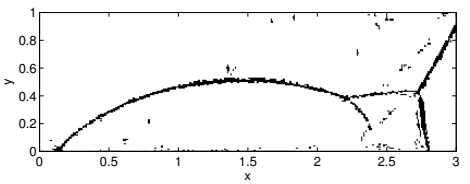

(g) Outlier, total detected

Figure 4.10: Detected troubled cells at $T = 0.2$, double Mach reflection problem, multiwavelet troubled-cell indicator, $n_x = 9$, $n_y = 7$, $k = 2$.

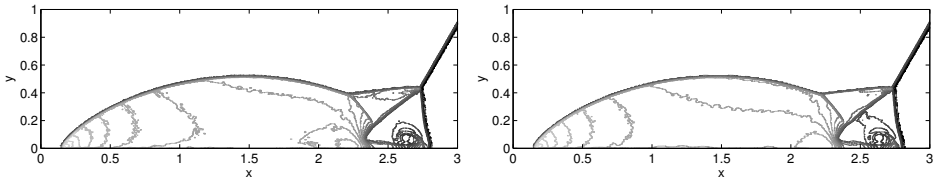

(a) Original, $C = 0.05$, contour

(b) Outlier, contour

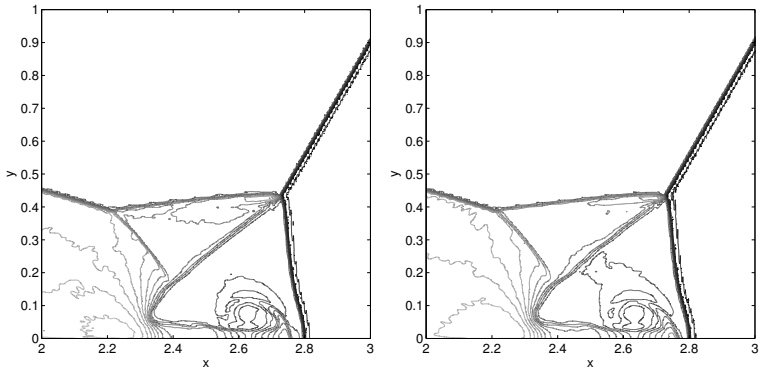

(c) Original, $C = 0.05$, zoom

(d) Outlier, zoom

Figure 4.11: Approximations at $T = 0.2$, double Mach reflection problem, multiwavelet troubled-cell indicator $n_x = 9$, $n_y = 7$, $k = 2$.

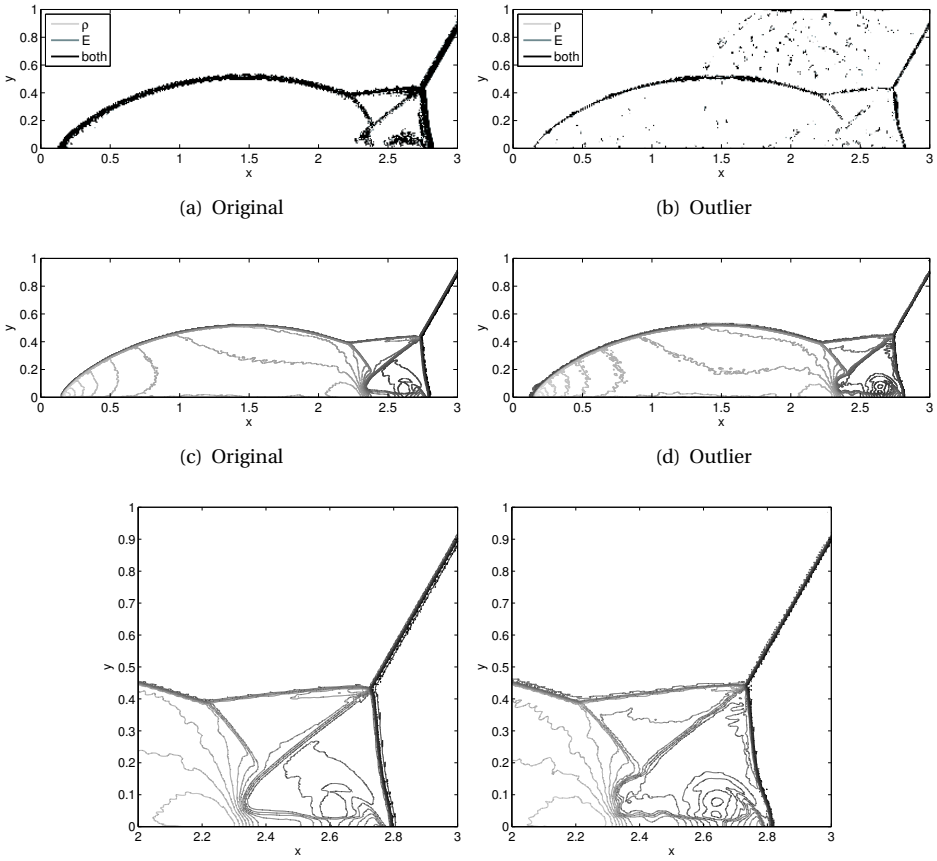

(a) Original (b) Outlier

(c) Original (d) Outlier

(e) Original (f) Outlier

Figure 4.12: Detected troubled cells and approximations at $T = 0.2$, double Mach reflection problem, KXRCF shock detector, $n_x = 9$, $n_y = 7$, $k = 2$.

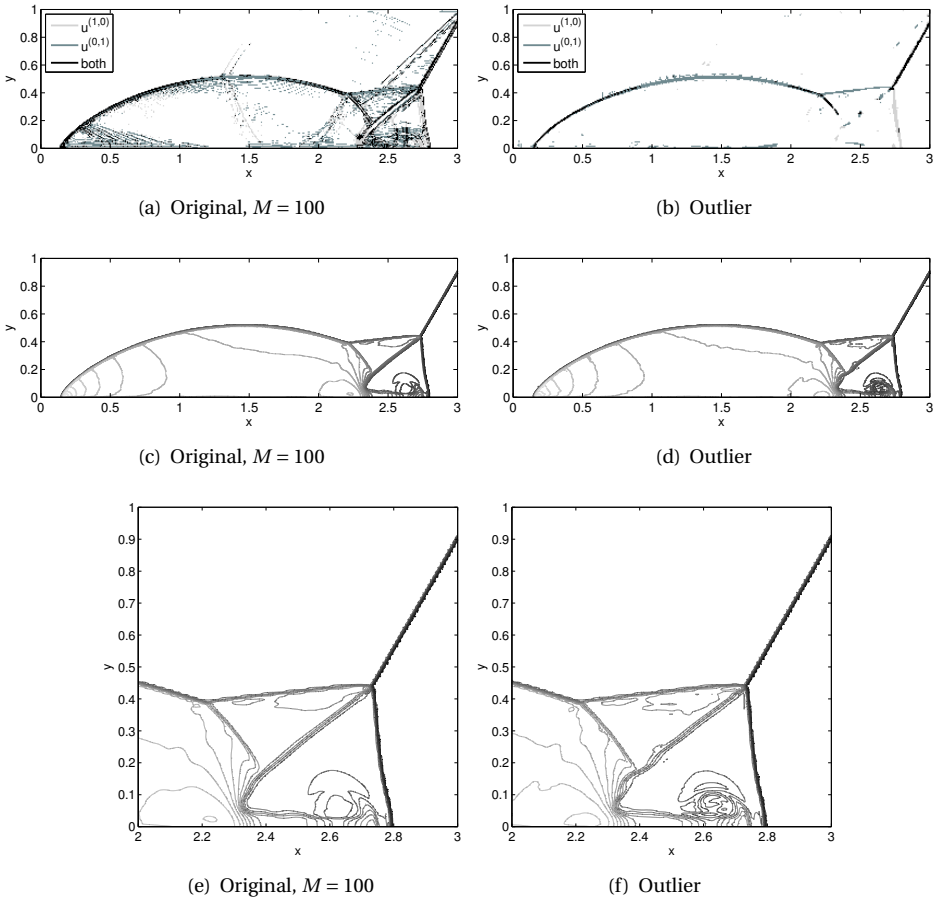

(a) Original, $M = 100$ (b) Outlier

(c) Original, $M = 100$ (d) Outlier

(e) Original, $M = 100$ (f) Outlier

Figure 4.13: Detected troubled cells and approximations at $T = 0.2$, double Mach reflection problem, minmod-based TVB indicator, $n_x = 9$, $n_y = 7$, $k = 1$.

4.7. COMPUTATIONAL COSTS

In this section, we discuss the computational costs of the outlier-detection algorithm [139]. First, we sort 2^{n-4} vectors of length 16 each. Here, the 'selection sort' sorting algorithm is used, which selects the minimum of the vector, swaps it with the vector's first value, and repeats these steps for the remaining values. The method is of order $\mathcal{O}(N^2)$ time complexity, but it is possible to use a more efficient sorting algorithm (for example, of order $\mathcal{O}(N)$) [126]. Once the vectors are sorted, we compute the quartiles and outer fences. Outliers are determined by comparing the smallest vector values with $Q_1 - 3(Q_3 - Q_1)$ and the largest components with $Q_3 + 3(Q_3 - Q_1)$. For the smallest values we start with testing whether $d_0^s < Q_1 - 3(Q_3 - Q_1)$. If d_0^s is not an outlier, then there are no other outliers, since $d_1^s \geq d_0^s \geq Q_1 - 3(Q_3 - Q_1)$. If d_0^s is an outlier, then we test d_1^s in the

same way. Note that (by construction) at maximum d_0^s, d_1^s, and d_2^s should be tested (as they are the only possible low outliers). Similarly, we test d_{15}^s and (possibly) d_{14}^s and d_{13}^s against $Q_3 + 3(Q_3 - Q_1)$ (depending on the outcome). Finally, the detected outliers in the left half of the local region are compared with the bounds of the left-neighboring region, and the outliers in the right half are compared with the right-neighboring region.

It should be noted that this novel method works well on a CPU. The local vectors can also be considered using parallel architectures. However, in that case, the costs for communication will be higher since local information should be distributed among the devices. On the other hand, it also typically results in fewer places where a limiter must be applied.

In Table 4.2, the computational times are shown for the test problems of Section 4.6, using either the original or the outlier-detection indication technique. Notice that the computational times using outlier detection are slightly longer than the original times, except for the KXRCF indicator. In that case, the number of detected elements for the original algorithm is much larger than when outlier detection is applied, such that the moment limiter is applied more often. For the rest of the examples, the increase in computational time is on average 2.9%, which is reasonable. It should be emphasized that the new method also reduces the number of tests by not having to find a problem-dependent parameter.

Table 4.2: Total computation time in seconds for the one-dimensional examples in Section 4.6.

	Multiwavelets		KXRCF		Minmod	
	Original	Outlier	Original	Outlier	Original	Outlier
Sod	0.187	0.208	0.208	0.212	0.231	0.256
Lax	0.263	0.280	0.299	0.290	0.329	0.366
blast wave	10.539	11.045	13.505	12.313	14.776	14.855
Shu-Osher	5.683	5.845	6.520	6.512	7.669	7.973

The total computation times for the double Mach reflection problem are presented in Table 4.3. Note that the case $k = 1$ (minmod-based TVB indicator) is much faster than $k = 2$. Also here, the computation time increases, on average by 2.6%. Since no tests for parameter finding are needed, the new method will still provide the results much faster.

Table 4.3: Total computation time in minutes for the double Mach reflection problem ($k = 2$ for multiwavelet and KXRCF indicator, $k = 1$ for minmod-based TVB indicator).

Multiwavelets		KXRCF		Minmod	
Original	Outlier	Original	Outlier	Original	Outlier
312	316	313	324	93	97

In addition to the total computation time, it is instructive to look at the computational overhead for applying the troubled-cell indicator and the limiter compared to the

temporal update. In Table 4.4, the results can be seen for the Shu-Osher problem, using either the parameter-dependent or the outlier-detection approaches.

Table 4.4: Computation time in seconds and percentages of total computation time for different parts of the Shu-Osher problem, 512 elements, $k = 2$.

	Total	Temporal update	Troubled-cell indication	Limiting
Full moment limiter				
	44.24	28.45 (64.3%)	-	15.71 (35.5%)
Multiwavelet troubled-cell indicator				
	Total	Temporal update	Troubled-cell indication	Limiting
$C = 0.01$	35.16	29.50 (83.9%)	0.70 (2.0%)	0.32 (0.9%)
Outlier	34.40	27.52 (80.0%)	1.51 (4.4%)	0.24 (0.7%)
KXRCF shock detector				
	Total	Temporal update	Troubled-cell indication	Limiting
Original	34.73	27.99 (80.6%)	1.42 (4.1%)	0.14 (0.4%)
Outlier	35.88	27.59 (76.9%)	2.37 (6.6%)	0.07 (0.2%)
Minmod-based TVB indicator				
	Total	Temporal update	Troubled-cell indication	Limiting
$M = 100$	39.85	25.98 (65.2%)	7.01 (17.6%)	0.28 (0.7%)
Outlier	38.82	26.86 (69.2%)	5.01 (12.9%)	0.16 (0.4%)

It should be noted that

- The computation is analyzed using a profiler tool, which leads to much longer computation times. In addition, the relations are different: the multiwavelet and minmod-TVB outlier-detection approaches are faster than the original methods, whereas the KXRCF outlier-detection approach takes more time than the original KXRCF method. In Table 4.2, this was exactly the other way round. However, note that the difference is very small (approximately 1 second). This behavior could also be profiler dependent.

- The percentages do not add to 100%: the rest of the computation time is used for pre- and post-processing.

- The full moment limiter needs *much* more time for limiting than the combinations with a troubled-cell indicator.

- For each method, the temporal update is computationally much more expensive than troubled-cell indication and limiting.

- For the multiwavelet troubled-cell indicator and the KXRCF shock detector, troubled-cell indication needs considerably more time in the outlier setting than in the original method (almost doubled). This is expected, since the original methods only compare with an upper bound, and the outlier-detection scheme is more involved.

- For all methods, the outlier-detection approach detects fewer cells than the original approach (see also Figure 4.9). Therefore, the limiting part of the outlier-detection methods is faster than that of the original schemes.
- The results for the minmod-based TVB limiter differ substantially. It should be noticed that characteristic field decompositions are required to apply the troubled-cell indicators, see Section 2.3.3. Therefore, the indication part requires more computation time.
- In the original minmod-based TVB indicator, Roe averages are used to decompose the differences with neighbors (Section 2.3.3). This is not needed for the outlier-detection approach, which is therefore faster.

4.8. CONCLUDING REMARKS

In this chapter, a new outlier-detection technique based on a boxplot mechanism has been introduced. This strategy is often used in statistics but has never been applied in this context before. The outlier-detection strategy can be applied to existing troubled-cell indication values to detect troubled cells. In this way, the problem-dependent parameters that standard indication techniques require are no longer needed. In two dimensions, the one-dimensional algorithm has been applied in the x- and y-direction separately.

The performance of the outlier-detection technique has been shown for various test problems in one and two dimensions, using the multiwavelet troubled-cell indicator, the KXRCF shock detector, and the minmod-based TVB indicator. The results were generally better than the original troubled-cell indicators using an optimized parameter: both the weak and the strong shock regions were detected, whereas smooth regions were not selected.

In the current outlier-detection technique, all spatial information is lost as only the indication values are used for detection. Therefore, it is important to consider the application to unstructured meshes separately. In the next chapter, the one-dimensional case is considered.

5

IRREGULAR MESHES

Multiresolution analysis for irregular meshes is more complicated than when uniform meshes are used. This is because there is no clear structure between the grids on the different levels (no equal division). In this chapter, we investigate the construction of a multiwavelet troubled-cell indicator for irregular meshes in one dimension. Two different irregular meshes are introduced in Section 5.1. The multiresolution analysis is discussed in Section 5.2. Multiwavelet-type functions are used to derive a relation between 'multiwavelet' coefficients on level $n-1$ and jumps in (derivatives of) the DG approximation (Section 5.3).

In addition to the difficulties for the multiwavelet theory, the current outlier-detection strategy does not incorporate spatial information, and therefore the applicability to irregular meshes should be verified. Section 5.4 contains a discussion of two other outlier-detection strategies.

Preliminary numerical results are shown and discussed in Section 5.5, and some concluding remarks are given in Section 5.6.

5.1. IRREGULAR MESHES

Daubechies et al. distinguish three different types of meshes: regular, semiregular, and irregular meshes (Figure 5.1) [43]. A regular mesh is uniform, consists of 2^n elements, and is formed by dividing every element into two subelements with the same width when going from one level to the next level (Figure 5.1(a)). A semiregular mesh also consists of 2^n elements, but begins with a nonuniform coarse mesh. Again, every element is divided midway to find the mesh at the next level (Figure 5.1(b)). Finally, irregular meshes are fully nonuniform: there is no regularity in going from one level to the next, but the total number of elements is still equal to 2^n (Figure 5.1(c)).

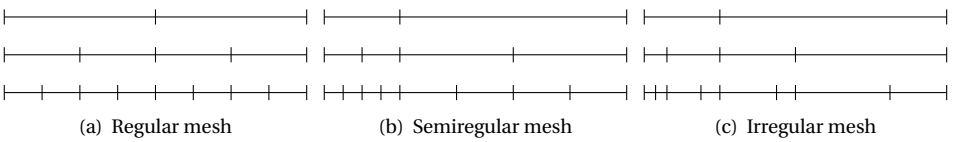

Figure 5.1: Three different types of meshes.

According to Daubechies [43], almost all research for nonuniform meshes concerns the semiregular case. Wavelets on stretched grids have been constructed in [41, 60]. Irregular meshes, however, are often used in practice, and are investigated in this dissertation. Irregular meshes are more complicated to describe and analyze as there is no clear structure between the grids on the different levels (no equal division).

In this section, two different irregular meshes are defined. Although these meshes are constructed on $[-1,1]$, it is possible to extend this theory to a general domain $[a,b]$. In the rest of this chapter, the notation of Figure 5.2 is used. Note that the DG approximation is computed on level n.

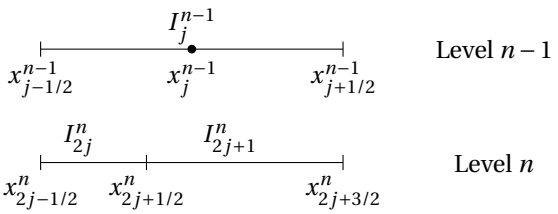

Figure 5.2: Element I_j^{n-1} in level $n-1$ and its irregular subdivision to elements I_{2j}^n and I_{2j+1}^n in level n.

5.1.1. SMOOTHLY-VARYING MESH

The first irregular mesh that we investigate is a so-called *smoothly-varying* mesh: its element widths vary smoothly as they depend on a smooth function [39, 89]. In this chapter, we specifically use the definition below.

Definition 5.1. *Define $\boldsymbol{\xi}$ as a vector containing the element boundaries of a 2^n-element uniform mesh on $[-1,1]$: $\xi_j = -1 + 2^{-n+1} j,\ j = 0,\ldots,2^n$. The vector with element bound-*

aries of a smoothly-varying mesh on $[-1,1]$ *is defined as* $f(\xi) = \xi + a\sin(2\pi\xi)$*, where* $a \in \mathbb{R}$ *is chosen such that the vector increases.*

The grid variable should increase: this means that $f'(\xi) = 1 + 2\pi a\cos(2\pi\xi) > 0$. Using that $-1 \le \cos(2\pi\xi) \le 1$ results in $-1/(2\pi) < a < 1/(2\pi)$. Note that the value of a is related to the variation in the element size: the larger the value of a, the more these sizes differ from each other. In this dissertation, the value $a = 0.1$ is used. The use of other values for a is left for future research.

5.1.2. RANDOM MESH

The second irregular mesh does not have a relation with a smooth function but is randomly generated. Although meshes usually adapt to a physical structure in the domain, this mesh is useful for testing the general applicability of the troubled-cell indicators.

Definition 5.2. *Let* $r_{j+1/2} \in (0,1)$ *be a random variable,* $b \in (0,1]$ *be a constant and* h *be the uniform mesh size (when* 2^n *elements are used on* $[-1,1]$*, then* $h = 2^{-n+1}$*). Then, a random mesh consisting of* 2^n *elements on* $[-1,1]$ *is constructed by defining [89]*

$$x^n_{-1/2} = -1, \quad x^n_{2^n-1/2} = 1, \quad x^n_{j+1/2} = -1 + (j+1)h + b(r_{j+1/2} - 1/2)h, \quad j = 0,\dots,2^n-2.$$

The size Δx^n_j of element I^n_j satisfies $\Delta x^n_j \in (h-hb, h+hb)$: the larger the value of b, the more irregular the mesh is. The difference with a uniform mesh is very small if $b < 0.8$. Only if $b \ge 0.8$ is it possible to see the nonuniformity easily. In the rest of this dissertation, the value $b = 0.8$ will be used [89].

5.2. MULTIRESOLUTION ANALYSIS

In this section, the scaling functions on level n are stated, and two different approaches for the construction of multiwavelets on irregular meshes are given. We also discuss the advantages and disadvantages of both methods.

5.2.1. LEVEL n

Define $\Delta x^n_j = x^n_{j+1/2} - x^n_{j-1/2}$ and $x^n_j = (x^n_{j-1/2} + x^n_{j+1/2})/2$ on level n (see Figure 5.2 for the notation). The scaling functions on level n are defined such that the element size is taken into account (cf. equation (2.16)):

$$\phi^n_{\ell j}(x) = \sqrt{\frac{2}{\Delta x^n_j}}\phi_\ell\left(\frac{2}{\Delta x^n_j}(x - x^n_j)\right), \quad \ell = 0,\dots,k,\ j = 0,\dots,2^n-1. \tag{5.1}$$

The relation between the DG coefficients and the scaling-function coefficients on level n is easy to derive. The global DG approximation of degree k can be expressed as

$$\begin{aligned} u_h(x) &= \sum_{j=0}^{2^n-1}\sum_{\ell=0}^{k} u^{(\ell)}_j \phi_\ell\left(\frac{2}{\Delta x^n_j}(x - x^n_j)\right) \\ &= \sqrt{\frac{\Delta x^n_j}{2}}\sum_{j=0}^{2^n-1}\sum_{\ell=0}^{k} u^{(\ell)}_j \phi^n_{\ell j}(x) = \sum_{j=0}^{2^n-1}\sum_{\ell=0}^{k} s^n_{\ell j}\phi^n_{\ell j}(x), \end{aligned}$$

such that the scaling-function coefficients equal $s_{\ell j}^n = \sqrt{\Delta x_j^n/2}\, u_j^{(\ell)}$. It should be noticed that this equation reduces to its original form if a uniform mesh of 2^n elements is used (see equation (2.22)).

5.2.2. SUPERCOMPACT MULTIWAVELETS

Supercompact multiwavelets are closely related to multiwavelets for uniform meshes. In the literature, the scaling functions on level $n-1$ are defined similarly to the functions on level n [6]:

$$\phi_{\ell j}^{n-1}(x) = \sqrt{\frac{2}{\Delta x_j^{n-1}}}\phi_\ell\left(\frac{2}{\Delta x_j^{n-1}}(x - x_j^{n-1})\right), \quad \ell = 0,\ldots,k,\ j = 0,\ldots,2^{n-1}-1. \tag{5.2}$$

These functions are then used to generate so-called *supercompact* multiwavelets. In the uniform setting, these multiwavelets differ slightly from Alpert's multiwavelets [4, 10]. For a nonuniform mesh, the decomposition and reconstruction steps depend on the element size, which makes them more time consuming than for a uniform mesh. Furthermore, multiwavelets that satisfy

$$\psi_{\ell j}^{n-1}(x) = \sqrt{\frac{2}{\Delta x_j^{n-1}}}\psi_\ell\left(\frac{2}{\Delta x_j^{n-1}}(x - x_j^{n-1})\right)$$

are discontinuous in x_j^{n-1} instead of the boundary of the DG mesh inside I_j^{n-1}, which is $x_{2j+1/2}^n$ (Figure 5.2). Therefore, it is unclear how to determine the exact representation of a DG approximation using supercompact multiwavelets. The use of supercompact multiwavelets for irregular meshes is left for future research.

5.2.3. ALPERT'S MULTIWAVELETS

A second option is to use Alpert's algorithm (Algorithm 2.1 in Section 2.4.3) for the specific irregular mesh. The corresponding algorithm is given in [56]: the only difference with Alpert's algorithm [4] is that no additional vanishing moments are added. Multiwavelets for one-dimensional irregular meshes have been designed in [97, 103].

It should be noticed that this construction is local, which means that the resulting bases are depending on the level and the position unless there is an affine mapping from the element to a reference element. Therefore, the QMF coefficients are in general location dependent, which slows down computations. On the other hand, the use of such multiwavelet space makes it possible to decompose the DG approximation to a multiwavelet expansion exactly.

In the rest of this chapter, we focus on the use of a multiwavelet-type basis which is location independent and able to represent the DG approximation exactly. However, a consequence of this choice is that the functions do not satisfy the exact definitions of a multiwavelet space.

5.3. MULTIWAVELET-TYPE BASIS CONSTRUCTION

In this section, multiwavelet-type functions for irregular meshes are defined. These functions do not fit in the classical wavelet framework: the differences with the origi-

nal multiwavelet theory are explained. Furthermore, the relation between 'multiwavelet' coefficients on level $n-1$ and jumps in (derivatives of) the DG approximation is derived.

5.3.1. MULTIWAVELET-TYPE BASIS

To find a decomposition which exactly reproduces the DG approximation, the functions on element I_j^{n-1} should explicitly be centered around $x_{2j+1/2}^n$. Therefore, we define the 'scaling-function' space S_{n-1}^{k+1} on level $n-1$, spanned by the functions

$$\phi_{\ell j}^{n-1}(x) = \begin{cases} \sqrt{\frac{1}{\Delta x_{2j}^n}}\phi_\ell\left(\frac{1}{\Delta x_{2j}^n}(x - x_{2j+1/2}^n)\right), & \text{if } x \in I_{2j}^n, \\ \sqrt{\frac{1}{\Delta x_{2j+1}^n}}\phi_\ell\left(\frac{1}{\Delta x_{2j+1}^n}(x - x_{2j+1/2}^n)\right), & \text{if } x \in I_{2j+1}^n, \end{cases} \tag{5.3a}$$

and similarly the 'multiwavelet' space $S_{n-1}'^{k+1}$ spanned by

$$\psi_{\ell j}^{n-1}(x) = \begin{cases} \sqrt{\frac{1}{\Delta x_{2j}^n}}\psi_\ell\left(\frac{1}{\Delta x_{2j}^n}(x - x_{2j+1/2}^n)\right), & \text{if } x \in I_{2j}^n, \\ \sqrt{\frac{1}{\Delta x_{2j+1}^n}}\psi_\ell\left(\frac{1}{\Delta x_{2j+1}^n}(x - x_{2j+1/2}^n)\right), & \text{if } x \in I_{2j+1}^n, \end{cases} \tag{5.3b}$$

$\ell = 0, \ldots, k,\ j = 0, \ldots, 2^{n-1} - 1$. Note that the 'scaling functions' are no longer polynomials on element I_j^{n-1}, which used to be the case for uniform meshes (equation (2.15)). In case of a uniform mesh we have $W_{n-1}^{k+1} \perp V_{n-1}^{k+1}$, $W_{n-1}^{k+1} \subset V_n^{k+1}$, but here the 'scaling functions' and 'multiwavelets' on level $n-1$ are both defined as functions in V_n^{k+1}: $S_{n-1}^{k+1} \subset V_n^{k+1}$ and $S_{n-1}'^{k+1} \subset V_n^{k+1}$. Due to this choice, we can only decompose to level $n-1$, and not to lower levels. To distinguish the functions from scaling-functions and multiwavelets according to the definitions in Section 2.4, quotes are being used.

The spaces defined above have many similarities with the classical framework. For example, the spaces satisfy $S_{n-1}^{k+1} \oplus S_{n-1}'^{k+1} = V_n^{k+1}$. The spaces themselves are orthonormal, which can be shown by computing

$$\begin{aligned} \langle \psi_{\ell j}^{n-1}, \psi_{mj}^{n-1} \rangle &= \int_{x_{j-1/2}^{n-1}}^{x_{j+1/2}^{n-1}} \psi_{\ell j}^{n-1}(x)\psi_{mj}^{n-1}(x)dx \\ &= \frac{1}{\Delta x_{2j}^n}\int_{x_{2j-1/2}^n}^{x_{2j+1/2}^n} \psi_\ell\left(\frac{1}{\Delta x_{2j}^n}(x - x_{2j+1/2}^n)\right)\psi_m\left(\frac{1}{\Delta x_{2j}^n}(x - x_{2j+1/2}^n)\right)dx \\ &+ \frac{1}{\Delta x_{2j+1}^n}\int_{x_{2j+1/2}^n}^{x_{2j+3/2}^n} \psi_\ell\left(\frac{1}{\Delta x_{2j+1}^n}(x - x_{2j+1/2}^n)\right)\psi_m\left(\frac{1}{\Delta x_{2j+1}^n}(x - x_{2j+1/2}^n)\right)dx. \end{aligned}$$

Using the transformations $\xi_1 = (x - x_{2j+1/2}^n)/\Delta x_{2j}^n$ and $\xi_2 = (x - x_{2j+1/2}^n)/\Delta x_{2j+1}^n$ in the first and second integral, respectively, we arrive at:

$$\langle \psi_{\ell j}^{n-1}, \psi_{mj}^{n-1} \rangle = \int_{-1}^{0} \psi_\ell(\xi_1)\psi_m(\xi_1)d\xi_1 + \int_0^1 \psi_\ell(\xi_2)\psi_m(\xi_2)d\xi_2 = \delta_{\ell m}.$$

Similarly, it is possible to show that $\langle \psi_{\ell j}^{n-1}, \phi_{mj}^{n-1} \rangle = 0$ (which means that $S_{n-1}^{k+1} \perp S_{n-1}'^{k+1}$) and $\langle \phi_{\ell j}^{n-1}, \phi_{mj}^{n-1} \rangle = \delta_{\ell m}$.

Furthermore, any 'scaling function' on level n can be expressed as a linear combination of 'scaling functions' and 'multiwavelets' on level $n-1$:

$$\phi_{r,2j}^{n-1} = \sum_{\ell=0}^{k} \left\{ \langle \phi_{\ell j}^{n-1}, \phi_{r,2j}^{n} \rangle \phi_{\ell j}^{n-1} + \langle \psi_{\ell j}^{n-1}, \phi_{r,2j}^{n} \rangle \psi_{\ell j}^{n-1} \right\},$$

$$\phi_{r,2j+1}^{n-1} = \sum_{\ell=0}^{k} \left\{ \langle \phi_{\ell j}^{n-1}, \phi_{r,2j+1}^{n} \rangle \phi_{\ell j}^{n-1} + \langle \psi_{\ell j}^{n-1}, \phi_{r,2j+1}^{n} \rangle \psi_{\ell j}^{n-1} \right\},$$

for $r = 0, \ldots, k,\ j = 0, \ldots, 2^{n-1} - 1$.

Here,

$$\begin{aligned} \langle \phi_{\ell j}^{n-1}, \phi_{r,2j}^{n} \rangle &= \int_{x_{2j-1/2}^{n}}^{x_{2j+1/2}^{n}} \phi_{\ell j}^{n-1}(x) \cdot \phi_{r,2j}^{n}(x)\, dx \\ &= \int_{x_{2j-1/2}^{n}}^{x_{2j+1/2}^{n}} \sqrt{\frac{1}{\Delta x_{2j}^{n}}} \phi_{\ell} \left(\frac{1}{\Delta x_{2j}^{n}} (x - x_{2j+1/2}^{n}) \right) \cdot \sqrt{\frac{2}{\Delta x_{2j}^{n}}} \phi_{r} \left(\frac{2}{\Delta x_{2j}^{n}} (x - x_{2j}^{n}) \right) dx. \end{aligned}$$

5

The use of $y = 2(x - x_{2j}^{n}) / \Delta x_{2j}^{n}$ yields

$$\langle \phi_{\ell j}^{n-1}, \phi_{r,2j}^{n} \rangle = \frac{1}{\sqrt{2}} \int_{-1}^{1} \phi_{\ell} \left(\frac{y-1}{2} \right) \phi_{r}(y)\, dy, \tag{5.4a}$$

which exactly equals the QMF coefficient $h_{\ell r}^{(0)}$ in the uniform case [136]. Similar results can be found for the rest of the QMF coefficients:

$$\langle \phi_{\ell j}^{n-1}, \phi_{r,2j+1}^{n} \rangle = \frac{1}{\sqrt{2}} \int_{-1}^{1} \phi_{\ell} \left(\frac{y+1}{2} \right) \phi_{r}(y)\, dy, \tag{5.4b}$$

$$\langle \psi_{\ell j}^{n-1}, \phi_{r,2j}^{n} \rangle = \frac{1}{\sqrt{2}} \int_{-1}^{1} \psi_{\ell} \left(\frac{y-1}{2} \right) \phi_{r}(y)\, dy, \tag{5.4c}$$

$$\langle \psi_{\ell j}^{n-1}, \phi_{r,2j+1}^{n} \rangle = \frac{1}{\sqrt{2}} \int_{-1}^{1} \psi_{\ell} \left(\frac{y+1}{2} \right) \phi_{r}(y)\, dy. \tag{5.4d}$$

Note that these QMF coefficients do not depend of the position in the irregular mesh. This makes the computation of these coefficients more efficient than when location-dependent QMF coefficients are used.

With the use of this framework, it is possible to give an exact representation of the DG approximation. Similar to the uniform case, the 'scaling-function' and 'multiwavelet' coefficients on level $n-1$ are defined by an orthogonal projection: $s_{\ell j}^{n-1} = \langle u_h, \phi_{\ell j}^{n-1} \rangle$ and $d_{\ell j}^{n-1} = \langle u_h, \psi_{\ell j}^{n-1} \rangle$. These coefficients are efficiently computed using decomposition and the QMF coefficients stated above [136].

5.3.2. JUMPS IN DG APPROXIMATIONS

One drawback of the 'multiwavelet' space defined above is that the cancelation property cannot be proven. This is because the standard vanishing-moment property does not hold but is replaced by the weighted vanishing moment property, which is described in this section. However, we are able to derive a relation between the 'multiwavelet' coefficients and jumps in (derivatives of) the DG approximation (cf. Section 3.1).

Lemma 5.1. *Define* $I_j^{n-1} = [x_{j-1/2}^{n-1}, x_{j+1/2}^{n-1})$, *and* $\psi_{\ell j}^{n-1}$ *as in equation (5.3b). The weighted vanishing-moment property on multiresolution level* $n-1$ *yields:*

$$\frac{1}{(\Delta x_{2j}^n)^{m+1/2}} \int_{I_{2j}^n} (x - x_{2j+1/2}^n)^m \psi_{\ell j}^{n-1}(x)\,dx + \frac{1}{(\Delta x_{2j+1}^n)^{m+1/2}} \int_{I_{2j+1}^n} (x - x_{2j+1/2}^n)^m \psi_{\ell j}^{n-1}(x)\,dx = 0, \tag{5.5}$$

$m = 0, \ldots, \ell + k$, $j = 0, \ldots, 2^{n-1} - 1$.

Proof. The proof uses the definition of $\psi_{\ell j}^{n-1}$ and the transformations

$$\xi_1 = \frac{x - x_{2j+1/2}^n}{\Delta x_{2j}^n}, \quad \xi_2 = \frac{x - x_{2j+1/2}^n}{\Delta x_{2j+1}^n}, \tag{5.6}$$

with $dx = \Delta x_{2j}^n d\xi_1 = \Delta x_{2j+1}^n d\xi_2$ and $x - x_{2j+1/2}^n = \Delta x_{2j}^n \xi_1 = \Delta x_{2j+1}^n \xi_2$. This means that the first component on the left-hand side of equation (5.5) equals

$$\frac{1}{(\Delta x_{2j}^n)^{m+1/2}} \int_{I_{2j}^n} (x - x_{2j+1/2}^n)^m \psi_{\ell j}^{n-1}(x)\,dx = \frac{\Delta x_{2j}^n}{(\Delta x_{2j}^n)^{m+1/2}} \int_{-1}^{0} (\Delta x_{2j}^n \xi_1)^m \sqrt{\frac{1}{\Delta x_{2j}^n}} \psi_\ell \left(\frac{\Delta x_{2j}^n \xi_1}{\Delta x_{2j}^n} \right) d\xi_1 = \int_{-1}^{0} \xi_1^m \psi_\ell(\xi_1)\,d\xi_1.$$

Similarly, we find that

$$\frac{1}{(\Delta x_{2j+1}^n)^{m+1/2}} \int_{I_{2j+1}^n} (x - x_{2j+1/2}^n)^m \psi_{\ell j}^{n-1}(x)\,dx = \int_0^1 \xi_2^m \psi_\ell(\xi_2)\,d\xi_2. \tag{5.7}$$

Using the standard vanishing-moment property of the multiwavelets (equation (3.1a)), the lemma is proved. □

Corollary 5.1. *For* $m = 0, \ldots, k + \ell$, $j = 0, \ldots, 2^{n-1} - 1$, *it holds that*

$$\int_{I_{2j}^n} (x - x_{2j+1/2}^n)^m \psi_{\ell j}^{n-1}(x)\,dx = -\left(\frac{\Delta x_{2j}^n}{\Delta x_{2j+1}^n} \right)^{m+1/2} \int_{I_{2j+1}^n} (x - x_{2j+1/2}^n)^m \psi_{\ell j}^{n-1}(x)\,dx. \tag{5.8}$$

We are now ready to formulate the relation between the 'multiwavelet' coefficients and the jumps in (derivatives of) the DG approximation.

Theorem 5.1. *Let* u_h *be a DG approximation of degree* k *on* $[-1, 1]$, *using an irregular mesh consisting of* 2^n *elements. For each* $\ell, m = 0, \ldots, k$, $j = 0, \ldots, 2^{n-1} - 1$ *define*

$$\tilde{c}_{m\ell}^n = \frac{1}{m!} \cdot \int_0^1 x^m \psi_\ell(x)\,dx, \tag{5.9a}$$

and let $u_h^{(m)}$ *be the* m*th derivative of* u_h. *Then, the 'multiwavelet' coefficients on level* $n-1$ *equal*

$$d_{\ell j}^{n-1} = \sum_{m=0}^{k} \tilde{c}_{m\ell}^n \left((\Delta x_{2j+1}^n)^{m+1/2} u_h^{(m)}(x_{2j+1/2}^{n,+}) - (\Delta x_{2j}^n)^{m+1/2} u_h^{(m)}(x_{2j+1/2}^{n,-}) \right). \tag{5.9b}$$

5

Proof. Using the Taylor expansions of u_h about $x^n_{2j+1/2}$ on elements I^n_{2j} and I^n_{2j+1} (equation (3.8)), we find

$$\begin{aligned} d^{n-1}_{\ell j} &= \int_{I^{n-1}_j} u_h(x)\psi^{n-1}_{\ell j}(x)dx \\ &= \sum_{m=0}^{k} \frac{1}{m!}\left(u_h^{(m)}(x^{n,-}_{2j+1/2}) \int_{I^n_{2j}} (x - x^n_{2j+1/2})^m \psi^{n-1}_{\ell j}(x)dx \right. \\ &\quad \left. + u_h^{(m)}(x^{n,+}_{2j+1/2}) \int_{I^n_{2j+1}} (x - x^n_{2j+1/2})^m \psi^{n-1}_{\ell j}(x)dx \right). \end{aligned}$$

Application of Corollary 5.1 yields

$$\begin{aligned} d^{n-1}_{\ell j} = \sum_{m=0}^{k} \frac{1}{m!}\left(u_h^{(m)}(x^{n,-}_{2j+1/2}) \cdot - \left(\frac{\Delta x^n_{2j}}{\Delta x^n_{2j+1}}\right)^{m+1/2} + u_h^{(m)}(x^{n,+}_{2j+1/2}) \right) \\ \cdot \int_{I^n_{2j+1}} (x - x^n_{2j+1/2})^m \psi^{n-1}_{\ell j}(x)dx. \end{aligned}$$

From equation (5.7) it follows that

$$\int_{I^n_{2j+1}} (x - x^n_{2j+1/2})^m \psi^{n-1}_{\ell j}(x)dx = (\Delta x^n_{2j+1})^{m+1/2} \int_0^1 \xi_2^m \psi_\ell(\xi_2)d\xi_2,$$

which means that

$$\begin{aligned} d^{n-1}_{\ell j} &= \sum_{m=0}^{k} \frac{1}{m!}\left(u_h^{(m)}(x^{n,-}_{2j+1/2}) \cdot - \left(\frac{\Delta x^n_{2j}}{\Delta x^n_{2j+1}}\right)^{m+1/2} + u_h^{(m)}(x^{n,+}_{2j+1/2}) \right) \\ &\quad \cdot (\Delta x^n_{2j+1})^{m+1/2} \int_0^1 \xi_2^m \psi_\ell(\xi_2)d\xi_2 \\ &= \sum_{m=0}^{k} \tilde{c}^n_{m\ell} \left((\Delta x^n_{2j+1})^{m+1/2} u_h^{(m)}(x^{n,+}_{2j+1/2}) - (\Delta x^n_{2j})^{m+1/2} u_h^{(m)}(x^{n,-}_{2j+1/2}) \right). \end{aligned}$$

□

If a uniform mesh is used, then the above theorem easily reduces to its original form (Theorem 3.1).

From this theorem, it follows that 'multiwavelet' coefficients become small if the underlying function is smooth, and the mesh width between two neighboring elements is not varying too much. Smoothly-varying meshes satisfy this condition by construction: their 'multiwavelet' coefficients can be used for the detection of troubled cells. For random meshes, the neighboring mesh widths can differ substantially. However, we will see in Section 5.5 that the coefficients are still useful for troubled-cell indication.

5.4. OUTLIER DETECTION FOR IRREGULAR MESHES

The standard troubled-cell indicators are designed such that they are also applicable to nonuniform meshes. For the outlier-detection approach of Chapter 4, however, the extension to nonuniform meshes is not straightforward. This is caused by the fact that all spatial information is lost when outlier detection is applied. In Section 5.5 we will see that the results for the original outlier-detection approach (Algorithm 4.2) are still useful. In addition, two different strategies are tested, which are explained in this section.

One way to include spatial information of the mesh in the algorithm is to weight the troubled-cell indication variable using the element size. Let $\mathbf{D} = (D_0, \ldots, D_{2^n-1})$ be the original troubled-cell indication vector that is used in Algorithm 4.2. Since the vector value D_j usually contains information about the boundary $x^n_{j+1/2}$, the vector with entries $D_j/(\Delta x^n_j + \Delta x^n_{j+1})$ provides more information about the element sizes, and can be used in Algorithm 4.2.

A second option is the use of a window-based technique [25]. A window is a fixed-length subsequence of the test sequence, which can be slid through the domain using a sliding step.

The original outlier-detection algorithm (Algorithm 4.2) is visualized in Figure 5.3(a). The domain is split into 16-element regions which are lying next to each other: the window has length 16, and the sliding step equals 16 as well. The spatial information is taken into account by ignoring outliers close to split boundaries if they are not detected with respect to the neighboring vector.

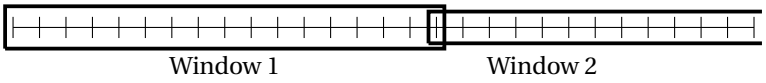

(a) Original approach: window length 16, sliding step 16.

(b) Sliding-window approach: window length 16, sliding step 4.

Figure 5.3: Window-based outlier detection using different sliding steps.

If we use outlier detection on local vectors of length 16 with a sliding step equal to 4, then this results in the windows of Figure 5.3(b). In each window, Algorithm 4.1 is used to detect troubled cells. Note that the inner elements of the domain are tested four times, with a smaller number of tests for elements close to the boundary of the domain.

In the original outlier-detection algorithm with sliding step 16 (Algorithm 4.2), outliers that are detected close to window boundaries should be ignored when they are not detected using the bounds of the neighboring window. If the sliding step is taken smaller than 16, then the detection of an outlier close to the window boundary is no longer problematic: in the next window, this element is positioned differently and will not be detected if the neighboring indication values are of the same order.

In the next section, the numerical results using different parameter-based or outlier-detection troubled-cell indicators can be compared.

5.5. NUMERICAL RESULTS

In this section, some preliminary numerical results are shown for the one-dimensional test cases based on the Euler equations. Here, the multiwavelet troubled-cell indicator [137–139], the KXRCF shock detector [83] and the minmod-based TVB indicator [29, 30] are applied either in their original form (with parameter) or using outlier detection. The moment limiter is applied in the detected troubled cells [81]. The results are computed for both a smoothly-varying mesh (definition 5.1, $a = 0.1$) and a random mesh (definition 5.2, $b = 0.8$). Again, time-history plots are shown, together with approximations at the final time. The original outlier-detection algorithm is tested on all three indication values (Figures 5.4–5.11). The techniques of Section 5.4 are only tested on the 'multiwavelet' coefficients (Figures 5.12 and 5.13). We will see that the approaches of Section 5.4 do not work well enough to be used in real-life applications.

5.5.1. ORIGINAL INDICATORS AND STANDARD OUTLIER DETECTION

In this section, the results are given for the original troubled-cell indicators, as well as the outlier-detection approach of Algorithm 4.2. For each test case, we first discuss the original and outlier-detection results for the smoothly-varying mesh, and then investigate the results for the random mesh.

The results for Sod's shock tube on a smoothly-varying mesh are given in Figure 5.4. The original KXRCF indicator only detects the shock and does not find the contact discontinuity. The original multiwavelet indicator does detect the shock and parts of the contact discontinuity, but not at every time step. This could be because the application of the limiter in this region slightly smears the approximation at the discontinuity, such that it is not detected at a later time. The same holds for the minmod-based TVB indicator, which also selects very few elements in the shock region of the tube. The approximations at the final time are slightly oscillatory. If outlier detection is applied to the different indication values, then more elements are detected in the shock region, part of the contact discontinuity is detected, and even the end points of the rarefaction wave are found using the 'multiwavelet' coefficients. Although the correct elements are detected, the final-time approximations still contain some oscillations since the limiter is not applied to as many elements.

The results for the random mesh (Figure 5.5) are satisfying and generally better than the smoothly-varying mesh. The original troubled-cell indicators for the random mesh perform similarly to the smoothly-varying case. Outlier detection on the indication values is very accurate: the correct regions are detected, and the approximations are free of spurious oscillations.

For Lax's shock tube on a smoothly-varying mesh (Figure 5.6), the original indicators nicely detect the shock and the contact discontinuity. However, oscillations in the final-time approximation are still found, which means that the limiter is not applied often enough. This most notably occurs because too few elements are detected near the contact discontinuity. The results improve if a smaller parameter is chosen. If outlier detection is applied, then more elements are detected. If the 'multiwavelet' coefficients are used for indication (Figure 5.6(d)), many left-travelling waves are detected in the rarefaction zone, where the approximation is smooth. The same holds for the KXRCF indication value (Figure 5.6(e)). The behavior for the minmod-based TVB indicator stands out (Fig-

ure 5.6(f)) since two left-travelling waves are detected which do not correspond to the rarefaction wave. Oscillations are still apparent in the final approximations.

For a random mesh, the original indicators work very well (Figure 5.7). If outlier detection is applied, then the contact discontinuity is resolved better using the 'multiwavelet' or minmod-based TVB indication values. For the KXRCF indicator, the amount of detected troubled cells is still too small to prevent oscillations. Also here, more elements are detected in the smooth region of the rarefaction wave (although fewer elements than in the smoothly-varying case). This is a complicated artifact of our outlier-detection method. It can be resolved by including the spatial information in the scheme.

For the blast-wave problem on a smoothly-varying mesh (Figure 5.8), the behavior is very similar to the uniform-mesh example (Chapter 4). The original KXRCF shock detector and minmod-based TVB indicator detect too many elements and the multiwavelet troubled-cell indicator works very well. The outlier-detection approach is much more accurate, and detects the correct regions for the 'multiwavelet' and the minmod-based TVB indication values (Figures 5.8(d) and 5.8(f)). For the KXRCF indicator, slightly more elements are detected in the upper-left corner of Figure 5.8(e). However, the number of detected troubled cells is much smaller than when the original indicator is used. Small oscillations are still found in the approximations. Note that the maximum peak in the KXRCF indicator is much improved by changing from the original to the outlier-detection approach.

For the random mesh (Figure 5.9), the number of detected cells using the original KXRCF shock detector and the minmod-based TVB indicator is too large. Many elements are detected and limited, which makes the simulations run for a long time. The discontinuities are much better captured if outlier detection is applied, but detection in smooth regions occurs very often (although the indication values are very small, and limiting is not needed). The inclusion of spatial information in the outlier-detection algorithm could solve this problem.

The results for the Shu-Osher problem on a smoothly-varying mesh (Figure 5.10) are also close to the uniform case (Chapter 4). The original multiwavelet and minmod-based TVB troubled-cell indicators select elements in the highly-oscillatory region. The outlier-detection approach selects exactly the correct number of elements, and the results are very good.

Similar conclusions can be drawn for the random mesh (Figure 5.11): the original multiwavelet and minmod-based TVB indicators detect too many elements in the highly-oscillatory region. The outlier-detection approach works well, although some elements are detected in smooth regions if the 'multiwavelet' or the KXRCF indication value is used. The result for the minmod-based TVB indication value is very accurate (Figure 5.11(f)). When outlier detection is applied to the 'multiwavelet' coefficients, one location is detected without a clear reason.

5.5.2. WEIGHTING THE INDICATION VARIABLE

The application of outlier detection to the weighted troubled-cell indication values does not work well. The computation for Sod's and Lax's shock tubes can be completed, but is very inaccurate as it detects the wrong elements: every element with a very small width is detected. The computation for the blast-wave and the Shu-Osher problem blows up.

5.5.3. OUTLIER DETECTION USING SLIDING-WINDOW TECHNIQUE

In this section, we test the sliding-window technique (Section 5.4). Note that all internal elements are tested four times when a sliding step of size 4 is used for windows of length 16. We label an element as troubled if it is detected at least twice by the outlier-detection algorithm. The results using the sliding-window technique on the 'multiwavelet' coefficients can be seen in Figures 5.12 (smoothly-varying mesh) and 5.13 (random mesh). The correct features can be recognized, but many elements that are close to the non-smooth regions are also detected, except for the blast-wave problem on a smoothly-varying mesh (Figure 5.12(e)). This is still the case if we label an element as troubled if it is marked at least three or four times by the sliding-window technique. These results are not satisfying enough to proceed in this direction.

5.6. CONCLUDING REMARKS

In this chapter, irregular meshes in one dimension have been studied. Alpert's multiwavelet algorithm can be applied for irregular meshes but leads to location-dependent QMF coefficients. Therefore, special multiwavelet-type functions have been defined, which use the same QMF coefficients as for a uniform mesh. It has been shown that, although the cancelation property no longer holds, the corresponding 'multiwavelet' coefficients still have a relation with the jumps in (derivatives of) the DG approximation across the element boundaries. In addition to a parameter-based multiwavelet troubled-cell indicator, two other outlier-detection techniques have been defined: one in which the indication values are weighted with the mesh width and another where a sliding-window technique is used.

We have tested several troubled-cell indicators on two different irregular meshes: a smoothly-varying mesh and a random mesh. In general, the original troubled-cell indicators work well, as long as a suitable problem-dependent parameter is chosen. When outlier detection is applied to the indication values, this parameter is no longer needed. The results using outlier detection are promising but in some examples (for example, the blast-wave problem with a random mesh), too many elements are detected in smooth regions. More research should be done to include spatial information in the algorithm. The inclusion of the mesh width and the use of sliding-window techniques does not work well since too many elements are detected.

In two dimensions, irregularity in both directions leads to a rectangular mesh that is not related to tensor products. In that case, it is very difficult to use multiresolution analysis and apply multiwavelet decomposition because the QMF coefficients need to take into account the varying mesh sizes. This part is left for future research, and the next chapter first focuses on a structured triangular mesh.

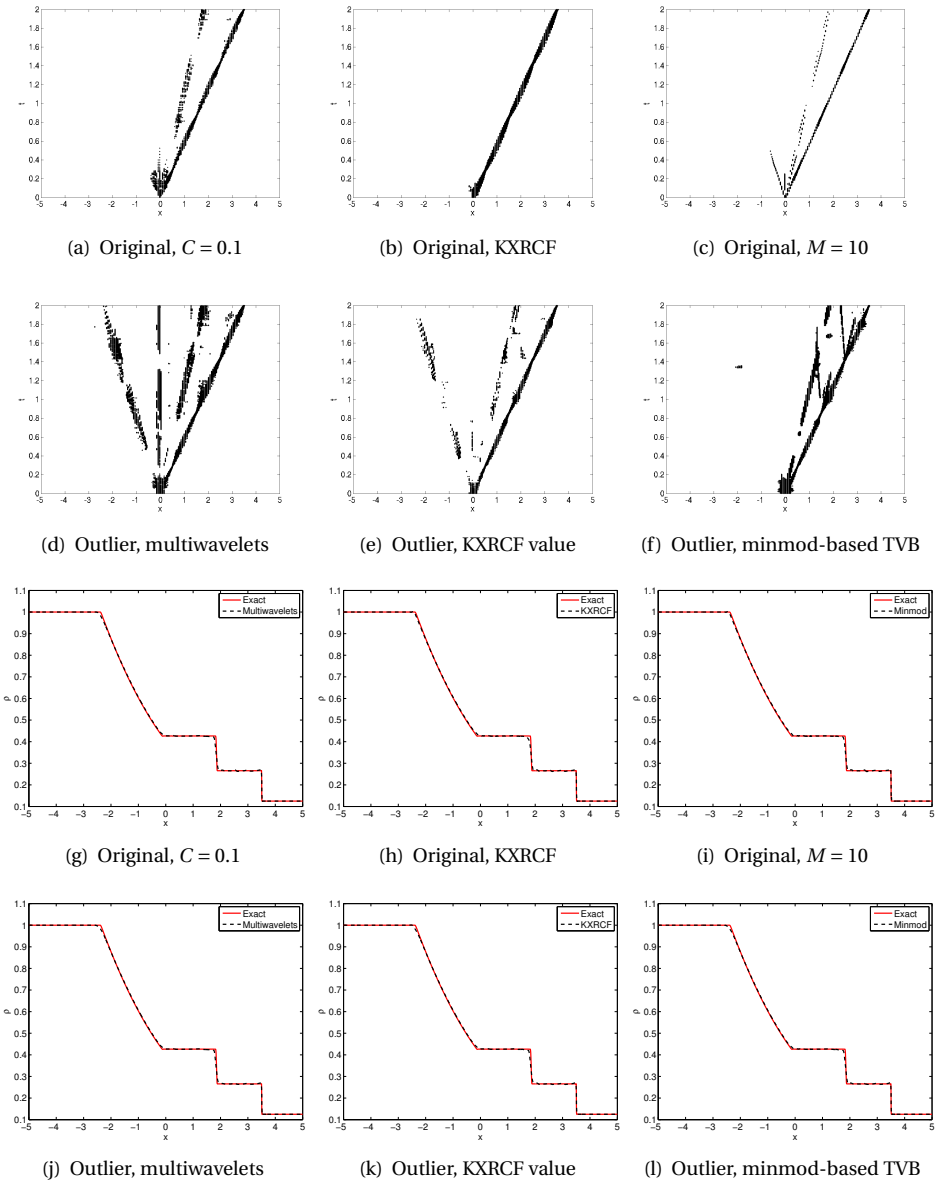

(a) Original, $C = 0.1$ (b) Original, KXRCF (c) Original, $M = 10$

(d) Outlier, multiwavelets (e) Outlier, KXRCF value (f) Outlier, minmod-based TVB

(g) Original, $C = 0.1$ (h) Original, KXRCF (i) Original, $M = 10$

(j) Outlier, multiwavelets (k) Outlier, KXRCF value (l) Outlier, minmod-based TVB

Figure 5.4: Sod's shock tube: time-history plot of detected troubled cells (rows 1 and 2), and approximation at final time $T = 2$ (rows 3 and 4), 256 elements, smoothly-varying mesh, $k = 2$. Algorithm 4.2 is applied to compute the outlier-detection results.

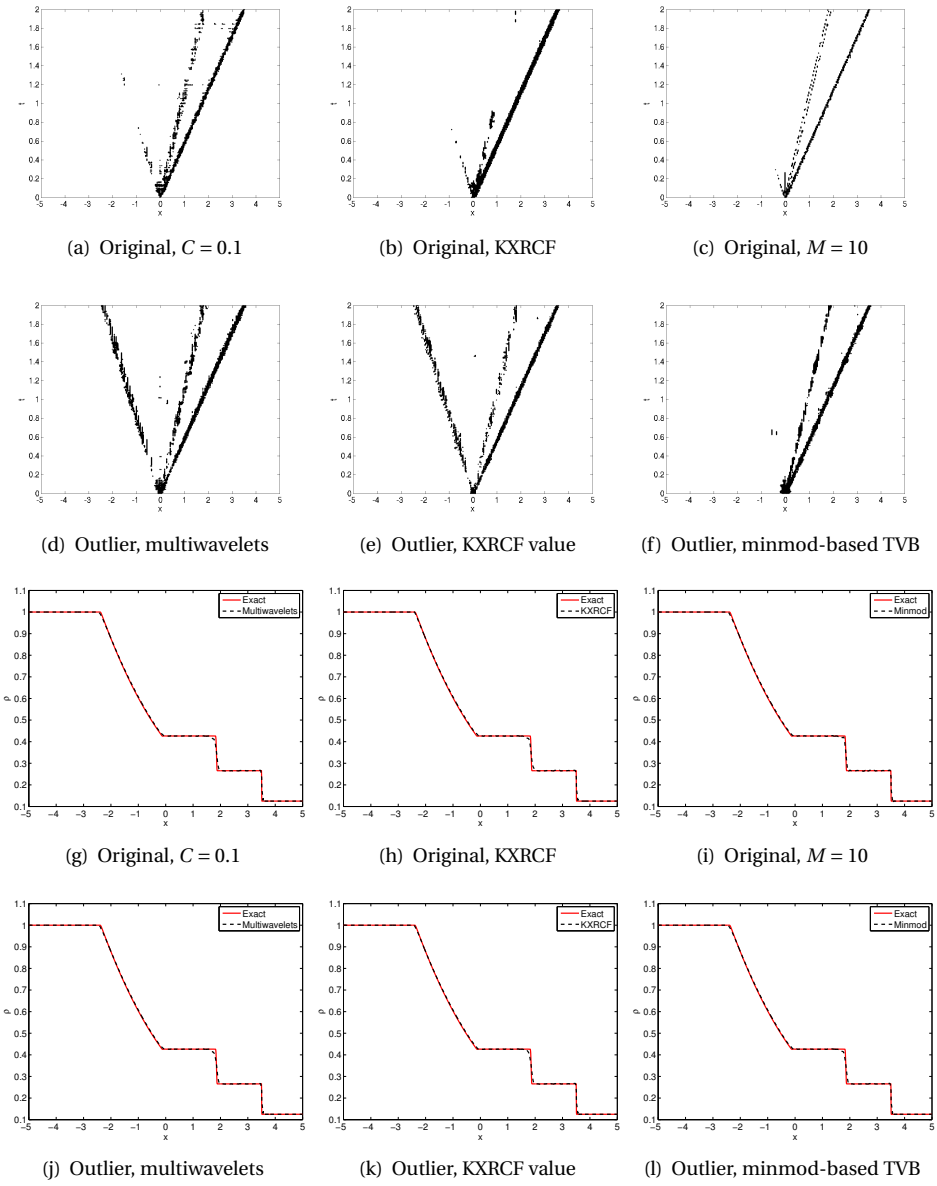

(a) Original, $C = 0.1$ (b) Original, KXRCF (c) Original, $M = 10$

(d) Outlier, multiwavelets (e) Outlier, KXRCF value (f) Outlier, minmod-based TVB

(g) Original, $C = 0.1$ (h) Original, KXRCF (i) Original, $M = 10$

(j) Outlier, multiwavelets (k) Outlier, KXRCF value (l) Outlier, minmod-based TVB

Figure 5.5: Sod's shock tube: time-history plot of detected troubled cells (rows 1 and 2), and approximation at final time $T = 2$ (rows 3 and 4), 256 elements, random mesh, $k = 2$. Algorithm 4.2 is applied to compute the outlier-detection results.

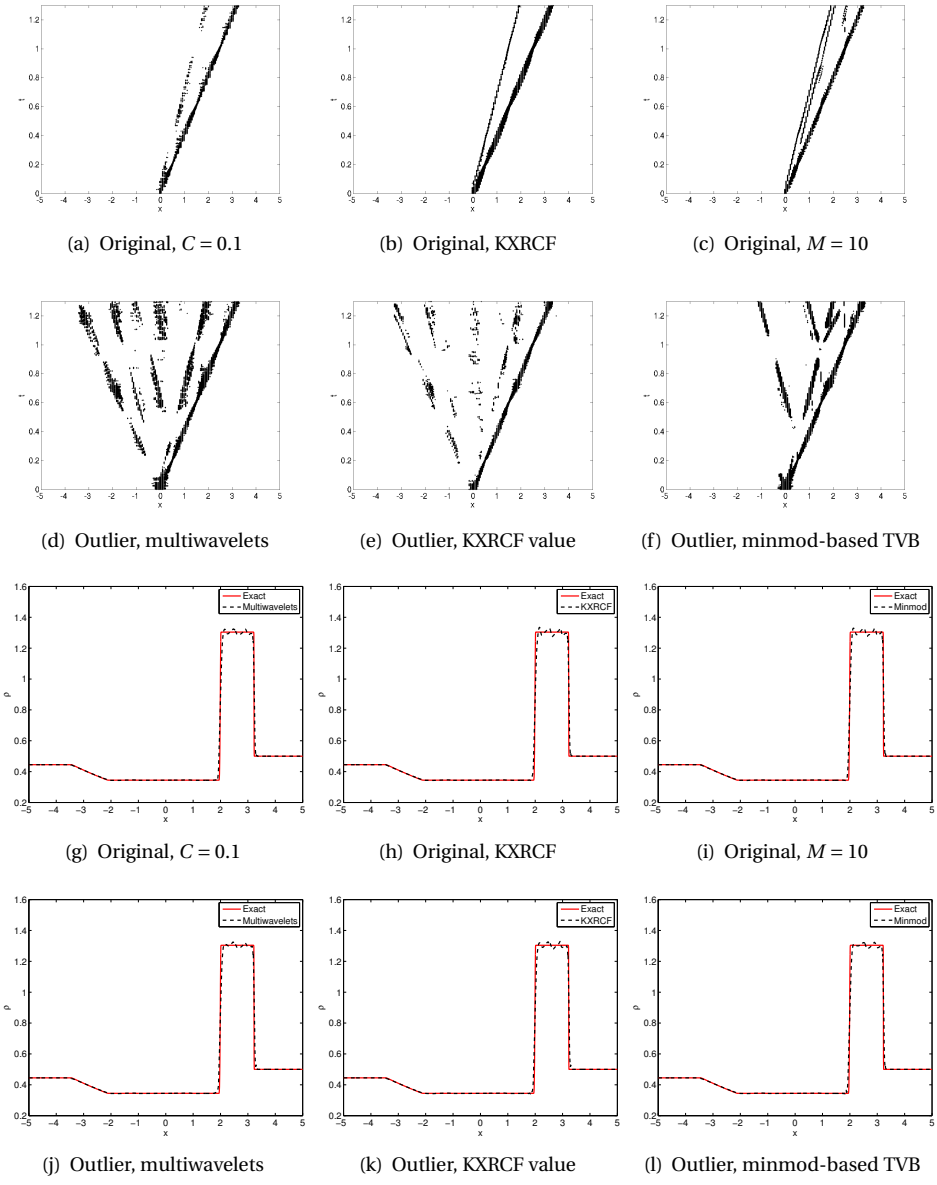

(a) Original, $C = 0.1$ (b) Original, KXRCF (c) Original, $M = 10$

(d) Outlier, multiwavelets (e) Outlier, KXRCF value (f) Outlier, minmod-based TVB

(g) Original, $C = 0.1$ (h) Original, KXRCF (i) Original, $M = 10$

(j) Outlier, multiwavelets (k) Outlier, KXRCF value (l) Outlier, minmod-based TVB

Figure 5.6: Lax's shock tube: time-history plot of detected troubled cells (rows 1 and 2), and approximation at final time $T = 1.3$ (rows 3 and 4), 256 elements, smoothly-varying mesh, $k = 2$. Algorithm 4.2 is applied to compute the outlier-detection results.

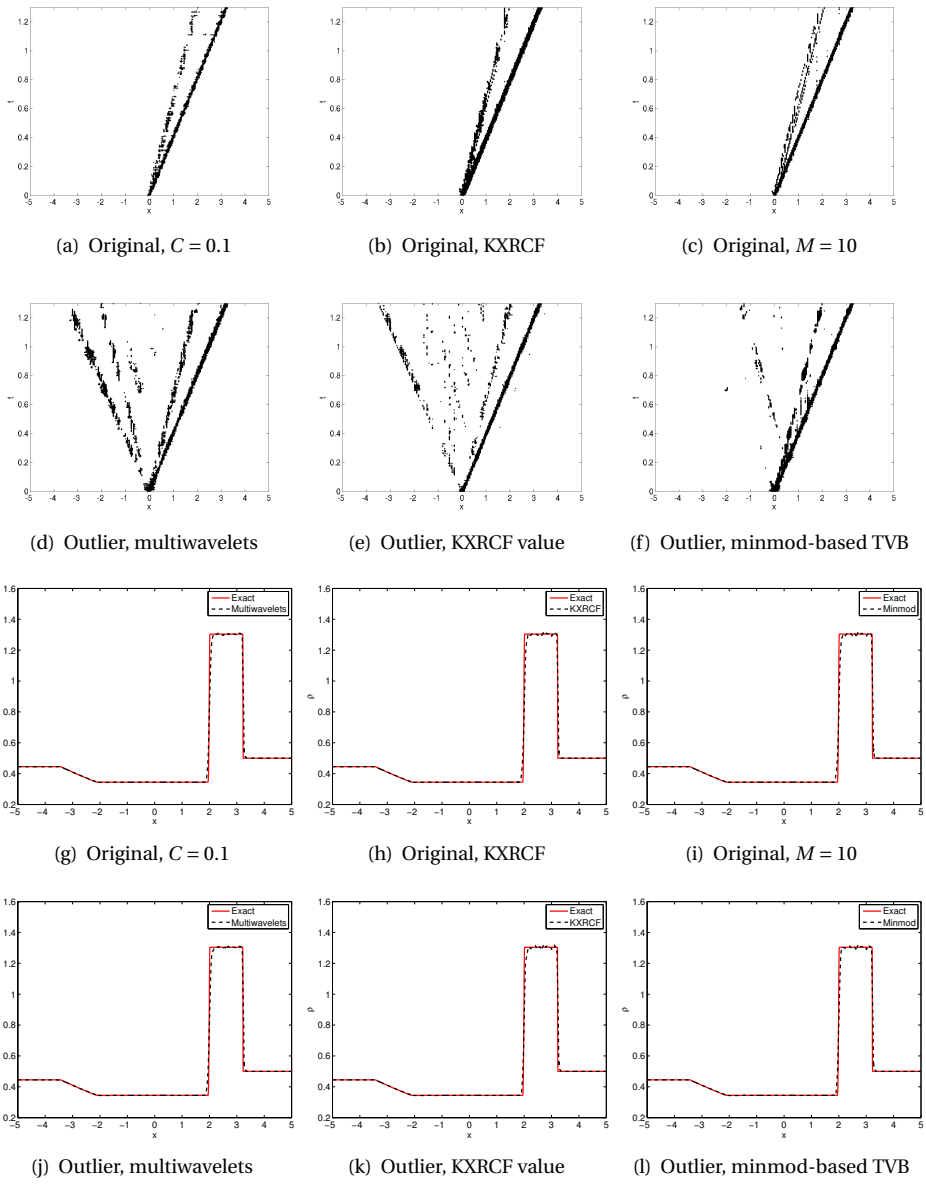

(a) Original, $C = 0.1$ (b) Original, KXRCF (c) Original, $M = 10$

(d) Outlier, multiwavelets (e) Outlier, KXRCF value (f) Outlier, minmod-based TVB

(g) Original, $C = 0.1$ (h) Original, KXRCF (i) Original, $M = 10$

(j) Outlier, multiwavelets (k) Outlier, KXRCF value (l) Outlier, minmod-based TVB

Figure 5.7: Lax's shock tube: time-history plot of detected troubled cells (rows 1 and 2), and approximation at final time $T = 1.3$ (rows 3 and 4), 256 elements, random mesh, $k = 2$. Algorithm 4.2 is applied to compute the outlier-detection results.

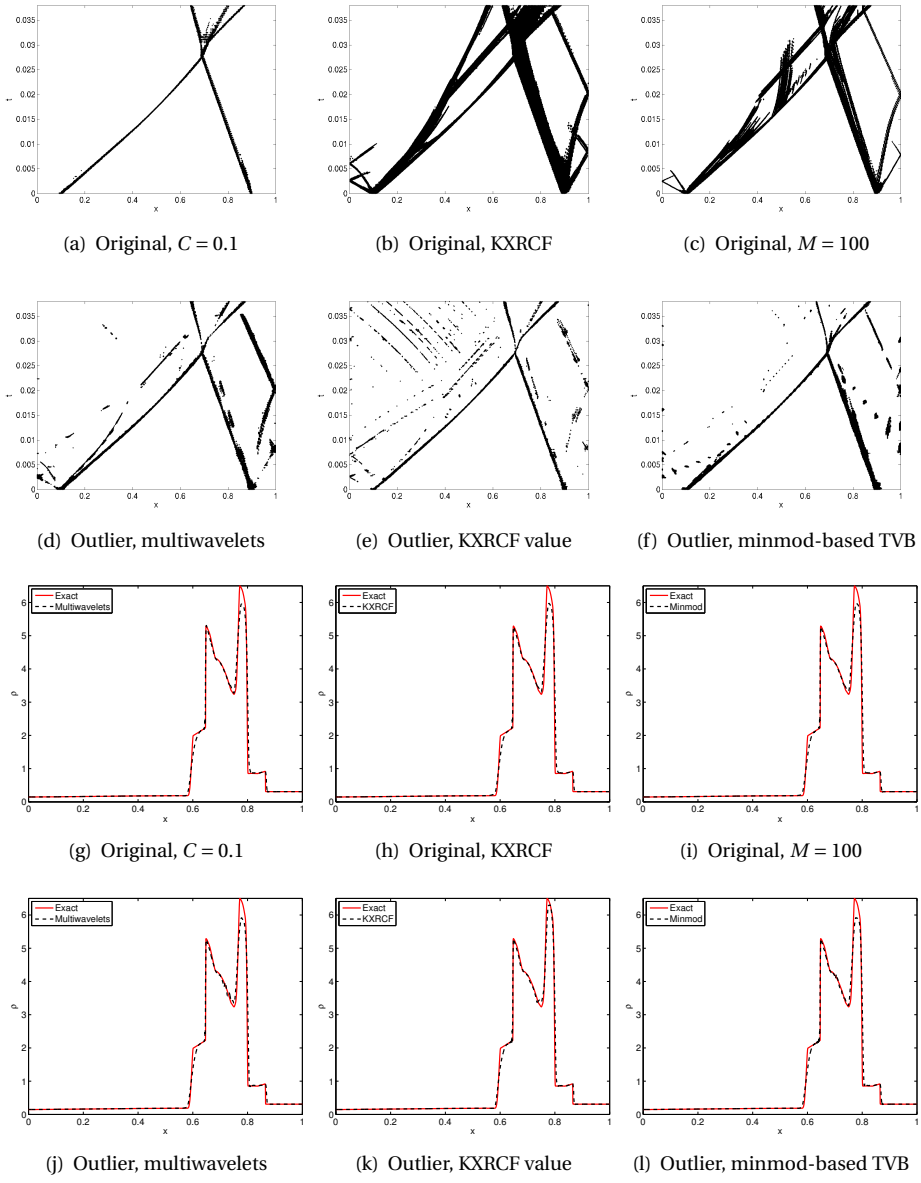

(a) Original, $C = 0.1$ (b) Original, KXRCF (c) Original, $M = 100$

(d) Outlier, multiwavelets (e) Outlier, KXRCF value (f) Outlier, minmod-based TVB

(g) Original, $C = 0.1$ (h) Original, KXRCF (i) Original, $M = 100$

(j) Outlier, multiwavelets (k) Outlier, KXRCF value (l) Outlier, minmod-based TVB

Figure 5.8: Blast-wave problem: time-history plot of detected troubled cells (rows 1 and 2), and approximation at final time $T = 0.038$ (rows 3 and 4), 512 elements, smoothly-varying mesh, $k = 2$. Algorithm 4.2 is applied to compute the outlier-detection results.

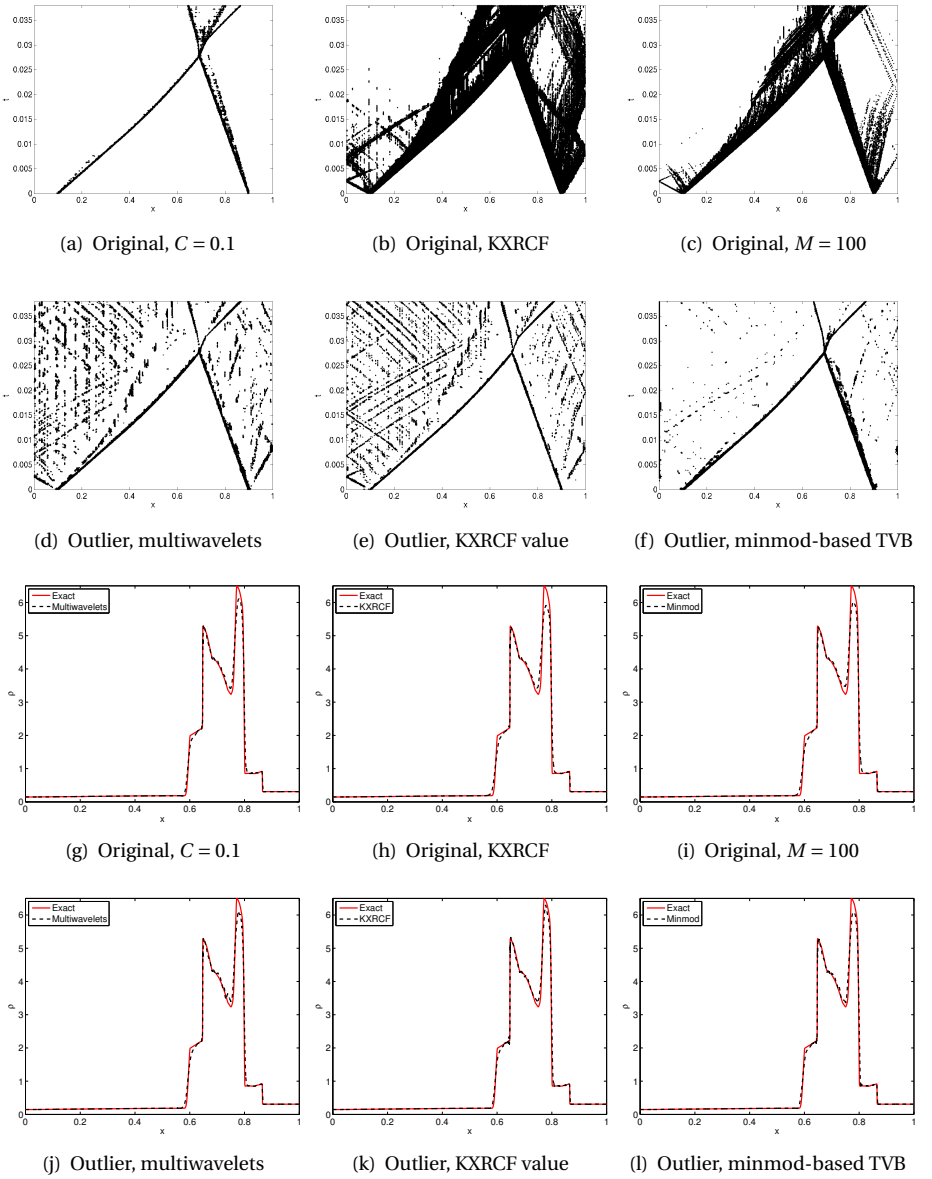

(a) Original, $C = 0.1$ (b) Original, KXRCF (c) Original, $M = 100$

(d) Outlier, multiwavelets (e) Outlier, KXRCF value (f) Outlier, minmod-based TVB

(g) Original, $C = 0.1$ (h) Original, KXRCF (i) Original, $M = 100$

(j) Outlier, multiwavelets (k) Outlier, KXRCF value (l) Outlier, minmod-based TVB

Figure 5.9: Blast-wave problem: time-history plot of detected troubled cells (rows 1 and 2), and approximation at final time $T = 0.038$ (rows 3 and 4), 512 elements, random mesh, $k = 2$. Algorithm 4.2 is applied to compute the outlier-detection results.

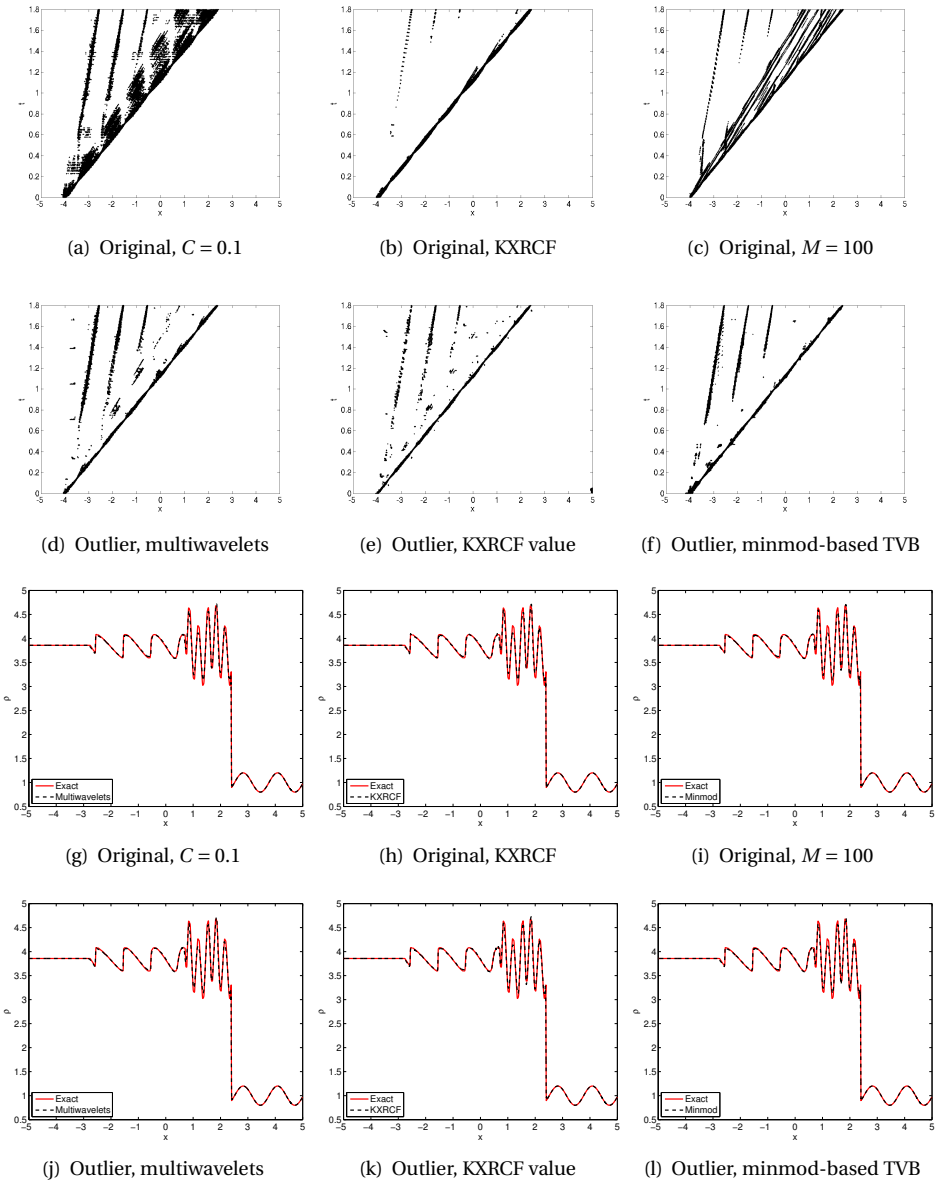

(a) Original, $C = 0.1$ (b) Original, KXRCF (c) Original, $M = 100$

(d) Outlier, multiwavelets (e) Outlier, KXRCF value (f) Outlier, minmod-based TVB

(g) Original, $C = 0.1$ (h) Original, KXRCF (i) Original, $M = 100$

(j) Outlier, multiwavelets (k) Outlier, KXRCF value (l) Outlier, minmod-based TVB

Figure 5.10: Shu-Osher problem: time-history plot of detected troubled cells (rows 1 and 2), and approximation at final time $T = 1.8$ (rows 3 and 4), 512 elements, smoothly-varying mesh, $k = 2$. Algorithm 4.2 is applied to compute the outlier-detection results.

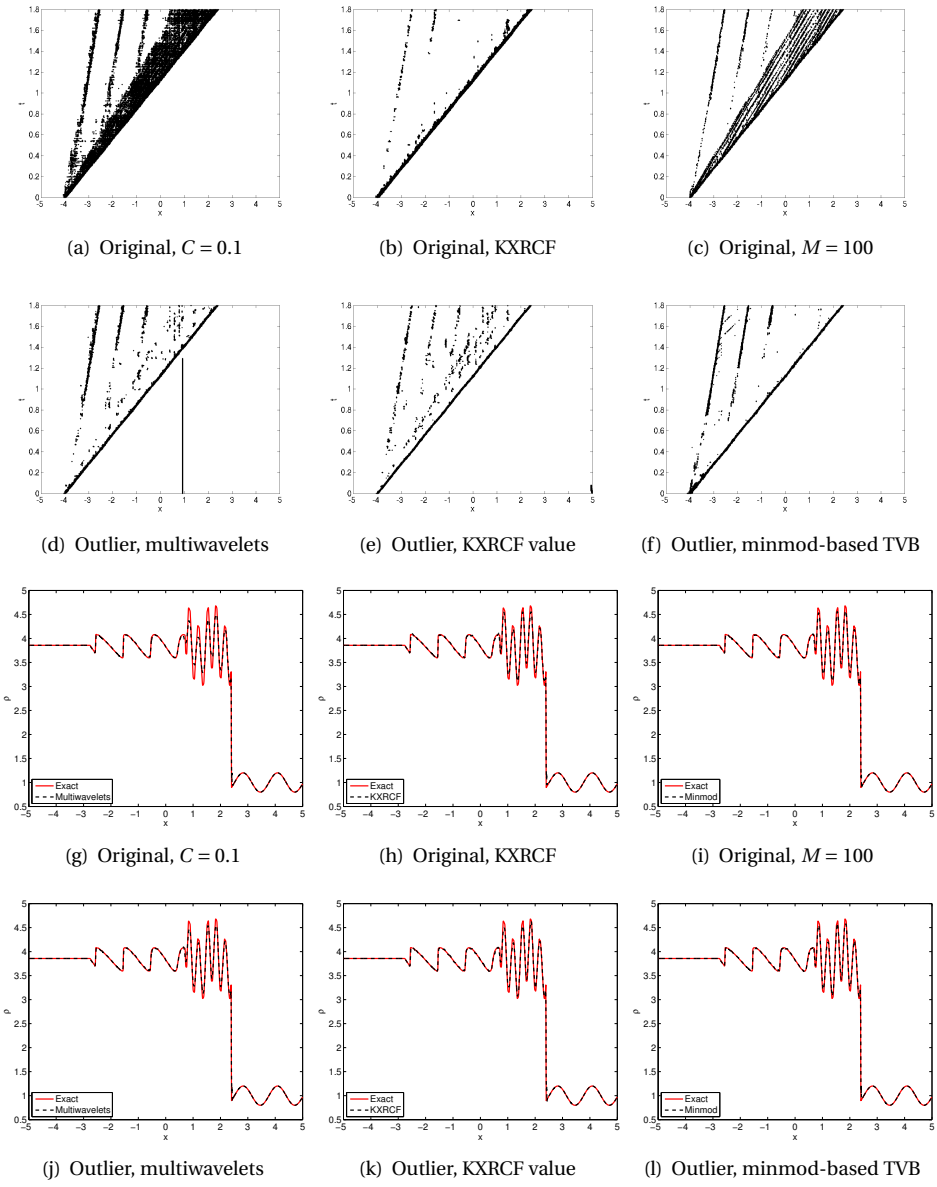

(a) Original, $C = 0.1$ (b) Original, KXRCF (c) Original, $M = 100$

(d) Outlier, multiwavelets (e) Outlier, KXRCF value (f) Outlier, minmod-based TVB

(g) Original, $C = 0.1$ (h) Original, KXRCF (i) Original, $M = 100$

(j) Outlier, multiwavelets (k) Outlier, KXRCF value (l) Outlier, minmod-based TVB

Figure 5.11: Shu-Osher problem: time-history plot of detected troubled cells (rows 1 and 2), and approximation at final time $T = 1.8$ (rows 3 and 4), 512 elements, random mesh, $k = 2$. Algorithm 4.2 is applied to compute the outlier-detection results.

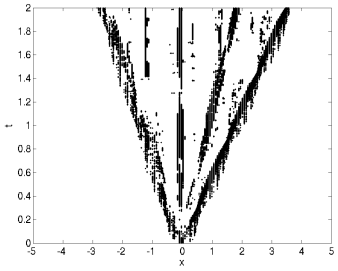

(a) Sod's shock tube, 256 elements

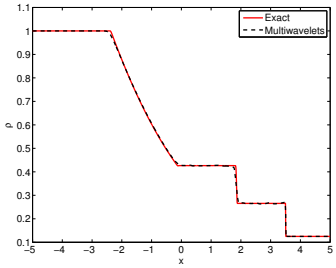

(b) Sod's shock tube, $T = 2$

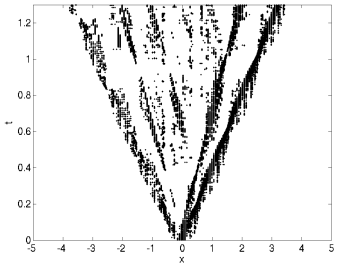

(c) Lax's shock tube, 256 elements

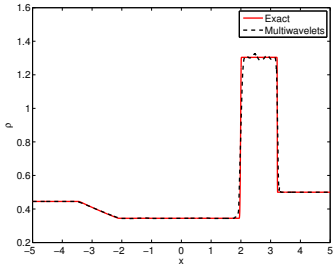

(d) Lax's shock tube, $T = 1.3$

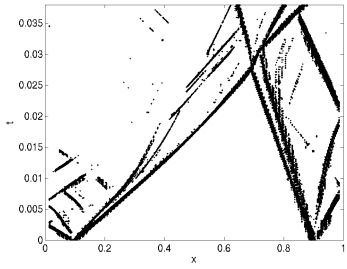

(e) Blast-wave problem, 512 elements

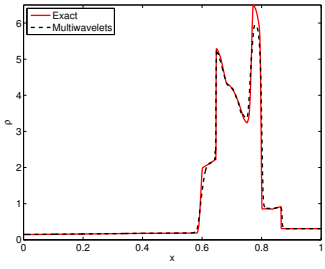

(f) Blast-wave problem, $T = 0.038$

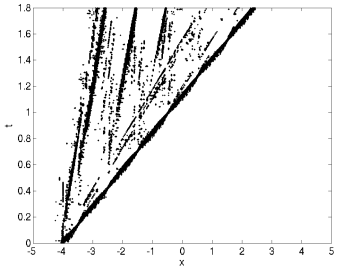

(g) Shu-Osher problem, 512 elements

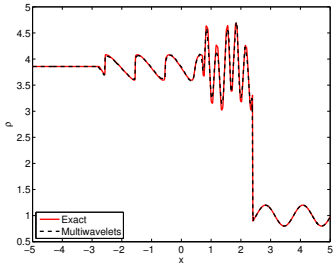

(h) Shu-Osher problem, $T = 1.8$

Figure 5.12: Time-history plots of detected troubled cells (left), and approximation at final times (right), smoothly-varying mesh with sliding-window technique on multiwavelet coefficients, $k = 2$.

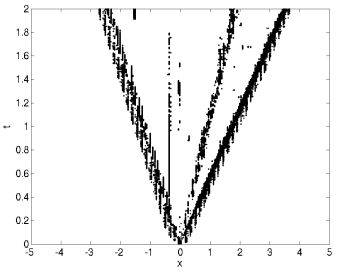

(a) Sod's shock tube, 256 elements

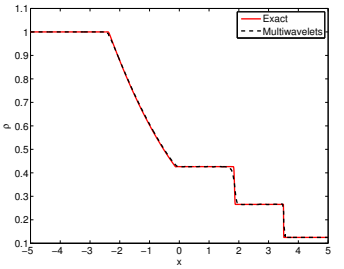

(b) Sod's shock tube, $T = 2$

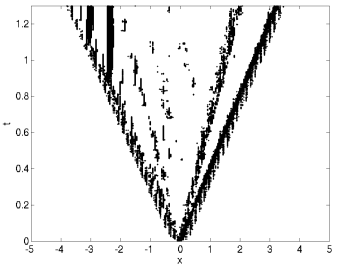

(c) Lax's shock tube, 256 elements

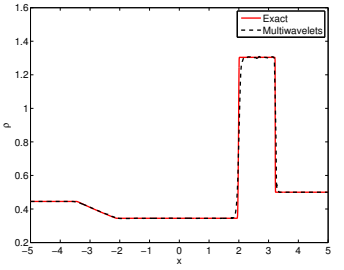

(d) Lax's shock tube, $T = 1.3$

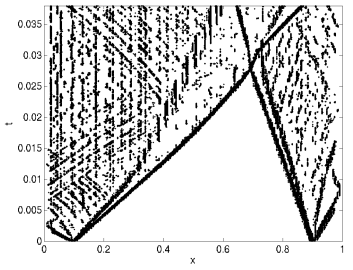

(e) Blast-wave problem, 512 elements

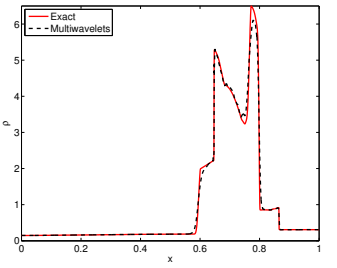

(f) Blast-wave problem, $T = 0.038$

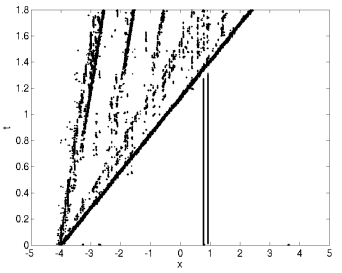

(g) Shu-Osher problem, 512 elements

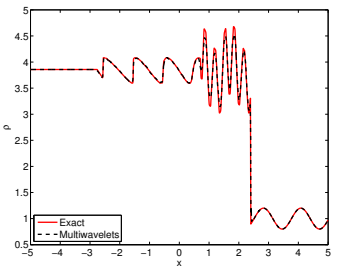

(h) Shu-Osher problem, $T = 1.8$

Figure 5.13: Time-history plots of detected troubled cells (left), and approximation at final times (right), random mesh with sliding-window technique on multiwavelet coefficients, $k = 2$.

6

STRUCTURED TRIANGULAR MESHES

In this chapter, an attempt is made to construct a multiwavelet troubled-cell indicator for structured triangular meshes. In Section 6.1, the triangular mesh is defined. Section 6.2 contains information about barycentric coordinates. In Section 6.3, the nodal DG method for triangular meshes is shortly discussed. The multiresolution analysis is described in Section 6.4. Both the parameter-based and the outlier-detection multiwavelet troubled-cell indicator are constructed for triangular meshes in Section 6.5. Preliminary results are shown in Section 6.6, and some concluding remarks are given in Section 6.7.

Parts of this chapter are submitted as a contribution to the conference proceedings of ICOSAHOM 2016 (Springer).

6.1. STRUCTURED TRIANGULAR MESH

In this section, the definition of a structured triangular mesh on a rectangular domain $\Omega \in \mathbb{R}^2$ is given, following the notation in [52, 140]. In order to compute the multiwavelet decomposition at a later time, the relation between the mesh on the finest level n and level $n-1$ is explained.

Definition 6.1. *Let i and j be space indices in the x- and y-direction, respectively, and let M account for the orientation of the triangle: $M = 1$ corresponds to triangles with the right angle located in the bottom-left corner, $M = 2$ belongs to the triangles with right angles in the upper-right corner. The uniform triangulation of a rectangular domain $\Omega \in \mathbb{R}^2$ on level n consists of 2^{2n+1} elements, and is expressed as $\mathcal{T}^n = \{T^n_{(i,j,M)}\}^{M=1,2}_{i,j=0,\dots,2^n-1} = \{T^n_\lambda\}_\lambda$, with $\lambda = (i,j,M)$, $i,j = 0,\dots,2^n-1$, $M = 1,2$.*

The triangulation on level $n-1$ is obtained by uniting four triangles on level n (Figure 6.1):

$$T^{n-1}_{(i,j,1)} = T^n_{(2i,2j,2)} \cup T^n_{(2i,2j,1)} \cup T^n_{(2i+1,2j,1)}, \cup T^n_{(2i,2j+1,1)},$$
$$T^{n-1}_{(i,j,2)} = T^n_{(2i+1,2j+1,1)} \cup T^n_{(2i+1,2j+1,2)} \cup T^n_{(2i,2j+1,2)} \cup T^n_{(2i+1,2j,2)},$$

with $i,j = 0,\dots,2^{n-1}-1$.

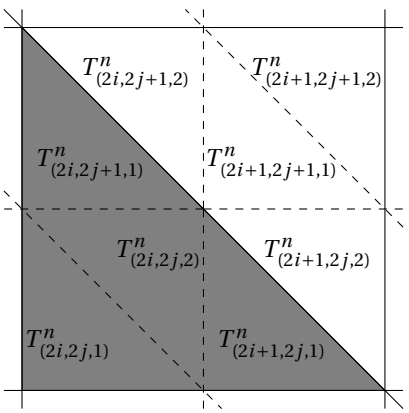

Figure 6.1: Triangulation $\mathcal{T}^n$ of a rectangular domain $\Omega \in \mathbb{R}^2$. Solid lines correspond to the elements $T^{n-1}_{(i,j,1)}$ and $T^{n-1}_{(i,j,2)}$ on level $n-1$.

6.2. BARYCENTRIC COORDINATES

Points inside a triangle are efficiently expressed using barycentric coordinates. In this section, several properties of the barycentric coordinate system are given.

Definition 6.2. *Let triangle T be defined by its vertices $\mathbf{P}_i = (x_i, y_i)^\top$, $i = 1,2,3$. Every point $\mathbf{P} = (x,y)^\top$ can be expressed in terms of the barycentric coordinates $\boldsymbol{\tau} = (\tau_1, \tau_2, \tau_3)^\top$*

with respect to triangle T as follows:

$$\begin{aligned} x &= \tau_1 x_1 + \tau_2 x_2 + \tau_3 x_3, \\ y &= \tau_1 y_1 + \tau_2 y_2 + \tau_3 y_3. \end{aligned} \tag{6.1}$$

The barycentric coordinates are uniquely given by requiring $|\boldsymbol{\tau}| = \tau_1 + \tau_2 + \tau_3 = 1$. If $\mathbf{P}$ is located inside T, then $\tau_i \geq 0, i = 1,2,3$.

The matrix-vector form of the transformation is useful for the computation of integrals on a triangle. Equation (6.1) is equivalent to the system

$$\begin{pmatrix} x \\ y \end{pmatrix} = A \begin{pmatrix} \tau_1 \\ \tau_2 \end{pmatrix} + \begin{pmatrix} x_3 \\ y_3 \end{pmatrix}, \quad \text{with} \quad A = \begin{pmatrix} x_1 - x_3 & x_2 - x_3 \\ y_1 - y_3 & y_2 - y_3 \end{pmatrix}.$$

The Jacobian of this transformation is given by

$$|\det(A)| = |x_1 y_2 - x_1 y_3 - x_3 y_2 - x_2 y_1 + x_2 y_3 + x_3 y_1| = 2|T|,$$

where we use that the area of T equals

$$|T| = \left| \frac{x_1(y_2 - y_3) + x_2(y_3 - y_1) + x_3(y_1 - y_2)}{2} \right|.$$

Integrals of functions on a triangle can therefore be transformed to barycentric coordinates as follows [146]:

$$\iint_T f(x,y)\,dx\,dy = 2|T| \int_0^1 \int_0^{1-\tau_1} f(x(\tau_1,\tau_2), y(\tau_1,\tau_2))\,d\tau_2\,d\tau_1. \tag{6.2}$$

The transformation from original coordinates to barycentric coordinates equals

$$\begin{pmatrix} \tau_1 \\ \tau_2 \\ \tau_3 \end{pmatrix} = \begin{pmatrix} x_1 & x_2 & x_3 \\ y_1 & y_2 & y_3 \\ 1 & 1 & 1 \end{pmatrix}^{-1} \begin{pmatrix} x \\ y \\ 1 \end{pmatrix}.$$

Using this expression, it is possible to relate the barycentric coordinates on different triangles which will be necessary when discussing multiwavelets. If $\mathbf{P}$ has barycentric coordinates $\boldsymbol{\tau}$ relative to triangle T (which is defined by $\{(x_i, y_i), i = 1,2,3\}$), then the barycentric coordinates $\boldsymbol{\tau}'$ with respect to T' (defined by $\{(x_i', y_i'), i = 1,2,3\}$) can be calculated using $\boldsymbol{\tau}' = M_{T \to T'} \boldsymbol{\tau}$, where

$$M_{T \to T'} = \begin{pmatrix} x_1' & x_2' & x_3' \\ y_1' & y_2' & y_3' \\ 1 & 1 & 1 \end{pmatrix}^{-1} \begin{pmatrix} x_1 & x_2 & x_3 \\ y_1 & y_2 & y_3 \\ 1 & 1 & 1 \end{pmatrix}. \tag{6.3}$$

The right matrix transforms $\boldsymbol{\tau}$ to $\mathbf{P}$, and the left matrix computes $\boldsymbol{\tau}'$ from $\mathbf{P}$ [146].

Finally, the midpoint subdivision of a triangle $T_\lambda^{n-1} = T_{\lambda_0}^n \cup T_{\lambda_1}^n \cup T_{\lambda_2}^n \cup T_{\lambda_3}^n$ can easily be described in barycentric coordinates, see Figure 6.2 [146].

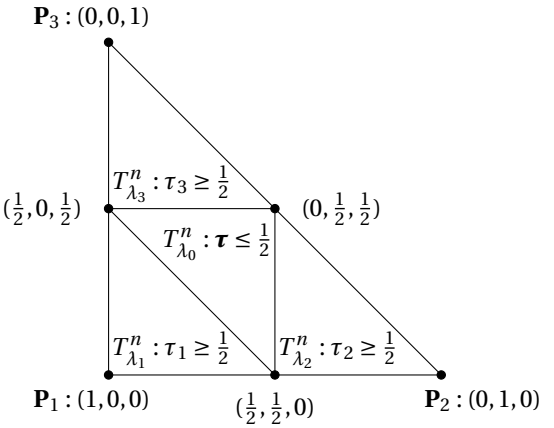

Figure 6.2: Midpoint subdivision of the triangle T^{n-1}_λ. All coordinates are given in barycentric form (τ_1,τ_2,τ_3).

6.3. DISCONTINUOUS GALERKIN METHOD

As discussed in Section 2.1, the discontinuous Galerkin method can be expressed either in the modal, or in the nodal form. Although the modal form is used for multiwavelet decomposition, the nodal form is computationally more attractive on a triangular mesh [27, 31, 68]. In this section, the nodal discontinuous Galerkin method on a triangular mesh is briefly described for the conservation law

$$\begin{cases} \frac{\partial u(\mathbf{x},t)}{\partial t} + \nabla \cdot \mathbf{f}(u(\mathbf{x},t),\mathbf{x},t) = 0, & \mathbf{x} \in \Omega \in \mathbb{R}^2, \\ u(\mathbf{x},t) = g(\mathbf{x},t), & \mathbf{x} \in \partial\Omega_i, \\ u(\mathbf{x},0) = f(\mathbf{x}), \end{cases}$$

where $\partial\Omega_i$ is the inflow boundary of Ω.

The approximation space is defined as

$$V_h = \{f : f \in \mathbb{P}^k(T^n_\lambda), \quad \forall\, T^n_\lambda \in \mathscr{T}^n\}, \tag{6.4}$$

where $\mathbb{P}^k(T^n_\lambda)$ is the space of polynomials of degree at most k on triangle T^n_λ. Note that this space has dimension $N_k = (k+1)(k+2)/2$. As a basis, the two-dimensional Lagrange-polynomials, $\{\ell_i\}_{i=1}^{N_k}$, are used, using N_k grid points $\mathbf{x}^i$ on triangle T^n_λ. These functions are not known explicitly [68]. The choice of the optimal nodal points is described in [68]. This leads to the following nodal DG approximation on triangle T^n_λ:

$$u_h(\mathbf{x}) = \sum_{i=1}^{N_k} u_h(\mathbf{x}^i)\ell_i(\mathbf{x}).$$

The weak form of the PDE is obtained by multiplying the equation by a test function, integrating over triangle T^n_λ, and applying the divergence theorem, which yields

$$\int_{T^n_\lambda} \left(\frac{\partial u_h}{\partial t}\ell_i(\mathbf{x}) - \mathbf{f}_h \cdot \nabla \ell_i(\mathbf{x}) \right) d\mathbf{x} = -\int_{\partial T^n_\lambda} \hat{\mathbf{n}} \cdot \mathbf{f}^* \ell_i(\mathbf{x})\, d\mathbf{x}.$$

The numerical flux, $\mathbf{f}^*$, is approximated by the local Lax-Friedrichs flux [68]. Let a and b be the DG approximations in the interior and the exterior of the triangle, respectively, and let $\mathbf{f} = (f_1, f_2)$. Using

$$C = \max_{u\in[a,b]} \left| \hat{n}_x \frac{\partial f_1}{\partial u} + \hat{n}_y \frac{\partial f_2}{\partial u} \right|,$$

the flux is chosen as

$$\mathbf{f}^*(a,b) = \frac{\mathbf{f}(a) + \mathbf{f}(b)}{2} + \frac{C}{2}\hat{\mathbf{n}}(a-b).$$

The explicit five-stage fourth-order low-storage Runge-Kutta method is used for time integration [23]. More details about the implementation of the nodal DG method for different problems can be found in [68].

6.4. MULTIRESOLUTION ANALYSIS

In this section, the multiresolution analysis for a triangular mesh is presented, together with the formulae for multiwavelet decomposition and reconstruction [140]. The scaling functions and multiwavelets are constructed for the so-called *base triangle*, T_B, which has vertices $\mathbf{P}_1 = (0,0)$, $\mathbf{P}_2 = (1,0)$, and $\mathbf{P}_3 = (0,1)$, and subdivision $T_B = T_0 \cup T_1 \cup T_2 \cup T_3$ (with numbering similar to Figure 6.2). The extension to general triangles is given as well.

6.4.1. SCALING-FUNCTION SPACE

In this section, the orthonormal scaling-function basis is constructed for the base triangle, using barycentric coordinates [146]. The scaling-function space on T_B is defined as $V^{k+1}(T_B) = \mathbb{P}^k(T_B)$, which means that the space is spanned by polynomials of total degree less than or equal to k on T_B. The standard monomial basis for $V^{k+1}(T_B)$ consists of N_k functions $\{1, x, y, x^2, xy, y^2, \ldots\}$. For the base triangle, the coordinates (x, y) transform to

$$\begin{aligned} x &= \tau_1 x_1 + \tau_2 x_2 + \tau_3 x_3 = \tau_2, \\ y &= \tau_1 y_1 + \tau_2 y_2 + \tau_3 y_3 = \tau_3 = 1 - \tau_1 - \tau_2 \end{aligned}$$

in barycentric coordinates. This means that the monomial basis is equivalent to the set

$$\{1, \tau_2, 1-\tau_1-\tau_2, \tau_2^2, (1-\tau_1-\tau_2)\tau_2, (1-\tau_1-\tau_2)^2, \ldots\}$$

in the barycentric coordinate system. Orthonormality of this basis is achieved by the application of the Gram-Schmidt procedure with respect to the inner product

$$\langle f, g\rangle = \int_0^1 \int_0^{1-\tau_1} f(\tau_1,\tau_2) g(\tau_1,\tau_2) d\tau_2 d\tau_1,$$

together with normalization. This results in the orthonormal scaling functions ϕ_{ℓ,T_B}, $\ell = 1,\dots,N_k$. The first six functions (corresponding to $k \le 2$) are given in [146]:

$$\phi_{1,T_B}(\tau_1,\tau_2) = \sqrt{2}, \tag{6.5a}$$
$$\phi_{2,T_B}(\tau_1,\tau_2) = (-2+6\tau_2), \tag{6.5b}$$
$$\phi_{3,T_B}(\tau_1,\tau_2) = 2\sqrt{3}(1-2\tau_1-\tau_2), \tag{6.5c}$$
$$\phi_{4,T_B}(\tau_1,\tau_2) = \sqrt{6}(1-8\tau_2+10\tau_2^2), \tag{6.5d}$$
$$\phi_{5,T_B}(\tau_1,\tau_2) = 3\sqrt{2}(-1+2\tau_1+6\tau_2-10\tau_1\tau_2-5\tau_2^2), \tag{6.5e}$$
$$\phi_{6,T_B}(\tau_1,\tau_2) = \sqrt{30}(1-6\tau_1+6\tau_1^2-2\tau_2+6\tau_1\tau_2+\tau_2^2), \tag{6.5f}$$

$\tau_1 \in [0,1]$, $\tau_2 \in [0,1-\tau_1]$.

The scaling-function space for a triangular mesh on level n is defined as the space of piecewise polynomials of total degree less than or equal to k on every triangle $T_\lambda^n \in \mathscr{T}^n$:

$$V_n^{k+1} = \{f : f \in \mathbb{P}^k(T_\lambda^n), \quad \forall\, T_\lambda^n \in \mathscr{T}^n\}. \tag{6.6}$$

The orthonormal basis for V_n^{k+1} can be found by substituting the correct barycentric coordinates (translation) and scaling the functions ϕ_{ℓ,T_B} [146]. Let $\boldsymbol{\tau}$ be the barycentric coordinates with respect to T_B, and let $\boldsymbol{\tau}'$ be the corresponding barycentric coordinates with respect to $T_\lambda^n \in \mathscr{T}^n$. The space V_n^{k+1} is spanned by $2^{2n+1}\cdot N_k$ functions that are obtained from ϕ_{ℓ,T_B} using

$$\phi_{\ell\lambda}^n(\tau_1',\tau_2',\tau_3') = \sqrt{\frac{1}{2|T_\lambda^n|}}\phi_{\ell,T_B}(\tau_1,\tau_2,\tau_3). \tag{6.7}$$

The orthogonal projection of an arbitrary function $f \in L^2(\Omega)$ onto V_n^{k+1} is given by

$$P_n^{k+1} f(\mathbf{x}) = \sum_{T_\lambda^n \in \mathscr{T}^n} \sum_{\ell=1}^{N_k} s_{\ell\lambda}^n \phi_{\ell\lambda}^n(\boldsymbol{\tau}),$$

which is the single-scale decomposition of f on level n. The scaling-function coefficients are given by $s_{\ell\lambda}^n = \langle f, \phi_{\ell\lambda}^n\rangle$. Note that if $f \in V_n^{k+1}$, then $P_n^{k+1} f = f$.

6.4.2. NODAL DG APPROXIMATION AND SCALING-FUNCTION EXPANSION

From equations (6.4) and (6.6) we see that the DG approximation space is equal to the scaling-function space on level n. This means that it is possible to express the nodal DG approximation as a scaling-function approximation in level n. In this section, the transformation from one basis to the other is given.

Since $u_h \in V_h = V_n^{k+1}$, we know that $u_h = P_n^{k+1} u_h$. Therefore, the global nodal DG approximation of degree k can be written as

$$u_h(\mathbf{x}) = \sum_{T_\lambda^n \in \mathscr{T}^n} \sum_{i=1}^{N_k} u_h(\mathbf{x}^i)\ell_i(\mathbf{x}) = \sum_{T_\lambda^n \in \mathscr{T}^n} \sum_{\ell=1}^{N_k} s_{\ell\lambda}^n \phi_{\ell\lambda}^n(\boldsymbol{\tau}).$$

Knowing the values $u_h(\mathbf{x}^i)$, we can efficiently compute the scaling-function coefficients by a matrix-vector multiplication. Let $\mathbf{s}_\lambda^n = (s_{1\lambda}^n, \ldots, s_{N_k\lambda}^n)^\top$, $\mathbf{u}_h = (u_h(\mathbf{x}^1), \ldots, u_h(\mathbf{x}^{N_k}))^\top$, and define a Vandermonde matrix by $V_{mi} = \phi_{i\lambda}^n(\boldsymbol{\tau}(\mathbf{x}^m))$, then $\mathbf{V}\mathbf{s}_\lambda^n = \mathbf{u}_h$ and $\mathbf{V}^{-1}\mathbf{u}_h = \mathbf{s}_\lambda^n$.

This procedure is very similar to the transformation from nodal to modal DG, see Section 2.1.2. This is because the scaling-function basis for V_n^{k+1} is closely related to the modal DG basis, which is given by the so-called *PKD polynomials* [48, 80]. The difference between both bases is the reference triangle that is used. This leads to a different Vandermonde matrix [68].

6.4.3. MULTIWAVELETS

In addition to the scaling-function space, the multiwavelet space should be defined. Similar to Section 2.4.3, this is done by computing the orthogonal complement of V_{n-1}^{k+1} in V_n^{k+1}:

$$V_{n-1}^{k+1} \oplus W_{n-1}^{k+1} = V_n^{k+1},$$

such that $W_{n-1}^{k+1} \perp V_{n-1}^{k+1}$, $W_{n-1}^{k+1} \subset V_n^{k+1}$. In Algorithm 6.1, the procedure to compute the multiwavelets for the base triangle is given, in a manner very similar to Alpert's construction in one dimension (Algorithm 2.1). Note that the number of multiwavelet basis functions for each element equals $3N_k$. The execution of this algorithm leads to the multiwavelets as provided in [122].

Similar to equation (6.7), the multiwavelets on triangle $T_\lambda^n \in \mathcal{T}^n$ are equal to

$$\psi_{\ell\lambda}^{m,n}(\tau_1', \tau_2', \tau_3') = \sqrt{\frac{1}{2|T_\lambda^n|}}\psi_\ell^m(\tau_1, \tau_2, \tau_3), \quad m = 1,2,3, \quad \ell = 1, \ldots, N_k.$$

The multiwavelet coefficients of a function f in level n are defined as $d_{\ell\lambda}^{m,n} = \langle f, \psi_{\ell\lambda}^{m,n}\rangle$.

In [56], a similar multiwavelet basis is constructed, but normalization is done in the L^∞-norm instead of the L^2-norm.

6.4.4. MULTIWAVELET DECOMPOSITION AND RECONSTRUCTION

In Section 6.4.2, the relation between the DG approximation and the scaling-function coefficients on level n was given. In this section, the scaling-function expansion on level n is decomposed to a multiwavelet expansion on level $n-1$ [146]. This theory is similar to the one-dimensional case (Section 2.4.4). The full decomposition is derived in [56, 116, 122].

DECOMPOSITION

By definition, the multiresolution analysis yields $V_n^{k+1} = V_{n-1}^{k+1} \oplus W_{n-1}^{k+1}$. In the following, the basis of $\mathbb{P}^k(T_\lambda^{n-1})$ is written as a vector of scaling functions $\boldsymbol{\phi}_\lambda^{n-1} = (\phi_{1\lambda}^{n-1}, \ldots, \phi_{N_k\lambda}^{n-1})^\top$. Because $V_{n-1}^{k+1} \subset V_n^{k+1}$, we can express $\boldsymbol{\phi}_\lambda^{n-1}$ in terms of $\boldsymbol{\phi}_{\lambda_i}^n$, $i = 0,1,2,3$, using the local numbering $T_\lambda^{n-1} = T_{\lambda_0}^n \cup T_{\lambda_1}^n \cup T_{\lambda_2}^n \cup T_{\lambda_3}^n$ (Figure 6.2). This means that

$$\boldsymbol{\phi}_\lambda^{n-1} = H_0\boldsymbol{\phi}_{\lambda_0}^n + H_1\boldsymbol{\phi}_{\lambda_1}^n + H_2\boldsymbol{\phi}_{\lambda_2}^n + H_3\boldsymbol{\phi}_{\lambda_3}^n. \tag{6.9a}$$

Algorithm 6.1 Yu's multiwavelet algorithm [146].

Let (τ_1,τ_2,τ_3) be the barycentric coordinates relative to $T_B = T_0 \cup T_1 \cup T_2 \cup T_3$ (with numbering as in Figure 6.2), and let $(\tau_1^m,\tau_2^m,\tau_3^m)$ correspond to T_m, $m = 1,2,3$. Define for $m = 1,2,3$, $\ell = 1,\ldots,N_k$:

$$f_\ell^{m,0}(\tau_1,\tau_2,\tau_3) = \begin{cases} \phi_{\ell,T_m}(\tau_1^m,\tau_2^m,\tau_3^m), & \text{on } T_m, \\ -\phi_{\ell,T_m}(\tau_1^m,\tau_2^m,\tau_3^m), & \text{on } T_B \backslash T_m, \\ 0, & \text{on } \mathbb{R}^2 \backslash T_B. \end{cases} \tag{6.8}$$

Use Gram-Schmidt to orthogonalize $f_\ell^{m,0}$ with respect to ϕ_{ℓ,T_B}, $\ell = 1,\ldots,N_k$. This leads to the functions $f_\ell^{m,1}$, $m = 1,2,3$, $\ell = 1,\ldots,N_k$.

Order the functions $f_\ell^{m,1}$ as $\left\{f_1^{1,1},f_1^{2,1},f_1^{3,1},\ldots,f_{N_k}^{1,1},f_{N_k}^{2,1},f_{N_k}^{3,1}\right\}$ and denote this set as $\left\{f_1^1,f_2^1,\ldots,f_{3N_k}^1\right\}$.

for $M = 1,\ldots,3N_k$ **do**

If at least one of the f_ℓ^M is not orthogonal to ϕ_{N_k+M,T_B} $(\ell = M,\ldots,3N_k)$, then reorder such that $\langle f_M^M,\phi_{N_k+M,T_B}\rangle \neq 0$.

for $\ell = M+1,\ldots,3N_k$ **do**

Construct f_ℓ^{M+1} such that the function is orthogonal to ϕ_{N_k+M,T_B}:

$$f_\ell^{M+1} = f_\ell^M - \frac{\left\langle f_\ell^M,\phi_{N_k+M,T_B}\right\rangle}{\left\langle f_M^M,\phi_{N_k+M,T_B}\right\rangle}\cdot f_M^M.$$

end for

end for

Gram-Schmidt orthonormalize $f_{3N_k}^{3N_k},f_{3N_k-1}^{3N_k-1},\ldots,f_1^1$ in that order.

Rename the multiwavelets, depending on the triangle they were mutilated to (based on equation (6.8)) to obtain ψ_ℓ^m, $m = 1,2,3$, $\ell = 1,\ldots,N_k$.

The $N_k \times N_k$ matrices H_i are similar to the QMF coefficients in the one-dimensional case [136], and are defined as

$$(H_i)_{p,q} = \langle \phi_{p\lambda}^{n-1}, \phi_{q\lambda_i}^{n} \rangle = \iint_{T_{\lambda_i}^n} \phi_{p\lambda}^{n-1}(x,y)\phi_{q\lambda_i}^{n}(x,y)dxdy, \quad i = 0,1,2,3,\ p,q = 1,\ldots,N_k,$$

using that $\phi_{q\lambda_i}^n$ is only nonzero in $T_{\lambda_i}^n$. We transform to barycentric coordinates $\boldsymbol{\tau}$ based on the vertices of $T_{\lambda_i}^n$. Using equations (6.2), (6.3) and (6.7), this yields

$$\begin{aligned}(H_i)_{p,q} &= 2|T_{\lambda_i}^n|\sqrt{\frac{1}{2|T_\lambda^{n-1}|}}\sqrt{\frac{1}{2|T_{\lambda_i}^n|}}\int_0^1\int_0^{1-\tau_1} \phi_p(M_{T_{\lambda_i}^n \to T_\lambda^{n-1}}\boldsymbol{\tau})\phi_q(\boldsymbol{\tau})d\tau_2 d\tau_1 \\ &= \sqrt{\frac{|T_{\lambda_i}^n|}{|T_\lambda^{n-1}|}}\int_0^1\int_0^{1-\tau_1} \phi_p(M_{T_{\lambda_i}^n \to T_\lambda^{n-1}}\boldsymbol{\tau})\phi_q(\boldsymbol{\tau})d\tau_2 d\tau_1 \\ &= \frac{1}{2}\int_0^1\int_0^{1-\tau_1} \phi_p(M_{T_{\lambda_i}^n \to T_\lambda^{n-1}}\boldsymbol{\tau})\phi_q(\boldsymbol{\tau})d\tau_2 d\tau_1,\end{aligned}$$

since $|T_{\lambda_i}^n| = |T_\lambda^{n-1}|/4$. For a structured triangular mesh, the matrices H_i do not depend on the mesh size [122].

Similarly, the multiwavelet basis can be written as $\boldsymbol{\psi}_\lambda^{m,n-1} = (\psi_{1\lambda}^{m,n-1},\ldots,\psi_{N_k\lambda}^{m,n-1})^\top$, $m = 1,2,3$. Because $W_{n-1}^{k+1} \subset V_n^{k+1}$, the vectors of multiwavelets can be written as

$$\boldsymbol{\psi}_\lambda^{m,n-1} = G_{m,0}\boldsymbol{\phi}_{\lambda_0}^n + G_{m,1}\boldsymbol{\phi}_{\lambda_1}^n + G_{m,2}\boldsymbol{\phi}_{\lambda_2}^n + G_{m,3}\boldsymbol{\phi}_{\lambda_3}^n, \quad \text{for } m = 1,2,3, \tag{6.9b}$$

with

$$(G_{m,i})_{p,q} = \langle \psi_{p\lambda}^{m,n-1}, \phi_{q\lambda_i}^n \rangle, \quad m = 1,2,3,\ i = 0,1,2,3,\ p,q = 1,\ldots,N_k.$$

The matrices $G_{m,i}$ are computed similarly to the matrices H_i.

From equation (6.9) and the fact that $\mathbf{s}_\lambda^{n-1} = \langle f, \boldsymbol{\phi}_\lambda^{n-1} \rangle$, $\mathbf{d}_\lambda^{m,n-1} = \langle f, \boldsymbol{\psi}_\lambda^{m,n-1} \rangle$, it follows that we can decompose the scaling-function coefficients on level n to scaling-function and multiwavelet coefficients on level $n-1$ as follows:

$$\mathbf{s}_\lambda^{n-1} = H_0\mathbf{s}_{\lambda_0}^n + H_1\mathbf{s}_{\lambda_1}^n + H_2\mathbf{s}_{\lambda_2}^n + H_3\mathbf{s}_{\lambda_3}^n, \tag{6.10a}$$

$$\mathbf{d}_\lambda^{1,n-1} = G_{1,0}\mathbf{s}_{\lambda_0}^n + G_{1,1}\mathbf{s}_{\lambda_1}^n + G_{1,2}\mathbf{s}_{\lambda_2}^n + G_{1,3}\mathbf{s}_{\lambda_3}^n, \tag{6.10b}$$

$$\mathbf{d}_\lambda^{2,n-1} = G_{2,0}\mathbf{s}_{\lambda_0}^n + G_{2,1}\mathbf{s}_{\lambda_1}^n + G_{2,2}\mathbf{s}_{\lambda_2}^n + G_{2,3}\mathbf{s}_{\lambda_3}^n, \tag{6.10c}$$

$$\mathbf{d}_\lambda^{3,n-1} = G_{3,0}\mathbf{s}_{\lambda_0}^n + G_{3,1}\mathbf{s}_{\lambda_1}^n + G_{3,2}\mathbf{s}_{\lambda_2}^n + G_{3,3}\mathbf{s}_{\lambda_3}^n, \tag{6.10d}$$

which is called the *multiwavelet decomposition* from level n to level $n-1$.

RECONSTRUCTION

For reconstruction, we use that the $4N_k \times 4N_k$ matrix

$$U = \begin{pmatrix} H_0 & H_1 & H_2 & H_3 \\ G_{1,0} & G_{1,1} & G_{1,2} & G_{1,3} \\ G_{2,0} & G_{2,1} & G_{2,2} & G_{2,3} \\ G_{3,0} & G_{3,1} & G_{3,2} & G_{3,3} \end{pmatrix}$$

is orthogonal: $UU^\top = I = U^\top U$. The first equality is due to decomposition, and the second equality leads to reconstruction. If we write out this equality, we find

$$H_{i_1}^\top H_{i_2} + G_{1,i_1}^\top G_{1,i_2} + G_{2,i_1}^\top G_{2,i_2} + G_{3,i_1}^\top G_{3,i_2} = \delta_{i_1,i_2} I, \quad i_1, i_2 = 0,1,2,3.$$

This means that left-multiplying equation (6.10a) by $H_i^\top$, equation (6.10b) by $G_{1,i}^\top$, equation (6.10c) by $G_{2,i}^\top$, and equation (6.10d) by $G_{3,i}^\top$ and summing yields

$$H_i^\top \mathbf{s}_\lambda^{n-1} + G_{1,i}^\top \mathbf{d}_\lambda^{1,n-1} + G_{2,i}^\top \mathbf{d}_\lambda^{2,n-1} + G_{3,i}^\top \mathbf{d}_\lambda^{3,n-1} = \mathbf{s}_{\lambda_i}^n, \quad i = 0,1,2,3, \tag{6.11}$$

which is exactly the reconstruction procedure.

6.5. MULTIWAVELET TROUBLED-CELL INDICATOR

In this section, a troubled-cell indicator based on multiwavelets is defined for triangular meshes [140]. The KXRCF shock detector and the minmod-based TVB indicator are both applicable to triangular meshes [31, 83], and are recommended to be used as reference schemes in future research. In [52], the norm of a vector with multiwavelet coefficients is used for the detection of troubled cells. However, that method requires knowledge of the discontinuity line and is therefore not useful for our applications.

Again, the number of multiwavelet coefficients is increased by a renumbering technique (similar to Section 3.2.2). This leads to the multiwavelet coefficients $\tilde{d}_{\ell\lambda}^{m,n-1}$, where $\ell = 1,\ldots,N_k$, $m = 1,2,3$, and λ belongs to the triangles in level n (instead of level $n-1$).

6.5.1. PARAMETER-BASED INDICATOR

The parameter-based multiwavelet troubled-cell indicator is defined similarly to the indicator for the one-dimensional and tensor-product two-dimensional case as was proposed in Section 3.2.4. The major difference lies in the number of coefficients that is needed for accurate detection. In the one-dimensional or tensor-product two-dimensional case, knowledge of the jump relation at element boundaries made it possible to use one coefficient per element for detection. In the triangular case, however, such a relation has not yet been proven, neither theoretically, nor numerically. However, since the cancelation property also holds in the triangular case, the coefficients are still useful for detection [40, 56]. We will use all multiwavelet coefficients for detection: triangle T_λ^n is detected as troubled if for any $m = 1,2,3$, $\ell = 1,\ldots,N_k$:

$$\left|\tilde{d}_{\ell\lambda}^{m,n-1}\right| > C \cdot \max_{T_\lambda^n \in \mathcal{T}^n} \left\{\left|\tilde{d}_{\ell\lambda}^{m,n-1}\right|\right\},$$

where $C \in [0,1]$ is a parameter that defines the strictness of the indicator. The parameter C is problem-dependent: it depends on the strength of different shocks in the domain. This limits the applicability of this troubled-cell indicator. Therefore, an outlier-detection approach is also considered.

6.5.2. OUTLIER-DETECTION APPROACH

In this section, a troubled-cell indication technique for the multiwavelet coefficients on a structured triangular mesh is proposed that is based on outlier detection. In this way, a problem-dependent parameter is not needed.

A triangle is detected as troubled if it is detected in either the x- or the y-direction, using the one-dimensional approach (Algorithm 4.2). Regions with triangles in the x-direction are split into local regions of size 16, as is visualized in Figure 6.3, and a similar approach is followed for regions in the y-direction. The resulting outlier-detection approach is given in Algorithm 6.2. Note that this approach is closely related to the outlier-detection algorithm for a rectangular tensor-product mesh.

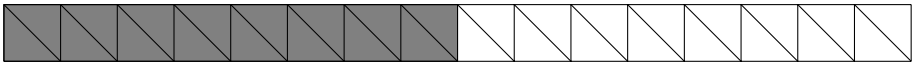

Figure 6.3: Split of a 32-triangle region in the x-direction into two local regions of size 16.

Algorithm 6.2 Outlier-detection algorithm for multiwavelet coefficients on triangular meshes, using local vectors.

for all $\ell = 1,\ldots,N_k$ **do**
  for all $m = 1,2,3$ **do**
    for all $i = 0,\ldots,2^n-1$ **do**
      Form troubled-cell indication vector $\mathbf{D}_{\ell i}^{m,n-1}$ consisting of multiwavelet coefficients $\tilde{d}_{\ell\lambda}^{m,n-1}$, where $\lambda = (i,j,M)$, with $j = 0,\ldots,2^n-1, M = 1,2$ (definition 6.1).

      Apply Algorithm 4.2 on page 61.
    end for
    for all $j = 0,\ldots,2^n-1$ **do**
      Form troubled-cell indication vector $\mathbf{D}_{\ell j}^{m,n-1}$ consisting of multiwavelet coefficients $\tilde{d}_{\ell\lambda}^{m,n-1}$, where $\lambda = (i,j,M)$, with $i = 0,\ldots,2^n-1, M = 1,2$ (definition 6.1).

      Apply Algorithm 4.2 on page 61.
    end for
  end for
end for
Label an element as troubled if it is detected in any application of Algorithm 4.2.

6.6. NUMERICAL RESULTS

In this section, some preliminary numerical results are shown for which the multiwavelet troubled-cell indicator has been tested [140]. The tests are done for examples based on the advection equation on $[0,1]\times[0,1]$, given by

$$u_t + \nabla\cdot(\mathbf{v}u) = 0.$$

Here, $\mathbf{v} = (v_1, v_2)^\top$ is the velocity vector, and $u = u(x,y,t)$ is the unknown quantity to be resolved.

The first set of test cases uses the linear advection equation, with a diagonally-direct-

ed velocity: $\mathbf{v} = \sqrt{2}/2 \cdot (1,1)^\top$. The following smooth initial conditions are used:

$$u_0^1(x,y) = \sin(2\pi x), \quad u_0^2(x,y) = \sin(2\pi y), \quad u_0^3(x,y) = \sin(2\pi(x+y)),$$

as well as the discontinuous initial conditions,

$$u_0^4 = \begin{cases} 1, \text{ if } x \geq 0.5, \\ 0, \text{ else,} \end{cases} \quad u_0^5 = \begin{cases} 1, \text{ if } y \geq 0.5, \\ 0, \text{ else,} \end{cases} \quad u_0^6 = \begin{cases} 1, \text{ if } x+y \geq 1, \\ 0, \text{ else,} \end{cases}$$

$$u_0^7 = \begin{cases} 1, \text{ if } x-y \leq 0, \\ 0, \text{ else,} \end{cases} \quad u_0^8 = \begin{cases} 1, \text{ if } (x-0.5)^2 + (y-0.5)^2 \leq 0.1, \\ 0, \text{ else,} \end{cases}$$

together with periodic boundary conditions. The exact solution of this boundary-value problem is equal to $u^i(x,y,t) = u_0^i(x - v_1 t, y - v_2 t)$, $i = 1,\ldots,8$. This means that the initial function should be recovered at the final time $T = \sqrt{2}$ [88]. Note that the relation between multiwavelet coefficients and jumps over element boundaries (as found in earlier chapters) is not known yet. These tests in many different directions (horizontal, vertical, diagonal in two directions, and circular) are performed to obtain more information about possible relations.

The final test case is the so-called *solid-body rotation problem*, where the velocity equals $\mathbf{v} = (y - 0.5, -x + 0.5)^\top$, the initial condition is taken equal to

$$u_0^9(x,y) = \begin{cases} 1, \text{ if } (x-0.4)^2 + (y-0.6)^2 \leq 0.05, \\ 0, \text{ else,} \end{cases}$$

and homogeneous Dirichlet boundary conditions are applied. In this test case, the initial condition is rotating through the domain. At final time $T = 2\pi$, the initial function should be recovered.

In the examples, the multiwavelet troubled-cell indicator is applied both using the parameter C, and with the outlier-detection approach. The vertex-based limiter (Section 2.2.2, [85]) is applied only to the detected elements. For the tests, the Matlab code of Hesthaven and Warburton is used [68], which is extended to the advection equation together with the vertex-based limiter by Raees et al. [106].

6.6.1. DETECTION ON INITIAL CONDITIONS

In order to investigate the information gleaned from multiwavelets on structured triangular meshes, in this section we first study the indicators applied to initial conditions in a DG basis. We then test the multiwavelet indication method at the final time of the approximation for the advection equation.

Figure 6.4 contains the results for the smooth functions u_0^i, $i = 1,2,3$. Here, the parameter-based multiwavelet troubled-cell indicator clearly detects the steepest gradients of the sine waves, whereas the outlier-detection approach applied to the multiwavelet coefficients detects few elements. Only for the diagonal sine wave (Figure 6.4(i)), several elements close to the boundary of the domain are detected. This can be explained by inspecting the corresponding multiwavelet coefficients (Figure 6.9). It is remarkable that more than half of the multiwavelet coefficients $\tilde{d}_{1\lambda}^{3,n-1}$ and $\tilde{d}_{3\lambda}^{3,n-1}$ equals zero (Figures 6.9(g) and 6.9(i), respectively). If a local vector of size 16 contains at least

ten zeros, then the bounds for detection are equal to zero (see equation (4.2)), such that all elements with nonzero coefficients are detected. This leads to Figure 6.4(i). Application of the outlier-detection algorithm to the rest of the multiwavelet coefficients in Figure 6.9 does not cause any detection.

Since the functions in Figure 6.4 are smooth, the outlier-detection results are preferred to the parameter-based results.

Figures 6.5 and 6.6 depict the results for the discontinuous initial conditions. Both indication techniques clearly detect the discontinuities. Note that the discontinuities of the circular waves in Figure 6.6 are more pronounced using the outlier-detection approach than using the parameter-based troubled-cell indicator.

In Figures 6.7–6.15, the multiwavelet coefficients corresponding to the different initial conditions are visualized. Clearly, the multiwavelet coefficients can be used to distinguish between smooth and nonsmooth regions. However, a clear meaning of the coefficients (as is the case in one and (tensor-product) two dimensions) is difficult to establish.

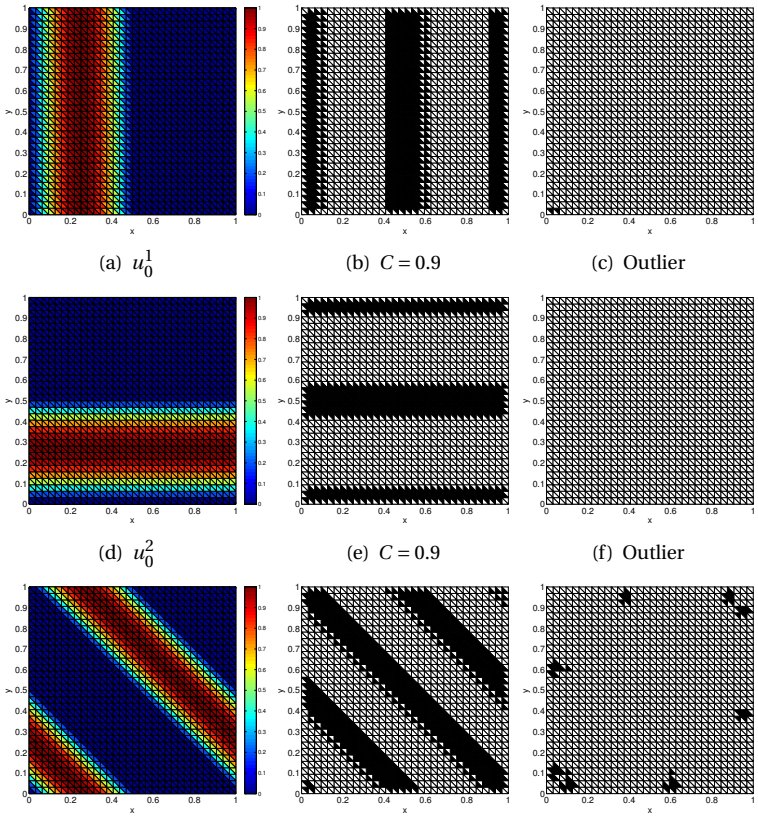

(a) u_0^1 (b) $C = 0.9$ (c) Outlier

(d) u_0^2 (e) $C = 0.9$ (f) Outlier

(g) u_0^3 (h) $C = 0.9$ (i) Outlier

Figure 6.4: Initial conditions (first column) and corresponding detected troubled cells, using the parameter-based multiwavelet troubled-cell indicator (second column) or outlier detection on the multiwavelet coefficients (third column), structured triangular mesh based on 32×32 rectangles, $k = 1$.

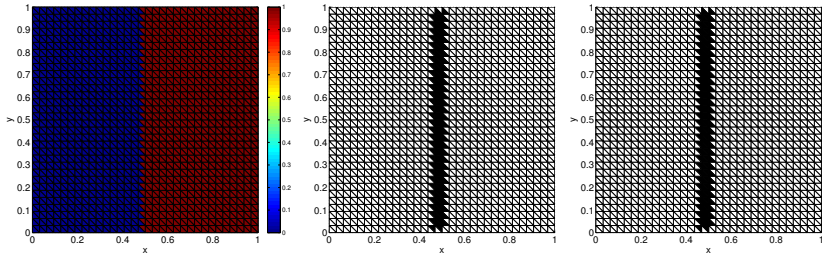

(a) u_0^4 (b) $C = 0.9$ (c) Outlier

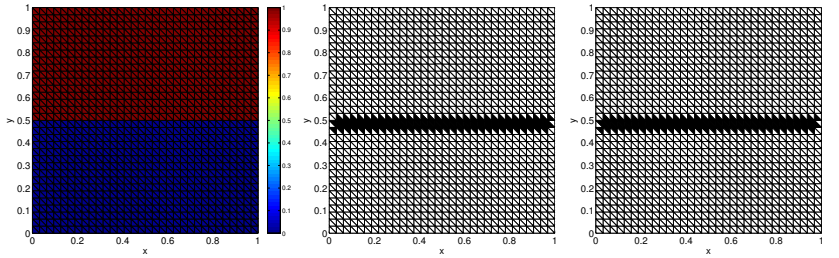

(d) u_0^5 (e) $C = 0.9$ (f) Outlier

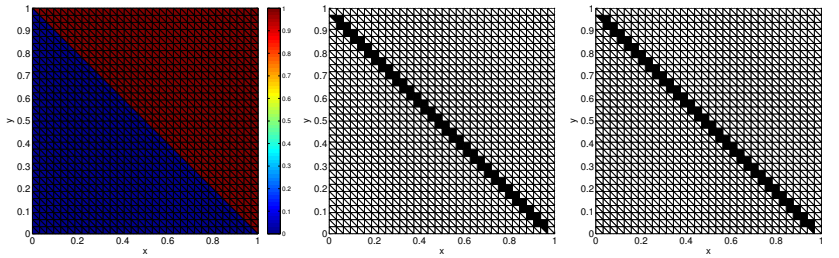

(g) u_0^6 (h) $C = 0.9$ (i) Outlier

Figure 6.5: Initial conditions (first column) and corresponding detected troubled cells, using the parameter-based multiwavelet troubled-cell indicator (second column) or outlier detection on the multiwavelet coefficients (third column), structured triangular mesh based on 32×32 rectangles, $k = 1$.

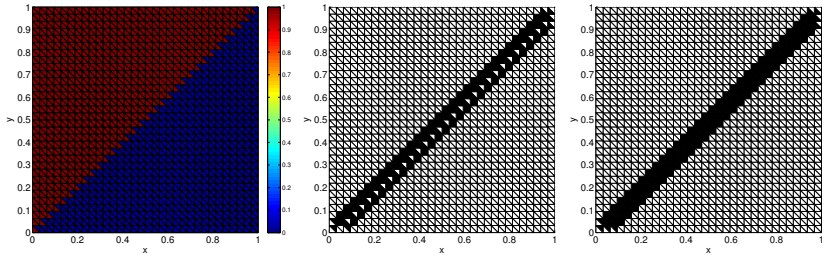

(a) u_0^7 (b) $C = 0.9$ (c) Outlier

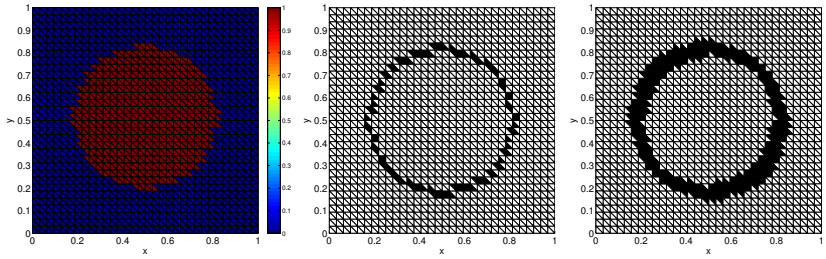

(d) u_0^8 (e) $C = 0.9$ (f) Outlier

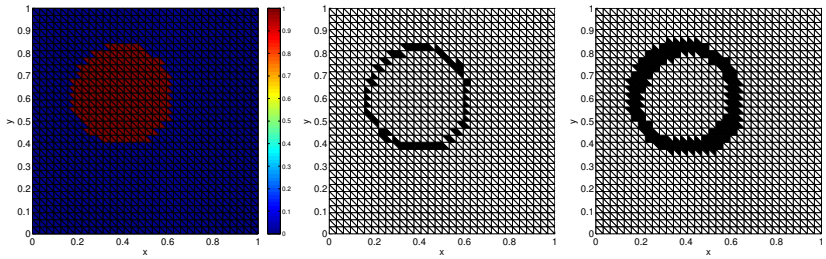

(g) u_0^9 (h) $C = 0.9$ (i) Outlier

Figure 6.6: Initial conditions (first column) and corresponding detected troubled cells, using the parameter-based multiwavelet troubled-cell indicator (second column) or outlier detection on the multiwavelet coefficients (third column), structured triangular mesh based on 32×32 rectangles, $k = 1$.

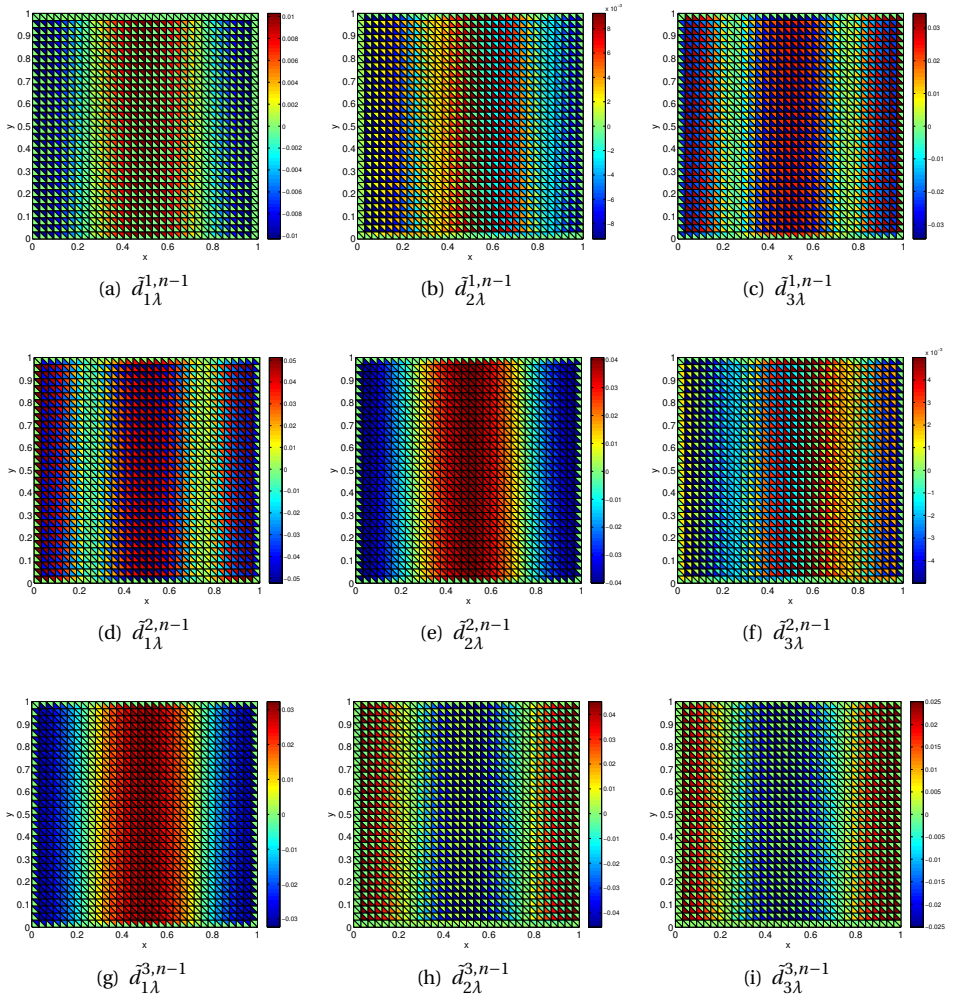

(a) $\tilde{d}_{1\lambda}^{1,n-1}$ (b) $\tilde{d}_{2\lambda}^{1,n-1}$ (c) $\tilde{d}_{3\lambda}^{1,n-1}$

(d) $\tilde{d}_{1\lambda}^{2,n-1}$ (e) $\tilde{d}_{2\lambda}^{2,n-1}$ (f) $\tilde{d}_{3\lambda}^{2,n-1}$

(g) $\tilde{d}_{1\lambda}^{3,n-1}$ (h) $\tilde{d}_{2\lambda}^{3,n-1}$ (i) $\tilde{d}_{3\lambda}^{3,n-1}$

Figure 6.7: Multiwavelet coefficients corresponding to u_0^1, structured triangular mesh based on 32×32 rectangles, $k = 1$.

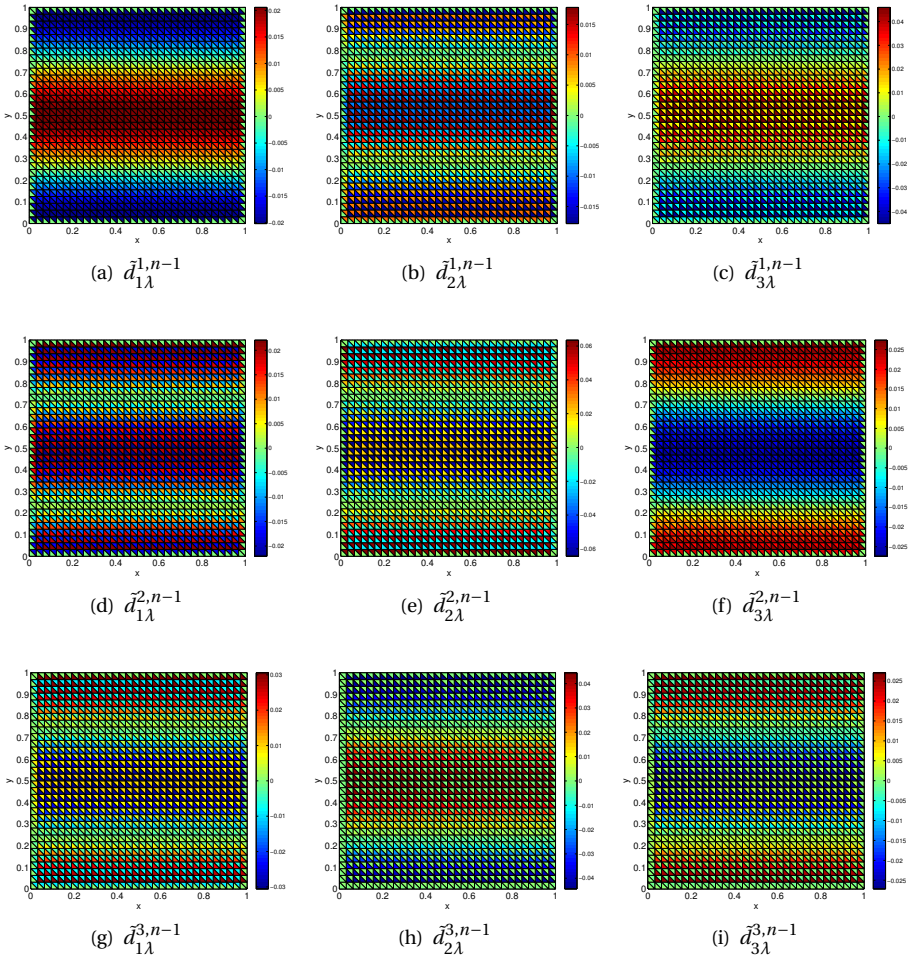

(a) $\tilde{d}_{1\lambda}^{1,n-1}$ (b) $\tilde{d}_{2\lambda}^{1,n-1}$ (c) $\tilde{d}_{3\lambda}^{1,n-1}$

(d) $\tilde{d}_{1\lambda}^{2,n-1}$ (e) $\tilde{d}_{2\lambda}^{2,n-1}$ (f) $\tilde{d}_{3\lambda}^{2,n-1}$

(g) $\tilde{d}_{1\lambda}^{3,n-1}$ (h) $\tilde{d}_{2\lambda}^{3,n-1}$ (i) $\tilde{d}_{3\lambda}^{3,n-1}$

Figure 6.8: Multiwavelet coefficients corresponding to u_0^2, structured triangular mesh based on 32×32 rectangles, $k = 1$.

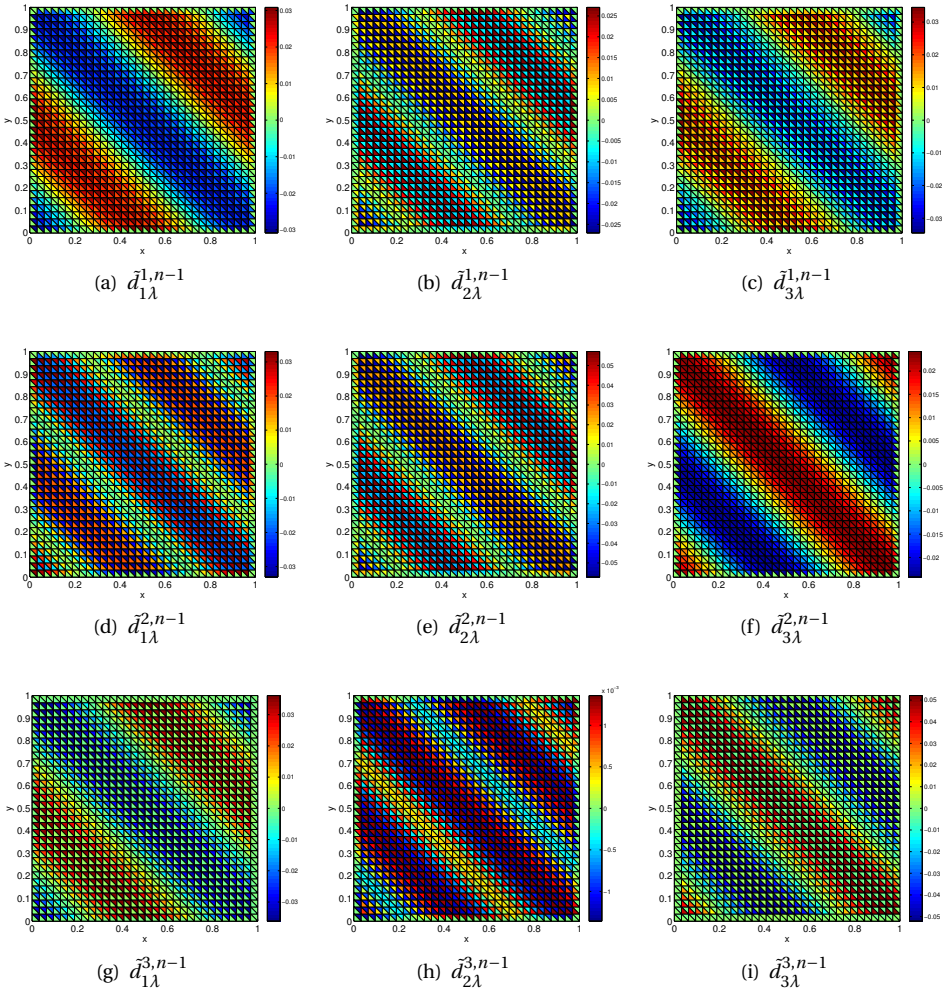

(a) $\tilde{d}_{1\lambda}^{1,n-1}$ (b) $\tilde{d}_{2\lambda}^{1,n-1}$ (c) $\tilde{d}_{3\lambda}^{1,n-1}$

(d) $\tilde{d}_{1\lambda}^{2,n-1}$ (e) $\tilde{d}_{2\lambda}^{2,n-1}$ (f) $\tilde{d}_{3\lambda}^{2,n-1}$

(g) $\tilde{d}_{1\lambda}^{3,n-1}$ (h) $\tilde{d}_{2\lambda}^{3,n-1}$ (i) $\tilde{d}_{3\lambda}^{3,n-1}$

Figure 6.9: Multiwavelet coefficients corresponding to u_0^3, structured triangular mesh based on 32×32 rectangles, $k = 1$. The detected troubled-cells by the outlier-detection algorithm in Figure 6.4(i) are caused by the coefficients $\tilde{d}_{1\lambda}^{3,n-1}$ and $\tilde{d}_{3\lambda}^{3,n-1}$.

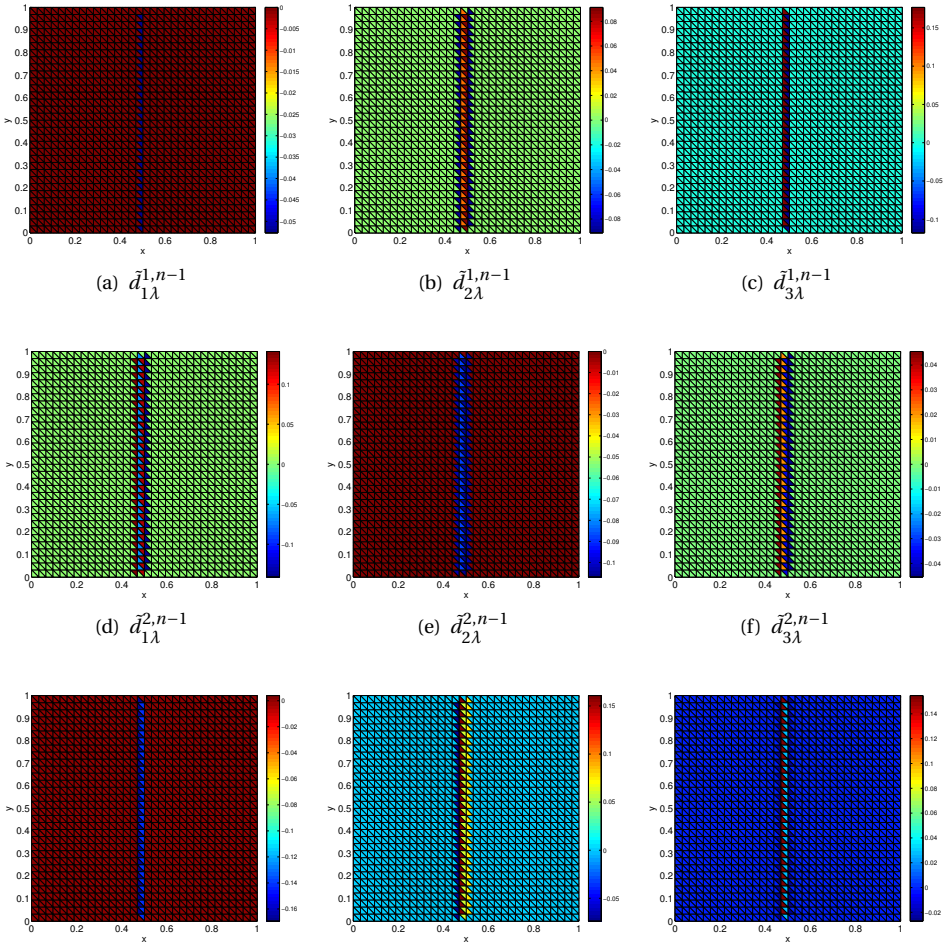

(a) $\tilde{d}_{1\lambda}^{1,n-1}$ (b) $\tilde{d}_{2\lambda}^{1,n-1}$ (c) $\tilde{d}_{3\lambda}^{1,n-1}$

(d) $\tilde{d}_{1\lambda}^{2,n-1}$ (e) $\tilde{d}_{2\lambda}^{2,n-1}$ (f) $\tilde{d}_{3\lambda}^{2,n-1}$

(g) $\tilde{d}_{1\lambda}^{3,n-1}$ (h) $\tilde{d}_{2\lambda}^{3,n-1}$ (i) $\tilde{d}_{3\lambda}^{3,n-1}$

Figure 6.10: Multiwavelet coefficients corresponding to u_0^4, structured triangular mesh based on 32×32 rectangles, $k = 1$.

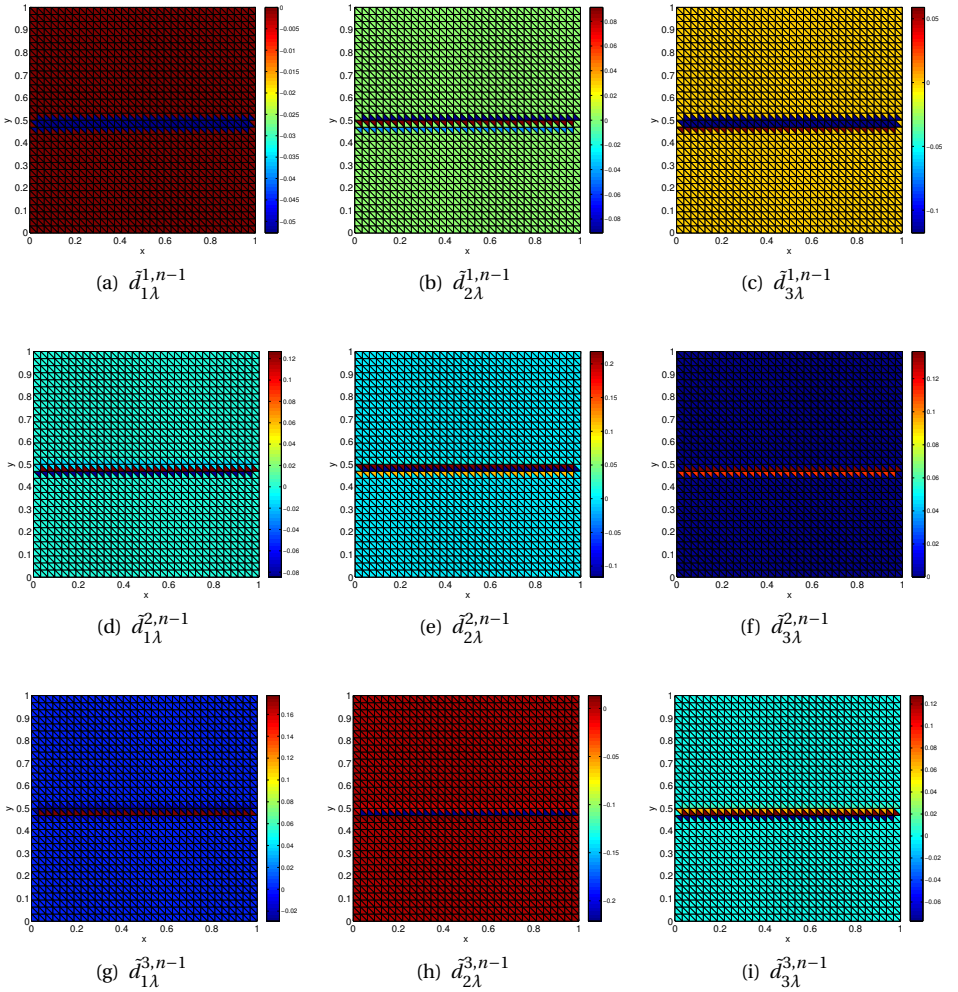

(a) $\tilde{d}_{1\lambda}^{1,n-1}$ (b) $\tilde{d}_{2\lambda}^{1,n-1}$ (c) $\tilde{d}_{3\lambda}^{1,n-1}$

(d) $\tilde{d}_{1\lambda}^{2,n-1}$ (e) $\tilde{d}_{2\lambda}^{2,n-1}$ (f) $\tilde{d}_{3\lambda}^{2,n-1}$

(g) $\tilde{d}_{1\lambda}^{3,n-1}$ (h) $\tilde{d}_{2\lambda}^{3,n-1}$ (i) $\tilde{d}_{3\lambda}^{3,n-1}$

Figure 6.11: Multiwavelet coefficients corresponding to u_0^5, structured triangular mesh based on 32×32 rectangles, $k = 1$.

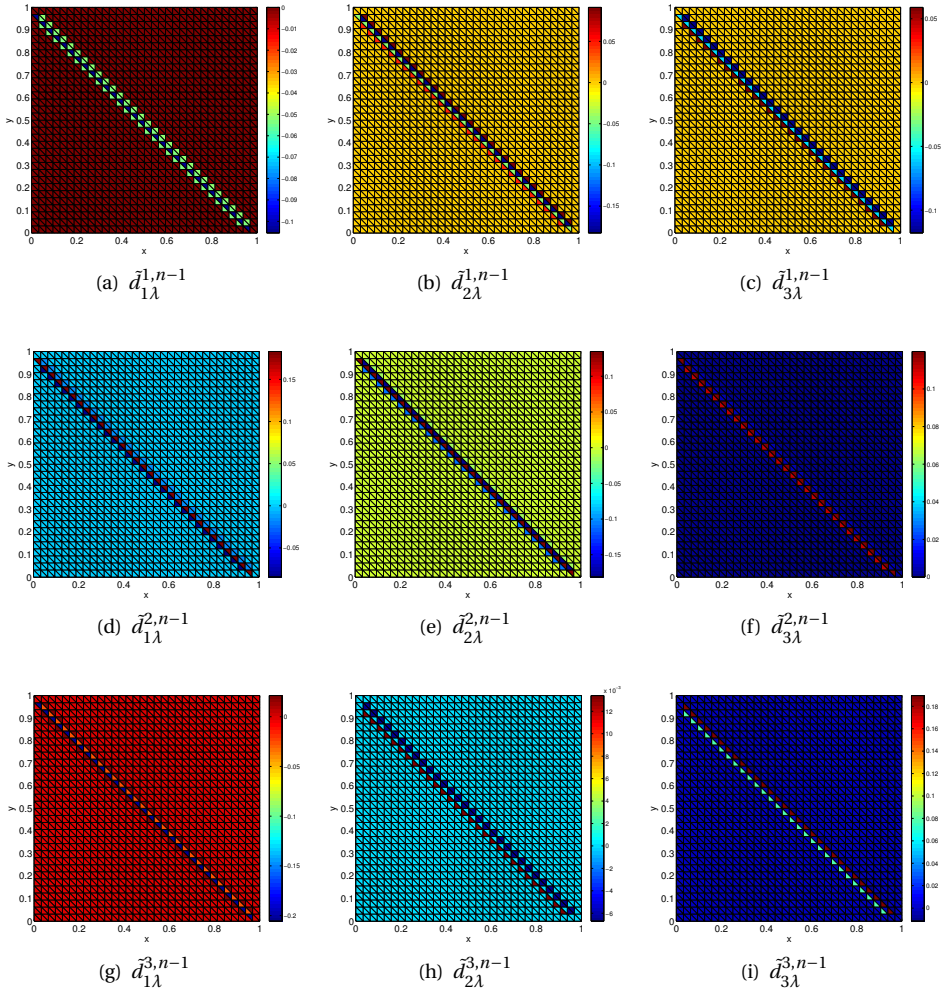

(a) $\tilde{d}_{1\lambda}^{1,n-1}$ (b) $\tilde{d}_{2\lambda}^{1,n-1}$ (c) $\tilde{d}_{3\lambda}^{1,n-1}$

(d) $\tilde{d}_{1\lambda}^{2,n-1}$ (e) $\tilde{d}_{2\lambda}^{2,n-1}$ (f) $\tilde{d}_{3\lambda}^{2,n-1}$

(g) $\tilde{d}_{1\lambda}^{3,n-1}$ (h) $\tilde{d}_{2\lambda}^{3,n-1}$ (i) $\tilde{d}_{3\lambda}^{3,n-1}$

Figure 6.12: Multiwavelet coefficients corresponding to u_0^6, structured triangular mesh based on 32×32 rectangles, $k = 1$.

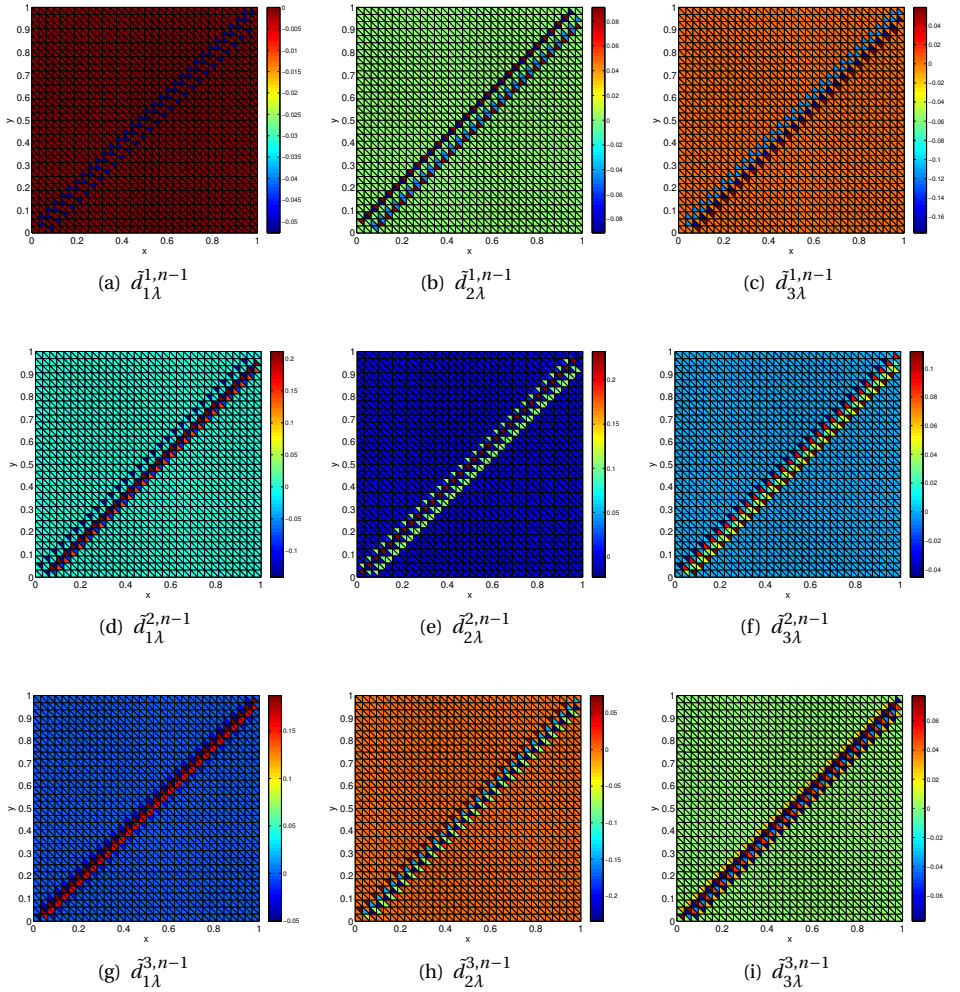

(a) $\tilde{d}_{1\lambda}^{1,n-1}$ (b) $\tilde{d}_{2\lambda}^{1,n-1}$ (c) $\tilde{d}_{3\lambda}^{1,n-1}$

(d) $\tilde{d}_{1\lambda}^{2,n-1}$ (e) $\tilde{d}_{2\lambda}^{2,n-1}$ (f) $\tilde{d}_{3\lambda}^{2,n-1}$

(g) $\tilde{d}_{1\lambda}^{3,n-1}$ (h) $\tilde{d}_{2\lambda}^{3,n-1}$ (i) $\tilde{d}_{3\lambda}^{3,n-1}$

Figure 6.13: Multiwavelet coefficients corresponding to u_0^7, structured triangular mesh based on 32×32 rectangles, $k = 1$.

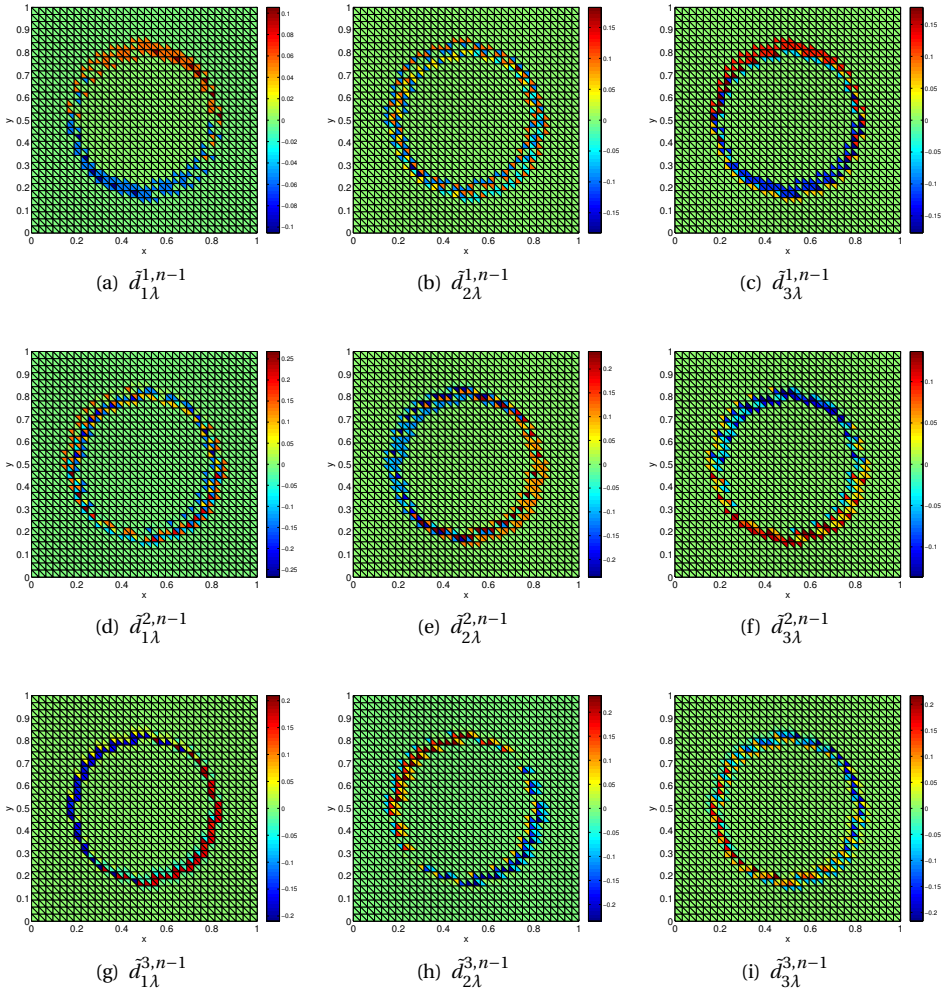

(a) $\tilde{d}_{1\lambda}^{1,n-1}$ (b) $\tilde{d}_{2\lambda}^{1,n-1}$ (c) $\tilde{d}_{3\lambda}^{1,n-1}$

(d) $\tilde{d}_{1\lambda}^{2,n-1}$ (e) $\tilde{d}_{2\lambda}^{2,n-1}$ (f) $\tilde{d}_{3\lambda}^{2,n-1}$

(g) $\tilde{d}_{1\lambda}^{3,n-1}$ (h) $\tilde{d}_{2\lambda}^{3,n-1}$ (i) $\tilde{d}_{3\lambda}^{3,n-1}$

Figure 6.14: Multiwavelet coefficients corresponding to u_0^8, structured triangular mesh based on 32×32 rectangles, $k = 1$.

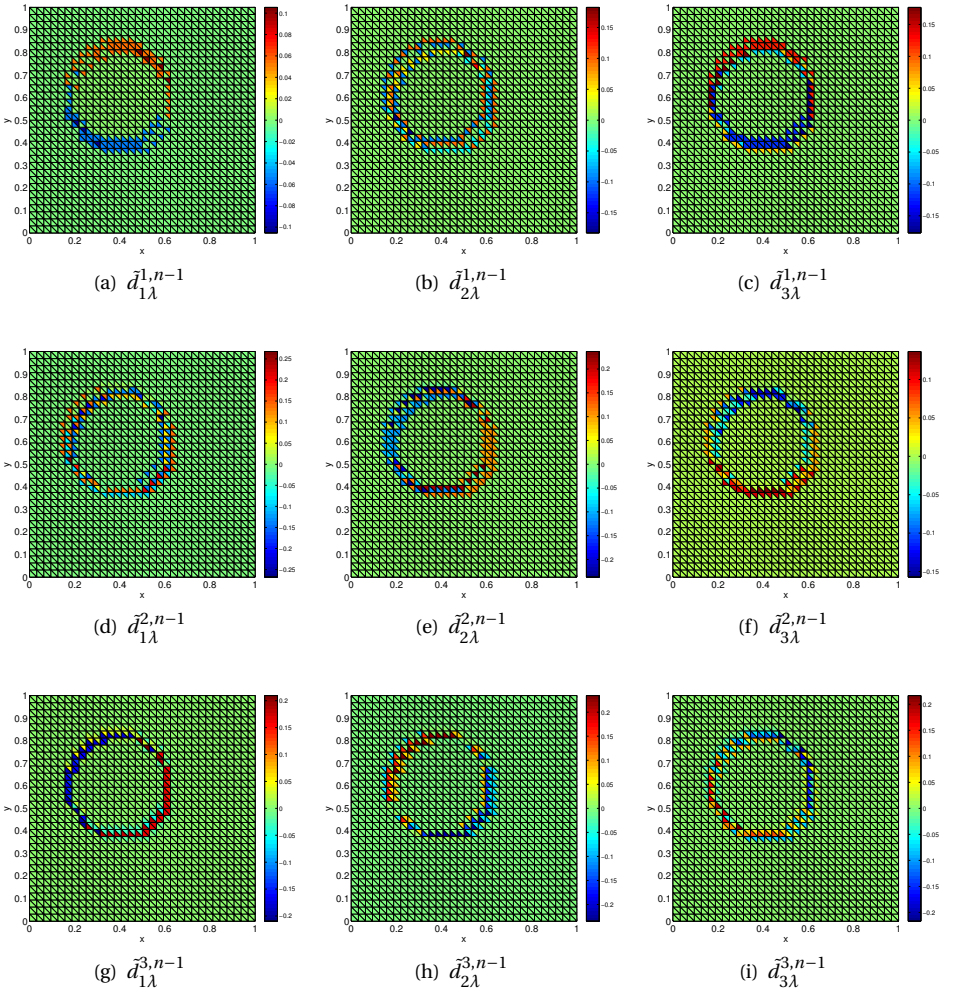

(a) $\tilde{d}_{1\lambda}^{1,n-1}$ (b) $\tilde{d}_{2\lambda}^{1,n-1}$ (c) $\tilde{d}_{3\lambda}^{1,n-1}$

(d) $\tilde{d}_{1\lambda}^{2,n-1}$ (e) $\tilde{d}_{2\lambda}^{2,n-1}$ (f) $\tilde{d}_{3\lambda}^{2,n-1}$

(g) $\tilde{d}_{1\lambda}^{3,n-1}$ (h) $\tilde{d}_{2\lambda}^{3,n-1}$ (i) $\tilde{d}_{3\lambda}^{3,n-1}$

Figure 6.15: Multiwavelet coefficients corresponding to u_0^9, structured triangular mesh based on 32×32 rectangles, $k = 1$.

6.6.2. DETECTION AT FINAL TIME

In this section, the approximations and detected troubled-cells are shown at the final time $T = \sqrt{2}$ for initial conditions u_0^i, $i = 1,\ldots,8$, and $T = 2\pi$ for u_0^9. Note that the exact solution equals the initial condition at these times.

The multiwavelet troubled-cell indicator is applied using either the parameter-based method or the outlier-detection approach (for which a problem-dependent parameter is not necessary). For the parameter-based method, the vertex-based limiter is applied only in the detected elements [85]. The outlier-detection scheme, however, turned out to only be stable if the limiter is also applied to all boundary elements. These elements are not always detected by the outlier scheme and are therefore not marked as such in the figures. Similar boundary problems were also observed in [53], where it was proposed to either use an adaptive mesh with more triangles near the boundary or ignore the boundary triangles for certain resolution levels.

The results for the smooth initial conditions are shown in Figure 6.16. For the sine wave in the x-direction and the diagonal direction (based on u_0^1 and u_0^3), the parameter-based multiwavelet troubled-cell indicator detects the steepest gradients. However, the results for the sine wave in the y-direction (corresponding to u_0^2) are quite different: almost no elements are detected, except for the bottom-left corner and the center of the domain (Figure 6.16(g)). It is expected that this is due to the alignment of the wave compared to the mesh, as well as the diagonal velocity that is used. Note that the one-dimensional pattern of the sine wave in the x-direction is also broken in the vicinity of the domain center (Figure 6.16(c)). It seems as if there is a small error in the numerical implementation of the boundary conditions (which are in a pre-existing code used by the author). However, the troubled-cell indicator performs well: the numerical artifacts are detected as troubled.

The outlier-detection algorithm detects few elements for the smooth functions. Only close to the boundary some elements are detected (see discussion in Section 6.6.1).

The results for the discontinuous functions can be inspected in Figures 6.17 and 6.18. Both the parameter-based indicator and the outlier-detection indicator select the horizontal and vertical discontinuities corresponding to u_0^4 and u_0^5 (Figures 6.17(c), 6.17(d), 6.17(g) and 6.17(h)). Furthermore, the parameter-based indicator does select the diagonal discontinuity belonging to u_0^6 in Figure 6.17(k), but detects few elements near the boundary discontinuities of that approximation. However, the outlier-detection approach detects the discontinuities near the boundaries as well (Figure 6.17(l)).

It should be noticed that in the current setup, both indicators are not able to detect the diagonal discontinuity of u_0^7 (Figure 6.18(c) and 6.18(d)). Both approaches (partly) detect elements near the boundary of the domain, where the approximation is also discontinuous. For the parameter-based indicator, the value of C should be chosen smaller to include all discontinuous regions. The use of $C = 0.5$, for example, leads to the detection of the correct elements (Figure 6.19(a)).

Considering the outlier-detection algorithm: inspection of the multiwavelet coefficients at the final time reveals that the discontinuous region is spread out wide, and therefore the local region of size 16 is too small to contain both continuous and discontinuous regions. At certain locations, all coefficients in a local vector belong to a discontinuous region, and therefore the fences are wide enough such that no elements are

detected. In Figure 6.19(b) local regions of size 32 are used instead of size 16. This partly solves the problem. Further research is needed to understand which outlier-detection strategy should be used.

The parameter-based results for the circular wave in combination with the linear advection equation (Figure 6.18(g)) are much better than for the solid-body rotation problem (Figure 6.18(k)). Apparently, a smaller value of C should be taken to detect the discontinuities of the rotating body sharply. The outlier-detection method detects more elements near the circular waves (Figures 6.18(h) and 6.18(l)) but is not as sharp as we expect compared to results for the quadrilateral mesh case [139]. Also here, the troubled zone is spread too much, such that the fences for detection are wide enough for the troubled cells not to be detected. The use of a wider stencil for local vectors will improve the method.

6.7. CONCLUDING REMARKS

In this chapter, the multiwavelet decomposition for structured triangular meshes has been given. Inspection of the multiwavelet coefficients reveals that they are very useful to detect nonsmooth regions in the underlying function. However, it is not yet known which coefficients are most useful for indication. Therefore, the troubled-cell indicators introduced in this chapter use all coefficients for detection. One indicator uses a problem-depending parameter, and the other indicator applies outlier detection to the multiwavelet coefficients, such that a problem-dependent parameter is no longer needed.

Preliminary results have been shown for different tests based on the two-dimensional advection equation. Applied to the initial conditions, both methods work well and detect the discontinuous regions accurately. The parameter-based method also selects smooth regions with steep gradients, which are not detected by the outlier-detection algorithm.

After time integration, the parameter-based troubled-cell indicator detects the correct features if a suitable choice for the parameter is made. The outlier-detection method gives good results, but for a diagonal square wave and a circular wave, it seems as if the optimal size of the local vectors is no longer equal to 16.

Although the formal relation between the DG approximation and multiwavelet coefficients is known, more research should be done to recognize which multiwavelet coefficient measures which feature of the underlying function. Also, an improvement of the outlier-detection strategy is needed to detect the correct regions in the diagonal square wave and the circular waves after time integration. Furthermore, tests for nonlinear PDEs such as the two-dimensional Euler equations, and comparisons with the KXRCF shock detector and the minmod-based TVB indicator should be performed to thoroughly test the applicability of multiwavelets and outlier detection for troubled-cell indication on triangular meshes.

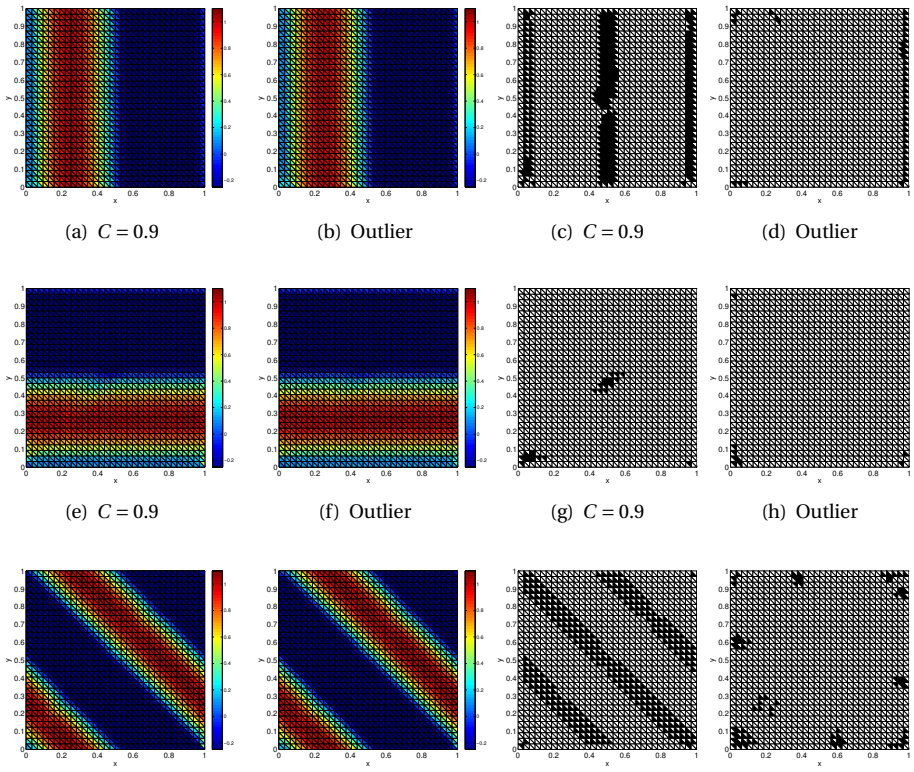

(a) $C = 0.9$ (b) Outlier (c) $C = 0.9$ (d) Outlier

(e) $C = 0.9$ (f) Outlier (g) $C = 0.9$ (h) Outlier

(i) $C = 0.9$ (j) Outlier (k) $C = 0.9$ (l) Outlier

Figure 6.16: Final-time approximations and corresponding detected troubled cells using initial conditions u_0^1 (first row), u_0^2 (second row), and u_0^3 (third row), using the parameter-based multiwavelet troubled-cell indicator or outlier detection on the multiwavelet coefficients, $T = \sqrt{2}$, structured triangular mesh based on 32×32 rectangles, $k = 1$.

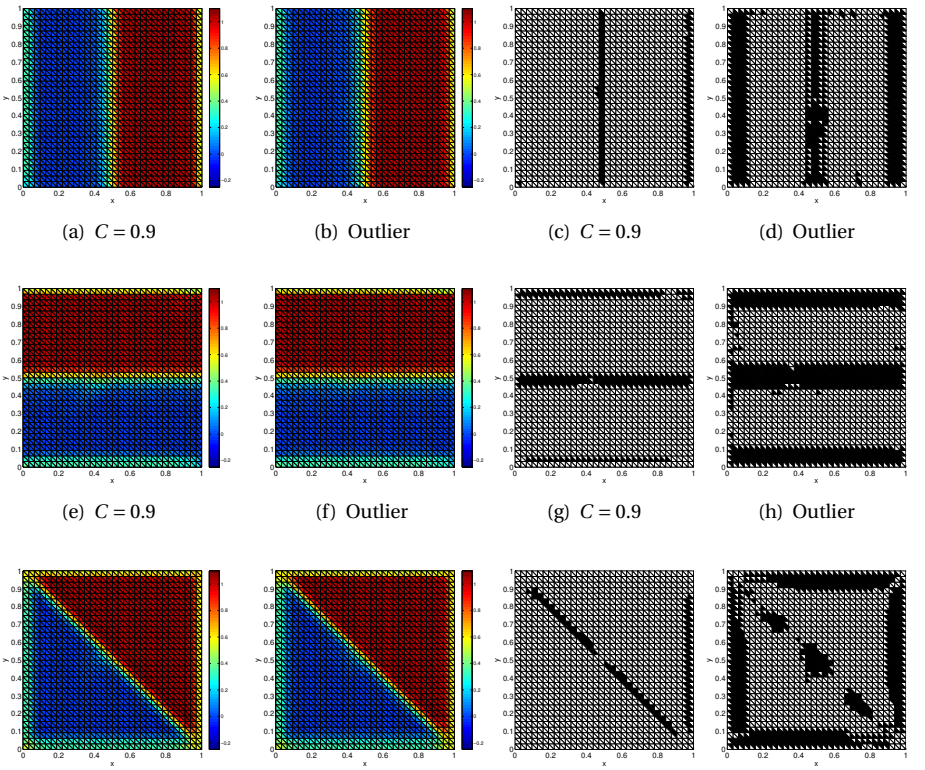

(a) $C = 0.9$ (b) Outlier (c) $C = 0.9$ (d) Outlier

(e) $C = 0.9$ (f) Outlier (g) $C = 0.9$ (h) Outlier

(i) $C = 0.9$ (j) Outlier (k) $C = 0.9$ (l) Outlier

Figure 6.17: Final-time approximations and corresponding detected troubled cells using initial conditions u_0^4 (first row), u_0^5 (second row), and u_0^6 (third row), using the parameter-based multiwavelet troubled-cell indicator or outlier detection on the multiwavelet coefficients, $T = \sqrt{2}$, structured triangular mesh based on 32×32 rectangles, $k = 1$.

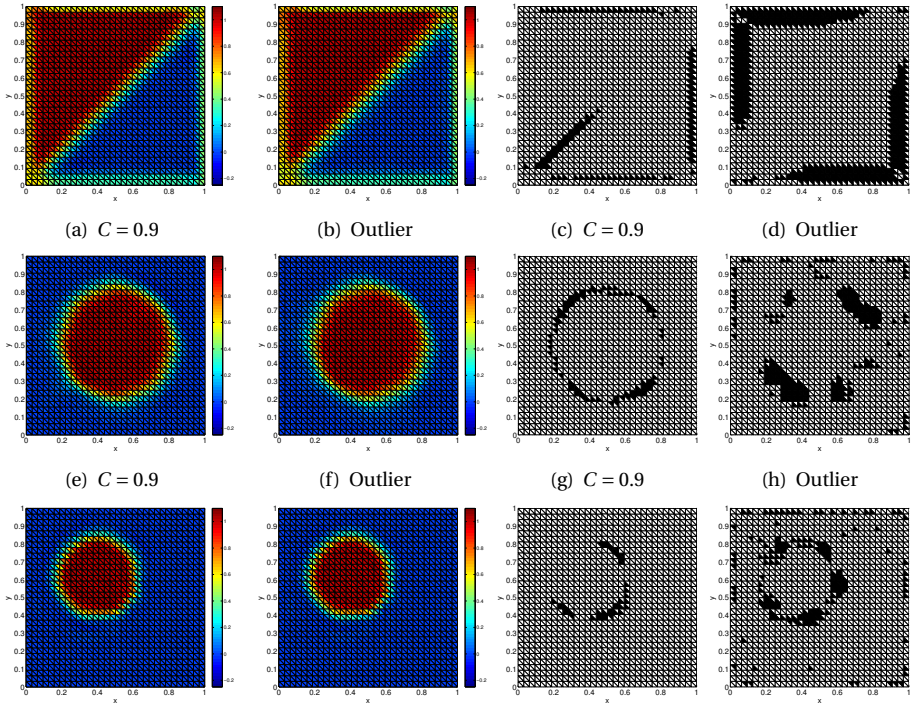

(a) $C = 0.9$ (b) Outlier (c) $C = 0.9$ (d) Outlier

(e) $C = 0.9$ (f) Outlier (g) $C = 0.9$ (h) Outlier

(i) $C = 0.9$ (j) Outlier (k) $C = 0.9$ (l) Outlier

Figure 6.18: Final-time approximations and corresponding detected troubled cells using initial conditions u_0^7 (first row), u_0^8 (second row), and u_0^9 (third row), using the parameter-based multiwavelet troubled-cell indicator or outlier detection on the multiwavelet coefficients, $T = \sqrt{2}$ for u_0^7 and u_0^8 and $T = 2\pi$ for u_0^9, structured triangular mesh based on 32×32 rectangles, $k = 1$.

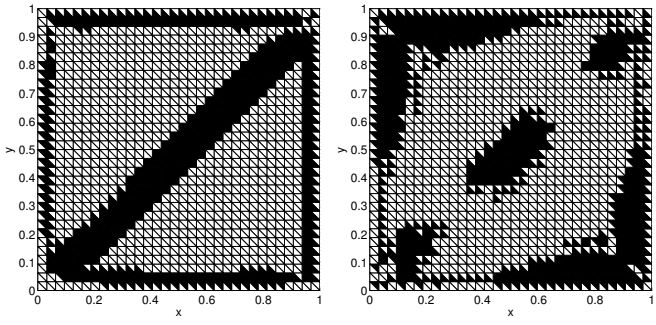

(a) $C = 0.5$ (b) Outlier, local vectors of size 32

Figure 6.19: Final-time detected troubled cells using initial condition u_0^7, using the parameter-based multiwavelet troubled-cell indicator or outlier detection on the multiwavelet coefficients, $T = \sqrt{2}$, structured triangular mesh based on 32×32 rectangles, $k = 1$.

7

CONCLUSIONS

In this dissertation, three research objectives have been addressed: the construction of a troubled-cell indicator based on multiwavelets to detect discontinuous regions in a DG approximation; the development of a method to remove problem-dependent parameters in troubled-cell indicators; and the investigation of the applicability of the troubled-cell indicators to irregular meshes. In this chapter, the conclusions for each objective are given.

7.1. MULTIWAVELET TROUBLED-CELL INDICATOR

In the first part of this dissertation, the use of multiwavelets for troubled-cell indication in one dimension and (tensor-product) two dimensions has been investigated. Chapter 3 contains a proof of the exact relation between multiwavelet coefficients on the highest decomposition level and the jumps in (derivatives of) the DG approximation. This relation makes it possible to use multiwavelet coefficients as a troubled-cell indicator: they suddenly increase in the neighborhood of a discontinuity in the approximation. The multiwavelet troubled-cell indicator detects an element as troubled if the corresponding multiwavelet coefficient is large enough in absolute value. This is tested by comparing the coefficient to the maximum coefficient (in absolute value) over the domain. Here, a parameter is required to define the strictness of the indicator.

The indicator has been tested for several problems based on the Euler equations in one and two dimensions. In the detected troubled cells, a limiter has been applied. The numerical results clearly show that a smaller parameter value leads to the detection of more elements. If a suitable value for the parameter is used, then the indicator works generally better than the KXRCF and Harten's shock detector. The smallest percentage of detected troubled cells is found together with a nonoscillatory approximation.

In the two-dimensional tensor-product case, the detector is able to distinguish between nonsmooth regions in the x-, y-, or diagonal directions. Therefore, the indicator can be used to select specific features in the approximation.

7.2. OUTLIER-DETECTION STRATEGY

Another area of investigation was the choice of parameters for troubled-cell indication. Each troubled-cell indicator requires a threshold parameter that should be chosen according to the test problem that is used. We found out that for each troubled-cell indicator, the sudden increase or decrease in the indication value with respect to neighboring values is important for detection. This led to the construction of a new outlier-detection technique based on a boxplot mechanism. Detection occurs when the indication value of a certain element differs significantly from the neighboring values (Chapter 4). With this technique, the problem-dependent parameter from the original indicators is no longer necessary as the parameter is chosen automatically. This outlier-detection technique not only applies to the multiwavelet troubled-cell indicator but can be applied to every troubled-cell indication value. Hence, different indication techniques are tested, comparing the parameter-based method to the outlier-detection approach in one and two dimensions. We found that the outlier-detection approach works well and generally better than the original parameter-based indicators. Both the weak and the strong shock regions have been detected, whereas smooth regions have not been selected. Since there is no need to tune a parameter depending on the problem, the method is very easy to apply.

7.3. IRREGULAR MESHES

Additionally, we investigated the extension of the multiwavelet troubled-cell indicator to irregular meshes in one dimension (Chapter 5), using techniques that are based on multiwavelet ideas. This was not straightforward since the multiwavelet theory is based on uniform meshes. A new multiwavelet-type basis has been constructed that can represent the DG approximation exactly. Also here, the 'multiwavelet' coefficients on the highest level are related to the jumps in (derivatives of) the DG approximation. In addition to the original outlier-detection strategy, two different techniques have been studied. The first option was to weight the indication value by the mesh width; the second approach was to use a sliding-window technique.

Tests have been performed for different problems based on the Euler equations, using a smoothly-varying or a random mesh. Here, different troubled-cell indicators have been applied, both in the parameter-based form and combined with outlier detection. The parameter-based methods work well as long as a suitable value for the parameter is chosen. The outlier-detection results are promising: accurate results are found without the need to choose a problem-dependent parameter. However, for some applications, many elements are detected in smooth regions. More research should be done to improve the method. Weighting the indication values or sliding-window techniques do not work well enough to proceed in that direction.

In two dimensions, irregularity in both directions leads to a rectangular mesh that is not related to tensor products. In that case, it is very difficult to design a multiresolution structure. This part is left for future research, and structured triangular meshes were first investigated.

7.4. STRUCTURED TRIANGULAR MESHES

Finally, an extension of the multiwavelet theory to structured triangular meshes has been investigated (Chapter 6). Inspection of the multiwavelet coefficients reveals that they are very useful for discontinuity detection, but the information that each multiwavelet coefficient provides is not yet fully understood. Both a parameter-based and an outlier-detection multiwavelet troubled-cell indicator have been constructed for this type of meshes.

The indicators have been tested on different problems using the two-dimensional advection equation. Applied to the initial conditions, both the parameter-based method and the outlier-detection technique work very well. The parameter-based method also detects steep gradients in smooth regions of the functions. The outlier-detection technique does not label these regions as troubled.

After time integration, the parameter-based method detects the correct elements if a suitable value for the parameter is chosen. The outlier-detection method works well for most examples, but if the troubled zone is spread out too wide, then local vectors of a larger size than 16 should be used.

8

RECOMMENDATIONS

Many interesting features of troubled-cell indicators remain to be investigated in the future. In this chapter, general recommendations for future research are presented. More specific recommendations have already been given in the earlier chapters.

8.1. MULTIWAVELETS

First of all, the properties of a multiwavelet expansion should be fully understood for different types of meshes. For irregular meshes, the correct multiwavelet space should be constructed, probably with the help of supercompact multiwavelets [6], or Alpert's multiwavelet algorithm [4]. It could also be that the projection of the DG approximation to a uniform mesh and the usual procedure for multiwavelet decomposition should be used.

For a two-dimensional tensor-product mesh, it could be valuable to investigate the use of genuinely two-dimensional multiwavelets for detection [56].

For structured triangular meshes, the meaning of each multiwavelet coefficient is not yet fully understood. More research is needed to link the coefficients to specific features of the underlying function.

8.2. PARAMETER FOR MULTIWAVELET TROUBLED-CELL INDICATION

Another research topic is concerned with the need to improve the parameter choice in the original multiwavelet troubled-cell indicator. This could, for example, be achieved using the decay of the DG coefficients for smooth functions [102], which might be related to the number of DG coefficients at which the moment limiter acts.

Another option is to use the cancelation property for multiwavelet coefficients [40]. This idea has already been used in a threshold for the construction of adaptive meshes [55, 56], and might also relate to the severity of the shocks.

Finally, the mean of the coefficients over the domain could be used as a threshold for detection [46].

8.3. OUTLIER DETECTION

The current outlier-detection algorithm is constructed for a mesh consisting of 2^n elements. This number is important since nonoverlapping local vectors of length 16 are used. Spatial information is included by the comparison of detected outliers with the fences of the neighboring regions. Future work will be to improve upon the performance in identifying local structures of the approximation, for example, by including the local spatial information in the statistical approach. This could be achieved using contour boxplots [143]. This technique could also be useful for meshes with a different number of elements, and for irregular meshes.

In two dimensions, the one-dimensional outlier-detection algorithm is currently applied in the x- and y-direction separately. The construction of a two-dimensional algorithm is of great importance. This could also help to improve the performance of the outlier-detection technique for structured triangular meshes.

8.4. EXTRA

Other research interests include the extension to irregular triangular meshes [17], spherical and cylindrical coordinate systems, the relation between the Fourier transform and multiwavelet coefficients, and speeding up the computations.

REFERENCES

[1] R. Abgrall. Multiresolution analysis on unstructured meshes: Applications to CFD. In B.N. Chetverushkin et al., editor, *Experimentation, Modelling and Computation in Flow, Turbulence and Combustion: Volume 2*. John Wiley & Sons, 1997. (Cited on page 4.)

[2] R. Abgrall and A. Harten. Multiresolution Representation in Unstructured Meshes. *SIAM Journal on Numerical Analysis*, 35(6):2128–2146, 1998. (Cited on page 5.)

[3] S. Adjerid, K.D. Devine, J.E. Flaherty, and L. Krivodonova. A posteriori error estimation for discontinuous Galerkin solutions of hyperbolic problems. *Computer Methods in Applied Mechanics and Engineering*, 191(11-12):1097–1112, 2002. (Cited on page 15.)

[4] B.K. Alpert. A Class of Bases in L^2 for the Sparse Representation of Integral Operators. *SIAM Journal on Mathematical Analysis*, 24(1):246–262, 1993. (Cited on pages 5, 6, 19, 21, 32, 39, 82, and 135.)

[5] B.K. Alpert, G. Beylkin, D. Gines, and L. Vozovoi. Adaptive Solution of Partial Differential Equations in Multiwavelet Bases. *Journal of Computational Physics*, 182:149–190, 2002. (Cited on pages 5, 17, 23, and 24.)

[6] S. Amat and M. Moncayo. Non-uniform multiresolution analysis with supercompact multiwavelets. *Journal of Computational and Applied Mathematics*, 235(1):334–340, 2010. (Cited on pages 6, 7, 82, and 135.)

[7] F. Aràndiga, R. Donat, and A. Harten. Multiresolution based on weighted averages of the hat function I: Linear reconstruction techniques. *SIAM Journal on Numerical Analysis*, 36(1):160–203, 1998. (Cited on page 4.)

[8] R.K. Archibald, G.I. Fann, and W.A. Shelton. Adaptive discontinuous Galerkin methods in multiwavelets bases. *Applied Numerical Mathematics*, 61(7):879–890, 2011. (Cited on pages 5, 10, 17, and 23.)

[9] A.Z. Averbuch and V.A. Zheludev. Lifting Scheme for Biorthogonal Multiwavelets Originated from Hermite Splines. *IEEE Transactions on Signal Processing*, 50(3):487–500, 2002. (Cited on page 6.)

[10] R.M. Beam and R.F. Warming. Multiresolution Analysis and Supercompact Multiwavelets. *SIAM Journal on Scientific Computing*, 22(4):1238–1268, 2000. (Cited on pages 6, 7, and 82.)

[11] J.J. Benedetto and A.I. Zayed, editors. *Sampling, Wavelets, and Tomography*. Applied and Numerical Harmonic Analysis. Birkhäuser, Boston, 2004. (Cited on page 6.)

[12] B.L. Bihari. Multiresolution Schemes for Conservation Laws with Viscosity. *Journal of Computational Physics*, 123(1):207–225, 1996. (Cited on page 4.)

[13] B.L. Bihari and A. Harten. Application of generalized wavelets: An adaptive multiresolution scheme. *Journal of Computational and Applied Mathematics*, 61:275–321, 1995. (Cited on page 4.)

[14] B.L. Bihari and A. Harten. Multiresolution Schemes for the Numerical Solution of 2-D Conservation Laws I. *SIAM Journal on Scientific Computing*, 18(2):315–354, 1997. (Cited on page 4.)

[15] B.L. Bihari, D.K. Ota, Z. Liu, and S.V. Ramakrishnan. Multiresolution Method on General Unstructured Meshes. *AIAA paper*, 40(7):1323–1330, 2002. (Cited on page 4.)

[16] R. Biswas, K.D. Devine, and J.E. Flaherty. Parallel, adaptive finite element methods for conservation laws. *Applied Numerical Mathematics*, 14:255–283, 1994. (Cited on pages 4 and 16.)

[17] G.-P. Bonneau. Multiresolution Analysis on Irregular Surface Meshes. *IEEE Transactions on Visualization and Computer Graphics*, 4(4):365–378, 1998. (Cited on page 136.)

[18] R. Bürger, R. Ruiz, and K. Schneider. Fully adaptive multiresolution schemes for strongly degenerate parabolic equations with discontinuous flux. *Journal of Engineering Mathematics*, 60(3):365–385, 2008. (Cited on page 5.)

[19] R. Bürger, R. Ruiz, K. Schneider, and M.A. Sepúlveda. Fully adaptive multiresolution schemes for strongly degenerate parabolic equations in one space dimension. *ESAIM: Mathematical Modelling and Numerical Analysis*, 42(4):535–563, 2008. (Cited on page 5.)

[20] C.S. Burrus, R.A. Gopinath, and H. Guo. *Introduction to Wavelets and Wavelet Transforms: A Primer*. Prentice-Hall, New Jersey, first edition, 1998. (Cited on page 18.)

[21] J.L. Díaz Calle, P.R.B. Devloo, and S.M. Gomes. Wavelets and adaptive grids for the discontinuous Galerkin method. *Numerical Algorithms*, 39(1):143–154, 2005. (Cited on page 5.)

[22] J.M. Carnicer, W. Dahmen, and J.M. Peña. Local Decomposition of Refinable Spaces and Wavelets. *Applied and Computational Harmonic Analysis*, 3:127–153, 1996. (Cited on pages 4 and 6.)

[23] M.H. Carpenter and C.A. Kennedy. Fourth-Order 2N-Storage Runge-Kutta Schemes. Technical Report 109112, NASA Langley Research Center, 1994. (Cited on page 105.)

[24] A.S. Cavaretta, W. Dahmen, and C.A. Micchelli. *Stationary Subdivision*, volume 453 of *Memoirs of the American Mathematical Society*. American Mathematical Society, Boston, 1991. (Cited on page 4.)

[25] V. Chandola. *Anomaly Detection for Symbolic Sequences and Time Series Data*. PhD thesis, University of Minnesota, 2009. (Cited on page 87.)

[26] G. Chiavassa and R. Donat. Point Value Multiscale Algorithms for 2D Compressible Flows. *SIAM Journal on Scientific Computing*, 23(3):805–823, 2001. (Cited on page 4.)

[27] B. Cockburn. An Introduction to the Discontinuous Galerkin Method for Convection-Dominated Problems. In *Advanced Numerical Approximation of Nonlinear Hyperbolic Equations*, volume 1697 of *Lecture Notes in Mathematics*, pages 151–268. Springer Berlin Heidelberg, 1998. (Cited on pages 4, 7, 10, 12, and 104.)

[28] B. Cockburn, S. Hou, and C.-W. Shu. The Runge-Kutta Local Projection Discontinuous Galerkin Finite Element Method for Conservation Laws IV: The multidimensional case. *Mathematics of Computation*, 54(190):545–581, 1990. (Cited on pages 4, 10, and 12.)

[29] B. Cockburn, S.-Y. Lin, and C.-W. Shu. TVB Runge-Kutta Local Projection Discontinuous Galerkin Finite Element Method for Conservation Laws III: One-Dimensional Systems. *Journal of Computational Physics*, 84:90–113, 1989. (Cited on pages 4, 10, 16, 56, and 88.)

[30] B. Cockburn and C.-W. Shu. TVB Runge-Kutta Local Projection Discontinuous Galerkin Finite Element Method for Conservation Laws II: General Framework. *Mathematics of Computation*, 52(186):411–435, 1989. (Cited on pages 3, 4, 10, 16, 56, 63, and 88.)

[31] B. Cockburn and C.-W. Shu. The Runge-Kutta Discontinuous Galerkin Method for Conservation Laws V: Multidimensional Systems. *Journal of Computational Physics*, 141(2):199–224, 1998. (Cited on pages 4, 7, 10, 12, 13, 16, 104, and 110.)

[32] A. Cohen. Wavelet Methods in Numerical Analysis. In P.G. Ciarlet and J.L. Lions, editors, *Handbook of Numerical Analysis*, volume 7 of *Handbook of Numerical Analysis*, pages 417–711. Elsevier, Amsterdam, 2000. (Cited on page 4.)

[33] A. Cohen, I. Daubechies, and J.-C. Feauveau. Biorthogonal Bases of Compactly Supported Wavelets. *Communications on Pure and Applied Mathematics*, 45(5):485–560, 1992. (Cited on page 4.)

[34] A. Cohen, N. Dyn, S.M. Kaber, and M. Postel. Multiresolution Schemes on Triangles for Scalar Conservation Laws. *Journal of Computational Physics*, 161:264–286, 2000. (Cited on page 4.)

[35] A. Cohen, S.M. Kaber, S. Müller, and M. Postel. Fully Adaptive Multiresolution Finite Volume Schemes for Conservation Laws. *Mathematics of Computation*, 72(241):183–225, 2003. (Cited on page 5.)

[36] F. Coquel, Y. Maday, S. Müller, M. Postel, and Q.H. Tran. New trends in multiresolution and adaptive methods for convection-dominated problems. In F. Coquel,

Y. Maday, S. Müller, M. Postel, and Q.H. Tran, editors, *Multiresolution and Adaptive Methods for Convection-Dominated Problems*, volume 29, pages 1–7. EDP Sciences, 2009. (Cited on page 5.)

[37] F. Coquel, M. Postel, N. Poussineau, and Q.H. Tran. Multiresolution technique and explicit-implicit scheme for multicomponent flows. *Journal of Numerical Mathematics*, 14(3):187–216, 2006. (Cited on page 5.)

[38] B. Costa and W.-S. Don. Multi-domain hybrid spectral-WENO methods for hyperbolic conservation laws. *Journal of Computational Physics*, 224(2):970–991, 2007. (Cited on pages 3 and 5.)

[39] S. Curtis, R.M. Kirby, J.K. Ryan, and C.-W. Shu. Postprocessing for the Discontinuous Galerkin Method over Nonuniform Meshes. *SIAM Journal on Scientific Computing*, 30(1):272–289, 2007. (Cited on page 80.)

[40] W. Dahmen. Wavelet methods for PDEs — some recent developments. *Journal of Computational and Applied Mathematics*, 128(1-2):133–185, 2001. (Cited on pages 24, 25, 110, and 135.)

[41] W. Dahmen, B. Gottschlich–Müller, and S. Müller. Multiresolution schemes for conservation laws. *Numerische Mathematik*, 88(3):399–443, 2001. (Cited on pages 4 and 80.)

[42] W. Dahmen, A. Kunoth, and K. Urban. Biorthogonal Spline Wavelets on the Interval — Stability and Moment Conditions. *Applied and Computational Harmonic Analysis*, 6:132–196, 1999. (Cited on page 4.)

[43] I. Daubechies, I. Guskov, P. Schröder, and W. Sweldens. Wavelets on irregular point sets. *Philosophical Transactions of The Royal Society of London A*, 357:2397–2413, 1999. (Cited on pages 5, 6, and 80.)

[44] I. Daubechies and W. Sweldens. Factoring Wavelet Transforms into Lifting Steps. *The Journal of Fourier Analysis and Applications*, 4(3):247–269, 1998. (Cited on page 6.)

[45] M.O. Domingues, O. Roussel, and K. Schneider. On space-time adaptive schemes for the numerical solution of PDEs. *ESAIM: Proceedings*, 16:181–194, 2007. (Cited on page 5.)

[46] W.-S. Don, Z. Gao, P. Li, and X. Wen. Hybrid Compact-WENO Finite Difference Scheme with Conjugate Fourier Shock Detection Algorithm for Hyperbolic Conservation Laws. *SIAM Journal on Scientific Computing*, 38(2):A691–A711, 2016. (Cited on page 136.)

[47] F. Dubeau, S. Elmejdani, and R. Ksantini. Non-uniform Haar wavelets. *Applied Mathematics and Computation*, 159(3):675–693, 2004. (Cited on page 6.)

[48] M. Dubiner. Spectral methods on triangles and other domains. *Journal of Scientific Computing*, 6(4):345–390, 1991. (Cited on page 107.)

[49] M. Dumbser, O. Zanotti, R. Loubère, and S. Diot. *A posteriori* subcell limiting of the discontinuous Galerkin finite element method for hyperbolic conservation laws. *Journal of Computational Physics*, 278:47–75, 2014. (Cited on page 4.)

[50] N. Dyn. Subdivision Schemes in Computer-Aided Geometric Design. In W.A. Light, editor, *Advances in Numerical Analysis*, Oxford, 1991. Clarendon Press. (Cited on page 4.)

[51] S.A.E.G. Falle, S.S. Komissarov, and P. Joarder. A multidimensional upwind scheme for magnetohydrodynamics. *Monthly Notices of the Royal Astronomical Society*, 297(1):265–277, 1998. (Cited on page 66.)

[52] M.A. Fortes and M. Moncayo. Multiresolution analysis and supercompact multiwavelets for surfaces. *Mathematics and Computers in Simulation*, 81(10):2129–2149, 2011. (Cited on pages 7, 102, and 110.)

[53] M.A. Fortes and M.L. Rodríguez. Non-uniform multiresolution analysis for surfaces and applications. *Applied Numerical Mathematics*, 75:123–135, 2014. (Cited on page 125.)

[54] M. Frigge, D.C. Hoaglin, and B. Iglewicz. Some Implementations of the Boxplot. *The American Statistician*, 43(1):50–54, 1989. (Cited on pages 57 and 59.)

[55] N. Gerhard, F. Iacono, G. May, S. Müller, and R. Schäfer. A High-Order Discontinuous Galerkin Discretization with Multiwavelet-Based Grid Adaptation for Compressible Flows. *Journal of Scientific Computing*, 62:25–52, 2015. (Cited on pages 5, 10, 26, 50, and 135.)

[56] N. Gerhard and S. Müller. Adaptive multiresolution discontinuous Galerkin schemes for conservation laws: multi-dimensional case. *Computational and Applied Mathematics*, 35:321–349, 2016. (Cited on pages 5, 7, 82, 107, 110, and 135.)

[57] S.S. Goh, Q. Jiang, and T. Xia. Construction of Biorthogonal Multiwavelets Using the Lifting Scheme. *Applied and Computational Harmonic Analysis*, 9(3):336–352, 2000. (Cited on page 6.)

[58] S. Gottlieb and C.-W. Shu. Total Variation Diminishing Runge-Kutta Schemes. *Mathematics of Computation*, 67(221):73–85, 1998. (Cited on page 12.)

[59] S. Gottlieb, C.-W. Shu, and E. Tadmor. Strong Stability-Preserving High-Order Time Discretization Methods. *SIAM Review*, 43(1):89–112, 2001. (Cited on page 12.)

[60] B. Gottschlich–Müller. *Multiscale Schemes for Conservation Laws*. PhD thesis, RWTH Aachen University, 1998. (Cited on page 80.)

[61] B. Gottschlich–Müller and S. Müller. Adaptive Finite Volume Schemes for Conservation Laws Based on Local Multiresolution Techniques. In M. Fey and R. Jeltsch, editors, *Hyperbolic Problems: Theory, Numerics, Applications*, volume 129 of *International Series of Numerical Mathematics*, pages 385–394. Birkhäuser, 1999. (Cited on page 5.)

[62] B. Gottschlich-Müller and S. Müller. On Multi-Scale Concepts for Multi-Dimensional Conservation Laws. In W. Hackbusch and G. Wittum, editors, *Numerical Treatment of Multi-scale Problems*, pages 119–133. Vieweg, 1999. (Cited on page 4.)

[63] A. Harten. ENO schemes with Subcell Resolution. *Journal of Computational Physics*, 83:148–184, 1989. (Cited on pages 4, 14, and 62.)

[64] A. Harten. Discrete multi-resolution analysis and generalized wavelets. *Applied Numerical Mathematics*, 12:153–193, 1993. (Cited on page 4.)

[65] A. Harten. Adaptive Multiresolution Schemes for Shock Computations. *Journal of Computational Physics*, 115(2):319–338, 1994. (Cited on pages 3 and 5.)

[66] A. Harten. Multiresolution Algorithms for the Numerical Solution of Hyperbolic Conservation Laws. *Communications on Pure and Applied Mathematics*, 48:1305–1342, 1995. (Cited on pages 3, 5, and 37.)

[67] A. Harten. Multiresolution Representation of Data: A General Framework. *SIAM Journal on Numerical Analysis*, 33(3):1205–1256, 1996. (Cited on page 4.)

[68] J.S. Hesthaven and T. Warburton. *Nodal Discontinuous Galerkin Methods: Algorithms, Analysis, and Applications*, volume 54 of *Texts in Applied Mathematics*. Springer, New York, 2008. (Cited on pages 1, 7, 12, 41, 44, 47, 104, 105, 107, and 112.)

[69] D.C. Hoaglin, B. Iglewicz, and J.W. Tukey. Performance of Some Resistant Rules for Outlier Labeling. *Journal of the American Statistical Association*, 81(396):991–999, 1986. (Cited on pages 57 and 59.)

[70] D.C. Hoaglin, F. Mosteller, and J.W. Tukey. *Understanding Robust and Exploratory Data Analysis*. Wiley series in probability and mathematical statistics. Wiley, first edition, 1983. (Cited on page 57.)

[71] N. Hovhannisyan, S. Müller, and R. Schäfer. Adaptive Multiresolution Discontinuous Galerkin Schemes for Conservation Laws. Report 311, Institut für Geometrie und Praktische Mathematik, Aachen, sep 2010. http://www.igpm.rwth-aachen.de/forschung/preprints2010. (Cited on pages 10, 19, and 32.)

[72] N. Hovhannisyan, S. Müller, and R. Schäfer. Adaptive multiresolution discontinuous Galerkin schemes for conservation laws. *Mathematics of Computation*, 83(285):113–151, 2014. (Cited on pages 5, 25, and 26.)

[73] M. Hubert and E. Vandervieren. An adjusted boxplot for skewed distributions. *Computational Statistics & Data Analysis*, 52:5186–5201, 2008. (Cited on page 59.)

[74] W.-L. Hung and M.-S. Yang. An omission approach for detecting outliers in fuzzy regression models. *Fuzzy Sets and Systems*, 157:3109–3122, 2006. (Cited on page 59.)

[75] F. Iacono, G. May, S. Müller, and R. Schäfer. A High-Order Discontinuous Galerkin Discretization with Multiwavelet-Based Grid Adaptation for Compressible Flows. Technical Report AICES-2011/08-02, Aachen Institute for Advanced Study in Computational Engineering Science, Aachen, aug 2011. http://www.aices.rwth-aachen.de/preprints. (Cited on pages 23 and 26.)

[76] D. Jizheng. *Fundamentals of Wavelets*. WIT Press, first edition, 2012. (Cited on page 6.)

[77] M.K. Kaibara and S.M. Gomes. A Fully Adaptive Multiresolution Scheme for Shock Computations. In E.F. Toro, editor, *Godunov methods: Theory and Applications*, pages 497–503. Springer US, 2001. (Cited on page 5.)

[78] F. Keinert. *Wavelets and Multiwavelets*. Studies in Advanced Mathematics. Chapman and Hall/CRC, Florida, 2004. (Cited on pages 3, 6, and 18.)

[79] D.I. Ketcheson, C.B. Macdonald, and S. Gottlieb. Optimal implicit strong stability preserving Runge-Kutta methods. *Applied Numerical Mathematics*, 59:373–392, 2009. (Cited on page 12.)

[80] T. Koornwinder. Two-Variable Analogues of the Classical Orthogonal Polynomials. In R. Askey, editor, *Theory and Application of Special Functions*, pages 435–495. Elsevier BV, 1975. (Cited on page 107.)

[81] L. Krivodonova. Limiters for high-order discontinuous Galerkin methods. *Journal of Computational Physics*, 226:879–896, 2007. (Cited on pages 2, 4, 13, and 88.)

[82] L. Krivodonova and J.E. Flaherty. Error estimation for discontinuous Galerkin solutions of two-dimensional hyperbolic problems. *Advances in Computational Mathematics*, 19:57–71, 2003. (Cited on page 15.)

[83] L. Krivodonova, J. Xin, J.-F. Remacle, N. Chevaugeon, and J.E. Flaherty. Shock detection and limiting with discontinuous Galerkin methods for hyperbolic conservation laws. *Applied Numerical Mathematics*, 48:323–338, 2004. (Cited on pages 3, 4, 15, 40, 41, 56, 63, 88, and 110.)

[84] P. Kumar and E. Foufoula-Georgiou. Wavelet analysis for geophysical applications. *Reviews of Geophysics*, 35(4):385–412, 1997. (Cited on page 57.)

[85] D. Kuzmin. A vertex-based hierarchical slope limiter for p-adaptive discontinuous Galerkin methods. *Journal of Computational and Applied Mathematics*, 233(12):3077–3085, 2010. (Cited on pages 4, 13, 14, 112, and 125.)

[86] P.D. Lax. Weak Solutions of Nonlinear Hyperbolic Equations and Their Numerical Computation. *Communications on Pure and Applied Mathematics*, 7:159–193, 1954. (Cited on pages 29, 43, and 64.)

[87] R.J. LeVeque. *Numerical Methods for Conservation Laws*. Lectures in Mathematics. Birkhäuser Verlag, Basel, second edition, 1992. (Cited on page 28.)

[88] R.J. LeVeque. *Finite Volume Methods for Hyperbolic Problems*. Cambridge Texts in Applied Mathematics. Cambridge University Press, New York, sixth edition, 2002. (Cited on pages 2, 11, 28, 51, and 112.)

[89] X. Li. *Smoothness-Increasing Accuracy-Conserving Filters for Discontinuous Galerkin Methods: Challenging the Assumptions of Symmetry and Uniformity*. PhD thesis, Delft University of Technology, 2015. (Cited on pages 80 and 81.)

[90] J. Maes and A. Bultheel. Stability analysis of biorthogonal multiwavelets whose duals are not in L_2 and its application to local semiorthogonal lifting. *Applied Numerical Mathematics*, 58(8):1186–1211, 2008. (Cited on page 6.)

[91] S. Mallat. *A Wavelet Tour of Signal Processing*. Academic Press, second edition, 1998. (Cited on pages 3, 6, 7, 27, 36, 37, 40, and 51.)

[92] Median. `http://en.wikipedia.org/wiki/Median`, July 2016. (Cited on page 58.)

[93] A. Meister, S. Ortleb, T. Sonar, and M. Wirz. An extended Discontinuous Galerkin and Spectral Difference Method with modal filtering. *ZAMM - Journal of Applied Mathematics and Mechanics / Zeitschrift für Angewandte Mathematik und Mechanik*, 93(6-7):459–464, 2013. (Cited on page 7.)

[94] S. Müller. *Adaptive Multiscale Schemes for Conservation Laws*, volume 27 of *Lecture Notes on Computational Science and Engineering*. Springer, 2003. (Cited on pages 5 and 6.)

[95] S. Müller. Multiresolution schemes for conservation laws. In R.A. DeVore and A. Kunoth, editors, *Multiscale, Nonlinear and Adaptive Approximation*, pages 379–408. Springer-Verlag Berlin Heidelberg, 2009. (Cited on page 5.)

[96] S. Müller and Y. Stiriba. Fully Adaptive Multiscale Schemes for Conservation Laws Employing Locally Varying Time Stepping. *Journal of Scientific Computing*, 30(3):493–531, 2007. (Cited on page 5.)

[97] D. Nagel. Effiziente Konstruktion von Multiwavelets auf nicht uniformen dyadischen Gitterhierarchien. Master's thesis, RWTH Aachen University, 2015. (Cited on pages 7 and 82.)

[98] R.D. Nair, M.N. Levy, and P.H. Lauritzen. Emerging Numerical Methods for Atmospheric Modeling. In P.H. Lauritzen, C. Jablonowski, M.A. Taylor, and R.D. Nair, editors, *Numerical Techniques for Global Atmospheric Models*, volume 80 of *Lecture Notes in Computational Science and Engineering*, chapter 9, pages 251–311. Springer Berlin Heidelberg, 2011. (Cited on page 12.)

[99] R. Nguyen van yen, M. Farge, and K. Schneider. Wavelet regularization of a Fourier-Galerkin method for solving the 2D incompressible Euler equations. In F. Coquel, Y. Maday, S. Müller, M. Postel, and Q.H. Tran, editors, *Multiresolution and Adaptive Methods for Convection-Dominated Problems*, volume 29, pages 89–107. EDP Sciences, 2009. (Cited on page 5.)

[100] R.T. Ogden. *Essential Wavelets for Statistical Applications and Data Analysis*. Birkhäuser Basel, first edition, 1997. (Cited on page 57.)

[101] G. W. Pan. *Wavelets in Electromagnetics and Device Modeling*. Wiley series in microwave and optical engineering. Wiley, first edition, 2003. (Cited on page 6.)

[102] P.-O. Persson and J. Peraire. Sub-Cell Shock Capturing for Discontinuous Galerkin Methods. In *44th AIAA Aerospace Sciences Meeting and Exhibit*. Aerospace Sciences Meetings, American Institute of Aeronautics and Astronautics (AIAA), 2006. (Cited on page 135.)

[103] S. Pistre. Konstruktion von Multiwavelets auf nicht-uniformen eindimensionalen Gitterhierarchien. Bachelor's thesis, RWTH Aachen University, 2013. (Cited on pages 7 and 82.)

[104] J.X. Qiu and C.-W. Shu. A Comparison of Troubled-Cell Indicators for Runge-Kutta Discontinuous Galerkin Methods Using Weighted Essentially Nonoscillatory Limiters. *SIAM Journal on Scientific Computing*, 27(3):995–1013, 2005. (Cited on pages 3, 4, 14, 40, 48, 49, 51, 62, 64, and 65.)

[105] Quartile. `http://en.wikipedia.org/wiki/Quartile`, July 2016. (Cited on pages 57 and 59.)

[106] F. Raees, D.R. van der Heul, and C. Vuik. A mass-conserving level-set method for simulation of multiphase flow in geometrically complicated domains. *International Journal for Numerical Methods in Fluids*, 81(7):399–425, 2016. (Cited on page 112.)

[107] H.L. Resnikoff and Jr. R.O. Wells. *Wavelet Analysis: The Scalable Structure of Information*. Springer, first edition, 1998. (Cited on page 6.)

[108] P.L. Roe. Approximate Riemann Solvers, Parameter Vectors, and Difference Schemes. *Journal of Computational Physics*, 43:357–372, 1981. (Cited on page 16.)

[109] O. Roussel and K. Schneider. An adaptive multiresolution method for combustion problems: application to flame ball-vortex interaction. *Computers & Fluids*, 34(7):817–831, 2005. (Cited on page 5.)

[110] O. Roussel, K. Schneider, A. Tsigulin, and H. Bockhorn. A conservative fully adaptive multiresolution algorithm for parabolic PDEs. *Journal of Computational Physics*, 188(2):493–523, 2003. (Cited on pages 3 and 5.)

[111] D.K. Ruch and P.J. van Fleet. *Wavelet theory: An Elementary Approach With Applications*. Wiley, New Jersey, first edition, 2009. (Cited on page 3.)

[112] R. Schäfer. *Adaptive multiresolution discontinuous Galerkin schemes for conservation laws*. PhD thesis, RWTH Aachen University, 2011. (Cited on page 5.)

[113] F. Schröder-Pander, T. Sonar, and O. Friedrich. Generalized Multiresolution analysis on unstructured grids. *Numerische Mathematik*, 86:685–715, 2000. (Cited on page 4.)

[114] N.C. Schwertman and R. de Silva. Identifying outliers with sequential fences. *Computational Statistics & Data Analysis*, 51:3800–3810, 2007. (Cited on page 59.)

[115] N.C. Schwertman, M.A. Owens, and R. Adnan. A simple more general boxplot method for identifying outliers. *Computational Statistics & Data Analysis*, 47:165–174, 2004. (Cited on page 59.)

[116] A.B. Shelton. *A multi-resolution discontinuous Galerkin method for unsteady compressible flows*. PhD thesis, Georgia Institute of Technology, 2008. (Cited on page 107.)

[117] Shock tube. `http://www.lr.tudelft.nl/organisatie/afdelingen/aerodynamics-wind-energy-flight-performance-and-propulsion/flight-performance-and-propulsion/propulsion-and-power/research/projects/flexible-asymmetric-shock-tube/`, September 2016. (Cited on pages 1 and 2.)

[118] Shock wave. `http://history.nasa.gov/SP-60/ch-5.html`, September 2016. (Cited on pages 1 and 2.)

[119] C.-W. Shu. Total-Variation-Diminishing Time Discretizations. *SIAM Journal on Scientific and Statistical Computing*, 9(6):1073–1084, 1988. (Cited on page 12.)

[120] C.-W. Shu and S. Osher. Efficient Implementation of Essentially Non-oscillatory Shock-Capturing Schemes. *Journal of Computational Physics*, 77:439–471, 1988. (Cited on pages 4 and 12.)

[121] C.-W. Shu and S. Osher. Efficient Implementation of Essentially Non-oscillatory Shock-Capturing Schemes, II. *Journal of Computational Physics*, 83:32–78, 1989. (Cited on pages 4, 29, 46, and 64.)

[122] F. Sieglar. Konstruktion von Multiwavelets auf Dreiecksgittern. Bachelor's thesis, RWTH Aachen University, 2013. (Cited on pages 7, 107, and 109.)

[123] B. Sjögreen and H.C. Yee. Multiresolution Wavelet Based Adaptive Numerical Dissipation Control for High Order Methods. *Journal of Scientific Computing*, 20(2):211–255, 2004. (Cited on pages 5 and 38.)

[124] J. Smoller. *Shock Waves and Reaction-Diffusion Equations*, volume 258 of *Grundlehren der mathematischen Wissenschaften*. Springer-Verlag, New York, second edition, 1994. (Cited on pages 29 and 40.)

[125] G.A. Sod. A Survey of Several Finite Difference Methods for Systems of Nonlinear Hyperbolic Conservation Laws. *Journal of Computational Physics*, 27:1–31, 1978. (Cited on pages 29 and 64.)

[126] Sorting algorithm. https://en.wikipedia.org/wiki/Sorting_algorithm, July 2016. (Cited on page 75.)

[127] R. Southern, P. Marais, and E. Blake. Wavelets for Multi-resolution Analysis of Triangular Surface Meshes. Technical Report CS00-11-00, University of Cape Town, 2000. (Cited on page 7.)

[128] Space Shuttle. http://www.nasa.gov/multimedia/imagegallery/image_feature_431.html, September 2016. (Cited on pages 1 and 2.)

[129] A. Suresh and H.T. Huynh. Accurate Monotonicity-Preserving Schemes with Runge-Kutta Time Stepping. *Journal of Computational Physics*, 136:83–99, 1997. (Cited on page 4.)

[130] W. Sweldens. The Lifting Scheme: A Custom-Design Construction of Biorthogonal Wavelets. *Applied and Computational Harmonic Analysis*, 3(2):186–200, 1996. (Cited on page 6.)

[131] W. Sweldens. The Lifting Scheme: A Construction of Second Generation Wavelets. *SIAM Journal on Mathematical Analysis*, 29(2):511–546, 1998. (Cited on page 6.)

[132] H. Tang and G. Warnecke. A Runge-Kutta discontinuous Galerkin method for the Euler equations. *Computers & Fluids*, 34:375–398, 2005. (Cited on page 30.)

[133] J.W. Tukey. *Exploratory Data Analysis*. Behavioral Science: Quantitative Methods. Addison-Wesley Publishing Company, first edition, 1977. (Cited on pages 57, 59, 60, 61, and 62.)

[134] O.V. Vasilyev and C. Bowman. Second-Generation Wavelet Collocation Method for the Solution of Partial Differential Equations. *Journal of Computational Physics*, 165:660–693, 2000. (Cited on page 6.)

[135] P.F. Velleman and D.C. Hoaglin. *Applications, Basics, and Computing of Exploratory Data Analysis*. Duxbury Press, Boston, 1981. (Cited on page 57.)

[136] M.J. Vuik. Limiting and shock detection for discontinuous Galerkin solutions using multiwavelets. Master's thesis, Delft University of Technology, 2012. (Cited on pages 3, 23, 24, 28, 84, and 109.)

[137] M.J. Vuik and J.K. Ryan. Multiwavelet troubled-cell indicator for discontinuity detection of discontinuous Galerkin schemes. *Journal of Computational Physics*, 270:138–160, 2014. (Cited on pages 12, 18, 23, 27, 36, 37, 38, 39, 56, 62, 63, 65, and 88.)

[138] M.J. Vuik and J.K. Ryan. Multiwavelets and Jumps in DG Approximations. In R.M. Kirby, M. Berzins, and J.S. Hesthaven, editors, *Spectral and High Order Methods for Partial Differential Equations — ICOSAHOM 2014*, volume 106 of *Lecture Notes in Computational Science and Engineering*. Springer International Publishing, 2015. (Cited on pages 33, 38, 56, 63, and 88.)

[139] M.J. Vuik and J.K. Ryan. Automated parameters for troubled-cell indicators using outlier detection. *SIAM Journal on Scientific Computing*, 38(1):A84–A104, 2016. (Cited on pages 57, 60, 62, 63, 75, 88, and 126.)

[140] M.J. Vuik and J.K. Ryan. Detecting discontinuities over triangular meshes using multiwavelets. Springer International Publishing, submitted. Conference proceedings of ICOSAHOM 2016. (Cited on pages 12, 102, 105, 110, and 111.)

[141] D.F. Walnut. *An Introduction to Wavelet Analysis*. Applied and Numerical Harmonic Analysis. Birkhäuser, Boston, first edition, 2002. (Cited on page 32.)

[142] Z. Wang, Q. Tang, W. Guo, and Y. Cheng. Sparse grid discontinuous Galerkin methods for high-dimensional elliptic equations. *Journal of Computational Physics*, 314:244–263, 2016. (Cited on page 5.)

[143] R.T. Whitaker, M. Mirzargar, and R.M. Kirby. Contour Boxplots: A Method for Characterizing Uncertainty in Feature Sets from Simulation Ensembles. *IEEE Transactions on Visualization and Computer Graphics*, 19(12):2713–2722, 2013. (Cited on page 136.)

[144] P. Woodward and P. Colella. The Numerical Simulation of Two-Dimensional Fluid Flow with Strong Shocks. *Journal of Computational Physics*, 54:115–173, 1984. (Cited on pages 29, 30, 44, 51, 64, and 66.)

[145] M. Yang and Z.J. Wang. A Parameter-Free Generalized Moment Limiter for High-Order Methods on Unstructured Grids. *Advances in Applied Mathematics and Mechanics*, 1(4):451–480, 2009. (Cited on pages 56 and 62.)

[146] T.P.Y. Yu, K. Kolarov, and W. Lynch. Barysymmetric Multiwavelets on Triangle. Technical Report 1997-006, Interval Research Corporation, 1997. (Cited on pages 7, 103, 105, 106, 107, and 108.)

[147] X. Zhang and C.-W. Shu. On maximum-principle-satisfying high order schemes for scalar conservation laws. *Journal of Computational Physics*, 229(9):3091–3120, 2010. (Cited on page 14.)

[148] H.Q. Zhu, Y. Cheng, and J.X. Qiu. A Comparison of the Performance of Limiters for Runge-Kutta Discontinuous Galerkin Methods. *Advances in Applied Mathematics and Mechanics*, 5(3):365–390, 2013. (Cited on pages 3, 16, and 56.)

[149] H.Q. Zhu and J.X. Qiu. Adaptive Runge-Kutta discontinuous Galerkin methods using different indicators: One-dimensional case. *Journal of Computational Physics*, 228(18):6957–6976, 2009. (Cited on pages 40, 51, and 62.)

ACKNOWLEDGMENTS

Many people (in)directly contributed to the research and the process that resulted in this dissertation. Here, I would like to express my gratitude to them. I am aware of the fact that this specific part of my dissertation is best read (together with the propositions). I hope I did not forget to mention anyone specifically. During my PhD, I constantly had to switch from Dutch to English, and vice versa. The same happens in this chapter, and het lijkt veel op hoe het voelde om als Nederlander in een internationale omgeving te werken.

First of all, I am very grateful to my daily supervisor and 'academic mother' Jennifer Ryan. You were always very interested, supportive, encouraging, and enthusiastic, and you are a very experienced researcher. You helped me a lot with the scientific writing and critically reviewed our papers and my dissertation. At the conferences we attended, you introduced me to many people in our field and helped me to build and extend an international network quickly. At the first day of my contract as a PhD researcher, you told me the sad news you found a job in the UK. I was extremely upset but decided I really wanted to keep working with you. We both adapted very quickly to the new situation, with weekly reports (I think I wrote hundreds of 'discussion points') and Skype meetings at fixed times. Even when you were very busy, you were always available for me. I realize that this was all 'voluntary' work for you since you did not have any formal relation with TU Delft anymore. Ik vind het heel bijzonder dat wij al die jaren Nederlands konden blijven praten. Je was heel betrokken, niet alleen bij het onderzoek, maar ook bij mijn hobbies, je oud-collega's in Delft, mijn familie en persoonlijk leven. It was a great pleasure to collaborate with you, and I am sure we became friends.

I would also like to thank my promotor Arnold Heemink. U was heel betrokken, ondanks dat mijn onderzoek niet precies met uw expertise overeenkwam. U las mijn maandoverzichten grondig door, waarna er meestal een inhoudelijke reactie volgde. Particularly in the final stage of my project, your senior support and wise suggestions really helped me.

I want to express my gratitude to the members of the doctoral committee who have read my dissertation, given many suggestions, and will take part in the defence.

I am grateful to DIAM for funding my research, and giving me the opportunity to visit Jennifer at the University of East Anglia, and to attend many international conferences. At the same time, I would like to thank the UEA for hosting me as a visiting researcher.

I had collaborations with many scientists worldwide, here I list some that helped me during my PhD research. I really appreciated talking to my 'academic grandfather' Chi-Wang Shu. He is very supportive and encouraging, and he always makes time to talk with students. I am grateful for the help that Nils Gerhard and Siegfried Müller (RWTH Aachen University) gave me. They helped me a lot with the understanding of multiwavelets and triangular meshes and also invited me to their institute. I had several discussions with Jianxian Qiu about our papers. Lilia Krivodonova read my first paper

before submission. Martina Wirz offered me useful suggestions on PKD polynomials at Oberwolfach. It was great to meet Mahsa Mirzagar, and her insights were very helpful. Furthermore, I would like to acknowledge my colleague Dennis for his great idea to use outlier detection for detecting troubled cells. Mede dankzij jouw input heb ik een supermooi artikel kunnen schrijven! Fahim, you helped me a lot with the DG Matlab code for triangular meshes in the final stage of my PhD. Thank you very much.

I feel indebted to my PhD mentors Henk Polinder and Wioleta Ruszel. We have had many good discussions about all PhD issues I can ever think of, and beyond.

I would like to thank the research group at UEA: the very enthusiastic Julia, Daniel and Xiong Meng.

I would like to express my appreciation to all my colleagues in the Numerical Analysis group. I really enjoyed my time here, and we have a great atmosphere. I could fill pages with personal memories about everyone. Here, I only mention some people.

For about three years, I shared the office with my friends Xiaozhou, Jing, and Peiyao. We have had a lot of fun together. Jing and Peiyao taught me some Chinese, while I tried to teach them Dutch. I loved to try Chinese dishes, and even got a Chinese name. Xiaozhou spent a lot of time teaching me everything about DG and is an excellent cook. Jing, Peiyao and I are close friends, we can talk about everything in life. I will never forget this time. Xie xie!

I spent many hours with Martin van Gijzen while teaching Numeriek. Daarnaast hield je goed in de gaten hoe het met mij ging, en kon ik altijd bij je aankloppen voor een praatje. Hetzelfde geldt voor Fred Vermolen, met wie ik regelmatig om de tafel gezeten heb. I thank Kees Lemmens for his Linux support, and Deborah Dongor and all secretaries who helped with administrative issues. For one and a half years, Manuel, Reinaldo and I formed the board of the SIAM Student Chapter. We had super nice ideas and it was great to organize different activities together. Menel en ik zijn al bevriend vanaf het eerste jaar van onze studie, en hebben daardoor een persoonlijke band opgebouwd. Het was fijn om ervaringen met Guido te delen: wij ervoeren veel dingen in het promotietraject op dezelfde manier.

I would like to acknowledge all my other colleagues: office mate Mohamed, Fei, Gabriella, Zaza, Jochen, Daniël, Luis, Behrouz (thanks for the dinner!), Baljaa, Lisa, Joost (our Linux and Python guru), Lech, Fahraz, Xin He and Jiao (we shared many lunches), Jok, Valia, Matthias (organization of seminars), Kees Oosterlee, Neil, Fons, Duncan, Domenico, Johan, Berna, en de pensionado's Jos, Peter en Guus. In addition, I would like to mention the former PhD students of our group: Paulien, Reijer, Rohit, Elwin, Yue, Marjon, Pavel, Miranda, Abdul. In addition to the nice discussions we had when you were employed at TU Delft, your dissertations were of great help in the final stage of my PhD.

Ondanks dat ik het aan de universiteit enorm naar mijn zin gehad heb, is er een plek waar ik veel liever ben, en dat is thuis. Ik wil mijn ouders heel hartelijk danken voor hun opvoeding, ondersteuning en liefde. Mijn vader stond mij altijd bij, hielp mij veel met praktische zaken, en deelde zijn ervaringen met me. Het is heel gaaf om in zijn voetsporen te treden en hem in mijn werk tegen te komen. Mijn moeder kent mij door en door, en geeft enorm veel liefde aan haar kinderen. Zij is mijn grote voorbeeld. Ook al mijn broers en zussen betekenen enorm veel voor mij. Jacolien & Gert en de kids, Adriaan, Nelleke, Giske, Dies en Hans: ik vind het heel fijn om samen gezin te zijn.

Ook Nicole was heel betrokken en bood altijd een luisterend oor. Ik vind het gaaf om al vanaf de middelbare school vriendin met je te zijn en alles met je te delen. Vincent en Adriaan, ik vind het heel bijzonder om met jullie deel uit te maken van de nieuwe generatie promovendi in onze familie.

Dank je wel, mijn lieve Jacco, voor je liefde, steun, aanmoediging en vertrouwen. Jij laat me stralen! Ik hou van jou en ben trots op jou.

Heere God, Vader in de hemel, U staat boven alle dingen, en hebt alles in Uw hand. Ik dank U voor Uw hulp en leiding in mijn leven, en voor de wonderen van Uw schepping.

Toen zag ik al het werk Gods: dat de mens niet kan uitvinden het werk dat onder de zon geschiedt, om hetwelk een mens arbeidt om te zoeken, maar hij zal het niet uitvinden; ja, indien ook een wijze zeide dat hij het zou weten, zo zal hij het toch niet kunnen uitvinden.

(Prediker/Ecclesiastes 8:17)

CURRICULUM VITÆ

Thea Vuik was born on March 18, 1989, in Capelle aan den IJssel, The Netherlands.

Between 2001 and 2007, she received secondary education at the Comenius College (Capelle aan den IJssel) and finished cum laude.

She began her studies in Applied Mathematics at Delft University of Technology in 2007. After her first year, she was awarded the Young Talent Encouragement Award 2008 (Royal Holland Society of Sciences and Humanities) for achieving the highest average grade at her propaedeutic diploma compared to all mathematics students at her university. In 2010 she finished her BSc degree (cum laude), and in 2012, she obtained her MSc diploma (cum laude). Her MSc thesis, entitled 'Limiting and shock detection for discontinuous Galerkin solutions using multiwavelets', formed the basis for the PhD project that she began in October 2012. From January 2013 she also became Visiting Researcher at the University of East Anglia, Norwich, United Kingdom, where she often visited her daily supervisor, dr. J.K. Ryan.

As a PhD candidate, Thea focused on the use of multiwavelets and outlier detection for troubled-cell indication in discontinuous Galerkin methods. She was often invited to give presentations at such places as Oberwolfach, Glasgow, Turin, and ICOSAHOM. She received a prize for giving the best student presentation at the 26th Biennial Numerical Analysis Conference, sponsored by the UK and Ireland section of SIAM (2015). In addition to her research, Thea was a member of the PhD Council at TU Delft (2014–2016), and founder, secretary and treasurer of the SIAM Student Chapter Delft (2014–2016). She was awarded the SIAM Student Chapter Certificate of Recognition for her outstanding contributions to the SIAM Student Chapter at TU Delft (2016). Teaching experiences include assisting in lab sessions (Numerical Methods for Ordinary Differential Equations and Calculus), rewriting the textbook on Numerical Methods for Ordinary Differential Equations, and the grading of exams.

Since November 2016, Thea is working as a scientific software engineer at VORtech in Delft.

LIST OF PUBLICATIONS

Books

C. Vuik, F.J. Vermolen, M.B. van Gijzen, M.J. Vuik: *Numerical Methods for Ordinary Differential Equations,* Delft Academic Press / VSSD, 2015.

Publications in Refereed Journals

- M.J. Vuik and J.K. Ryan. *Automated parameters for troubled-cell indicators using outlier detection.* SIAM Journal on Scientific Computing, 38(1):A84–A104, 2016. 1 citation.
- M.J. Vuik and J.K. Ryan. *Multiwavelet troubled-cell indicator for discontinuity detection of discontinuous Galerkin schemes.* Journal of Computational Physics, 270:138–160, 2014. 13 citations.

Publications in Refereed Proceedings and Lecture Notes

- M.J. Vuik and J.K. Ryan. *Detecting discontinuities over triangular meshes using multiwavelets.* Submitted as a contribution to the conference proceedings of ICOSAHOM 2016.
- M.J. Vuik and J.K. Ryan. *Multiwavelets and Jumps in DG Approximations.* In R.M. Kirby, M. Berzins, and J.S. Hesthaven, editors, Spectral and High Order Methods for Partial Differential Equations — ICOSAHOM 2014, volume 106 of Lecture Notes in Computational Science and Engineering. Springer International Publishing, 2015. 1 citation.

Presentations and Conference Participation

- Invited Speaker:
  - *Applied Mathematics seminar.* May 23, 2016. University of East Anglia, United Kingdom.
  - *Workshop 'Recent Developments in the Numerics of Nonlinear Hyperbolic Conservation Laws'.* September 14–18, 2015. Oberwolfach, Germany.
  - *Miniworkshop 'High order reconstruction and well balancing techniques for hyperbolic conservation and balance laws'.* April 15–16, 2015. Turin, Italy.
  - *Werkgemeenschap Scientific Computing Spring Meeting.* May 23, 2014. Centrum Wiskunde & Informatica (CWI), Amsterdam.
- Mini-symposium Speaker:
  - *International Conference on Spectral and High Order Methods.* June 27–July 1, 2016. Rio de Janeiro, Brazil.
  - *26th Biennial Numerical Analysis Conference.* June 23–26, 2015. Glasgow, UK.
  - *International Conference on Spectral and High Order Methods.* June 23–27, 2014. Salt Lake City, USA.
  - *International Conference on Applied Mathematics, Modeling and Computational Science.* August 26–30, 2013. Waterloo, Canada.